Growth, Defect Structure and Critical Currents in $YBa_2Cu_3O_{7-\delta}$ Thin Films

Groei, Defektstruktuur en Kritische Stromen in Dunne $YBa_2Cu_3O_{7-\delta}$ Lagen

Cover: three dimensional impression of the surface of a laser ablated $YBa_2Cu_3O_{7-\delta}$ film, etched in the dislocation specific wet-chemical etchand Br/ethanol (and imaged by means of atomic force microscopy). At dislocation sites the film dissolves faster, resulting in the formation of square, sharp bottomed etch pits. The density of etch pits is a measure for the density of dislocations emerging at the film surface.

This work is part of the research program of FOM (stichting Fundamenteel Onderzoek der Materie), which is financially supported by NWO (Nederlandse organisatie voor Wetenschappelijk Onderzoek). The work was carried out at:

Vrije Universiteit
Faculty of Sciences
Division of Physics and Astronomy
De Boelelaan 1081
NL-1081 HV Amsterdam
The Netherlands

ISBN 90-9014604-0

VRIJE UNIVERSITEIT

Growth, Defect Structure and Critical Currents in $YBa_2Cu_3O_{7-\delta}$ Thin Films

ACADEMISCH PROEFSCHRIFT

ter verkrijging van de graad van doctor aan
de Vrije Universiteit te Amsterdam,
op gezag van de rector magni...cus
prof.dr. T. Sminia,
in het openbaar te verdedigen
ten overstaan van de promotiecommissie
van de faculteit der Exacte Wetenschappen n Natuurkunde en Sterrenkunde
op dinsdag 1 mei 2001 om 13.45 uur
in het hoofdgebouw van de universiteit,
De Boelelaan 1105

door

Jeroen Marcel Huijbregtse

geboren te Middelburg

Promotor: prof.dr. R.P. Griessen
Copromotor: dr. B. Dam

Voor mijn ouders

Contents

Chapter 1

General introduction

Fundamental investigations of high-T_c superconductors have mainly been done for single crystalline materials. In this thesis we consider thin …lms and show that their intrinsic defect structure quite paradoxically leads to improved superconducting properties. In particular, this thesis addresses three central questions: (i) what is the structural defect that is responsible for the extremely high superconducting currents that can be passed without dissipation (ii) what is the mechanism by which these defects are induced during …lm growth and (iii) can we control the growth process in such a way that we can tune the superconducting properties? In this chapter the basic concepts are introduced and a research strategy is developed.

1.1 The microstructural basis of high j_c

After the discovery of the …rst high-T_c (HT_c) superconductor in 1986 [1], the transition temperature T_c, below which the zero resistivity state is reached, quickly raised above the liquid nitrogen temperature of 77 K for $YBa_2Cu_3O_{7\,i\,\pm}$ in 1987 [2]. Since this temperature is commercially feasible, technological application of HT_c cuprates in high current, high frequency and highly sensitive magnetic devices have become more interesting [3]. Examples of large scale applications are power cables that transport electrical currents with low energy dissipation and powerful superconducting magnets. One of the major drawbacks of the cuprates is their brittleness, which makes their processing di¢cult. Thin …lms do not su¤er from this limitation. They are applicable in electronic applications such as passive microwave components (resonators, antennas), magnetometers and digital circuits.

However, as outlined below, a problem arises if one tries to pass a transport current at density j without dissipation through such a material. Cuprate superconductors are characterized [4] by an extremely small coherence length », which is of the order of the unit cell (for instance, » = 1:5 nm for $YBa_2Cu_3O_{7\,i\,\pm}$ along the CuO_2 planes at low temperatures). This parameter sets the length scale for spatial variations in the superconducting order parameter (or the density of superconducting electrons). On the other hand, the length scale for the spatial variations in magnetic induction (the magnetic penetration depth ¸) is two orders of magnitude larger. It can be shown [4] that for ¸=» > $1=\sqrt{2}$ a mixed state occurs above a magnetic …eld B_{c1} in which normal and superconducting regions coexist. These normal regions of size 2» carry a quantized amount of magnetic ‡ux $©_0 = 2{:}068 \pounds 10^{i\,15}$ Tm^2 and are called vortices. The areal density n_v of vortices is given by $B = n_v©_0$, where $B = {}^1{}_0H$ is the local magnetic induction. The presence of vortices within a superconducting matrix is not a problem by itself. As long as the vortex cores do not overlap, there is a fully superconducting path within the material. However, if a current (density) j is passed through the superconductor, a Lorentz force F_L is exerted on the vortices, which equals $j©_0$ per unit length in a perpendicular con…guration. The problem is that these vortices will start to move under in‡uence of F_L. In such a situation an electrical current passes through the normal core of the vortex [5], causing dissipation and noise.

To avoid this problem, either the creation of vortices has to be prevented or vortex motion must be prohibited. Let us consider the creation of vortices …rst. As discussed above, at magnetic …elds below $B_{c1} = ©_0 \ln(¸=») = (4¼¸^2)$ there are no vortices. In cuprate superconductors the penetration depth ¸ is large, which results in a small lower critical …eld B_{c1}. Therefore, the self-…eld of a current that is passed through such a superconductor will immediately introduce vortices. Moreover, in many technological applications an external magnetic …eld is present (in addition to the earth magnetic …eld). Hence, preventing the creation of vortices is not a feasible solution to circumvent dissipation. Fortunately, nature provides an alternative solution. Within the superconductor, there are always energetically more favorable sites for vortices. These are defects in the crystal structure, ranging from small defects (such as oxygen vacancies) to extended defects (such as grain boundaries). At those sites, the super-

conducting order parameter is depressed and it costs less energy to drive such regions in the normal state within the superconducting condensate. Consequently, a certain current (density) is necessary to depin a vortex from the energetically favorable defect sites. The current which overcomes the pinning force exerted by defects is called the critical current density j_c.

In this simple picture, the superconducting properties improve by adding defects! There is, however, an optimum for j_c with respect to structural disorder. If the material becomes too defective, the superconducting order parameter is depressed everywhere. The pinning sites in such a material are not very effective, which results in a low j_c. Hence, the highest j_c is expected in structurally perfect superconductors containing localized defective regions. On the other hand, such regions should not be so large that they act as weak links between different parts of the superconductor. Weak links limit the critical current again.

Soon after the discovery of bulk HT_c superconductors, the first $YBa_2Cu_3O_{7-\delta}$ single crystals were synthesized [6]. In single crystals the vortex pinning is facilitated by randomly distributed point defects, resulting in a j_c of the order of 10^{10} A/m^2 [7]. Artificially inducing columnar defects by means of heavy ion irradiation only locally depresses superconductivity and j_c increases by a factor of ten [8]. Surprisingly, the critical currents in as-grown $YBa_2Cu_3O_{7-\delta}$ films [9] (i.e., without any attempt to induce disorder artificially) are even larger. As shown in this thesis, current densities up to 10^{12} A/m^2 are found at low temperatures and small magnetic fields. Compared to single crystals, the structural quality of these films is much poorer [10]. Therefore, it was concluded [11, 12] that correlated disorder (extended defects) are responsible for both the high currents and the strong magnetic field dependence of these currents, analogous to irradiated single crystals. However, somehow the natural disorder in films is far more effective in pinning vortices than the artificially induced disorder in single crystals.

Remarkably, in the first ten years after the discovery of the first cuprate superconductor, the specific defect responsible for the high currents in films was not identified. Motivated by this peculiar state of affairs, in September 1996 the present Ph.D. work was started to address pinning in films from a materials science point of view. The main goal of this thesis is to identify the dominant natural pinning sites in thin films of $YBa_2Cu_3O_{7-\delta}$ grown by pulsed laser deposition on single crystalline (100) $SrTiO_3$ substrates. Clearly, if one wishes to tune the superconducting properties, we need to control the density of these defects. Hence, the mechanism by which correlated disorder is induced during the fabrication of such films is equally important.

In the remaining of this chapter we expose the strategy (i) to identify the strongest pinning sites (ii) to unravel the mechanism by which they are created and (iii) to find a way to tailor the superconducting properties of the films making use of the first two points. Finally, we note that this Ph.D. research project is divided into two parts. The present thesis concentrates on the microstructural properties of the $YBa_2Cu_3O_{7-\delta}$ films. While our emphasis is on establishing qualitative (or semi-quantitative) corre-

lations between the defect structure and superconducting properties of these …lms, a subsequent thesis by F.C. Klaassen [13] will cover ‡ux pinning in detail.[1]

1.2 Basic ingredients

To investigate pinning in …lms, we …rst have to …nd a reproducible deposition process. Only when we can reproducibly vary one type of defects, we can identify the defects that are responsible for pinning. The two basic ingredients, …lm growth and ‡ux pinning, are shortly discussed below.

1.2.1 Growth of epitaxial …lms

In general, thin …lms result from condensation of the evaporated constituents onto a substrate material. Although there are many techniques to evaporate these constituents [14], the process of …lm growth is, in …rst approximation, the same. In all thin …lm growth processes, elevated substrate temperatures and pressures are used to ensure that the desired phase is thermodynamically stable and that it is kinetically allowed to form at the applied growth conditions. Inducing crystallization does not necessarily result in the formation of epitaxial …lms. Epitaxial …lms are structurally aligned with the substrate material. This is only possible if the substrate and …lm material are structurally compatible. For instance, the …lm and substrate material must have comparable lattice constants and thermal expansion coe¢cients. In this thesis, we grow orthorhombic $YBa_2Cu_3O_{7-\pm}$ …lms epitaxially onto cubic (100) $SrTiO_3$ substrates (1% lattice mismatch).

We employ pulsed laser ablation (PLD) [15] to deposit the $YBa_2Cu_3O_{7-\pm}$ …lms. Besides the relatively low capital costs as compared to for instance molecular beam epitaxy, the main strength of PLD is its simplicity. By repeatedly irradiating a target material with an intense laser beam in the UV range, virtually any material can be produced in thin …lm form. Moreover, the target composition is faithfully reproduced in the …lm at su¢ciently large laser energies. In addition, due to the high background pressures that can be employed (up to about 1 mbar), there is no need for a post-anneal treatment to correct for oxygen de…ciencies in the deposition of oxide materials. The versatility of PLD is nicely illustrated by the various materials that we successfully evaporated during the last few years. Apart from epitaxial $REBa_2Cu_3O_{7-\pm}$ …lms (RE = Y, Nd, Pr, Eu), these are: epitaxial RE_2CuO_4 …lms (RE = Sm, Pr, Nd), and epitaxial $Sr_xLa_{1-x}CuO_2$ …lms (so-called in…nite layers [16], the parent structure of the cuprates), but also compounds such as nanocrystalline YH_x (switchable mirrors [17]) and submicron Y_2O_3 precipitates have been prepared.

The basic simplicity of PLD turned out to be somewhat misleading. In the deposition of complex multi-component oxides such as $YBa_2Cu_3O_{7-\pm}$ it is di¢cult to transfer the composition from the target exactly to the substrate. Non-stoichiometric transfer

[1] The critical current measurements that are presented in this thesis are performed by F.C. Klaassen. More extensive measurements, including measurements of the dynamical relaxation rate, will be presented in his thesis [13].

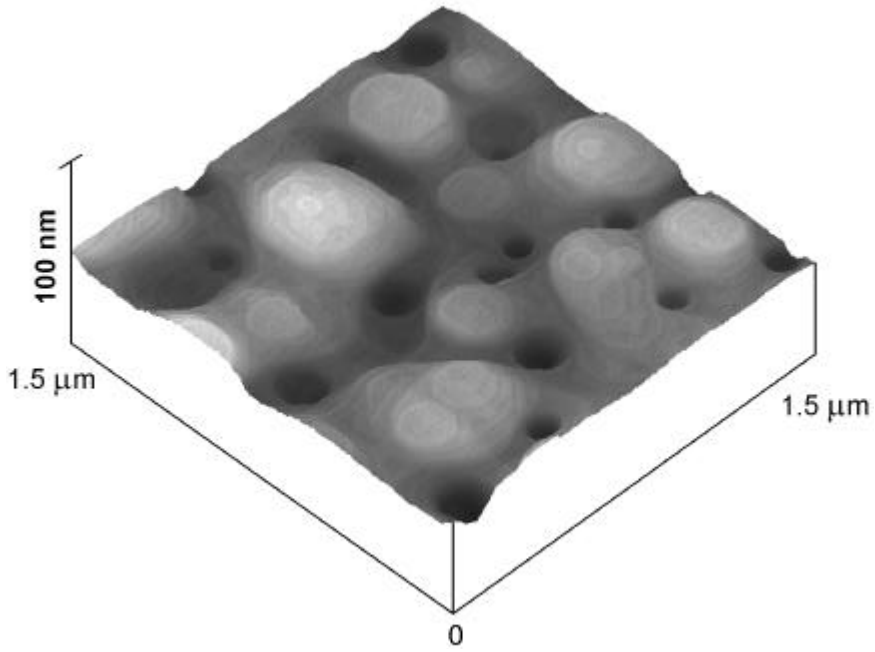

Figure 1.1: Atomic force microscope (AFM) height image of a 150 nm thick $YBa_2Cu_3O_{7-\delta}$ …lm pulsed laser deposited on (100) $SrTiO_3$, revealing the presence of many structural defects (bright is high and dark is low). The surface morphology consists of semi-regularly spaced growth islands that are separated by trenches. Within the trenches some deeper depressions can be discerned, corresponding to the sites where dislocations (linear defects) emerge. If the islands are slightly misoriented, the growth islands are separated by low-angle grain boundaries (planar defects). Note the large height scale, indicating that there is appreciable thickness modulation.

results in precipitates (inclusions of di¤erent composition and structure) and point defects in the …lm material, which in‡uence the superconducting properties of the …lm. As shown in chapter 2, the …lm composition is a sensitive function of the laser energy. Laser irradiation of a target material induces structural modi…cations. Moreover, di¤usion processes take place in multi-component targets if constituents are preferentially ablated. Both processes cause the …lm composition to be di¤erent from the target composition. Consequently, also the homogeneity of the laser beam spot is an important issue. This has to be taken into account in the design of the PLD system, for instance by using projection optics or a beam homogenizer. Having recognized the importance of the laser characteristics in PLD, high-quality epitaxial $YBa_2Cu_3O_{7-\delta}$ …lms can be reproducibly grown.

Without going into the details of the microstructure of $YBa_2Cu_3O_{7-\delta}$ films, a number of interesting features can already be derived from the surface morphology of the as-grown films. In Fig. 1.1 a typical atomic force microscope (AFM) height image of a high quality $YBa_2Cu_3O_{7-\delta}$ film pulsed laser deposited on (100) $SrTiO_3$ is shown. The surface morphology is far from flat. It consists of growth islands which are more or less regularly distributed and are of comparable size (typically, their diameter is of the order of 100 nm). Assuming that the growth islands have a certain misorientation, they are separated by low angle grain boundaries. Moreover, as this particular film is around 150 nm thick, the height scale reveals that the thickness fluctuations are considerable. In addition, within the trenches separating the growth islands some deeper depressions ("holes") can be distinguished. Such locations are indicative of dislocations (linear defects) emerging at the surface of the film.
All these observations indicate that our epitaxial films, although of a very high overall structural quality (as measured by means of X-ray diffraction), are far from perfect. As schematically summarized in Fig. 1.2, point defects, thickness modulations, linear defects (dislocations) and planar defects are present as possible pinning sites for vortices. These films belong to a class of materials which is completely different from that of single-crystals, where all defect densities are orders of magnitude smaller.

1.2.2 Strong vortex pinning

The morphological features of the thin film described above have some direct consequences for the pinning of vortices, which determines the maximum current density that can be passed without dissipation. This critical current density depends strongly on temperature and magnetic field (number of vortices). In this section we introduce the parameters that determine j_c and show how temperature and magnetic field enter the concept of vortex pinning in a qualitative way.

Magnitude of j_c

Due to its positive self-energy ε_l per unit length, a vortex will always try to minimize its length. Thickness fluctuations as observed in Fig. 1.1 are, therefore, preferential sites for vortices [see Fig. 1.2(b)]. However, as will be shown in chapter 4, the contribution to vortex pinning from such surface corrugations as compared to structural defects is insignificant in films. Structural defects with a size of the order of 2ξ (the size of the normal core of the vortex) are responsible for the strongest vortex pinning phenomena. Due to the complete overlap of vortex core and defect, the condensation energy is fully gained. This energy gain is called the pinning energy. The largest pinning effects are expected in the case of linearly correlated disorder [18, 19], as schematically shown in Fig. 1.2(c). Linear defects with a radius $\approx \xi$ can pin vortices over their full length. Moreover, linear defects only locally depress superconductivity and leave the bulk unaffected. At low fields the repulsive interaction between vortices can be neglected and the critical current density approaches the theoretical single-vortex limit. This limit is given by the depairing current density $j_{c0} = \Phi_0/(3\sqrt{3}\mu_0\lambda^2\xi)$ [20]. Above the depairing limit superconductivity is destroyed,

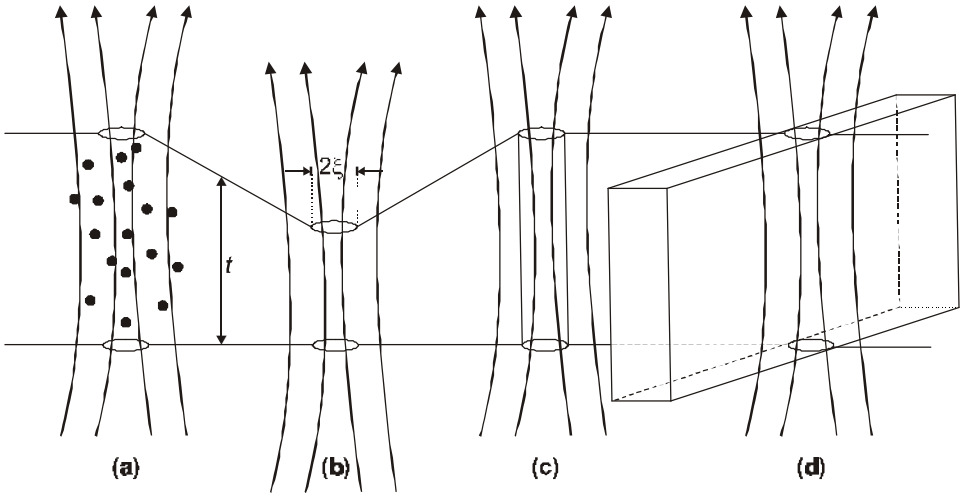

Figure 1.2: Schematic illustration of vortex pinning by di¤erent kinds of structural disorder that are all present in our thin …lms. The vortices are indicated by magnetic …eld lines and have a normal core of size 2»; the …lm thickness varies and is indicated by t. Note that the magnetic …eld falls of over a characteristic length scale ¸ À ». Shown are: (a) a vortex pinned by point defects (b) a vortex pinned by a thickness modulation (minimizing its length), (c) a vortex pinned by a linear defect, and (d) a vortex pinned by a planar defect (note that the vortex is unpinned along the direction of the planar defect).

no matter how strong vortex pinning is. At this point, the temperature dependence enters the problem. Qualitatively, both ¸ and » increase with increasing temperature, causing a decrease in j_{c0}.

Characteristic shape of $j_c(B)$

The repulsive vortex-vortex interaction quickly falls o¤ with increasing vortex spacing d_{vv} ($\frac{1}{4} 1/\sqrt{n_v} \_ 1/\sqrt{B}$). At low …elds d_{vv} is much larger than the average linear defect spacing d ($\frac{1}{4} 1/\sqrt{n}$ where n is the number of linear defects per unit area) and all vortices occupy a defect site. With increasing magnetic …eld, the in‡uence of vortex-vortex interaction becomes stronger and vortices tend to form a lattice, in order to minimize the total interaction energy. In the presence of linear defects, the vortices slightly move away from these lattice positions to …nd a linear defect site. On the one hand pinning energy is gained, while on the other hand some interaction energy has to be payed. As long as the vortices …nd a defect site, the current density remains constant (and high). However, when the vortex and defect spacing are of the same order of magnitude ($d_{vv} \frac{1}{4} d$), the increase in interaction energy is comparable

to the pinning energy and not all pinning sites can be occupied by vortices. Especially pinning sites that are close to each other cannot be used e¤ectively. At this point j_c starts to decrease. At even larger magnetic …elds (d_{vv} ¿ d), there are more vortices than pinning sites. In this situation, the additional vortices are only weakly pinned and the critical current quickly decreases with increasing magnetic …eld.
In this picture, a cross-over …eld $B^¤$ [18, 19] is expected in the magnetic …eld dependence of j_c. Below $B^¤$ vortex-vortex interactions are less important than vortex-defect interactions and j_c does not depend on the magnetic …eld (and approaches j_{c0}). Above $B^¤$ there are weakly pinned vortices and j_c decreases rapidly with increasing magnetic …eld. Apart from a geometrical constant re‡ecting the defect distribution, vortex-vortex interactions and the shape of the pinning potential (vortex-defect interaction), $B^¤$ is essentially determined by the linear defect density n: $B^¤ ¼ n©_0$.

1.3 Strategy

Having introduced the basic ingredients, we now formulate the strategy that we follow to prove that linear defects are the most important pinning sites in $YBa_2Cu_3O_{7\,i\,±}$ …lms.
First of all, in order to correlate the microstructure and superconducting properties in di¤erent …lms, it is necessary to control the deposition process in such a way that identical …lms can be made. The conditions for reproducibility in pulsed laser deposition are investigated in chapter 2. Here, it is shown that the laser energy is a critical parameter in the deposition process. We develop a phenomenological model that explains the experimentally observed dependence of …lm composition on laser energy.
Next, we investigate the origin of high critical currents in these …lms (chapter 3). To identify linear defects as the dominant pinning sites, we …rst develop a technique to determine the density as well as the length and lateral distribution of linear defects in …lms. The density of linear defects turns out to be easily tunable by the deposition conditions. Measuring the superconducting current density as a function of magnetic …eld for a large series of …lms yields compelling evidence for the dominant behavior of threading dislocations as vortex pinning sites in …lms. A comparison is made between …lms containing natural linear defects (dislocations) and single crystals with arti…cial columnar defects (introduced by heavy ion irradiation).
In chapter 4, the in‡uence of alternative natural pinning sites is investigated. In addition to threading dislocations, the defect structure is characterized by point defects, precipitates, planar defects (such as twin planes, anti-phase boundaries and low-angle grain boundaries) and thickness ‡uctuations. Employing a post-anneal treatment to change the relative densities of these defects, we study the contribution to vortex pinning by defects other than linear defects. Special attention is paid to the critical current density at high magnetic …elds. Transmission electron microscopy is performed to show that threading dislocations are neither related to twinning dislocations nor part of low-angle grain boundaries.

Having established the importance of threading dislocations in vortex pinning in thin …lms of $YBa_2Cu_3O_{7\,i\,\pm}$, we concentrate now on how these linear defects are formed during the growth process.
Chapter 5 serves as an introduction to the remaining two chapters. It consists of a discussion of the possible mechanisms for the formation of threading dislocations. Since the dislocations originate at or close to the substrate-…lm interface, these mechanisms are either related to the substrate or to the initial stages of …lm growth. All mechanisms related to the nature of the substrate material are shown to be inoperative and we concentrate on the $YBa_2Cu_3O_{7\,i\,\pm}$ nucleation and growth mechanism in the following two chapters.
In chapter 6 we investigate whether threading dislocations are induced by precipitates, which form preferentially during nucleation of the …rst monolayer. Threading dislocations may form when such precipitates are overgrown. The precipitates result from non-unit cell nucleation of $YBa_2Cu_3O_{7\,i\,\pm}$ on $SrTiO_3$. This nucleation process is in‡uenced by the terminating plane of the substrate material. Therefore, we develop a new procedure to prepare SrO-terminated (100) $SrTiO_3$ substrates (in addition to the well-known TiO_2-termination). Tailoring the substrate termination and/or the …lm composition, allows us to control preferential precipitation. Threading dislocations are always present, showing that preferential precipitation during …lm nucleation cannot be the main origin of the dislocations. The dislocation density, however, can be enhanced by creating arti…cially secondary phases at the interface.
If the threading dislocations in $YBa_2Cu_3O_{7\,i\,\pm}$ …lms are also not created during the nucleation stage, they must form in the following stages of growth. In chapter 7, we make use of the substrate termination to study the full growth mechanism. A self-assembled island structure develops above a critical …lm thickness, which depends sensitively on the substrate termination used. Threading dislocations are introduced from this point on. The relation between islands and threading dislocations is revealed and the in‡uence of the deposition parameters on the kinetics is discussed. Finally, we propose a general approach to study the growth of hetero-epitaxial systems.
On the basis of our comprehensive and systematic investigation, we conclude that the peculiar nature of hetero-epitaxial growth of complex oxides is basically responsible for the high critical currents in $YBa_2Cu_3O_{7\,i\,\pm}$ …lms.

References

[1] J.G. Bednorz and K.A. Müller, Z. Phys. B 64, 189 (1986)

[2] M.K. Wu, J.R. Ashburn, C.J. Torng, P.H. Horr, R.L. Meng, L. Gao, Z.J. Huang, Y.Q. Wang, and C.W. Chu, Phys. Rev. Lett. 58, 908 (1987)

[3] M. Cyrot and D. Pavuna, Introduction to superconductivity and high-T_c materials (World Scienti…c, London, 1992)

[4] M. Tinkham, Introduction to superconductivity (McGraw-Hill, New York, 1996)

[5] J. Bardeen and M.J. Stephen, Phys. Rev. 140, 1197A (1965)

[6] L.S. Schneemeyer, J.V. Waszczak, T. Siegrist, R.B. van Dover, L.W. Rupp, B. Batlogg, R.J. Cava, and D.W. Murphy, Nature (London) 328, 601 (1987)

[7] L. Civale, A.D. Marwick, M.W. McElfresh, T.K. Worthington, A.P. Malozemo¤, F.H. Holtzberg, J.R. Thompson, and M.A. Kirk, Phys. Rev. Lett. 65, 1164 (1990)

[8] L. Civale, A.D. Marwick, T.K. Worthington, M.A. Kirk, J.R. Thompson, L. Krusin-Elbaum, Y. Sun, J.R. Clem, and F. Holtzberg, Phys. Rev. Lett. 67, 648 (1991)

[9] P. Chaudhari, R.H. Koch, R.B. Laibowitz, T.R. McGuire, and R.J. Gambino, Phys. Rev. Lett. 58, 2684 (1987)

[10] R. Ramesh, D.M. Hwang, T. Venkatesan, T.S. Ravi, L. Nazar, A. Inam, X.D. Wu, B. Dutta, G. Thomas, A.F. Marshall, and T.H. Geballe, Science 247, 57 (1990)

[11] T.L. Hylton and M.R. Beasley, Phys. Rev. B 41, 11669 (1990)

[12] L.R. Tessler, J. Provost and A. Maignan, Appl. Phys. Lett. 58, 528 (1991)

[13] F.C. Klaassen, Ph.D. thesis in preparation (2001)

[14] R. Wördenweber, Supercond. Sci. Technol. 12, R86 (1999)

[15] D.B. Chrisey and G.K. Hubler, Pulsed Laser Deposition of Thin Films (Wiley, New York, 1994)

[16] M.G. Smith, A. Manthiram, J. Zhou, J.B. Goodenough, and J.T. Markert, Nature (London) 351, 549 (1991)

[17] J.N. Huiberts, R. Griessen, J.H. Rector, R.J. Wijngaarden, J.P. Dekker, D.G. de Groot, and N.J. Koeman, Nature (London) 380, 231 (1996)

[18] D.R. Nelson and V.M. Vinokur, Phys. Rev. Lett. 68. 2398 (1992)

[19] D.R. Nelson and V.M. Vinokur, Phys. Rev. B 48, 13060 (1993)

[20] G. Blatter, M.V. Feigel'man, V.B. Geshkenbein, A.I. Larkin, and V.M. Vinokur, Rev. Mod. Phys. 66, 1125 (1994)

Chapter 2

Conditions for stoichiometric transfer in pulsed laser deposition

The laser ‡uence dependence of the composition of laser ablated $YBa_2Cu_3O_{7\,i\,\pm}$ …lms is investigated and interpreted in terms of laser induced target modi…cations. Both target degradation (at ‡uence $J < 1{:}0$ J/cm^2) and di¤usion-assisted preferential ablation ($1{:}0 < J < 1{:}3$ J/cm^2) are responsible for non-stoichiometric transfer in pulsed laser deposition. A one dimensional, moving boundary di¤usion-model is developed to describe di¤usion-assisted preferential ablation. This model predicts stoichiometric transfer at large ablation rates. Indeed for J À $1{:}3$ J/cm^2 stoichiometric deposition is found, resulting in precipitate-free …lms. Slightly o¤-stoichiometric …lms, deposited in the di¤usion-assisted preferential ablation regime, exhibit the best superconducting properties ($T_c = 91{:}0$ K, ¢$T_c = 0{:}4$ K). These high quality …lms can be produced with a remarkably high reproducibility.[1]

[1]This chapter is based on the paper by J.M. Huijbregtse, B. Dam, J.H Rector, and R. Griessen, J. Appl. Phys. 86, 6528 (1999)

2.1 Introduction

Pulsed laser deposition (PLD) is a powerful technique for the deposition of thin …lms of a wide range of materials, including metals, diamond, semiconductors and ceramic oxide materials [1]. One of the reasons for the widespread use of PLD is the ability to directly transfer the composition from multi-component targets to the substrate. This stoichiometric deposition makes PLD highly suitable for the deposition of high-T_c superconductors such as $YBa_2Cu_3O_{7\,i\,\pm}$. In practice one …nds, however, that …lms are only approximately stoichiometric.

Although epitaxial $YBa_2Cu_3O_{7\,i\,\pm}$ …lms are obtained by PLD that exhibit sharp resistive transitions at critical temperatures $T_c > 90$ K and critical current densities of 10^{11} ¡ 10^{12} A/m^2 at 4.2 K (see chapters 3 and 4 or Ref. [2] for a review), the surface morphology of these …lms is often poor. A large particle density is usually observed when examining the surface morphology by atomic force microscopy. Obviously, for many technological applications, a ‡at surface is required. Generally, two types of particles are distinguished [3]: droplets (large particles with a diameter > 0:5 ¹m that are transferred directly from the target) and precipitates (secondary phases). The density of droplets is reduced by lowering the laser beam ‡uence [4, 5], changing the deposition geometry [6], using velocity …ltration [7] or crossed ‡ux techniques [8]. It has also been shown that carefully preparing and conditioning the target material signi…cantly reduces the droplet density [9, 10, 11]. Precipitates (diameter < 0:5 ¹m) are segregation products, resulting from o¤-stoichiometries in the …lm. Due to the limited solubility in $YBa_2Cu_3O_{7\,i\,\pm}$ [12], small deviations from the 123 stoichiometry induce precipitates. O¤-stoichiometries also in‡uence the electrical and structural properties of the thin …lms [13, 14, 15, 16, 17]. Therefore, to optimize both the surface morphology and the physical properties, it is important to understand the mechanisms and the limitations of the conservation of composition in the PLD process.

Although several ablation mechanisms have been identi…ed [1, 18], in realistic thin …lm deposition processes the target is repeatedly irradiated by laser pulses and subsurface processes become dominant. In the laser induced melt, phase transitions may occur. Moreover, any o¤-stoichiometric ablation process has to be sustained by volume di¤usion if it is to yield persistently o¤-stoichiometric …lms. Therefore, in the long run, these subsurface processes determine whether the material transfer is stoichiometric or not. In $YBa_2Cu_3O_{7\,i\,\pm}$ for example, a phase separation in the target takes place [4, 19, 20, 21] below the threshold ‡uence J_{th} = 1.0 J/cm^2 and the resulting …lms are non-stoichiometric below J_{th}. Note, that in this case, we can not draw any conclusion about the ablation mechanism itself. In the pulsed laser deposition of $SrTiO_3$ [21, 22] preferential ablation of Sr occurs. It was found, however, that upon continued irradiation of the target surface, o¤-stoichiometric Sr-rich …lms can only persistently be obtained if the volume di¤usion of Sr towards the target surface is fast enough to replenish the surface depletion of Sr. If the volume di¤usion can not keep up with the preferential ablation speed, eventually stoichiometric …lms are obtained. Therefore, preferential ablation alone is not su¢cient to explain persistent non-stoichiometric deposition.

In the present chapter, we study the PLD of $YBa_2Cu_3O_{7-\pm}$ …lms, without, however, going into the details of the ablation mechanism itself. We show that above J_{th} also in $YBa_2Cu_3O_{7-\pm}$ di¤usion-assisted preferential ablation plays a role in the ablation process. Using a phenomenological model, we conclude that it is in fact the pulsed character in combination with di¤usion that is responsible for the persistence of the non-stoichiometric deposition process. From the model it is also predicted that stoichiometric transfer should eventually occur at large ‡uences. Indeed we observe stoichiometric, precipitate-free …lms at $J \geq 1.3$ J/cm^2. The best physical properties are found for slightly o¤-stoichiometric …lms (i.e., with some precipitates) that are deposited in the di¤usion-assisted preferential ablation regime. Finally, special attention is paid to the reproducibility. We …nd that the reproducibility of these …lms is remarkably good. Without any exception, all …lms exhibit a $T_c > 90$ K. This remarkable reproducibility is attributed to the excellent laser characteristics and the design of the laser beam trajectory, resulting in a well controlled, reproducible and uniform laser spot.

2.2 PLD set-up and experimental procedures

In our pulsed laser deposition set-up a KrF excimer laser beam (QUESTEK Impulse 4750GL: wavelength 248 nm, pulse duration ¿ = 30 ns) is guided into an ultra high vacuum system onto the target at an inclination of 45±, see Fig 2.1(a). The pulse frequency of the laser is set at 5 Hz, while the ‡uence J [in J/cm^2] is varied by means of an optical attenuator. In order to obtain a spatially homogeneous spot on the target, projection optics (OPTEC SA) is used and a homogeneous part of the beam is selected by a circular mask with a diameter of 8.3 mm. This spot is projected onto the target (5£ demagni…cation). To account for energy losses at windows and mirrors, the laser ‡uence is measured inside the deposition chamber at the position of the target.

All depositions are performed using a high density, polycrystalline tetragonal $YBa_2Cu_3O_{6+x}$ target (PRAXAIR, > 99:9% pure raw materials) which can be rotated during deposition. The substrates are glued on a resistive heater with silver paint and the temperature is measured both with a thermocouple and a pyrometer. During all deposition runs, the target-to-substrate distance d_{T-S} is …xed at 3.5 cm and the oxygen pressure p_{O_2} is set at 15 Pa. The deposition rate is measured with a retractable quartz crystal monitor, located 2 cm above the target.

Using these settings, two sets of experiments are performed in which only the ‡uence of the laser beam is varied. First, thin amorphous $YBa_2Cu_3O_{6+x}$ …lms are deposited on (100) Si substrates at room temperature from a stationary target. The composition of these …lms is measured with Rutherford backscattering spectrometry (RBS), using 2.0 MeV He^+. After …lm deposition, the composition of the irradiated target spots is determined, also by means of RBS. Secondly, crystalline c-axis oriented 140 nm thick $YBa_2Cu_3O_{7-\pm}$ …lms are deposited onto (100) $SrTiO_3$ substrates from a rotating target. In order to obtain superconducting …lms, the substrate is heated to 815±C during deposition. Immediately after deposition, the …lms are quenched in

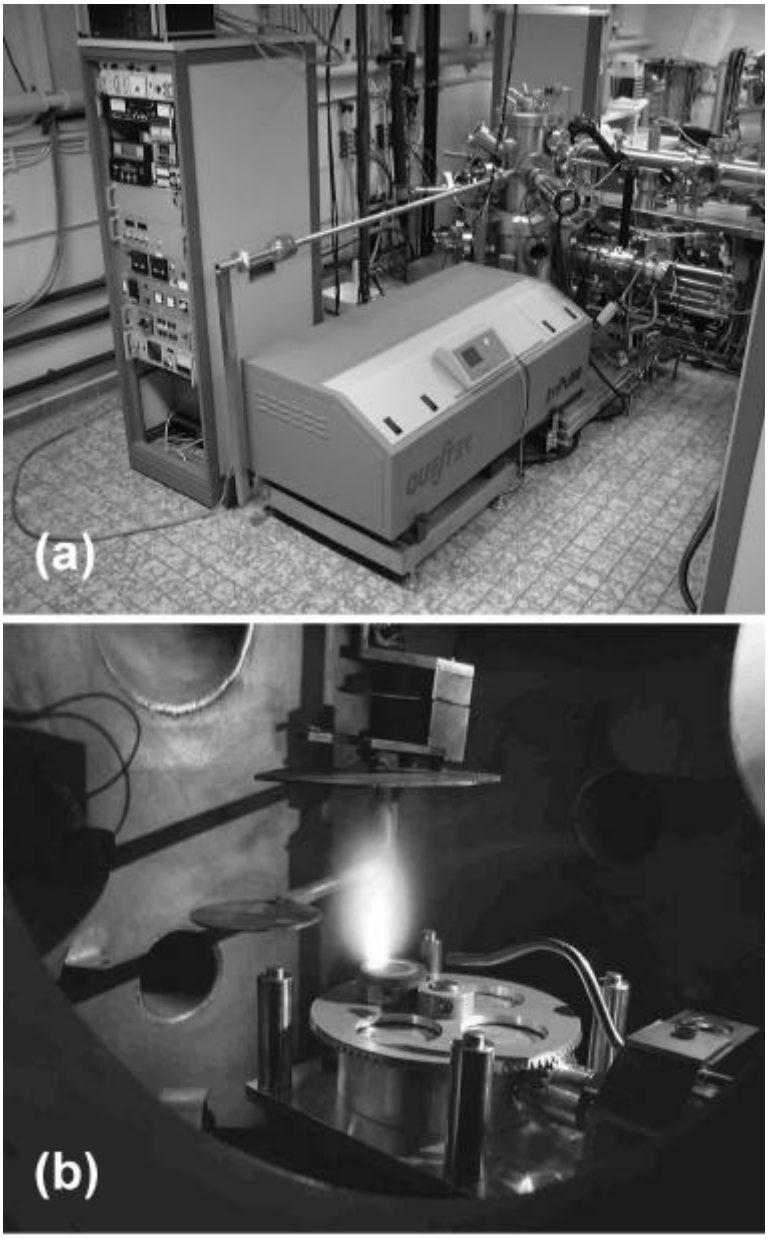

Figure 2.1: Pulsed laser deposition (PLD) set-up: (a) full set-up, consisting of an excimer laser (QUESTEK), projection optics and an UHV system and (b) ablation of an $YBa_2Cu_3O_{6+x}$ target in an oxygen background pressure, showing the formation of a plume.

pure oxygen. It is not necessary to perform additional heat treatments to optimize the superconducting properties.
To analyze the surface morphology of the crystalline …lms, we use atomic force microscopy (AFM) in the tapping mode (NANOSCOPE IIIa multimode system). The AFM measurements are performed ex situ, using Si tips. The …lms are structurally characterized by means of X-ray di¤raction (XRD) in a RIGAKU rotating anode di¤ractometer, using $CuK_{®}$ radiation (¸ = 1:541871 Å). After carefully aligning the …lms with respect to the (00l)-axis, µ ¡ 2µ di¤raction scans are recorded. The c-axis length is determined by averaging the results obtained from several (00l)-lines (l = 1 ¡ 8). Rocking curves widths are determined by means of separate ! scans, using the (005)-re‡ection. For all crystalline …lms, we measured the transition to superconductivity resistively in a four point probe con…guration.

2.3 Stoichiometry and …lm properties

2.3.1 Amorphous $YBa_2Cu_3O_{6+x}$ …lms

Although PLD is generally known for its stoichiometric transfer, e.g. in $SrTiO_3$ it was found that this is only true at su¢ciently large ‡uences [21, 22]. In order to …nd the conditions for stoichiometric transfer in the PLD of $YBa_2Cu_3O_{7¡±}$ …lms, we measured the …lm composition as a function of ‡uence. However, it is not possible to accurately determine the …lm composition by means of RBS of …lms deposited on $SrTiO_3$ substrates, due to overlap of the substrate and …lm contributions in the RBS spectrum. Therefore, we performed RBS measurements on amorphous $YBa_2Cu_3O_{6+x}$ …lms that are deposited on Si wafers at room temperature at ‡uences between 0.50 and 3.0 J/cm^2. Since we are interested in the transfer of the di¤erent cation species, it is not necessary that these …lms are crystalline. The thickness of the amorphous …lms (typically 50 nm) is controlled in such a way that the substrate, Y, Ba and Cu contributions in the RBS spectrum are well separated. The relative concentrations [Cu]/[Y], [Ba]/[Y] and [Cu]/[Ba] are calculated from the total peak area of the Y, Ba and Cu signals using the RUMP simulation program [23] with an accuracy of a few percent.
Starting from a freshly sandpapered target, we …nd that the transfer is initially stoichiometric for all ‡uences employed (0.50 < J < 3.0 J/cm^2). However, when we preablate the target prior to the actual …lm deposition with 300 (or more) laser shots, we …nd that the …lm composition deviates from the 123 stoichiometry in certain well-de…ned ‡uence regimes. In Fig. 2.2 the measured composition is plotted for amorphous …lms deposited at various ‡uences after the target has been preirradiated with 600 shots. In this …gure, we can identify three ‡uence regions. In the low ‡uence region I (J < 1:0 J/cm^2) the deposited …lms are Cu rich and Y poor. The …lms are Cu poor and slightly Y rich in region II (at ‡uences between 1.0 and 1.3 J/cm^2). In region III ¡ at ‡uences above 1.3 J/cm^2 ¡ the resulting thin …lms are stoichio-

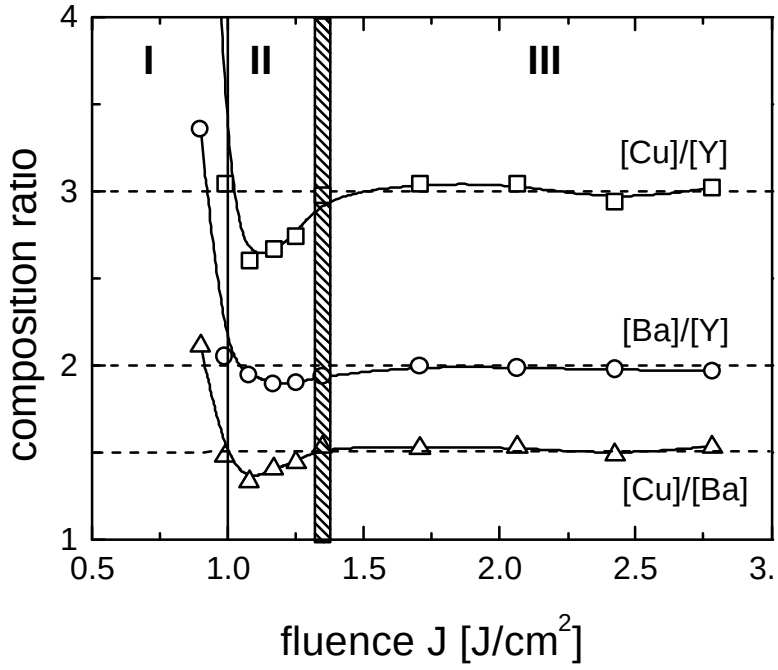
I
II
III
[Cu]/[Y]
[Ba]/[Y]
[Cu]/[Ba]
composition ratio
fluence J [J/cm^2]
4
3
2
1
0.5
1.0
1.5
2.0
2.5
3.

metric. These three ‡uence regions are always observed when preablating the target. Even after a preablation period of 10^4 shots, the same three regimes are found.
From these measurements it also follows that the deposition is stoichiometric for all ‡uences when starting from a fresh target (without preablation). Why do we use preablation at all? The most important reason for using preablation is to clean the target material from loose grains which greatly a¤ect the quality of the …lm surface. Another practical reason is that we want to have a constant deposition rate. Since the deposition rate decreases rapidly with time to a constant value [19], preablation is required. Also, the target surface reorients itself towards the incoming laser beam [20], which causes an increase in ‡uence by a factor $\sqrt{2}$ during ablation. Concluding, preablation is applied to ensure a well-de…ned starting situation for the actual …lm deposition.
Region I extends up to the threshold ‡uence $J_{th} = 1{:}0$ J/cm^2 and was reported earlier [4, 20]. However, as the Cu-de…ciency in region II is very small, the second region was not observed. Because ‡uence regime I is well understood [4, 20, 21], we focus on region II and the crossover to region III in the remaining of this chapter.
How do we explain the persistent o¤-stoichiometry in region II? Apart from particularities of the laser-target interaction, a possible explanation for the non-stoichiometric transfer in region II is scattering of the cations at ambient oxygen molecules [15]. Since the scattering rate is di¤erent for each cation species, this could in principle induce o¤-stoichiometries in the …lm. Foote et al. [15, 24] found that the e¤ect of scattering increases with increasing oxygen pressure p_{O_2} and target-to-substrate distance $d_{T\,i\,S}$ (at a …xed ‡uence). In our experiments the ‡uence is varied, while both $d_{T\,i\,S}$ and p_{O_2} are kept constant. However, the most important parameter is the position of the substrate with respect to the top of the plasma plume (see Fig. 2.1(b) for an example): when increasing the plume-substrate distance the e¤ect of scattering increases. In our experimental set-up, there is a separation between the substrate and the plume below 1.3 J/cm^2, whereas at higher ‡uences the substrate is inside the plume. If scattering is important, it should become more dominant at smaller ‡uences. In order to …nd out if scattering is the origin of the ‡uence dependence of the composition in region II, the deposition of amorphous …lms was repeated at a larger $d_{T\,i\,S}$ of 4.5 cm. Now the plume touches the substrate at a ‡uence of 1.5 J/cm^2. If scattering plays an important role, we expect that: (i) the e¤ect is more pronounced and (ii) that region II extends up to 1.5 J/cm^2. However, experimentally we …nd that the composition of the …lms deposited at $d_{T\,i\,S} = 4{:}5$ cm exhibits the same ‡uence dependence as in Fig. 2.2, showing the same three ‡uence regions. Thus, we conclude that scattering of cations at oxygen atoms is not the origin of region II.
If the deviations from stoichiometry in region II are not induced during the transfer of material from the target to the substrate, they must be induced at an earlier stage. Therefore, we investigated the irradiated target material in more detail. The composition of the target spots, irradiated with ‡uences in region II and III, was measured using RBS with the He^+ beam parallel to the direction of the incoming laser beam [see Fig. 2.3(a)]. The RBS spectrum is simulated with the two concentration pro…les shown in Fig. 2.3(b), using the RUMP program [23]. Ideally, the target composi-

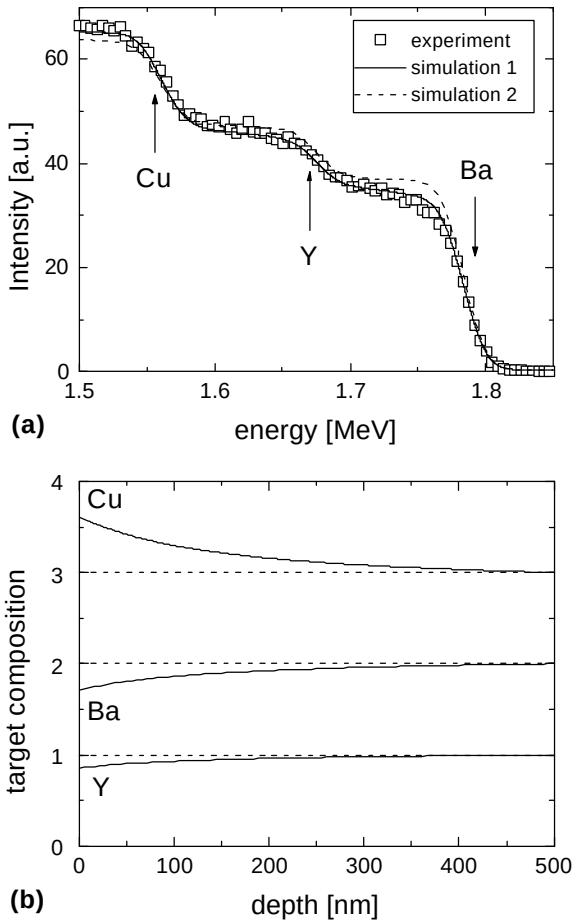

Figure 2.3: After irradiating the $YBa_2Cu_3O_{6+x}$ target with 900 laser shots at a fluence of 1.2 J/cm^2 (region II) the composition of the irradiated spot was measured by means of RBS: (a) measured and simulated RBS spectra and (b) composition profiles used for the RBS simulation (1 = no profile; 2 = Y + Ba diffusion profile).

tion should be $Y_1Ba_2Cu_3$, independently of the depth within the target (simulation 1). However, the simulated RBS spectrum shows that the Ba (and Y) content is too high, while the Cu content is too low. Introducing a gradual Cu enrichment (and an Y + Ba depletion) towards the surface of the target brings the simulated and measured spectra closer. Since the compositional deviations from stoichiometry in the target are opposite to those in the …lm (see Fig. 2.2), we infer that Y and Ba are preferentially ablated with respect to Cu in region II.
RBS measurements on target spots irradiated with a ‡uence from region III show the same spectrum as the unirradiated target. These spectra show no indication of concentration pro…les. Since region II persists upon further irradiation, we conclude that the same di¤usion-assisted preferential ablation mechanism is active as in the PLD of $SrTiO_3$ [21, 22]. This mechanism will be described in detail in the discussion.
The ‡uence not only a¤ects the composition, but also the droplet density on the …lm. Generally, the droplet density increases with ‡uence [4, 5, 10]. Since on amorphous …lms all particles are droplets, the droplet density can directly be determined by means of optical microscopy. We …nd that the droplet density on amorphous …lms increases somewhat with ‡uence, but the absolute density is always low ($< 10^4$ per cm^2). We attribute this low droplet density to the use of a high density, tetragonal target [9, 10, 11]. Using a lower density orthorhombic target results in higher droplet densities ($> 10^5$ per cm^2). As will be shown in the next section, the density of precipitates on crystalline …lms is usually some orders of magnitude larger (10^6 ¡ 10^7 per cm^2). Therefore, we conclude that compositional e¤ects are mainly determining the particle density of a …lm.

2.3.2 Crystalline $YBa_2Cu_3O_{7¡±}$ …lms

Having identi…ed three ‡uence regions, we now proceed to investigate the e¤ect of ‡uence on the quality of crystalline, 140 nm thick $YBa_2Cu_3O_{7¡±}$ …lms. All …lms are deposited on (100) $SrTiO_3$ substrates at a temperature of $815^{±}C$, p_{O_2} = 15 Pa and $d_{T¡S}$ = 3:5 cm. Prior to each deposition run, the target was preablated. We did not investigate …lms deposited in region I, since the o¤-stoichiometries are so large that it is not possible to obtain superconducting …lms. Moreover, the deposition rate is unpractically low.

Film properties

Immediately after deposition, the surface morphology of region II and III …lms is examined ex situ by AFM. The results are shown in Fig. 2.4. It is clear that there is a large di¤erence in particle density. The slightly o¤-stoichiometric …lms deposited with a ‡uence in region II show a high density of particles ($10^7/cm^2$). As argued above, these particles are precipitates resulting from o¤-stoichiometries in the …lm. The …lms deposited at J À 1:3 J/cm^2 are essentially precipitate-free (10^4 ¡ $10^5/cm^2$), indicating stoichiometric deposition.
In order to identify the nature of the precipitates in region II, we use the pseudoternary equilibrium phase diagram of $YO_{1:5}$-BaO-CuO [25]. Strictly speaking, this phase dia-

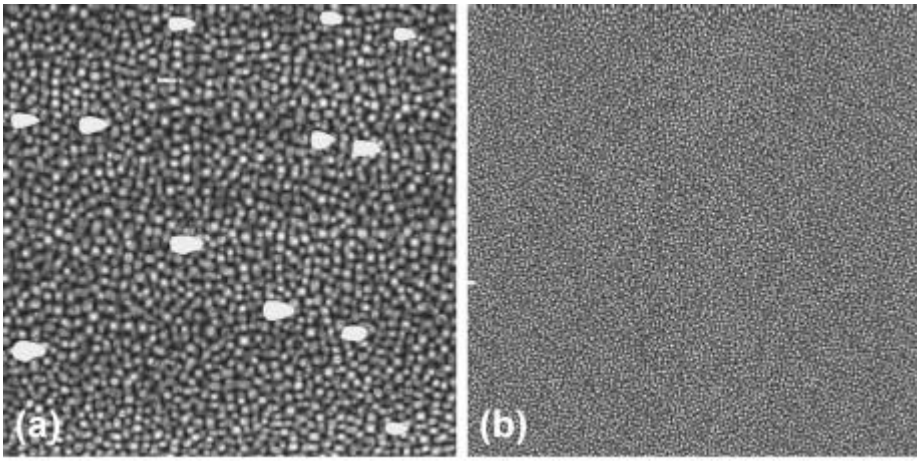

Figure 2.4: AFM height images of two crystalline $YBa_2Cu_3O_{7-\pm}$ …lms laser deposited on (100) $SrTiO_3$ substrates with a ‡uence in: (a) region II (J = 1:2 J/cm^2); scan size 10 ¹m and (b) region III (J = 3:0 J/cm^2); scan size 20 ¹m. Both …lms are deposited at 815±C, p_{O_2} = 15 Pa and d_{T-S} = 3:5 cm. Note the di¤erence in scan size; bright is high and dark is low.

gram is only valid at 850±C and 5:5 £ 10^{-3} atm. However, since the actual deposition temperature is somewhat lower, it can be argued [26] that we are allowed to employ it here. From this diagram, it follows that a Cu de…ciency (Fig. 2.2) induces precipitates of Y_2BaCuO_5 and $BaCuO_2$. Indeed, in literature these phases have been found in $YBa_2Cu_3O_{7-\pm}$ …lms [26, 27].

Intuitively, one would expect the non-stoichiometric …lms to be inferior as compared to the stoichiometric ones, because of the segregation process involved. Structural characterization by XRD, however, shows that the opposite is true. Films deposited with a ‡uence in region II are qualitatively better than the precipitate-free …lms in region III. In Fig. 2.5(a) rocking curves of the (005)-re‡ection of …lms deposited on comparable substrates but in di¤erent ‡uence regimes are shown. The full width at half maximum (FWHM) of a region II …lm is 0.094±, compared to a FWHM of 0.25± of a region III …lm, indicating a large mosaic spread. We also observe a di¤erence in c-axis length. Averaging the (00l)-re‡ections, for region II …lms we typically …nd c-axis lengths between 11.68 and 11.69 Å, whereas the c-axis length of region III …lms is slightly larger: 11:70 ¡ 11:71 Å. Both values, however, are close to the bulk value of 11.68 Å [28].

The structural distortion in the region III …lms is most likely due to the occurrence of oxygen vacancies [29] and Y-Ba disorder [30, 31]. A measure for both the chain oxygen de…ciency and the amount of disorder of Y and Ba atoms, is given by the

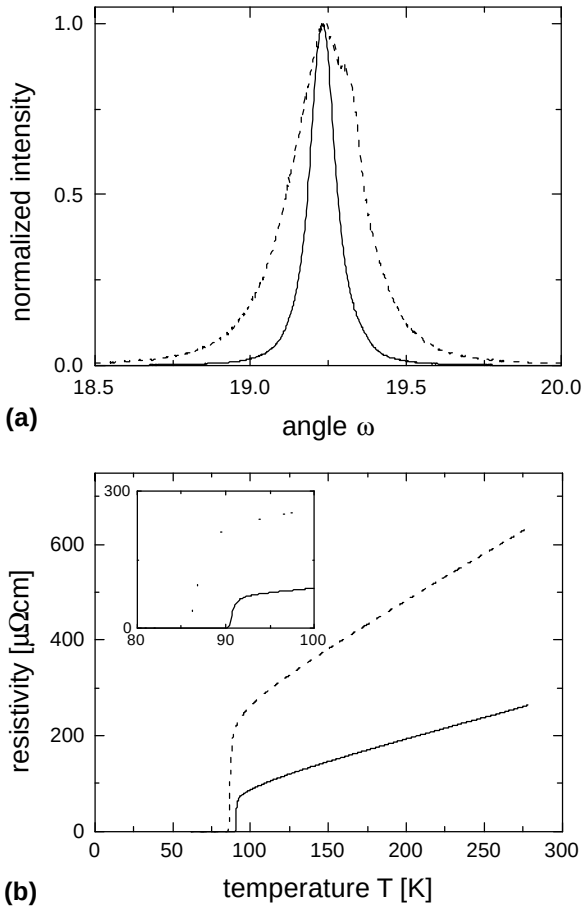

Figure 2.5: Comparison between two crystalline $YBa_2Cu_3O_{7-\delta}$ …lms deposited on (100) $SrTiO_3$ substrates at ‡uences in region II (full line; J = 1:2 J/cm^2) and region III (dashed line; J = 3:0 J/cm^2): (a) (005) XRD rocking curves and (b) resistivity ½ vs. temperature T curves. Both …lms are deposited at 815±C, p_{O_2} = 15 Pa and d_{T-S} = 3:5 cm.

ratio of the integrated intensities of the (005) and (004)-re‡ections, I(005)/I(004) [29, 30, 31]. Ideally, in the absence of any disorder or de…ciency, this ratio is equal to 14.8. In oxygen de…cient …lms I(005)/I(004) increases, whereas disorder between Y and Ba atoms causes I(005)=I(004) to decrease. We …nd that region II …lms show values that are very close to the optimal value (for the …lm shown in Fig. 2.5(a) I(005)=I(004) = 14:4). In region III, however, the observed ratio is signi…cantly larger than the optimal value [I(005)=I(004) = 17:3 for the …lm in Fig. 2.5(a)], indicating an oxygen de…ciency in the chains.

As shown in Fig. 2.5(b), the oxygen de…ciencies in the region III …lms translate into higher resistivities, lower critical temperatures T_c and broader transitions as compared to region II …lms. The oxygen de…ciencies might be related to the fact that the substrate is not at its optimal position with respect to the plume: in region III the length of the plume is much larger than the target-to-substrate distance. Indeed, the properties of stoichiometric …lms improve when positioning the substrate in top of the plume ($89 < T_c < 90$ K). This is achieved by either increasing the target-substrate distance or by raising the background oxygen pressure [32]. However, the quality of these …lms is still not as good as that of the region II …lms.

In fact, in literature it has often been reported that slightly o¤-stoichiometric …lms have better properties than stoichiometric …lms [13, 15, 17, 26, 33]. If the di¤usion of one of the cation species during …lm growth is the rate limiting factor in forming $YBa_2Cu_3O_{6+x}$, a small excess amount of this element actually promotes the growth process, yielding better superconducting properties. It has been suggested [34] that Y is this di¤usion rate limiting element. Indeed, in our region II …lms we have a small Y-enrichment (see Fig. 2.2), indicating the importance of di¤usion for the growth process. Unfortunately, the o¤-stoichiometry in region II always results in the formation of precipitates (see Fig. 2.4).

Consequently, we have to …nd a compromise between superconducting properties and the quality of the surface. From Fig. 2.2 it follows that there are two optimal ‡uences: on the boundary between regions I and II and on the boundary between regions II and III. Indeed, as reported in a previous paper [20], we …nd that at a ‡uence of 1.0 J/cm^2 excellent superconducting …lms are obtained. However, the surface morphology of these …lms is not reproducible. We attribute this to the strong ‡uence dependence of the composition transfer around 1.0 J/cm^2 (Fig. 2.2). Due to small ‡uctuations in the laser ‡uence, in practise the deposition is always o¤-stoichiometric. Therefore, the best …lms are found at the boundary between region II and III for J ¼ 1:3 J/cm^2, combining good superconducting properties and reasonably low precipitate densities (10^6/cm^2). The ‡uence for optimal …lms is indicated by the shaded area in Fig. 2.2. As will be shown in the next section …lms deposited at J = 1:3 J/cm^2 exhibit a remarkable reproducibility, both in surface morphology and superconducting properties.

Reproducibility

In a period of several months, 30 …lms were deposited under identical deposition conditions at a ‡uence of 1.3 J/cm^2. The distribution from …lm to …lm in T_c is

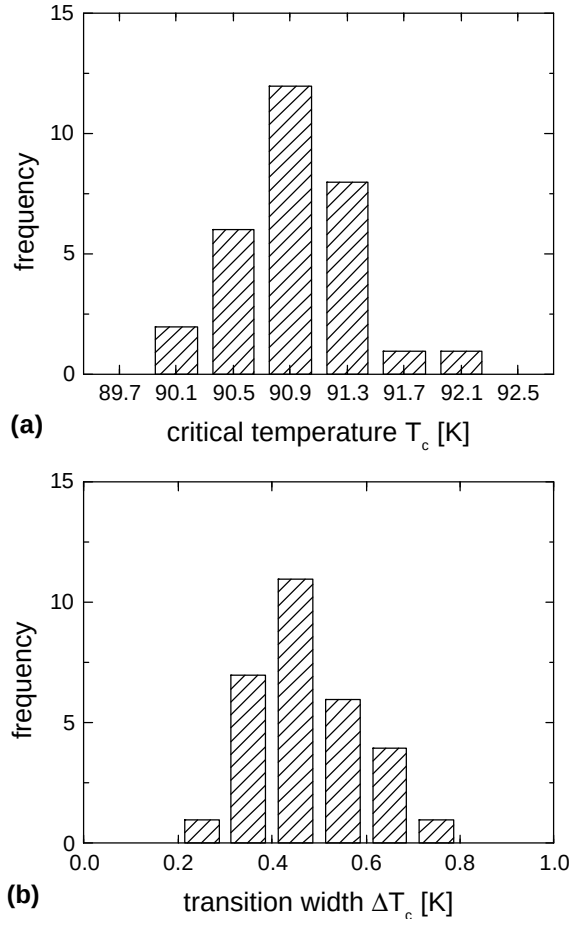

Figure 2.6: Distribution in: (a) critical temperature T_c and (b) width of the resistive transition ¢T_c for 30 crystalline $YBa_2Cu_3O_{7\,i\,\pm}$ …lms deposited on (100) $SrTiO_3$ substrates under similar deposition conditions (815±C, p_{O_2} = 15 Pa and $d_{T\,i\,S}$ = 3:5 cm). Both T_c and ¢T_c are determined from the derivative of the ½(T) curves.

shown in Fig. 2.6(a), taking all …lms into account. In this histogram, T_c is de…ned as the maximum in the derivative of the resistivity ½ with respect to temperature. The average value is 91.0 K, which corresponds to an average T_c(½ = 0) = 90:4 K. The spread in T_c is extremely small: we …nd a standard deviation of only 0.4 K! The transition width ¢T_c (de…ned as the FWHM of the peak in the d½=dT curve) is on average 0.4 K and also shows an extremely narrow distribution, see Fig. 2.6(b).
Although there are numerous reports mentioning $YBa_2Cu_3O_{7\,i\,\pm}$ …lms with a high T_c and a small ¢T_c, there are very few reports [35] on the reproducibility of the PLD process. This suggests that pulsed laser deposition is generally not very reproducible. We attribute the remarkable reproducibility found here to the quality of the laser beam (homogeneity, pulse-to-pulse stability, etc.) and the use of projection optics, which ensures that the energy density at the target is well de…ned. As the composition transfer is ‡uence dependent, it is also important that the energy is tuned by an optical attenuator instead of by defocusing the laser beam. Since defocusing results in a an inhomogeneous laser beam pro…le, the deposition contains contributions from all ‡uence regions. Therefore, unless by chance the e¤ects from region I and II balance, the deposition is non-stoichiometric and certainly irreproducible.

2.4 Laser-target interaction

The existence of an ablation threshold in the PLD of $YBa_2Cu_3O_{7\,i\,\pm}$, separating regions I and II was discussed in two previous publications [4, 20]. In these papers, however, no distinction between regions II and III was made. Here, we will discuss the origin of these ‡uence regions in detail. For completeness, we start with a short discussion of region I.

2.4.1 Region I: target degradation

In the region below the threshold ‡uence for ablation of $YBa_2Cu_3O_{6+x}$, large deviations from stoichiometry occur (see Fig. 2.2). Previous work [4, 20] revealed that below this ablation threshold the phase of the target changes as a result of the repetitive melting by the laser irradiation. This degradation of the target material is a consequence of the incongruent melting point of $YBa_2Cu_3O_{6+x}$ (123). When 123 is heated, it transforms [12] into Y_2BaCuO_5 + liquid (211 + $L^{[p]}$), which subsequently separates in Y_2O_3 + a liquid ($L^{[q]}$) of a di¤erent composition. Finally, also the Y_2O_3 melts. In laser ablation, at small ‡uences, the energy of the laser is su¢cient to transform the 123 phase into 211 + $L^{[p]}$ (or Y_2O_3 and $L^{[q]}$), but insu¢cient to melt it completely. Because the molten phases are more easily ablated than the remaining solid phases, a phase separation is induced. The oscillating melting and solidifying conditions enhance the phase separation of 211 and Y_2O_3 even further. Consequently [4, 19, 20], the deposition rate decreases drastically in time and eventually drops to zero for $J < J_{th}$. As a result, we observe an Y de…ciency in the resulting thin …lms (Fig. 2.2), in accordance with an Y enrichment (211 and Y_2O_3) in the target [4, 19, 20].

We note that the incongruent melting of $YBa_2Cu_3O_{7-\delta}$ is the origin of the phase separation. Therefore, in congruently melting materials, this mechanism for non-stoichiometric transfer is absent. Indeed, in congruently melting $SrTiO_3$, the lowest fluence region is not found [21]. We do, however, observe non-stoichiometric deposition of $SrTiO_3$ at low fluences, completely analogous to the region II that was found in the present investigation of $YBa_2Cu_3O_{7-\delta}$.

2.4.2 Region II: diffusion-assisted preferential ablation

Increasing the fluence slightly above 1.0 J/cm^2 still results in off-stoichiometric films (region II). Although Cu and Ba are the most volatile elements, we believe that the ablation process itself is preferential with respect to Y and Ba. At this point we can only speculate about the nature of this preferential ablation process. The depletion of Y and Ba at the target surface is, however, unambiguously measured by RBS (Fig. 2.3). In this section we show that the concentration gradients in the target and the film off-stoichiometry upon prolonged deposition can indeed be explained by a diffusion-assisted preferential ablation mechanism in region II. In this mechanism the pulsed character of PLD plays a crucial role.

To arrive at this conclusion, we developed a 1-D diffusion model for diffusion-assisted preferential ablation (see Fig. 2.7). First of all, we assume that the top layer of the target material is immediately molten as soon as the laser irradiation begins. Only a small part of this molten top layer of the target is ablated. In the model the ablation process (of all elements) is simulated by imposing a movement of the target surface inwards with a constant velocity R/τ. Here R is the thickness of the layer of target material that is removed by one shot and τ the time of one laser pulse (the ablation time). Consequently, the position of the target surface $x(t)$ as a function of time is given by $x(t) = Rt/\tau$.

If there is no preferential ablation, the target gets thinner in time and all cation concentrations are unaffected and equal to the composition in the bulk of the target. To take preferential ablation into account, we introduce an excess particle flux Φ_i^q (> 0) of element i of the target material at the moving target surface [in atoms/(m^{2}s)]. This excess flux acts as the driving force for diffusion in the molten top layer of the target material. As a result, a concentration profile builds up in the target.

Now, the problem reduces to solving the diffusion equation

$$\frac{\partial c^i}{\partial t} = D_i \frac{\partial^2 c^i}{\partial x^2}, \tag{2.1}$$

where $c^i = c^i(x;t)$ is the concentration of element i [in atoms/m^3] in the target at position x at time t. The diffusion constant of element i in the melt is given by D_i [in m^2/s]. The ablation process starts at $t = 0$, for which $x = 0$. From then on the target surface moves inwards ($x > 0$). The simplest form of the excess flux is a constant value. However, this is not the most realistic choice. As a result of preferential ablation of element i, its surface concentration $c^i(x = \infty)$ decreases in time. Consequently, also the amount of preferential ablated material will decrease. Therefore, we assume that

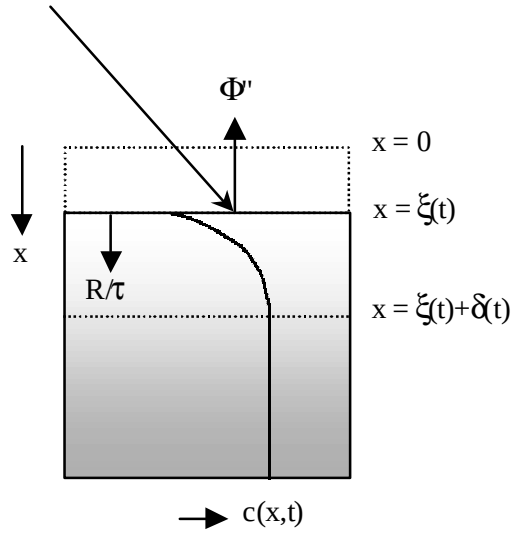

Figure 2.7: Schematic representation of di¤usion-assisted preferential ablation. The ablation of all target elements is represented by a movement of the target surface x = » inwards at a velocity R/¿, whereas the preferential ablation is simulated by imposing an excess ‡ux ©^{q} of one element at this moving boundary. As a result, a concentration pro…le c(x; t) of the preferentially ablated element builds up over a characteristic distance ± (it is assumed that the thickness of the molten top layer is much larger than ±).

the excess ‡ux and the surface concentration are proportional: ©$^{q}_{i}$ = Kc^{i}(x = »). Here K has the dimension of a velocity. Then, the appropriate starting and boundary conditions are:

$$c^i(x > 0; t = 0) = c^i_0 \tag{2.2}$$

$$c^i(x = \infty; t > 0) = c^i_0 \tag{2.3}$$

$$-D_i \left(\frac{\partial c^i}{\partial x} \right)_{x=\xi(t)} = -K c^i(x = \xi(t)), \tag{2.4}$$

where c^i_0 is the initial concentration of element i in the target (i.e., the bulk value). To solve this moving boundary problem, we employ Goodman's integral method [36]. This approximate analytical method assumes that there is some …nite di¤usive penetration depth ±(t), measured relative to the position of the moving interface, in which there is a deviation from the initial concentration (see Fig. 2.7). By expanding

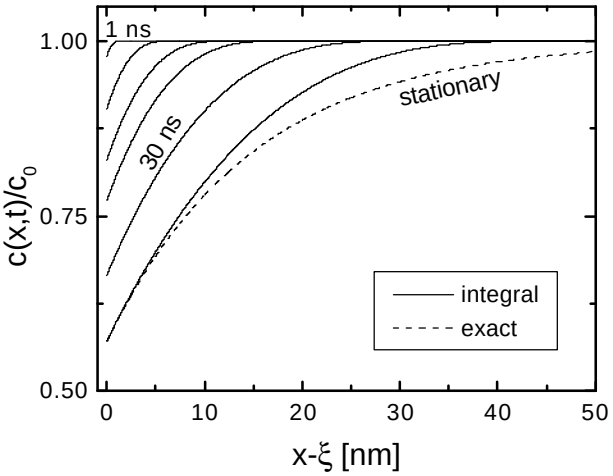

Figure 2.8: Calculated concentration pro…les $c(x;t)$ in the target as a result of di¤usion-assisted preferential ablation after 1, 5, 10, 15 and 30 ns, using Eq. (2.6) with $R = 20$ nm/shot, $¿ = 30$ ns, $D_i = 10^{-8}$ m^2/s and $K = 0{:}5$ m/s. The two lowest curves correspond to the stationary situation, using the integral method (full line) and the exact solution (Eq. (2.7), dotted line).

$c^i(x;t)$ into a third order polynomial and requiring that it is a smooth function at $x = »(t) + ±(t)$, the following relation between t and $±$ is obtained when integrating Eq. (2.1) from $x = »$ to $x = » + ±$:

$$t = - \frac{¿}{4R}± + \frac{3D_i¿^2}{4R^2} \ln \frac{3D_i}{3D_i - R±=¿} . \qquad (2.5)$$

From this equation it is clear that in the limit $t \to \infty$, $±$ approaches a stationary value $±_{stat} = 3D_i¿=R$. The concentration pro…le of element i in the target material is given by:

$$\frac{c^i(x;t)}{c_0^i} = 1 - \frac{K±}{3D_i + K±}\left[1 - 3\left(\frac{x - »}{±}\right) + 3\left(\frac{x - »}{±}\right)^2 - \left(\frac{x - »}{±}\right)^3\right] , \qquad (2.6)$$

where $x = x(t) = Rt=¿$ and $±(t)$ follows from Eq. (2.5). As $±$ approaches $±_{stat}$, the concentration pro…le becomes essentially time independent when measured relative to the position of the moving boundary (see Fig. 2.8). From the composition measurements and the measured di¤usion pro…les in the target, we estimate the proportionality constant K to be 0.5 m/s. The di¤usion constant is approximated by a typical value for di¤usion in a melt: $D_i ¼ 10^{-8}$ m^2/s.

In Fig. 2.8, also the exact steady state solution is shown. This solution is:

$$\frac{c^i(x;t)}{c_0^i} = 1 - \frac{K}{K + R/\zeta}\exp\left[-\frac{R(x - \infty)}{D_i\zeta}\right]. \qquad (2.7)$$

In fact, the integral method is a polynomial expansion of the exact solution. In the stationary situation, the difference between the two solutions is expected to be maximal. Therefore, from Fig. 2.8 we conclude that the integral method gives an estimate of the non-stationary diffusion profiles within 5%. However, the most important source of errors is the model itself. In principle, one should solve both the heat and diffusion equations in the presence of two moving boundaries in the target material: a vapor-liquid interface and a liquid-solid interface. Additional complications are the temperature dependence of the properties of the target material and the fact that both interfaces are not straight. However, we use the model to understand qualitatively how non-stoichiometric transfer can occur in PLD and, more importantly, what conditions are needed to reach persistent stoichiometric transfer of the target composition to the substrate.

As argued above, in region II there are two excess particle fluxes of the preferentially ablated Y and Ba atoms, Γ_Y^q and Γ_{Ba}^q. The total flux F_i^q of each preferentially ablated atom species i (= Y or Ba) as a function of time contains two contributions:

(i) The flux as a result of the ablation of all elements. For element i this corresponds to a flux of $Rc^i(x = \infty)/\zeta$.

(ii) The excess flux as a result of the preferential ablation of element i: $\Gamma_i^q = Kc^i(x = \infty)$.

Using Eq. (2.6), the total flux can now be written as

$$F_i^q(t) = \frac{K + \frac{R}{\zeta}}{1 + \frac{K\delta(t)}{3D_i}}c_0^i, \qquad (2.8)$$

where i = Y or Ba. The important point now is that all fluxes F_i^q are proportional to the bulk target concentration c_0^i as soon as the stationary state is reached ($F_i^q = Rc_0^i/\zeta$ when $\delta = \delta_{stat}$). Therefore, in the stationary state the deposition is stoichiometric. So, as long as the stationary situation is not reached the transfer is non-stoichiometric. To get an impression of how fast this steady state is reached, the time dependence of the penetration depth $\delta(t)$ is plotted in Fig. 2.9, taking typical removal rates R = 2, 20 and 200 nm/shot for a fixed ablation time ζ = 30 ns. From Fig. 2.9, it is clear that there is a considerable non-stationary and, therefore, off-stoichiometric period within the ablation time ζ, depending on the value of R.

The situation described above applies to continuous irradiation, whereas in PLD we have repetitive laser irradiation. The period between the laser pulses is 0.2 s, many orders of magnitude larger than the actual ablation time of 30 ns. Therefore, the concentration profile in the target material that is induced during one laser shot as a result of preferential ablation, will be smoothed due to diffusion from the bulk.

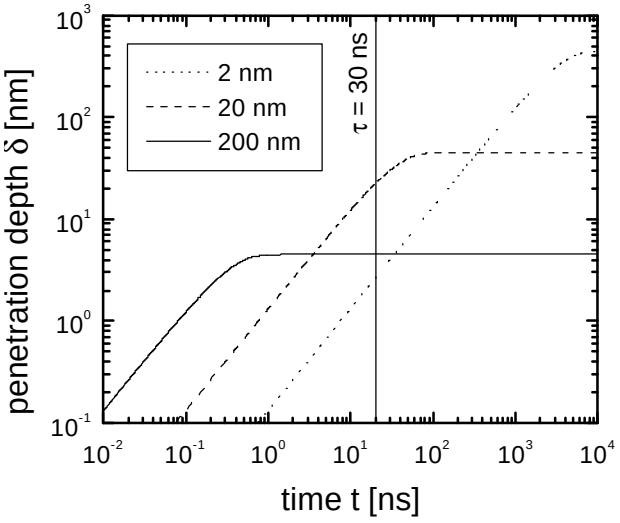

Figure 2.9: Calculated di¤usive penetration depth ± as a function of time t according to Eq. (2.5) for R = 2, 20 and 200 nm/shot, taking ¿ = 30 ns. In the calculation $D_i = 10^{i8}$ m^2/s.

However, because of the fast cooling of the target [37] the concentration pro…le is not fully relaxed. The next laser shot again induces a concentration pro…le, which again gets partially smoothed out in the subsequent cooling down period of the target and so on. Therefore, during each laser shot a certain time is needed to reach the stationary state again (if it is reached at all). During this time the deposition is incongruent and the o¤-stoichiometry in the …lms is maintained. Thus this mechanism accounts for both persistent non-stoichiometric deposition (Fig. 2.2) and the existence of a concentration pro…le in the target (Fig. 2.3), even after irradiating the target for as many as 10^4 shots.

The di¤usion pro…le induced in the target is the result of a balance between di¤usion during a laser pulse (due to preferential ablation) and di¤usion in-between consecutive laser pulses. In a previous publication on the PLD of $SrTiO_3$ [22], we estimated the di¤usion constant of Sr in the target, using the measured Sr concentration pro…le in the target and the excess ‡ux of Sr with respect to Ti (as estimated from the …lm composition) in combination with Eq. (2.4). Strictly speaking, this is not correct. However, after prolonged irradiation the di¤usion pro…le may be regarded as an average of the ‡uctuating di¤usion pro…le over many pulses and the calculation should give an upper estimate for the di¤usion constant. Indeed, we obtained [22] a di¤usion constant for Sr that is of the order of di¤usion constants in melts: 2:2 £ 10^{i8} m^2/s. Repeating this calculation for the PLD of $YBa_2Cu_3O_{7\,i\,\pm}$, we …nd a di¤usion

constant for Y and Ba of the same order of magnitude (3 ± 10^{-8} m^2/s). Therefore, the diffusion constant used for the calculations is reasonable.
We conclude that the non-stoichiometric transfer in region II is caused by diffusion-assisted preferential ablation of Y and Ba from the target. This mechanism persists because of the pulsed character of the deposition method. Between consecutive laser pulses the diffusion profile in the target partially relaxes. Therefore, there always is a period of non-stationary diffusion during the next laser pulse, yielding persistent non-stoichiometric transfer.

2.4.3 Region III: stoichiometric deposition

Although it is expected that preferential ablation of Y and Ba still takes place at fluences $J > 1.3$ J/cm^2, truly stoichiometric films are deposited in region III. Following the line of reasoning of the preceding section, stoichiometric transfer only takes place if the stationary state is almost immediately reached during each laser pulse. From Fig. 2.9 it follows that the stationary state is reached sooner for larger R, the thickness of the layer removed from the target by one shot. Since R is proportional to the deposition rate, one should reach stoichiometric deposition when increasing the deposition rate. In figure 2.10 the measured deposition rate is plotted versus the fluence after 600 shots of preablation (starting from a fresh target, the rate decays roughly exponentially with time to a constant value [19]). Below $J_{th} = 1.0$ J/cm^2 this deposition rate is zero and increases monotonically above J_{th}. Therefore, at large J stoichiometric deposition is expected. From this argument it follows, that the crossover between region II and III is not so abrupt, as was already suggested by the shaded area in Fig. 2.2. This is the reason that some precipitates are always found around 1.3 J/cm^2. At very large fluences, however, the precipitate density is greatly reduced and we find that the deposition process is truly stoichiometric [see Fig. 2.4(b)]. In fact, Auciello and co-workers [38] already observed in 1988 that the film composition approaches stoichiometry at large fluences. They proposed that at such high fluences also target material from a thickness larger than the compositionally altered surface layer is removed.
One may wonder at this point whether increasing the fluence is the only way to reach stoichiometric deposition. From a dimensional analysis we know that the stationary state is reached at a time of the order of $t_\diamond$ (see also Fig. 2.9), which is defined as

$$t_\diamond = D_i \left(\frac{\tau}{R} \right)^2 . \qquad (2.9)$$

This relation shows that it is in fact the ablation rate R/τ that determines how fast the stationary state is reached. Thus, an alternative way to reach stoichiometric deposition is to reduce the pulse duration τ. By decreasing the laser pulse duration, it should be possible to reach stoichiometric deposition for all fluences larger than the threshold fluence.
In the previous section, it was shown that the properties of stoichiometric films deposited at high fluences are relatively poor (see Fig. 2.5). Since it is the thickness R of the layer that is removed by one shot and not the deposition rate itself that de-

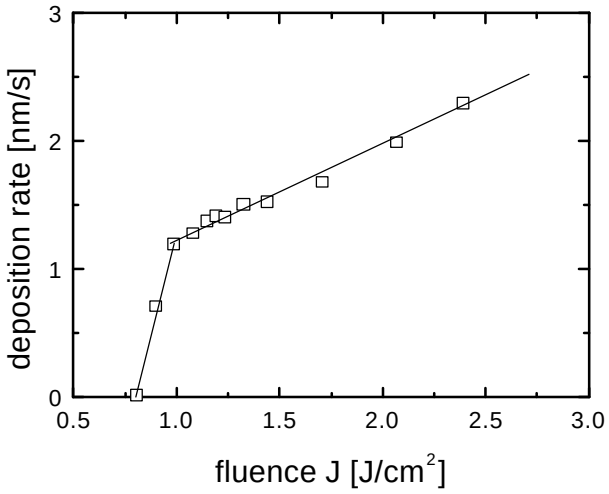

Figure 2.10: Deposition rate measured as a function of fluence J when ablating a stationary $YBa_2Cu_3O_{6+x}$ target after a preablation period of 600 laser shots (at p_{O_2} = 15 Pa and $d_{T\,i\,S}$ = 3.5 cm).

termines stoichiometric transfer, it should be possible to obtain stoichiometric films at a lower deposition rate (by selecting a smaller part of the beam). Apart from changing the deposition geometry ($d_{T\,i\,S}$) and the ambient oxygen pressure, this is an alternative way to optimize the properties of stoichiometric films.

We finally address the question why the composition transfer is stoichiometric for all three fluence regions if we do not preablate the target. There are two opposing effects: (i) preferential ablation of Y and Ba in all three regions and (ii) a phase transformation in the target resulting in the formation of Y_2BaCuO_5 and Y_2O_3 in region I, which effectively means preferential ablation of Cu. Therefore, the net effect in region I during the first few hundred laser shots is a stoichiometric film composition. Upon ablating longer, the ablation of Y and Ba is suppressed and the effect of the phase transformation becomes dominant. The initial stoichiometric ablation in region II is related to the same two target processes, since the initial fluence is a factor p_2 smaller due to fact that the target surface has not yet reoriented itself towards the laser [20]. Therefore, initially the fluence is smaller than the threshold fluence and again the two contributions from the phase separation and the preferential ablation compensate each other. In region III the reorientation of the target surface is much faster due to the higher energy. Therefore, the period of non-stoichiometric transfer is very short and does not show up in the RBS measurements.

Note, that the existence of initial stoichiometric deposition implies that one should be able to obtain stoichiometric films when scanning the laser beam across the target,

independently of the applied ‡uence or beam homogeneity. However, the drawback is that some target grains are ejected from the target to the substrates, resulting in a poor …lm surface morphology.

Summarizing, there are two mechanisms by which non-stoichiometric transfer occurs during the pulsed laser deposition of $YBa_2Cu_3O_{7\,i\,\pm}$: (i) phase separation in the target material and (ii) di¤usion-assisted preferential ablation. These mechanisms apply to the PLD of other materials as well. For instance, it was illustrated [21] that the second mechanism is responsible for the non-stoichiometric deposition in the PLD of $SrTiO_3$ at ‡uences below 1.3 J/cm^2, whereas the phase separation does not occur in this congruently melting material. We note that the numerical values for the threshold ‡uences quoted here depend on the quality of the target material (i.e., density, preferential orientation, etc.). Therefore, they may di¤er slightly from target to target.

2.5 Conclusions

We …nd that in PLD of $YBa_2Cu_3O_{7\,i\,\pm}$, the …lm composition is a sensitive function of the laser ‡uence. This is a direct consequence of laser induced modi…cations in the target material, much more than a change in ablation mechanism. Below the threshold ‡uence J_{th} = 1:0 J/cm^2 (‡uence region I), a phase separation is induced in the target. As a result, the deposited …lms are non-stoichiometric. At ‡uences slightly larger than the threshold ‡uence (region II: 1:0 < J < 1:3 J/cm^2), the ablation process is preferential with respect to Y and Ba. Since also di¤usion pro…les of Y and Ba are observed in the ablated target material, we attribute the non-stoichiometric transfer to volume-di¤usion-assisted preferential ablation. This mechanism is described by a phenomenological 1-D di¤usion model, in which the ablation process is simulated by a moving boundary and the preferential ablation of Y and Ba is taken into account by imposing two additional atom ‡uxes at the (moving) boundary. From the model, it follows that the material transfer from the target to the substrate is non-stoichiometric as long as the di¤usion in the target is non-stationary. Because of the pulsed character of the deposition technique, the di¤usion pro…le relaxes in-between consecutive laser pulses and there always is a period of non-stationary di¤usion giving persistent non-stoichiometric deposition. However, the non-stationary periods are reduced considerably by increasing the ablation rate. Consequently, stoichiometric deposition is expected to take place for: (i) large ‡uences and/or (ii) short laser pulses.

Indeed, for ‡uences J À 1:3 J/cm^2 the exact $Y_1Ba_2Cu_3$ composition is found (region III). As a result of the stoichiometric deposition, the surface quality of these …lms is very good. We …nd precipitate densities of 10^4/cm^2 in combination with reasonable superconducting (89 < T_c < 90 K) and structural (0:1$^\pm$ < FWHM < 0:2$^\pm$) properties. In region II, the di¤usion-assisted preferential ablation regime, higher precipitate densities are observed (10^7/cm^2). However, the structural (FWHM < 0:1$^\pm$) and

superconducting ($90 < T_c < 91$ K) quality is better than in region III, suggesting that the growth process actually requires some o¤-stoichiometry.
In conclusion, the best $YBa_2Cu_3O_{7\ i\ \pm}$ …lms are found at the boundary between regions II and III at a ‡uence of 1.3 J/cm^2. These …lms, combine both a low precipitate density (typically 10^6/cm^2), superior structural (FWHM < 0:1$^{\pm}$ and c = 11:70 Å) and superconducting properties (T_c = 91:0 K; ¢T_c = 0:4 K) with a remarkable reproducibility. Our experiments show that PLD can be a highly reproducible deposition technique, when a well-de…ned, uniform and reproducible laser spot is used.[2] The excellent reproducibility allows us to relate the superconducting properties to the microstructure, as will be shown in the following chapters.

References

[1] D.B. Chrisey and G.K. Hubler, Pulsed Laser Deposition of Thin Films (Wiley, New York, 1994)

[2] R.K. Singh and D. Kumar, Mat. Sci. Eng. R 22, 113 (1998)

[3] S. Proyer, E. Stangl, M. Borz, B. Hellebrand, and D. Bäuerle, Physica C 257, 1 (1996)

[4] B. Dam, J. Rector, M.F. Chang, S. Kars, D.G. de Groot, and R. Griessen, Appl. Surf. Sci. 86, 13 (1995)

[5] Y. Watanabe, M. Tanamura, S. Matsumoto, and Y. Seki, J. Appl. Phys. 78, 2029 (1995)

[6] B. Holzapfel, B. Roas, L. Schultz, P. Bauer, and G. Saemann-Ischenko, Appl. Phys. Lett. 61, 3178 (1992)

[7] E.V. Pechen, A.V. Varlashkin, S.I. Krasnosvobodtsev, B. Brunner, and K.F. Renk, Appl. Phys. Lett. 66, 2292 (1995)

[8] M.D. Strikovsky, E.B. Klyuenkov, S.V. Gaponov, J. Schubert, and C.A. Copetti, Appl. Phys. Lett. 63, 1146 (1993)

[9] R.K. Singh, D. Bhattacharya, and J. Narayan, Appl. Phys. Lett. 61, 483 (1992)

[10] D.S. Misra and S.B. Palmer, Physica C 176, 43 (1991)

[11] C.C. Chang, X.D. Wu, R. Ramesh, X.X. Xi, T.S. Ravi, T. Venkatesan, D.M. Hwang, R.E. Muenchenhausen, S. Foltyn, and N.S. Nogar, Appl. Phys. Lett. 57, 1814 (1990)

[2] These observations have been used in the design and development of a second PLD system in our group, consisting of a LAMBDA PHYSIK KrF (¸ = 248 nm, ¿ = 25 ns) laser, projection optics (including a beam homogenizer) and a relatively small high vaccuum system. The use of a beam homogenizer resulted in a reproducible lowering of the density of precipitates to about 10^5/cm^2 at a ‡uence of 1.4 J/m^2. No noticeable di¤erences in microstructural and superconducting properties between $YBa_2Cu_3O_{7\ i\ \pm}$ …lms deposited in the QUESTEK and LAMBDA PHYSIK system are found, showing that PLD is indeed a highly reproducible deposition technique.

[12] M. Murakami, M. Morita, K. Doi, K. Miyamoto, and H. Hamada, Jpn. J. Appl. Phys. 28, L399 (1989)

[13] N.G. Chew, S.W. Goodyear, J.A. Edwards, J.S. Satchell, S.E. Blenkinsop, and R.G. Humpreys, Appl. Phys. Lett. 57, 2016 (1990)

[14] Y. Watanabe, Y. Seo, M. Tanamura, H. Asami, and Y. Matsumoto, J. Appl. Phys. 78, 5126 (1995)

[15] M.C. Foote, B.B. Jones, B.D. Hunt, J.B. Barner, R.P. Vasquesz, and L.J. Bajuk, Physica C 201, 176 (1992)

[16] M.E. Gaevski, A.V. Bobyl, D.V. Shantsev, R.A. Suris, V.V. Tret'yakov, Y.M. Galperin, and T.H. Johansen, J. Appl. Phys. 84, 5089 (1998)

[17] V. Matijasevic, P. Rosenthal, K. Shinohara, A.F. Marshall, R.H. Hammond, and M.R. Bearsley, J. Mater. Res. 6, 682 (1991)

[18] R. Kelly, J.J. Cuomo, P.A. Leary, J.E. Rothenberg, B.E. Braren, and C.F. Aliotta, Nucl. Instrum. Methods Phys. Rev. B 9, 329 (1985)

[19] S.R. Foltyn, R.C. Dye, K.C. Ott, E. Peterson, K.M. Hubbard, W. Hutchinson, R.E. Muenchausen, R.C. Estler, and X.D. Wu, Appl. Phys. Lett. 59, 594 (1991)

[20] B. Dam, J. Rector, M.F. Chang, S. Kars, D.G. de Groot, and R. Griessen, Appl. Phys. Lett. 65, 1581 (1994)

[21] B. Dam, J.H. Rector, J. Johansson, S. Kars, and R. Griessen, Appl. Surf. Sci. 96-98, 679 (1996)

[22] B. Dam, J.H. Rector, J. Johansson, J. Huijbregtse, and D.G. de Groot, J. Appl. Phys. 83, 3386 (1998)

[23] L.R. Doolittle, Nucl. Instrum. Methods Phys. Rev. B 9, 344 (1985)

[24] M.C. Foote, R.P. Vasquez, B.B. Jones, B.D. Hunt, and J.B. Barner, J. Electronic Mater. 23, 849 (1994)

[25] B.T. Ahn, V.Y. Lee, R. Beyers, T.M. Gür, and R.A. Huggins, Physica C 167, 529 (1990)

[26] J.P. Gong, M. Kawasaki, F. Fujito, R. Tsuchiya, M. Yoshimoto, and H. Koinuma, Phys. Rev. B 50, 3280 (1994)

[27] O. Eibl and B. Roas, J. Mater. Res. 5, 2620 (1990)

[28] F. Izumi, H. Asano, T. Ishigaki, E. Takayama-Mromachi, Y. Uchida, N. Watanabe, and T. Nishikawa, Jpn. J. Appl. Phys. 26, L649 (1987)

[29] Jinhua Ye and Keikichi Nakamura, Phys. Rev. B 48, 7554 (1993)

[30] Jinhua Ye and Keikichi Nakamura, Phys. Rev. B 50, 7099 (1994)

[31] Jinhua Ye and Keikichi Nakamura, Physica C 254, 113 (1995)

[32] H.S. Kim and H.S. Kwok, Appl. Phys. Lett. 61, 2234 (1992)

[33] N. Kanda, M. Kawasaki, T. Kitajima, and H. Koinuma, Phys. Rev. B 56, 8419 (1997)

[34] B. Dam, J.H. Rector, J.M. Huijbregtse, and R. Griessen, Physica C 305, 1 (1998)

[35] A. Wong, R. Liang, M. Gardner, and W.N. Hardy, J. Appl. Phys. 82, 3019 (1997)

[36] T.R. Goodman, Advances in Heat Transfer, edited by T.F. Irvin and J.P. Hartnett (Acadamic Press, New York, 1964), Vol. 1, p. 51

[37] A.N. Jette and W.J. Green, J. Appl. Phys. 68, 5273 (1990)

[38] O. Auciello, A.R. Krauss, J. Santiago-Aviles, A.F. Schreiner, and D.M. Gruen, Appl. Phys. Lett. 52, 239 (1988)

Chapter 3

Origin of high critical currents

Thin …lms of the high-temperature superconductor $YBa_2Cu_3O_{7\,¡\,\pm}$ exhibit both a large critical current (the superconducting current density generally lies between 10^{11} and 10^{12} A/m^2 at 4.2 K in zero magnetic …eld) and a rapid decrease in current with magnetic …eld. Both features point to the importance of strong vortex pinning along extended defects. However, it has hitherto been unclear which type of defect ¡ dislocations, grain boundaries, surface corrugation and anti-phase boundaries ¡ is responsible. Making use of a novel sequential wet-chemical etching technique, we …nd that: (i) all dislocations (edge, screw and mixed) can be mapped quantitatively by this technique and (ii) threading dislocations are the defects that provide the strong pinning centres responsible for the high critical currents observed in these thin …lms. In contrast to arti…cially generated columnar defects, these natural linear defects exhibit self-organized short-range order. Therefore, $YBa_2Cu_3O_{7\,¡\,\pm}$ thin …lms o¤er an attractive system for investigating the properties of vortex matter in a superconductor with a tailored defect structure.[1]

[1]This chapter is based on papers by B. Dam, J.M. Huijbregtse, F.C. Klaassen, R.C.F. van der Geest, G. Doornbos, J.H. Rector, A.M. Testa, S. Freisem, J.C. Martinez, B. Stäuble-Pümpin, and R. Griessen, Nature (London) 399, 439 (1999) and by J.M. Huijbregtse, B. Dam, R.C.F. van der Geest, F.C. Klaassen, R. Elberse, J.H. Rector and R. Griessen, Phys. Rev. B 62, 1338 (2000)

3.1 Introduction

In the last few years the quality of high-T_c superconducting thin …lms has improved signi…cantly. Thin …lms have become more and more single-crystalline like. However, the magnitude of the superconducting current density j_s in …lms is still orders of magnitude larger than in single crystals.[2] In $YBa_2Cu_3O_{7\,i\,\pm}$ …lms for example, j_s is as high as 10^{12} A/m^2 (at small magnetic …elds and low temperatures) while in single crystals it is typically 10^{10} A/m^2 [2]. The high j_s of …lms is generally attributed [3] to the strong pinning [4, 5] of vortices to extended defects. In single crystals the transport properties are mainly determined by randomly distributed point defects (e.g. oxygen vacancies), leading to weak collective pinning [5]. The high j_s values found in …lms must thus be caused by extended defects which are speci…c for …lms such as substrate induced anti-phase boundaries [6], dislocations [7, 8, 9] or surface roughness [9, 10]. Although there are experimental results [11, 12] pointing to the importance of pinning by dislocations in …lms, no quantitative relation between the dislocation density and the pinning properties could be established. In this chapter, we demonstrate that the linear defect structure of a …lm can be mapped quantitatively and that an unambiguous relation exists between the as-grown dislocation density n_{disl} and the strong pinning behavior of j_s in $YBa_2Cu_3O_{7\,i\,\pm}$ thin …lms.

Instead of looking at the as-grown surface morphology, we investigate wet-etched …lms. It has been suggested [7] that the density of screw dislocations can be determined by counting the number of spiral outcrops [13, 14] at the …lm surface. However, in this way the total dislocation density (edge, screw and dislocations of mixed character) is severely underestimated [15] for two reasons: (i) edge dislocations do not give rise to such a clear topological structure and (ii) not all screw dislocations generate growth spirals. Wet-chemical etching in combination with atomic force microscopy reveals the full dislocation structure and allows for a statistical analysis. Not only the length but also the lateral dislocation distribution can be determined. We …nd that dislocations are generated in the early stages of growth, i.e. close to the substrate-…lm interface. Since dislocations cannot end inside a crystal [16], they persist up to the …lm surface parallel to the c-axis, resulting in a uniform length distribution. In principle, such threading dislocations can pin vortices along their entire length. At …rst sight this situation seems very similar to arti…cial linear defects created by irradiating single crystals with heavy ions [17, 18]. However, in our …lms the linear defects are inherently growth-induced and exhibit short-range ordering, whereas arti…cial columnar defects are randomly distributed. In principle, the non-random dislocation distribution enhances the pinning e¢ciency. Since we can also tune the threading dislocation density at will without a¤ecting either the length or the lateral distribution of these linear defects, …lms are very attractive to study vortex matter. For instance, the predicted Mott-insulator vortex phase [4, 19] may be observable in thick laser ablated $YBa_2Cu_3O_{7\,i\,\pm}$ …lms at low dislocation densities.

[2] Due to thermal activation [1], the measured superconducting current density j_s is always smaller than the true critical current density j_c (the di¤erence increases with temperature). We use the symbol j_c for: (i) theoretical estimates and (ii) when correcting j_s for relaxation e¤ects.

3.2 Revealing dislocations

As is well-known in (bulk) metallurgy [20], dislocation densities can be reliably determined by counting the number of etch pits formed upon applying a suitable dislocation sensitive etchand. In the case of $YBa_2Cu_3O_{7-\pm}$ ...lms, the etchand is a 1 Vol.% Br in ethanol solution [15, 21, 22, 23, 24]. To analyze the surface morphology of both the as-grown and the etched ...lms, we use atomic force microscopy (AFM) in the tapping mode. In order to investigate the persistence of etch pits upon repeated etching, a speci...c area on the ...lm surface is identi...ed by means of two perpendicular engraved markers. Using the large range of the AFM tube scanner (maximum scan size 100 ¹m), horizontal displacements of the AFM tip of about 20 ¹m with respect to these reference markers can be reproduced. In this way surface features can be traced back, even after repeatedly etching and remounting of the sample.
Below, we show how wet-chemical etching in 1 Vol.% Br-ethanol reveals dislocations. As a ...rst step, the development of etch pits at defect sites is described. Since sputtered ...lms exhibit spiral outcrops (i.e. screw dislocations), we use these ...lm to test our etching technique. Finally, the persistence of etch pits upon repeated etching at defect sites is probed in PLD ...lms, indicating that the defects that are revealed are indeed linear defects.

3.2.1 Principle of etching

The surface morphology of as-grown PLD ...lms[3] is generally characterized by a semi-regularly spaced array of growth islands, separated by trenches [see Fig. 3.1(a)]. These trenches have a depth of up to 20% of the ...lm thickness. In the trenches some deeper depressions can be discerned. Changing the deposition conditions (substrate temperature T_{sub} and oxygen pressure p_{O_2}) mainly a¤ects the size D of the islands, i.e. the spacing between trenches. Since our PLD ...lms grow by 2D nucleation and growth [15, 25], there are no spiral outcrops at the surface. Therefore, from the surface morphology only, it is not possible to determine the (screw) dislocation density.
In order to reveal dislocations ending at the ...lm surface, we apply a dislocation sensitive etchand. For etching to start on a ‡at, defect-free crystal surface, a negative (or inverse) 2D-nucleus has to be formed [20, 26]. Analogously to growth by 2D-nucleation, the radius of this nucleus, R, has to exceed some critical value $R^{¤}$ to become a stable and expanding nucleus. This is due to the positive edge free energy term in the total Gibbs free energy change:

$$¢G(r) = ¡¼R^2h¢¹ + 2¼R°h. \qquad (3.1)$$

Here ° is the edge free energy, h the height of the nucleus and ¢¹ the di¤erence in chemical potential between atoms in the solid and those dissolved (¢¹ > 0). After a stable (negative) nucleus has been formed, dissolution proceeds by fast lateral

[3] All PLD ...lms in this chapter are prepared in the QUESTEK set-up, using 3:0 < d_{T-S} < 3:5 cm, 750 < T_{sub} < 850±C and 15 < p_{O_2} < 50 Pa at a ‡uence J = 1:3 J/cm^2 (as measured at the target).

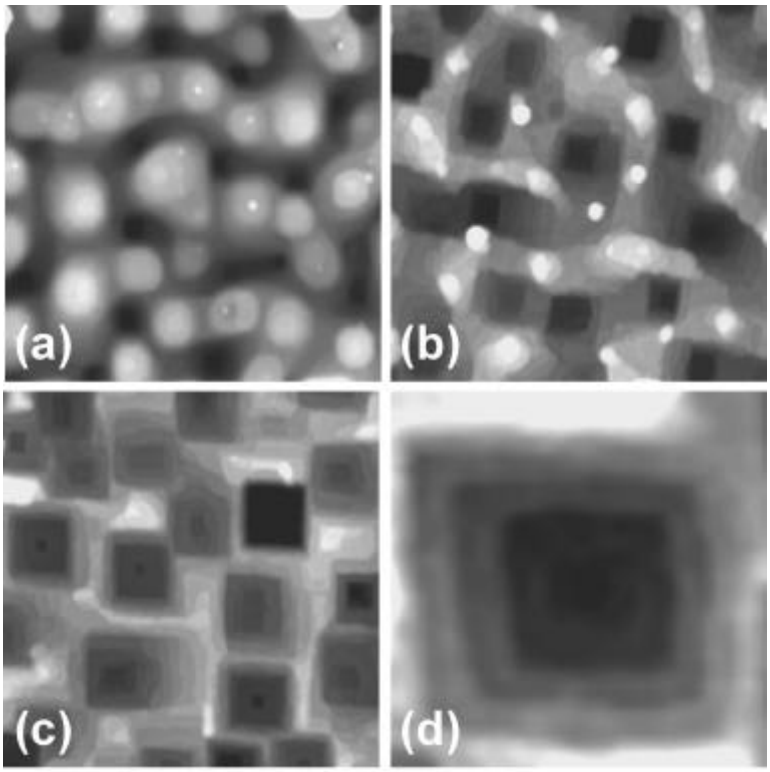

Figure 3.1: Surface morphology of a 110 nm thick $YBa_2Cu_3O_{7-\delta}$ laser deposited on (100) $SrTiO_3$ and subsequently etched in 1 Vol.% Br-ethanol: (a) as-grown surface morphology consisting of semi-regularly spaced growth islands separated by trenches (b) after 5 s of etching both the as-grown surface morphology and the formation of etch pits can be discerned and (c) after 10 s of etching only sharp-bottomed etch pits are visible. In these three AFM height images of 1:0 £ 1:0 μm^2 dark is low and bright in high. In (d) a close up (225 £ 225 nm^2) of an etch pit is shown that consists of steps of several unit cells (u.c.) in height: 11 nm (5 u.c.), 2.4 (2 u.c.), 3.6 nm (3 u.c.), and 2.4 nm (2 u.c.) from high to low, corresponding to an average inclination angle of $7.5^{\pm}$.

movement of the negative steps. In the absence of defects, nucleation is a random process and the crystal gets thinner, while, on average, the surface remains ‡at.
The situation is di¤erent in the presence of defects. A defect provides for a site where locally either ° is reduced and/or ¢ ¹ is increased, i.e. a site where the activation energy for dissolution is lowered. Therefore, at defect sites repetitive preferential nucleation takes place and an etch pit forms. However, as soon as the defect ends, there is no longer a source for preferential nucleation and the surface gets ‡at again. In the case of extended defects such as dislocations, repetitive preferential nucleation at the linear defect sites results in persistent, sharp-bottomed etch pits.
As follows from Fig. 3.1(a), as-grown PLD …lms are not ‡at. Upon etching a …lm with a rough surface, but without defects, steps proceed by fast lateral movement and the surface smoothens upon etching. In the presence of linear defects, the roughness …rst increases [creation of etch pits, whereas the original surface roughness has not yet been smoothed, see Fig. 3.1(b)] and then decreases [etch pits persist, whereas the surface in-between the pits becomes ‡atter, see Fig. 3.1(c)]. Hence, upon etching $YBa_2Cu_3O_{7-\delta}$ …lms in Br-ethanol the growth islands are erased and an ensemble of square, sharp-bottomed etch pits forms. As shown in Fig. 3.1(d), within an etch pit concentric steps can be discerned. These steps are usually several unit-cells in height. Clearly, the pits are not negative spirals. Negative spirals are only expected at extremely small undersaturations [27]. As the etch pits are symmetric [28], we infer that the dislocation line is perpendicular to the …lm plane (i.e., parallel to the c-axis of the …lm).
The square edges of the pits are roughly parallel to the [100] and [010] directions, indicating that the etch pit shape is determined by the slowest etching step directions. These directions are indeed parallel to the strongest chemical bonds [29]. Since on $SrTiO_3$ substrates all etch pits have the same orientation, we infer that the in-plane crystal orientation of the …lms is good (except for the occurrence of twin boundaries which are generally present in $YBa_2Cu_3O_{7-\delta}$ …lms deposited on $SrTiO_3$). The etch pits are not bounded by low index crystal planes. The slope of the sides of the etch pits varies between 7 and 12± and appears to be determined by the etching kinetics.

3.2.2 Etching sputtered …lms

To prove that we are revealing dislocations, we etched sputtered $YBa_2Cu_3O_{7-\delta}$ …lms.[4] The surface morphology of sputtered …lms consists of large growth spirals of unit-cell step height and a large (>100 nm) step spacing, resulting in growth islands up to 2.5 ¹m in diameter (see Fig. 3.2). Since sputtered …lms grow in a spiral growth mode, we can exactly identify the position where screw dislocations are located (i.e. at the spiral outcrop). We …nd that etch pits develop both at the spiral core and randomly around the core (Fig. 3.2). The pit at the spiral core has to be due to a screw dislocation and from the unit-cell step height we infer that this dislocation has a Burger's vector of 1.2 nm. Generally, the vertical etch rate is determined by the stress …eld around

[4] These …lms are prepared by S. Freisem (Kamerlingh Onnes Laboratory, Leiden University), according to the procedure described in Ref. [30].

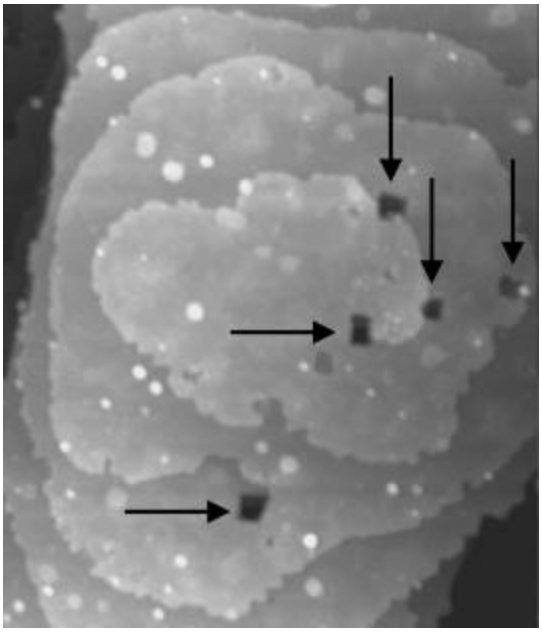

Figure 3.2: AFM height image of a unit cell height (1.2 nm) double spiral on a 200 nm thick $YBa_2Cu_3O_{7-\delta}$ film sputtered on (100) $SrTiO_3$. After etching for 20 s, the growth features are still intact but small etch pits have developed at the spiral cores (screw dislocations, horizontal arrows) and across the spiral (edge dislocations, vertical arrows). The image size is $0{:}85 \times 1{:}0\ \mu m^2$. Some etched material is redeposited in the form of small precipitates.

the dislocation. Since this magnitude of the stress depends on the size of the Burger's vector and not on its direction, etching reveals all dislocations. Therefore, the pits within the spiral that are not related to any growth feature have to be of an edge character. Note, that the spiral in Fig. 3.2 is in fact a double spiral originating from two screw dislocations with Burger's vectors of opposite sign [31]. Consequently, also at the other end of the spiral a screw dislocation is expected. Indeed, we find another etch pit exactly at this position, proving that dislocations are revealed.

3.2.3 Repetitive etching

How do we prove that the defects, that are revealed by etching, are really linear defects, i.e. defects that have a length comparable to the film thickness? To answer this question we followed an ensemble of etch pits upon repeated etching PLD films, by marking an area on the film surface using a set of engraved perpendicular markers. Since both the depth of etch pits increases and the film thickness decreases upon

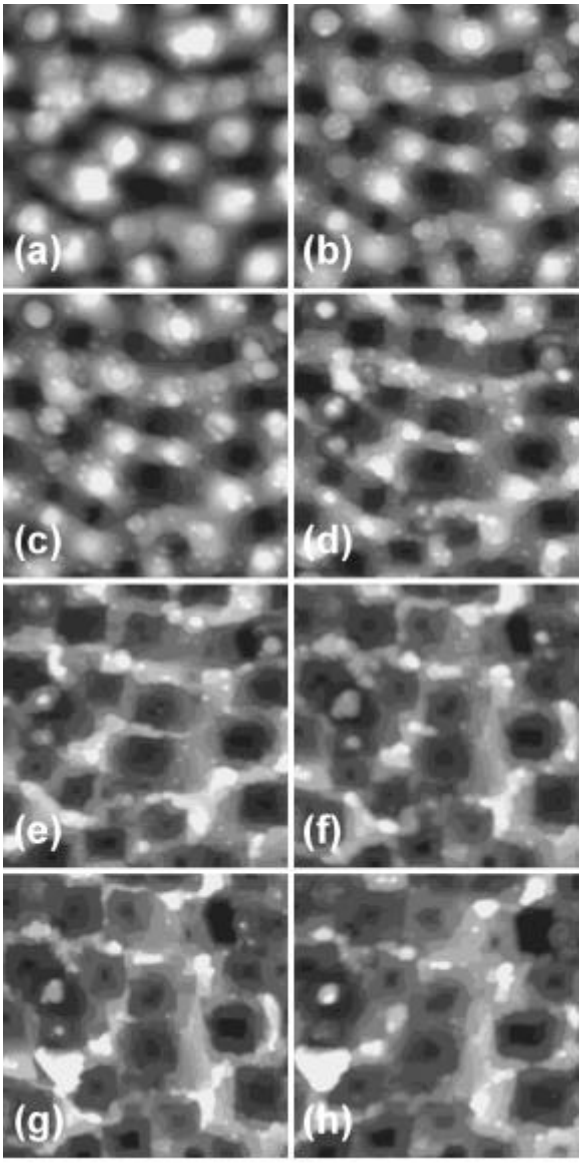

Figure 3.3: Surface morphology of a 490 nm thick $YBa_2Cu_3O_{7\,i\,\pm}$ …lm laser deposited on (100) $SrTiO_3$. Consecutive AFM height images are taken after repetitive etching of the same area (0:5 £ 0:5 $^1m^2$): (a) as-deposited, (b) 10 s, (c) 15 s, (d) 20 s, (e) 25 s, (f) 30 s, (g) 35 s, and (h) 40 s etched, showing the persistence of etch pits upon prolonged etching. The average etching rate, estimated by fully etching o¤ the …lm, is about 1 nm/s. In the upper left corner, a precipitate is revealed upon etching.

repeated etching, we are able to follow the etch pits in the …lm. A sequence of consecutive etch experiments is shown in Fig. 3.3.
In this …gure, it can be seen that etch pits develop at the periphery of the islands and that all etch pits persist upon repeated etching. Since the bottoms of the etch pits do not turn ‡at but remain sharp, there is a persistent source for preferential etching. Thus, we conclude that we are indeed dealing with linear defects of a considerable length. In Fig. 3.3 some etch pits are hampered in their development (see for instance the etch pit in the upper left corner). Upon prolonged etching …rst a precipitate is revealed and then an etch pit forms again, indicating that dislocations can end and originate again at precipitates [16]. However, in all etching experiments this fraction is small (< 5%). Since the lateral size of the etch pits increases upon repeated etching (Fig. 3.3), it becomes more and more di¢cult to follow the individual etch pits. Although initially overlapping etch pits can still be distinguished due to their pronounced square shape, at a certain moment this is not possible any more. Consequently, it is impossible to follow the etching process down to the substrate. A better method to investigate the length distribution of linear defects is to etch …lms of various thickness (see section 3.3.2).

Concluding, we …nd that the density of linear defects in $YBa_2Cu_3O_{7\,i\,\pm}$ …lms can be quantitatively determined by combining Br-ethanol etching with AFM. We identi…ed some of the pits as being due to screw dislocations with a unit-cell Burger's vector. As etch pit formation is due to the stress energy within the dislocation core (and does not depend on the direction of the Burger's vector) both edge and screw dislocations with Burger's vectors of one unit-cell or higher are revealed. Although in principle we can observe dislocations tilted with respect to the c-axis, none of those were detected. Note that dislocations running parallel to the substrate are not revealed in our experiments.

3.3 Dislocation density and distribution

3.3.1 Tuning the dislocation density

Having a tool to determine dislocation densities, we investigate now the mechanism by which dislocations are induced during growth. Therefore, we take a closer look at the position of the dislocations (or etch pits) with respect to the as-grown …lm surface. Figure 3.4 shows two AFM height images recorded directly after deposition and after etching the same …lm. Since these images are taken on the same position, we infer that dislocations are mainly situated around the islands in the holes in the trenches (in fact this can also be seen in Figs. 3.1(b) and 3.3). Apparently, surface depressions form at positions where dislocations emerge at the …lm surface. Indeed, Frank predicted [32] such depressions to form as a result of the strain energy associated with dislocations. However, the depressions in our …lms are much wider than predicted and they do not form around all dislocations.

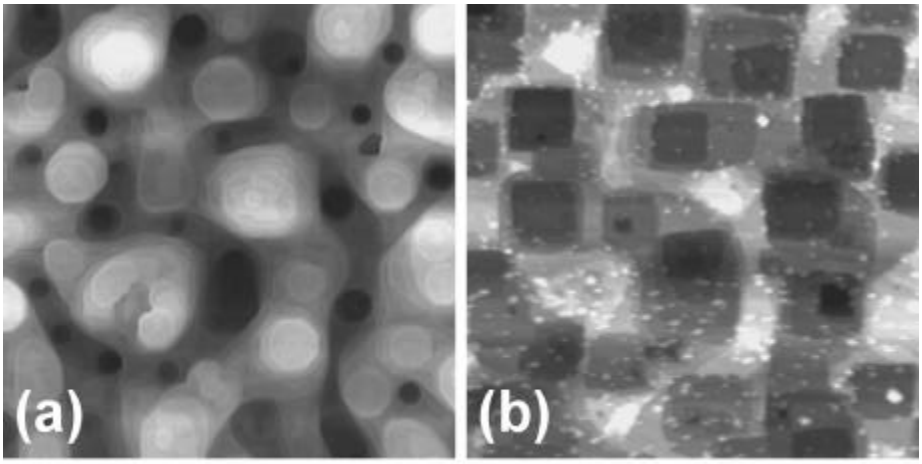

Figure 3.4: AFM height images of a $YBa_2Cu_3O_{7-\delta}$ ...lm laser deposited on (100) $SrTiO_3$ taken on the same position (scan size 2.0 ¹m): (a) as-grown surface morphology and (b) etched for 5 s. Every hole in the as-grown ...lm surface corresponds to an etch pit, indicating that dislocations are situated around the growth islands. On the etched ...lm surface some material is redeposited in the form of small precipitates.

To check the relation between the location of dislocations and the island structure we deposited a series of 150 nm thick $YBa_2Cu_3O_{7-\delta}$ ...lms with various sizes of the growth islands. By increasing T_{sub} from 750 to 850±C and p_{O_2} from 15 to 50 Pa, the island diameter D can be varied reproducibly between 125 and 450 nm, respectively [25]. In Fig. 3.5 the dislocation density as measured by etching these ...lms for ¼20 s in Br-ethanol is plotted as a function of the density of growth island $n_{island} = 1/D^2$, showing that on average there is about one dislocation per island. By manipulating the island density the dislocation density can be varied reproducibly. In this way n_{disl} can be increased up to 68 $^{1}m^{-2}$. Unfortunately, the range over which n_{disl} can be tuned is limited. As shown in Fig. 3.6, the superconducting transition temperature T_c decreases only slightly when increasing n_{disl}. Up to now, T_c could not be maintained above 90 K when decreasing the island size below 125 nm.

3.3.2 Dislocation distribution

At this point we are not only able to quantitatively determine dislocation densities, but we can also tune their density. In this section both the length (along the c-axis of $YBa_2Cu_3O_{7-\delta}$) and lateral (in the ab-plane) distribution of the growth-induced linear defects are investigated as a function of the defect density.

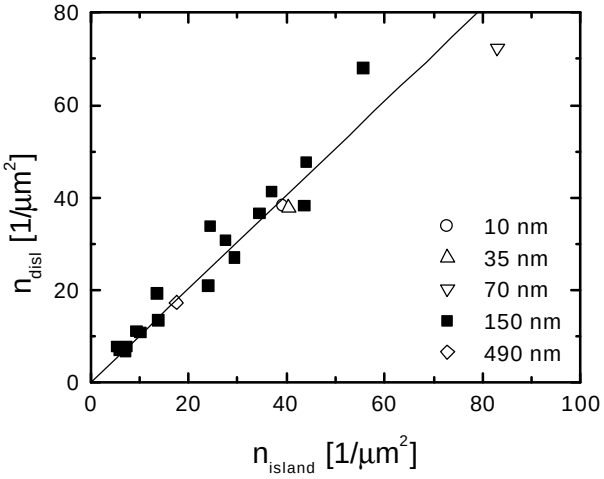

Figure 3.5: Dislocation density n_{disl} as measured by etching as a function of the density of growth islands n_{island} of 10 to 490 nm thick $YBa_2Cu_3O_{7-\pm}$ …lms laser deposited on (100) $SrTiO_3$ substrates. By manipulating n_{island} the number of dislocations can be tuned. The …lm thickness a¤ects neither n_{disl} nor n_{island}.

Length distribution

So far, we determined dislocation densities at or close to the …lm surface. In order to investigate the length distribution of dislocations, additional …lms were grown with a thickness of 10, 35, 70 and 490 nm at di¤erent deposition conditions. All these …lms exhibit the same characteristic island structure as in Fig. 3.1(a), even for …lms as thin as 10 nm (see Fig. 3.7 for an example). Etching these …lms and plotting the results in Fig. 3.5, we …nd that the relation between islands and dislocations does not depend on …lm thickness. As the …lms with a thickness of 10, 35 and 150 nm are deposited under similar conditions, this observation indicates that n_{island} and therefore also n_{disl} do not depend on the …lm thickness. Since dislocations cannot end inside a crystal [16], this implies that dislocations have to run through the entire …lm thickness. Hence, they must be formed at the substrate-…lm interface. Therefore, the distribution of dislocation lengths is uniform: all dislocations have a length comparable to the …lm thickness. Indeed, TEM studies [33] on laser ablated $YBa_2Cu_3O_{7-\pm}$ on (100) $SrTiO_3$ substrates revealed such threading dislocations with a density of the order of $10^{1}m^{-2}$ that extend from the interface all the way up to the …lm surface.[5]

[5] In chapter 4 the results of both cross-sectional and planar view (High Resolution) TEM measurements are presented.

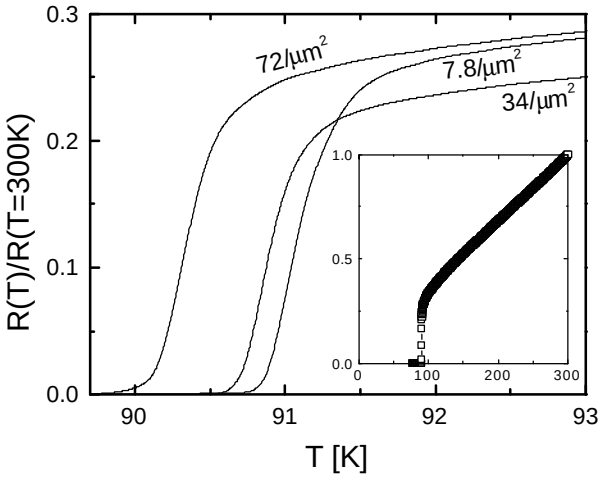

Figure 3.6: Normalized electrical resistance R as a function of temperature T for three $YBa_2Cu_3O_{7-\delta}$ films laser deposited on (100) $SrTiO_3$ with dislocation densities n_{disl} = 7.8, 34 and 72 μm^{-2}; R (T) is normalized with respect to R (T = 300 K). The transition temperature T_c decreases with increasing n_{disl}. The inset shows R (T) / R (T = 300 K) over a larger temperature range for the film with n_{disl} = 72 μm^{-2}. A typical value for the resistivity of films with intermediate n_{disl} is 83 $\mu\Omega$-cm at 100 K.

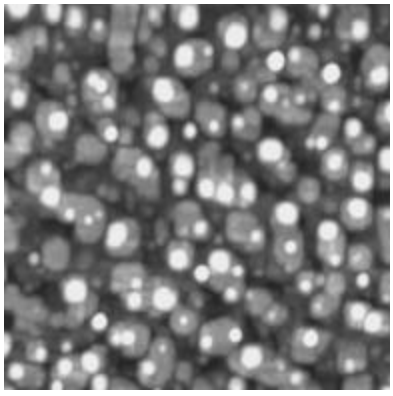

Figure 3.7: AFM height image of a 10 nm thick $YBa_2Cu_3O_{7-\delta}$ film laser deposited on (100) $SrTiO_3$ with an island density of 70 / μm^2, indicating that the familiar morphology is already formed after depositing a few monolayers of $YBa_2Cu_3O_{7-\delta}$. The image size is 1.0 £ 1.0 μm^2.

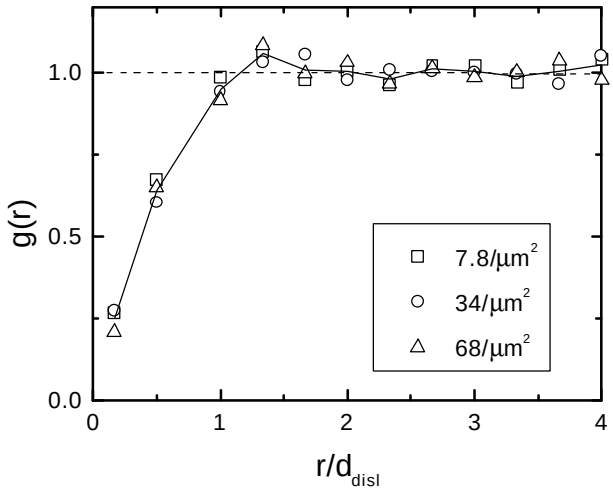

Figure 3.8: Radial dislocation distribution function g(r) of three $YBa_2Cu_3O_{7-\delta}$ films laser deposited on (100) $SrTiO_3$ with dislocation densities n_{disl} = 7.8, 34 and 68/μm^2. By normalizing the radial coordinate r with respect to the average dislocation spacing $d_{disl} = 1/\sqrt{n_{disl}}$, the function $g(r/d_{disl})$ scales onto an universal curve; g(r) = 1 for a random distribution (dashed line).

Lateral distribution

As dislocations are situated around the growth islands (Fig. 3.4), the in-plane defect distribution is not completely random. To quantify this short-range ordering, we determined the radial dislocation distribution function g(r) from the etch pit distribution [34] as measured by AFM. Taking a certain etch pit as a reference point, we count the number of pits $\Delta N(r)$ within a ring of width Δr at a distance r. Then,

$$g(r) = \frac{\Delta N(r)}{2n_{disl}\pi r \Delta r}. \qquad (3.2)$$

This procedure is repeated with every dislocation as a reference dislocation and finally averaged. In order to improve the statistics, periodic boundary conditions are used. The outcome of this statistical analysis is shown in Fig. 3.8 for three films with dislocation densities of 7.8, 34 and 68 μm^{-2}. By normalizing r with respect to the average dislocation spacing d_{disl} ($= 1/\sqrt{n_{disl}}$), all curves scale onto a single radial distribution function $g(r/d_{disl})$, indicating that the distribution is universal. For comparison, the result for a random distribution (g(r) = 1) is included. We note that the decrease of g(r) for small r is not an artifact of the analysis. By etching films very shortly, we are able to distinguish etch pits that are only 30 nm apart. Moreover, because of their characteristic square shape even overlapping etch pits can

be resolved. Obviously, the statistics become poor at small r and we estimate the lower limit of our analysis to be 50 nm, which corresponds to $r=d_{disl}$ = 0:41, 0.29 and 0.14 for n_{disl} = 7:8, 34 and 68 $^1m^{i\,2}$ respectively. The most striking di¤erence between the measured defect distribution and a random distribution (Fig. 3.8) is found at small distances, $r < d_{disl}$. Below the average dislocation spacing, there is only a small chance to …nd another dislocation, pointing to short-range ordering of the defects. In chapter 7 of this thesis we will discuss the origin of this self-organization of defects in more detail.

3.4 Strong pinning by dislocations

3.4.1 The characteristic …eld

To decide whether natural linear defects are the main source of strong vortex pinning in thin …lms, we measured the superconducting current density $j_s(B;T)$ as a function of temperature (4:2 < T < 80 K) and magnetic …eld (B 7 T) of a series of …lms with various threading dislocation densities, see Fig. 3.9. Here, we determined j_s from the magnetic moment of ring patterned …lms (outer diameter typically 3.0 mm; width 0.50 mm) by means of a capacitance torque magnetometer [35], applying magnetic …elds at an angle of 10± from the c-axis. The high magnetic …eld regime is probed by sweeping the magnetic …eld at a rate of 40 mT/s (from 0 to 7 T). To measure the low …eld regime accurately, additional low …eld sweeps (up to 1 T) are performed at a sweep rate of 1 mT/s.

In all …lms, independently of the defect density, we …nd that $j_s(B;T)$ exhibits a plateau for magnetic …elds $B < B^¤$. Above this so-called characteristic …eld $B^¤$, a gradual transition to a power-law behavior is found ¡ that is $j_s(B) / B^®$ (with $¡\frac{1}{2} . ® . ¡1$ at low temperatures). Experimentally, we determine $B^¤$ by …tting

$$j_s(B) = \frac{j_s(0)}{1 + k_1 x^® \exp[¡1=x]} \tag{3.3}$$

in a linear j_s ¡ B plot, where $x = B=k_2$ (here ®, k_1 and k_2 are …tting constants). The form of this empirical function is found to give a good description of the …eld dependence over a large …eld range. Then, $B^¤$ is de…ned by the crossing of the tangent at the in‡ection point and the low …eld plateau $j_s(0)$. Now, plotting this characteristic …eld $B^¤$ at 4.2 K against the measured threading dislocation density, we …nd the remarkable correlation shown in Fig. 3.10: $B^¤$ is proportional to the dislocation density and the slope of the …t is ¼ 0:7$©_0$ per dislocation, where $©_0$ is the ‡ux quantum ($©_0$ = 2:068 £ $10^{i\,15}$ Tm^2). We conclude that $B^¤ = 0:7B_©$, where the so-called matching …eld $B_© ´ n_{disl}©_0$ corresponds to the density of linear defects naturally present in $YBa_2Cu_3O_{7¡±}$ …lms. From Fig. 3.10 it also follows that the value of the current density at $B < B^¤$ decreases only marginally[6] with the density

[6] In chapter 4 we will explore the origin of this second order e¤ect.

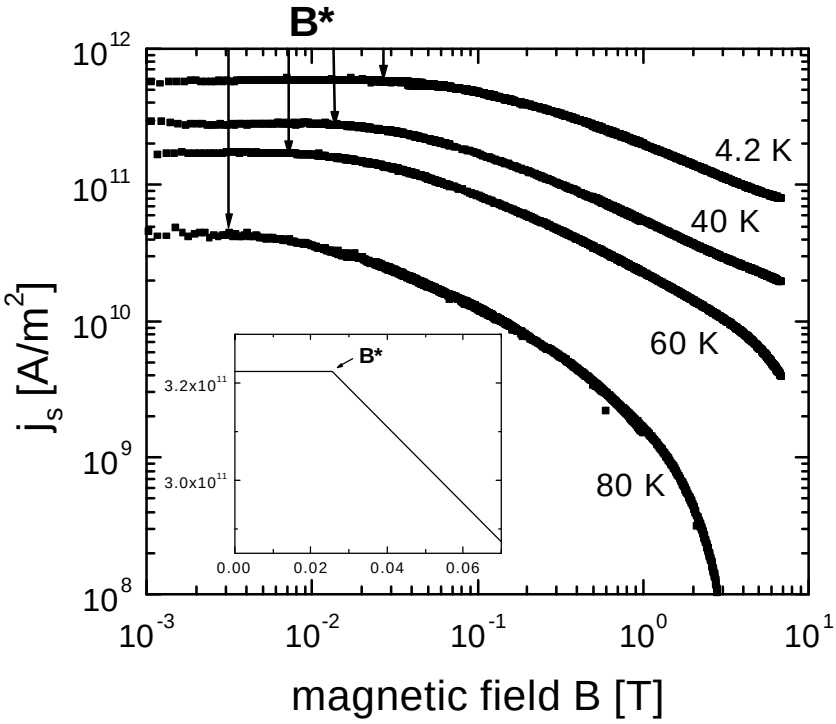

Figure 3.9: Magnetic …eld dependence of the superconducting current density $j_s(B;T)$ of a sample with $n_{disl} = 6{=}^1m^2$ at various temperatures. The inset shows the de…nition of the characteristic …eld B¤: in a linear plot of $j_s(B)$ the data is …tted to Eq. (3.3) and B¤ is determined by the crossing of the tangent at the in‡ection point and the low …eld plateau.

of linear defects. This shows that the superconducting current density at low …elds is solely determined by the pinning of single vortices along extended defects. This is, as far as we know, the …rst report of an unambiguous quantitative relation between the characteristic …eld B¤ (or the matching …eld B©) and the density of natural linear defects in a superconductor. At low magnetic …elds, when the number of threading dislocations is much larger than the number of vortices, all vortices are pinned and j_s is of the order of the depairing current j_{c0} [4, 5]. For $B < B^¤$ we …nd transport currents up to $7 £ 10^{11}$ A/m^2, close to $j_{c0} ¼ 4 £ 10^{12}$ A/m^2 (corresponding to a magnetic penetration depth ¸ = 140 nm and a coherence length » = 1:5 nm).
However, because of the one-to-one correspondence between islands (n_{island}) and dislocations (n_{disl}) the identi…cation of the strongest pinning defect might be ambiguous. There could be other types of extended defects related to the island size. Two important experimental observations provide conclusive evidence that threading dis-

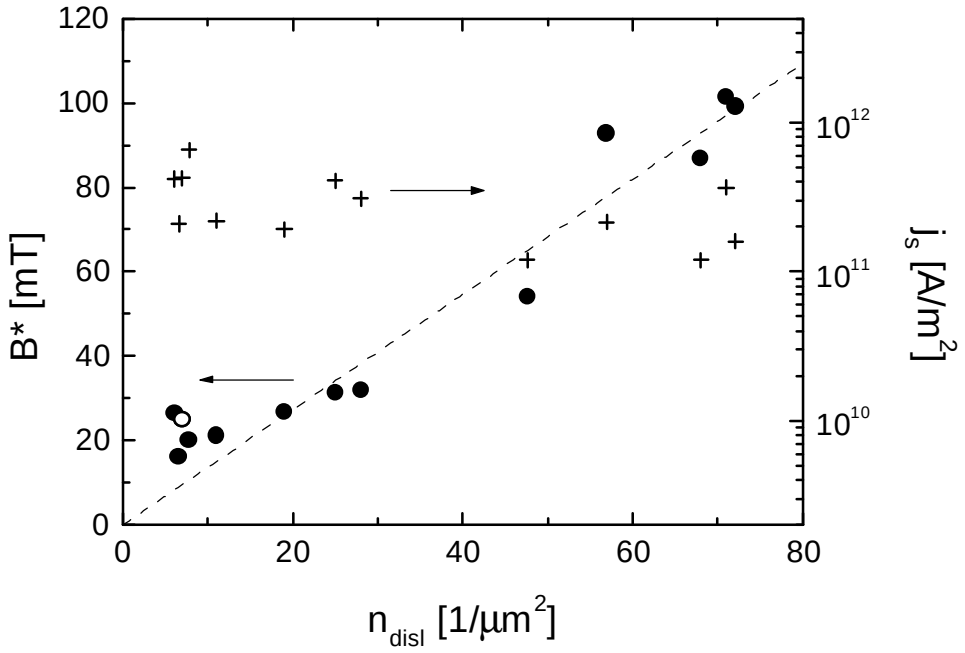

Figure 3.10: The characteristic …eld $B^{¤}$ (4:2 K) and the low …eld superconducting current density j_s ($B < B^{¤}$; 4:2 K) as a function of the dislocation density n_{disl}, as determined from the measured etch pit density. $B^{¤}$ is plotted as …lled circles (the open circle corresponds to the sputtered …lm shown in Fig. 3.2) and j_s as plus signs; the dotted line is a …t to the data ($B^{¤}$).

locations are the most important defects in these …lms. First of all, in sputtered …lms the relation between dislocation density and island density does not hold: n_{island} is more than an order of magnitude smaller than n_{disl}. Yet, we …nd that the characteristic …eld $B^{¤}$ is determined by the dislocation density (as indicated by the open circle in Fig. 3.10). The second argument comes from PLD …lms themselves. It turns out that we can manipulate n_{island} by means of annealing the …lms for 30 minutes at temperatures around 800±C in a ‡ow of 97% Ar and 3% O_2 after deposition.[7] As shown in Figs. 3.11(a) and 3.11(b), we observe a signi…cant reconstruction of the …lm surface upon post-annealing. The …lms not only become much ‡atter (root-mean-square roughness 2:1 ! 1:6 nm), but also the size of the growth features increases drastically

[7]Details of this procedure and its e¤ect on the microstructural and superconducting properties are presented in chapter 4.

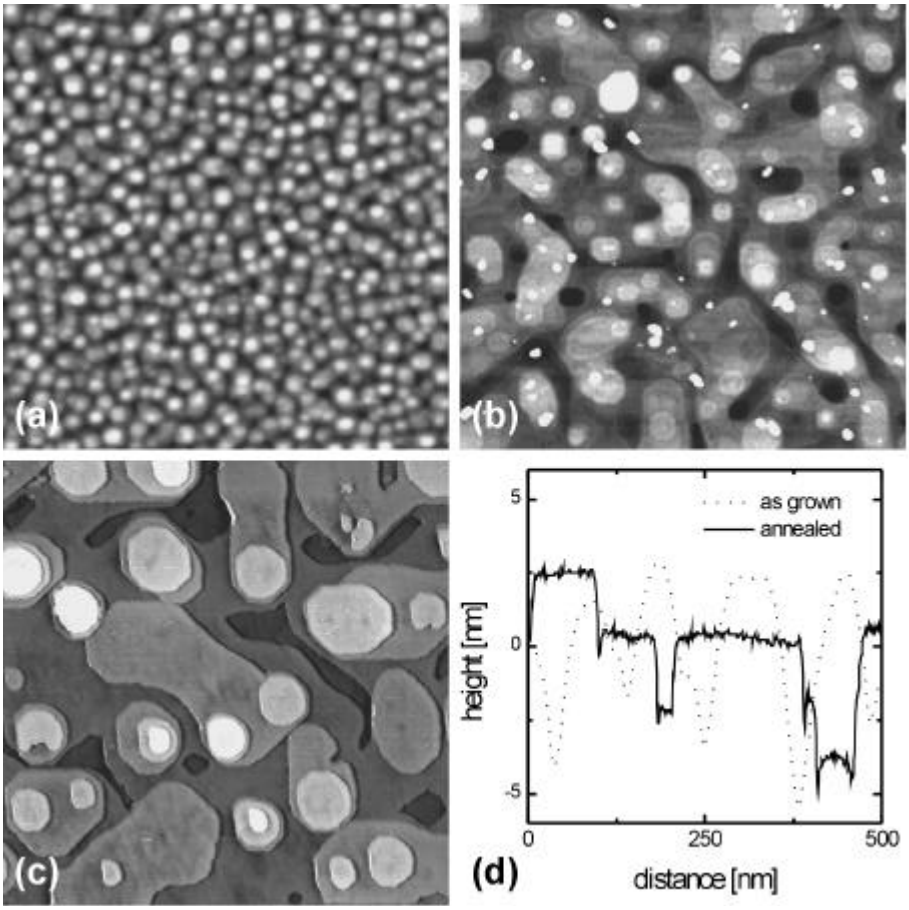

Figure 3.11: In‡uence of post-annealing on the surface morphology of a 41 nm thick $YBa_2Cu_3O_{7-\pm}$ …lm laser deposited on (100) $SrTiO_3$ with a large island density. Shown are two AFM height images of 1:75 £ 1:75 $^1m^2$ (a) after deposition (n_{island} = 105 $^1m^{-2}$) and (b) after post-annealing the same …lm for 30 minutes at 800±C in ‡owing Ar + 3% O_2 (n_{island} = 19 $^1m^{-2}$) and (c) an STM image of 1:00 £ 1:00 $^1m^2$ after post-annealing. In (d) the typical height variations are shown as measured after deposition [AFM image (a)] and after the anneal treatment [STM image (c)]. Both n_{island} and the roughness are greatly reduced upon annealing. We note that upon annealing small o¤-stoichiometries segregate to the …lm surface and form small secondary phases, as can be seen in (b).

(leading to a drastic decrease of their density: n_{island} = 105 ! 19 $^{1}m^{i2}$). To illustrate these points, in Fig. 3.11(c) a scanning tunneling microscope (STM) image of the surface morphology after post-annealing is shown.[8] Interestingly, the step height of the islands after post-annealing is exactly equal to two $YBa_2Cu_3O_{7\,i\,\pm}$ unit cells (2.4 nm), see Fig. 3.11(d). Since the dislocation density as measured by etching does not change as much as the island density upon post-annealing (37% and 55%, see chapter 4), the relation between n_{island} and n_{disl} (Fig. 3.5) is lost. Yet, B¤ remains determined by n_{disl} and not by n_{island}. We conclude that threading dislocations are the most important source for strong pinning in $YBa_2Cu_3O_{7\,i\,\pm}$ …lms.
Finally, we stress that post-annealing only has an e¤ect on the surface morphology (n_{island}) if the anneal temperature is higher than the applied deposition temperature. It is the highest temperature that determines the surface di¤usion distance and, therefore, the resulting surface morphology. Our post-anneal experiments also indicate that the relation between growth morphology and etch pit density depends on the growth parameters. For instance, if one chooses a lower deposition rate some post-annealing will already occur during deposition, yielding a decrease of the islands density with increasing …lm thickness. This may also explain the fact that some authors observe an increase of the island size with increasing …lm thickness [36].

3.4.2 Comparison with arti…cial linear defects

At …rst sight, one might think that the matching behavior of …lms is the same as that of single crystals with arti…cially induced strong pinning defects (for example, columnar defects produced by heavy ion irradiation ¡ see the review by Civale [18]). However, there are a number of essential di¤erences:
First, the nature of the transition in j_s [Fig. 3.12(a)]. In irradiated crystals, the transport current density above $B_{©}$ scales as 1=B (® = ¡1) suggesting a collective pinning behavior; whereas in …lms with a low dislocation density the $1=\sqrt{B}$ (® = $¡\frac{1}{2}$) dependence is indicative of a shear of unpinned vortices around those strongly bound to dislocations, albeit with a too-large absolute value for j_s [7]. Below $B_{©}$, for …lms we …nd a plateau in j_s, while in irradiated single crystals j_s decays exponentially up to $B_{©}$. According to Krusin-Elbaum et al. [37], the exponential decay is due to the inherently random spatial distribution of the arti…cially produced linear defects in single crystals. In such a case, not all defect sites can accommodate a vortex, since the vortex-vortex interaction dominates over the pinning energy whenever the defects are too close to each other. In contrast, in thin …lms we …nd a highly non-random radial distribution function as the growth-induced linear defects are much more evenly distributed, see Fig. 3.8. As a result, the vortex lattice easily adapts to the available pinning sites, and the transport current remains constant up to ¼ $B_{©}$. The shape of j_s around $B_{©}$ is determined by the actual radial distribution function, the vortex-vortex interaction and the pinning energy. We note that in …lms, the average vortex distance at $B_{©}$ is about equal to the penetration depth ¸. Furthermore, the diameter $2r_d$ of

[8] STM measurements are performed in the constant current mode using mechanically sharpened PtIr tips, operated at a bias voltage of 700 mV and tunneling currents around 100 pA.

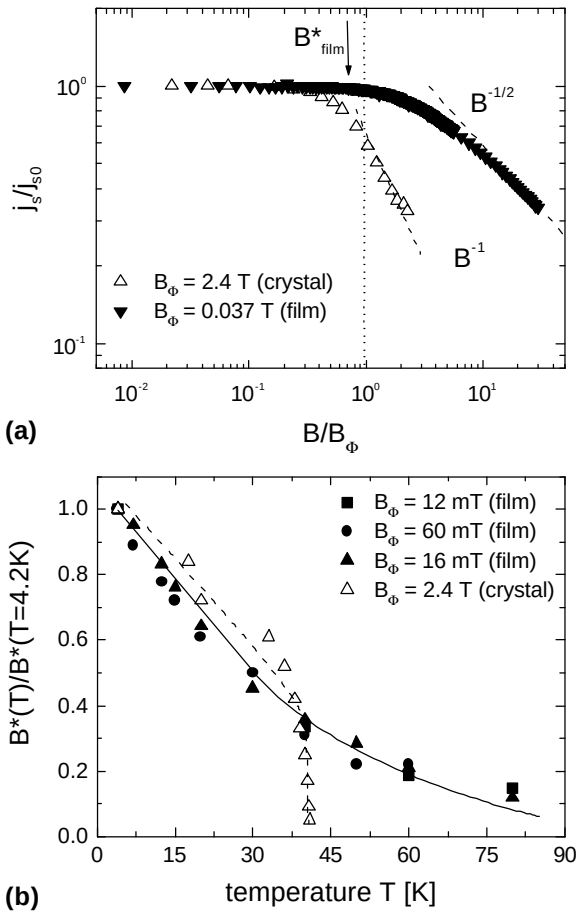

Figure 3.12: Comparison of a heavy-ion-irradiated $YBa_2Cu_3O_{7-\delta}$ single crystal [37] ($B_\odot$ equals the irradiation dose) with a thin …lm ($B_\odot$ equals n_{disl}): (a) the superconducting current density j_s normalized to its value at 4.2 K (j_{s0}); due to the non-random spatial order of natural linear defects, the current density of the thin …lms remains approximately constant up to $B_\odot$ and (b) the characteristic …eld $B^\star$ normalized to its value at 4.2 K; for the thin …lms, $B^\star$ remains …nite up to at least 80 K.

dislocations ($2r_d$ ¼ 1 ¡ 2 nm [38]) is much smaller than the that of columnar defects ($2r_{CD}$ ¼ 7 ¡ 10 nm) and is comparable to the coherence length of the superconductor (» = 1:5 nm at 4.2 K).
Second, the temperature dependence of B¤ [Fig. 3.12(b)]. In thin …lms we do not observe any deleterious thermal depinning e¤ects, which in irradiated samples reduce B¤ to zero at a thermal depinning temperature T_{dp} = 40 K. In …lms, B¤ initially also decreases linearly with temperature but, instead of a sudden drop to zero at ¼40 K, a ‡attening is observed above 50 K [Fig. 3.12(b)]. The absence of low temperature depinning behavior is in agreement with calculations [4, 5, 37] which imply that ideally T_{dp} is above 80 K. The reduced T_{dp} in single crystals is attributed to the fact that the irradiation process not only generates amorphous tracks but also numerous point defects around these tracks [37]. Natural linear defects leave the bulk of the superconducting …lm intact and T_{dp} is not depressed.

3.4.3 Implications for vortex pinning

The short-range ordering of the defect structure could make $YBa_2Cu_3O_{7\,i\,\pm}$ …lms a good candidate for observing the true Mott-insulator vortex phase [4, 19], which was predicted to occur at low temperatures when the applied magnetic …eld (k c-axis) exactly equals the matching …eld $B_{©} = n_{disl}©_0$. In this situation all linear defects are occupied by exactly one vortex. Consequently, introducing another vortex requires a large energy. Therefore, both a characteristic jump in the (reversible) magnetization as well as a diverging tilt and compression modulus of the vortex lattice are expected. So far, however, only remnants of these characteristics have been observed [39]. As was numerically shown by Wengel and Täuber [39, 40], this is not surprising because the true Mott-insulator phase is only expected for (i) weakly interacting vortices, i.e. when the average defect spacing d_{disl} is considerably larger than the magnetic penetration depth ¸ ($¸=d_{disl}$ ¿ 0) and (ii) for a regular array of columnar defects. Since in our …lms the defect distribution exhibits short-range ordering, the latter condition is much better satis…ed than for randomly distributed columnar defects in irradiated single crystals. What about the …rst condition? The smallest dislocation density obtained thus far is 7.8 $^1m^{i\,2}$, corresponding to d_{disl} = 358 nm, i.e. larger that the bulk ab-penetration depth at zero temperature $¸_{ab}(0)$ = 145 nm [41]. Yet, we did not observe the predicted characteristic jump in the magnetization. However, in thin …lms one should compare d_{disl} to the e¤ective [42] penetration depth ¤ ¼ $2¸^2=t$, where t is the …lm thickness, which is signi…cantly larger (¤ ¼ 280 nm for t = 150 nm). Therefore, in order to observe the Mott insulator phase one should (i) decrease ¤ by depositing thicker …lms and (ii) increase d_{disl} by depositing …lms with lower dislocation densities (using $T_{sub} > 850^{\pm}$C). As in our …lms both the length and the radial distribution do not depend on the …lm thickness (for 10 < t < 490 nm) nor on the defect density (for 7:8 < n_{disl} < 68 $^1m^{i\,2}$), it will be meaningful to search for the Mott-insulator phase in thick laser ablated $YBa_2Cu_3O_{7\,i\,\pm}$ …lms with a low density of natural linear defects.

3.5 Conclusions

In this chapter, the origin of the high transport current densities in $YBa_2Cu_3O_{7-\delta}$ thin …lms compared to single crystals was identi…ed. Threading dislocations were found to be the dominant source of strong pinning in …lms. To arrive at this conclusion, we …rst developed a sequential wet-chemical etching technique which enables us to determine the density of all dislocations (edge, screw and mixed character), when combined with atomic force microcopy. Since dislocations can only end at interfaces, they persist from the substrate-…lm interface up to the …lm surface parallel to the c-axis, resulting in a uniform length distribution. As these threading dislocations are mainly situated around growth islands, we can tune their density between 5 and 70 μm^{-2} reproducibly by manipulating the size of the growth features. To obtain a certain defect density we only need to adjust the substrate temperature and oxygen background pressure. Measuring the superconducting current density as a function of the applied magnetic …eld, we …nd a plateau: the current is constant up to a characteristic …eld B^* and decays rapidly at larger …elds. The proportionality between B^* and the measured dislocation density in both PLD and sputtered …lms is compelling evidence that the high current densities in $YBa_2Cu_3O_{7-\delta}$ thin …lms are due to strong vortex pinning by natural linear defects.

Statistical analysis of the lateral defect distribution in …lms with various dislocation densities shows that the radial dislocation distribution function $g(r)$ can be scaled onto a single curve $g(r=d_{disl})$, where d_{disl} is the average dislocation spacing. Both the length as well as the radial dislocation distribution do not depend on the density of defects nor on the …lm thickness. Interestingly, $g(r=d_{disl})$ approaches zero for small distances $r < d_{disl}$, indicating that the defect distribution exhibits short-range ordering. As a result, …lms behave essentially di¤erent from heavy ion irradiated single crystals, containing randomly distributed columnar defects. For instance, in …lms the pinning sites are more e¢ciently used due to the reduced in‡uence of vortex-vortex interactions. Moreover, the bulk of single crystals is also a¤ected by the irradiation process (resulting in a strongly reduced depinning temperature).

Both the tunability of the defect density and the self-organization of threading dislocations provide an attractive possibility to study vortex matter in a new class of materials: …lms with a tailored non-random distribution of linear strong pinning defects. For technological applications the challenge is to …nd ways to increase the dislocation density while keeping the non-random radial distribution intact.

References

[1] H.G. Schnack, R. Griessen, J.G. Lensink, and W. Hai-Hu, Phys. Rev. B 48, 13178 (1993)

[2] L. Civale, A.D. Marwick, M.W. McElfresh, T.K. Worthington, A.P. Malozemo¤, F.H. Holtzberg, J.R. Thompson, and M.A. Kirk, Phys. Rev. Lett. 65, 1164 (1990)

[3] T.L. Hylton and M.R. Beasley, Phys. Rev. B 41, 11669 (1990)

[4] D.R. Nelson and V.M. Vinokur, Phys. Rev. B 48, 13060 (1993)

[5] G. Blatter, M.V. Feigel'man, V.B. Geshkenbein, A.I. Larkin, and V.M. Vinokur, Rev. Mod. Phys. 66, 1125 (1994)

[6] T. Haage, J. Zegenhagen, J.Q. Li, H.-U. Habermeier, M. Cardona, Ch. Jooss, R. Warthmann, A. Forkl, and H. Kronmüller, Phys. Rev. B 56, 8404 (1997)

[7] J. Mannhart, D. Anselmetti, J.G. Bednorz, A. Catana, Ch. Gerber, K.A. Müller, and D.G. Schlomm, Z. Phys. B 86, 177 (1992)

[8] H. Douwes, P.H. Kes, Ch. Gerber, and J. Mannhart, Cryogenics 33, 486 (1993)

[9] F.C. Klaassen, J.M. Huijbregtse, B. Dam, R. van der Geest, G. Doornbos, J.H. Rector, R. Elberse, and R. Griessen, in Physics and Materials Science of Vortex States, Flux Pinning and Dynamics, edited by R. Kossowsky, S. Bose, V. Pan, and Z. Durusoy (Kluwer Academic, Dordrecht, 1999)

[10] Ch. Jooss, A. Forkl, R. Warthmann, H.-U. Habermeier, B. Leibold, and H. Kronmüller, Physica C 266, 235 (1996)

[11] D.H. Lowndes, D.K. Christen, C.E. Klabunde, Z.L. Wang, D.M. Kroeger, J.D. Budai, Shen Zhu, D.P. Norton, Phys. Rev. Lett. 74, 2355 (1995)

[12] A. Díaz, L. Mechin, P. Berghuis, and J.E. Evetts, Phys. Rev. Lett. 80, 3855 (1998)

[13] Ch. Gerber, D. Anselmetti, J.G. Bednorz, J. Mannhart, and D.G. Schlomm, Nature 350, 279 (1991)

[14] M. Hawley, I.D. Raistrick, J.G. Beery, and R.J. Houlton, Science 251, 1587 (1991)

[15] B. Dam, N.J. Koeman, J.H. Rector, B. Stäuble-Pümpin, U. Poppe, and R. Griessen, Physica C 261, 1 (1996)

[16] D. Hull, Introduction to dislocations (Pergamon Press, Oxford, United Kingdom, 1975)

[17] L. Civale, A.D. Marwick, T.K. Worthington, M.A. Kirk, J.R. Thompson, L. Krusin-Elbaum, Y. Sun, J.R. Clem, and F. Holtzberg, Phys. Rev. Lett. 67, 648 (1991)

[18] L. Civale, Supercond. Sci. Technol. 10, A11 (1997)

[19] D.R. Nelson and V.M. Vinokur, Phys. Rev. Lett. 68, 2398 (1992)

[20] R.B. Heimann, in Au‡ösung von Kristallen, edited by V.D. Fréchette, H. Kirsch, L.B. Sand, and F. Trojer (Springer-Verlag, Vienna, Austria, 1975)

[21] R.P. Vasquez, B.D. Hunt, and M.C. Foote, Appl. Phys. Lett. 53, 2692 (1988)

[22] A. Roshko, S.E. Russek, K.A. Trott, S.C. Sanders, M.E. Johansson, J.S. Martens, and D. Zhang, IEEE Trans. Appl. Supercond. 5, 1733 (1995)

[23] F. Miletto Granozio, U. Scotti di Uccio, M. Valentino, G.G. Condorelli, I.L. Fragalà, and G. Malandrino, Physica C 271, 83 (1996)

[24] C.T. Lin and W.Y. Liang, Physica C 225, 275 (1994)

[25] B. Dam, J.H. Rector, J.M. Huijbregtse, and R. Griessen, Physica C 305, 1 (1998)

[26] F.R.N. Nabarro, Theory of Crystal Dislocations (Oxford University Press, Oxford, Great Britain, 1967)

[27] B. Dam and B. Stäuble-Pümpin, J.Mat. Sci.: Mater. Electron. 9, 217 (1998)

[28] D. Eissler, H.S. Wang, and W. Dietsche, Appl. Phys. Lett. 62, 1292 (1993)

[29] L.E.C. van de Leemput, P.J.M. van Bentum, F.A.J.M. Driessen, J.W. Gerritsen, H. van Kempen, and L.W.M. Scheurs, J. Cryst. Growth 98, 551 (1989)

[30] S. Freisem, A. Brockho¤, D.G. de Groot, B. Dam, and J. Aarts, J. Magn. Magn. Mat. 165, 380 (1997

[31] H.P. Lang, H. Haefke, G. Leemann, and H.-J. Güntherodt, Physica C 194, 81 (1992)

[32] F.C. Frank, Acta Crystallogr. 4, 498 (1951)

[33] O. Eibl and B. Roas, J. Mater. Res. 5, 2620 (1990)

[34] D. Rose, K. Durose, W. Palosz, A. Szczerbakow, and K. Grasza, J. Phys. D: Appl. Phys. 31, 1009 (1998)

[35] M. Qvarford, K. Heeck, J.G. Lensink, R.J. Wijngaarden, and R. Griessen, Rev. Sci. Instrum. 63, 5726 (1992)

[36] D.H.A. Blank, M.E. Bijlsma, R. Moerman, H. Rogalla, F.J.B. Stork, and A. Roshko, J. Alloys Compd. 251, 31 (1997)

[37] L. Krusin-Elbaum, L. Civale, J.R. Thomson, and C. Field, Phys. Rev. B 53, 11744 (1996)

[38] Y. Gao, K.L. Merkle, G. Bai, H.L.M. Chang, and D.J. Lam, Physica C 174, 1 (1991)

[39] C. Wengel and U.C. Täuber, Phys. Rev. Lett. 78, 4845 (1997)

[40] C. Wengel and U.C. Täuber, Phys. Rev. B 58, 6565 (1998)

[41] J.E. Sonier, R.F. Kie‡, J.H. Brewer, D.A. Bonn, J.F. Carolan, K.H. Chow, P. Dosanjh, W.N. Hardy, Ruixing Liang, W.A. MacFarlane, P. Mendels, G.D. Morris, T.M. Riseman, and J.W. Schneider, Phys. Rev. Lett. 72, 744 (1994)

[42] E.H. Brandt, Rep. Prog. Phys. 58, 1465 (1995)

Chapter 4

Comparison of dislocations with alternative pinning sites

Although vortex pinning in $YBa_2Cu_3O_{7-\delta}$ films on (100) $SrTiO_3$ is dominated by threading dislocations, many other natural pinning sites are present. To identify the contribution from twin planes, surface corrugations and point defects, we manipulate the relative densities of all defects by post-annealing films with various as-grown dislocation densities, n_{disl}. While a universal magnetic field B dependence of the superconducting current density $j_s(B;T)$ is observed (independently of n_{disl}, temperature T and the anneal treatment), the defect structure changes considerably upon annealing. Correlating the microstructure to $j_s(B;T)$, it becomes clear that surface roughness, twins and point defects are not important at low magnetic fields compared to linear defect pinning. Transmission electron microscopy indicates that threading dislocations are not part of grain boundaries neither are they related to the twin domain structure. These results confirm that $j_s(B;T)$ is essentially determined by pinning along threading dislocations, naturally induced during the growth process. Even in high magnetic fields, where the vortex density outnumbers n_{disl}, it appears that linear defects stabilize the vortex lattice via the vortex-vortex interaction.[1]

[1]This chapter is based on the paper by J.M. Huijbregtse, F.C. Klaassen, A. Szepielow, J.H. Rector, B. Dam, R. Griessen, B.J. Kooi, and J.Th.M. de Hosson, to be submitted to Supercond. Sci. Technol.

4.1 Introduction

The early observation of both high superconducting current densities (typically between 10^{11} and 10^{12} A/m^2 at low temperatures in zero magnetic …eld) and numerous structural defects in thin epitaxial …lms of the high-T_c superconductor $YBa_2Cu_3O_{7\,i\,\pm}$ called for the identi…cation of the strongest pinning defect [1]. Grain boundaries [2, 3], twin boundaries [4, 5], anti-phase boundaries [6, 7, 8], screw dislocations [9, 10, 11, 12], edge dislocations [13, 14], precipitates [15, 16, 17] and surface roughness [18, 19, 20, 21] have been suggested as good candidates. Due to the di¢culties in controlling the defect density, quantitative studies unambiguously relating the density of a speci…c defect to the superconducting current density characteristics could not be performed so far. In the previous chapter, we succeeded in controlling threading dislocations in thin …lms of $YBa_2Cu_3O_{7\,i\,\pm}$ by carefully manipulating the growth conditions. This allowed us to relate the high superconducting current densities in these …lms to strong pinning of vortices along dislocations in a semi-quantitative way: a plateau B¤ was found in the magnetic …eld dependence of the superconducting current density j_s (B), which is directly proportional to the measured density of all dislocations (i.e., both edge, screw and dislocations of mixed character). The proportionality constant was determined to be $0{:}7©_0$ at low temperatures, where $©_0 = 2{:}068 \pounds 10^{i\,15}$ Tm^2 is the ‡ux quantum, showing that dislocations are the main origin of the high currents. Recently, Klaassen et al. [22] reported the existence of a similar plateau in the dynamical relaxation rate below B¤. Moreover, the temperature dependence of both B¤ and j_s (B < B¤) was explained in terms of the Bose glass theory [23, 24], taking thermal ‡uctuations into account [25]. Thus the long existing question why …lms can carry such high currents compared to single crystals [26, 27] appears to be solved now.

In the present chapter, we focus our attention to alternative natural pinning sites (such as twin boundaries, precipitates, point defects and surface roughness) that are operative in combination with threading dislocations. In order to manipulate the relative densities of all defects, we perform annealing experiments on …lms with various as-grown dislocation densities. Indeed signi…cant changes are found, both in the superconducting current characteristics and in the microstructure of these …lms. As a result, the contribution from the alternative pinning sites compared to linear defect pinning can be identi…ed. Remarkably, the e¤ect of linear defects is not con…ned to the low magnetic …eld region. It appears that linear defects stabilize the vortex lattice via the long-ranged vortex-vortex interactions up to …elds as high as 7 T (at low temperatures). The results indicate that natural linear defects are extremely e¢cient pinning sites compared to arti…cially induced columnar defects [28], which are usually introduced at much higher densities.

This chapter is organized as follows. First, we discuss the post-annealing procedure and the results of the torque measurements and the microstructural investigation. Next, we correlate vortex pinning to the defect structure, using some additional transmission electron microscope observations to distinguish threading dislocations from twinning dislocations and low-angle grain boundaries.

4.2 The post-anneal treatment

For the present investigation, we use a series of 110 nm thick $YBa_2Cu_3O_{7-\delta}$ films[2] on low miscut (100) $SrTiO_3$ substrates, measuring 10 × 10 × 1.0 mm^3, with threading dislocation densities of 28, 50, and 68 μm^{-2} (see below). All films are divided into two parts; one part is subjected to a two step post-anneal [29]. First, these parts are quickly (15°C/minute) heated in a quartz tube oven to the anneal temperature T_a = 800°C in a flowing 97% Ar + 3% O_2 mixture (total flow of 1.0 l/minute) and kept at this temperature for t_a = 30 minutes. Subsequently, the samples are cooled down (2.0°C/minute) to 500°C, changing to a 100% O_2 atmosphere around 600°C. The films are kept in this second anneal stage for another 30 minutes and then slowly cooled down (< 2°C/minute). During heating the $YBa_2Cu_3O_{7-\delta}$ films go through the orthorhombic-to-tetragonal structural phase transition in the low oxygen content atmosphere (losing oxygen). Hence, rearrangement of atoms (at T_a) takes place in the tetragonal phase. During cooling down in the 100% oxygen atmosphere, the films take up oxygen and go through the tetragonal-to-orthorhombic transition. The second anneal stage is incorporated to ensure full oxygenation.
We stress that as-deposited and post-annealed parts of the same film are compared in superconducting and microstructural properties (as a function of the as-grown threading dislocation density). A second series of samples, prepared under identical conditions as the first series, exhibits identical microstructural parameters as the first series. Hence, the microstructural effects reported below are not due to small differences in the preparation procedure.

4.2.1 Effect on the superconducting current

We measured the superconducting current density $j_s(B;T)$ on films patterned in a ring geometry by means of capacitive torque magnetometry [25, 30] for temperatures 4.2 ≤ T ≤ 80 K, sweeping the magnetic field at a rate of 40 mT/s (from 0 to 7 T) at an angle of 10° from the c-axis. The rings have a diameter of 3.0 mm and a width of 125 μm. The $j_s(B;T)$ results for films with as-grown dislocation densities n_{disl} of 28 μm^{-2} (low) and 68 μm^{-2} (high) before and after the post-anneal procedure are shown in Fig. 4.1. The current density exhibits the well-known behavior of linear defect pinning: it is constant up to the characteristic field B^* (as indicated by arrows) and decays rapidly above this field. Both B^* and $j_s(B < B^*)$ strongly depend on temperature. To determine B^* accurately, additional low field sweeps (up to 1 T) are performed at a sweep rate of 1 mT/s. The as-grown and post-annealed parts of the low n_{disl} sample behave in the same way. Typically, $B^*(T = 10\ K) = 39$ mT and $j_s(B = 0; T = 10\ K) = 4.6 \times 10^{11}$ A/m^2. On the other hand, in the high n_{disl} sample we distinguish two significant effects: (i) B^* reduces by annealing and (ii) $j_s(B < B^*)$ increases. For instance, B^* goes down from 90 to 65 mT at 10 K, while $j_s(B = 0; T = 10\ K)$ increases from 2.7 × 10^{11} to 5.0 × 10^{11} A/m^2.

[2] The films are prepared in the QUESTEK set-up, using 3.0 < d_{T-S} < 3.5 cm, 750 < T_{sub} < 850°C and 15 < p_{O_2} < 50 Pa at a fluence J = 1.3 J/cm^2 (as measured at the target).

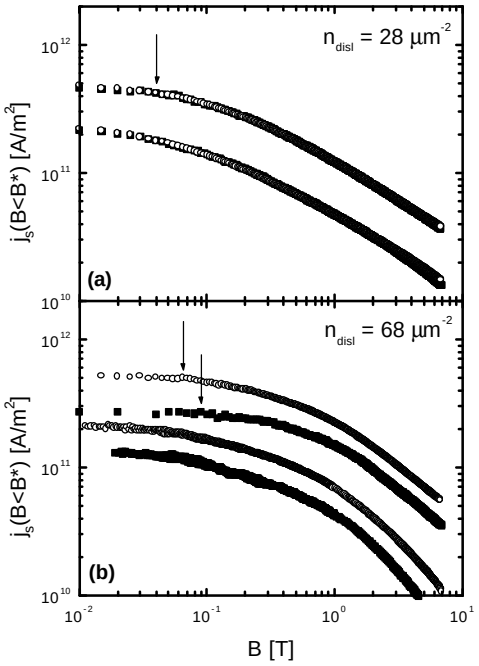

Figure 4.1: In‡uence of post-annealing on the magnetic …eld dependence of the transport current density $j_s(B)$ in 110 nm thick $YBa_2Cu_3O_{7-\pm}$ …lms deposited on (100) $SrTiO_3$ with di¤erent as-grown dislocation densities (n_{disl}): (a) a low $n_{disl} = 28\ ^1m^{-2}$ sample at temperatures T = 10 and 40 K and (b) a high $n_{disl} = 68\ ^1m^{-2}$ sample at T = 10 and 50 K for the as-deposited (solid squares) and post-annealed (open circles) parts of the same sample. The arrows indicate the characteristic …eld $B^¤$ at 10 K. Both j_s and $B^¤$ decrease with increasing T.

We capture the essence of the magnetic …eld dependence of $j_s(T)$ in three phenomenological parameters (see Fig. 4.2). While the low …eld behavior is determined by both $B^¤(T)$ and $j_s(B < B^¤;T)$, the high …eld behavior can be approximated by a power-law dependence, i.e. $j_s(B \grave{A} B^¤;T) / B^{®(T)}$. Comparing the low and high n_{disl} sample, it appears that $j_s(B < B^¤;T)$ is independent of the dislocation density after the anneal procedure. However, the high …eld behavior is very di¤erent: …lms with a high as-grown dislocation density exhibit a much quicker drop in j_s than …lms with a low dislocation density. We …nd $®(4:2 < T < 70\ K) ¼ ¡0:57$ for the low n_{disl} sample, while ®(T) decreases from -0.75 to -1.1 with increasing T for the high n_{disl} sample. It is important to note that ®(T) is independent of the post-anneal treatment.

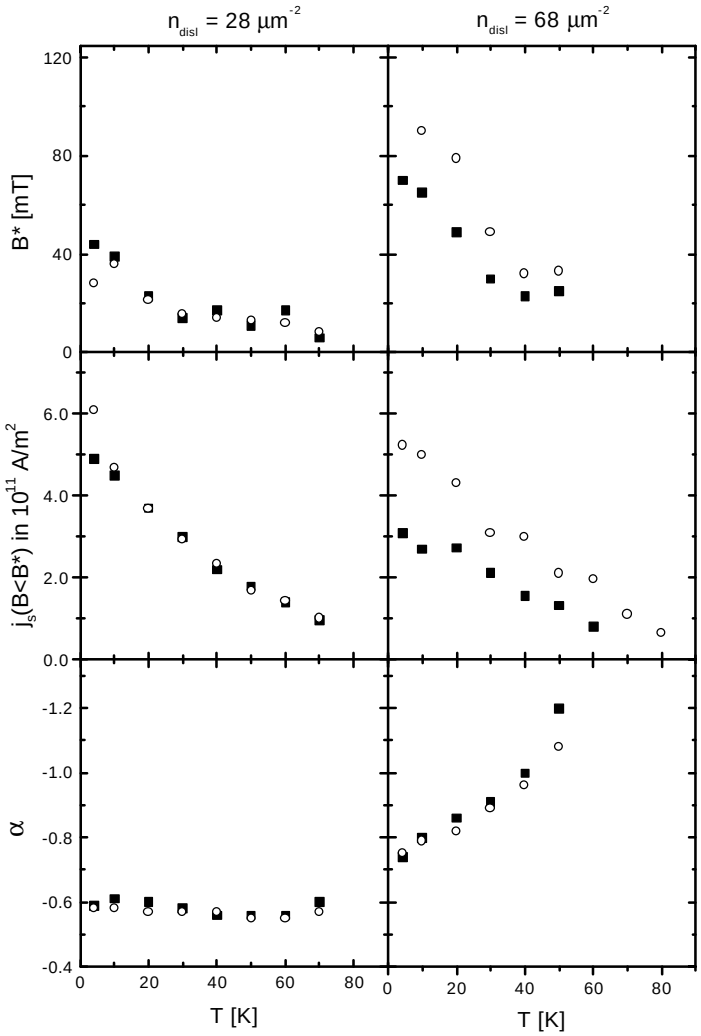

Figure 4.2: In‡uence of post-annealing on the transport current density $j_s(B;T)$ in 110 nm thick $YBa_2Cu_3O_{7-\delta}$ …lms on (100) $SrTiO_3$ with a low (n_{disl} = 28 μm^{-2}, left column) and high (n_{disl} = 68 μm^{-2}, right column) as-grown dislocation density. Shown are the temperature dependence of: (top panel) the characteristic …eld $B^*(T)$, (middle panel) the low magnetic …eld transport current density j_s ($B < B^*;T$), and (lower panel) the high magnetic …eld power-law exponent $\alpha(T)$ for the as-deposited (solid squares) and post-annealed parts (open circles).

To correlate these characteristics in the superconducting current density to pinning by various natural defects, we now investigate the microstructure of the …lms before and after the post-anneal procedure in detail.

4.2.2 Microstructural consequences

The annealing procedure takes place at a temperature comparable to the average deposition temperature (typically, T_{sub} ¼ T_a = 800±C) of the $YBa_2Cu_3O_{7\,i\,\pm}$ …lms. Therefore, we expect clear changes in the microstructure. Combining atomic force microscopy (AFM), x-ray di¤raction (XRD), Rutherford backscattering spectrometry (RBS) and electrical resistivity measurements, we …nd four pronounced e¤ects.

Surface roughness

The large e¤ect of post-annealing on the surface roughness was already mentioned in chapter 3 for a …lm with a high as-grown dislocation density. Here, we discuss this effect in a more general context. In Fig. 4.3, AFM height images of three …lms deposited at decreasing substrate temperature T_{sub} = 850, 800 and 750±C (increasing dislocation density) are shown before and after the post-anneal treatment. The as-grown surface morphology consists of semi-regularly spaced islands separated by trenches. As shown in chapter 3, the deeper depressions within the trenches correspond to the sites where threading dislocations emerge. Since dislocations are situated around the islands in as-deposited …lms, the island density n_{island} and dislocation density are proportional (the proportionality constant being close to 1). Therefore, n_{island} can be used as a quick measure for n_{disl}. Upon annealing the island density decreases, suggesting that the dislocation density has changed. In addition, the surface ‡attens considerably (note that the same height scales are used). For example, the root-mean-square (rms) roughness decreases from 4 to 2 nm, typically.[3]

Dislocation density

To check whether the dislocation density changes upon annealing or not, we perform wet-chemical etching experiments. In …gure 4.4, AFM images corresponding to the same …lms as in Fig. 4.3 are shown after etching in 1% Br-ethanol, to reveal all threading dislocations. n_{disl} is determined by averaging the number of square, sharp-bottomed etch pits for di¤erent areas of the same …lm, using etch times between 20 and 90 s. We …nd that the dislocation density only decreases signi…cantly in …lms with the highest as-grown dislocation density (from n_{disl} = 68 $^1m^{i\,2}$ to 43 $^1m^{i\,2}$). Indeed dislocation annihilation is expected to be easier in these …lms, since the average distance d_{disl} between dislocations is relatively small (d_{disl} ¼ $1=\sqrt{n_{disl}}$). It is important to note that the correlation between island density and dislocation density is lost upon post-annealing: the dislocation density outnumbers the island density.

[3] See chapter 3 for the AFM cross-sections of an as-grown and a post-annealed sample.

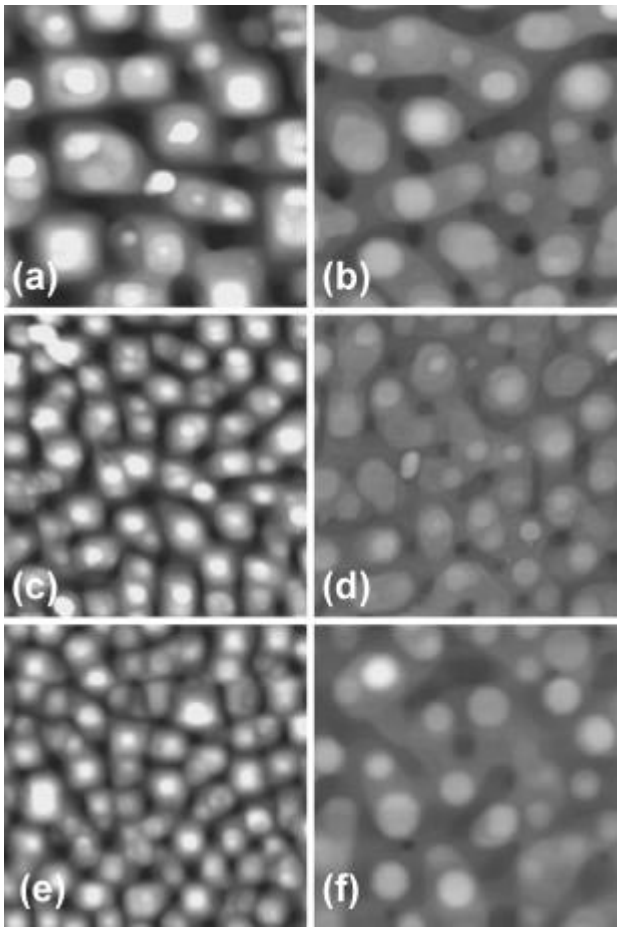

Figure 4.3: E¤ect of post-annealing on surface morphology. AFM height images (1:0 £ 1:0 μm^2) of 110 nm thick $YBa_2Cu_3O_{7-\pm}$ …lms on (100) $SrTiO_3$ with di¤erent as-grown dislocation densities n_{disl} after deposition (left column) and after the post-anneal procedure (right column): (a,b) n_{disl} = 28 μm^{-2}, (c,d) n_{disl} = 50 μm^{-2}, and (e,f) n_{disl} = 68 μm^{-2}. Each pair of images is taken on as-grown and post-annealed parts of the same …lm. Upon post-annealing both the island density and the surface roughness decrease. The e¤ects are more pronounced for higher n_{disl}. The height scale is 50 nm; the image conditions (color table, contrast, etc.) are the same for all images.

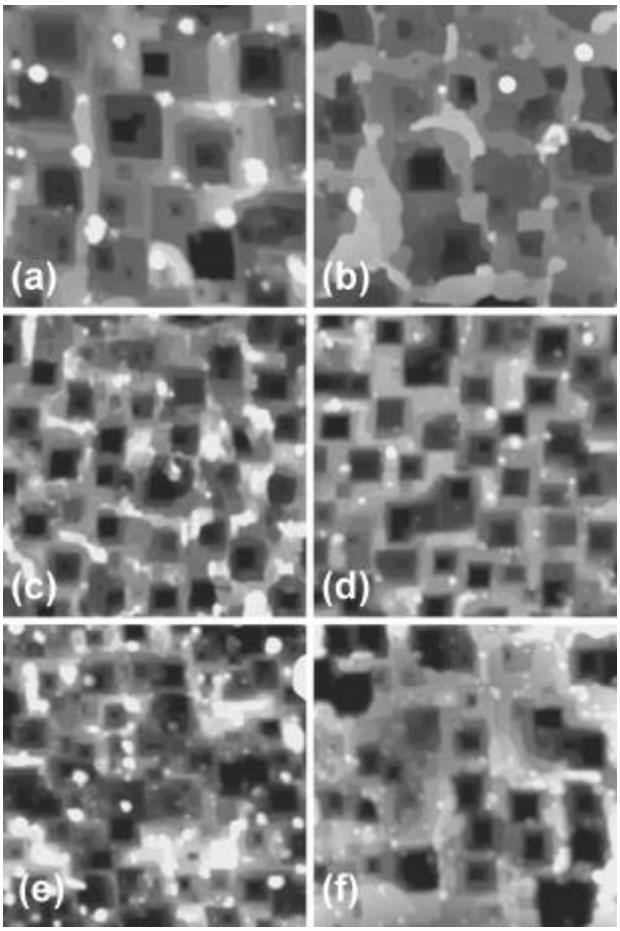

Figure 4.4: E¤ect of post-annealing on the dislocation density (n_{disl}), as determined by counting the number of etch pits formed upon dislocation speci…c wet-chemical etching. Shown are AFM height images (1:0£1:0 $^1m^2$) of the same …lms as in Fig. 4.3 after Br-ethanol etching the as-grown (AD, left column) and post-annealed (PA, right column) parts: (a) AD: n_{disl} = 28 $^1m^{i\,2}$ and (b) PA: n_{disl} = 24 $^1m^{i\,2}$; (c) AD: n_{disl} = 50 $^1m^{i\,2}$ and (d) PA: n_{disl} = 51 $^1m^{i\,2}$; (e) AD: n_{disl} = 68 $^1m^{i\,2}$ and (f) PA: n_{disl} = 43 $^1m^{i\,2}$. Post-annealing only a¤ects n_{disl} in …lms with a high as-grown dislocation density. The height scale is 50 nm; the image conditions (color table, contrast, etc.) are the same for all images

Crystallinity

A measure often used for the crystallinity of $YBa_2Cu_3O_{7-\delta}$ …lms is the full width at half maximum of its (005)-rocking curve, $\phi!_{005}$. In Fig. 4.5(a) an example of such an XRD measurement is shown (! scan). Upon annealing $\phi!_{005}$ reduces from $0.16^{\pm}$ to $0.14^{\pm}$, showing that the lateral (in-plane) correlation length has increased. This is a general trend: $\phi!_{005}$ decreases upon post-annealing, the e¤ect being larger for higher n_{disl}. However, …lms with a high as-grown dislocation density (deposited at a low substrate temperature) always have slightly broader rocking curves, even after the post-anneal procedure ($\phi!_{005} \approx 0{:}2^{\pm}$). Finally, we performed RBS angular scans around the [001] direction to study the crystallinity, using 2.0 MeV He^+. The result for the …lm with the highest as-grown dislocation density, comparing the as-deposited and post-annealed part, are shown in Fig. 4.5(b). Upon annealing, the channel minimum yield for the Ba signal $\hat{A}_{Ba}$ decreases from 3.7% to 2.5%, while the full width at half minimum of the [001] channel dip decreases (from $1.9^{\pm}$ to $1.6^{\pm}$), con…rming the improved crystallinity. The RBS results also indicate that as-deposited high n_{disl} …lms are already of a good crystallinity [31].

Doping

The …lms go through the tetragonal ($YBa_2Cu_3O_{6+x}$) to orthorhombic ($YBa_2Cu_3O_{7-\delta}$) structural phase transition twice during the post-anneal process. Therefore, the oxygen content of the …lms may have changed considerably. As both the c-axis lattice constant and the resistivity ½ of the …lm are sensitive functions of the oxygen content, we performed XRD and electrical transport measurements on the as-grown and post-annealed parts. Typical results are shown in Fig. 4.6 for …lms with a high as-grown dislocation density. The (007) peak in the $\mu - 2\mu$ scan shows a shift to higher angles (smaller c-axis) and a clearer K_{α_1}-K_{α_2} splitting (indicative of the improved crystallinity), see Fig. 4.6(a). The increase in intensity also evidences improved crystallinity in the direction along the c-axis, although part of the increase may result from a slightly di¤erent alignment. Calculating the c-axis length from the (00l)-re‡ections for $l = 1 - 8$, we observe a general trend: on the average, the c-axis decreases from 11.70 to 11:69 Å upon annealing, independently of the dislocation density. This effect can be attributed to (i) an increase in oxygen content, (ii) an improvement of the crystallinity, including Y/Ba disorder and O chain ordering or (iii) a combination of both. To separate these e¤ects, let us examine the resistive transition, using a four-probe con…guration in combination with a well de…ned strip geometry ($0{:}50 \pounds 4{:}0$ mm^2). By post-annealing both the resistivity ½ and the T_c go down for all …lms, see Fig. 4.6(b) for an example. The decrease in ½ is larger in …lms with a higher as-grown n_{disl}. An improvement of crystallinity alone would lower ½ and increase T_c, whereas an increase in charge carrier density above the optimal doping lowers both ½ and T_c. Therefore, we conclude that the crystallinity improves and that the …lms are slightly overdoped after annealing.

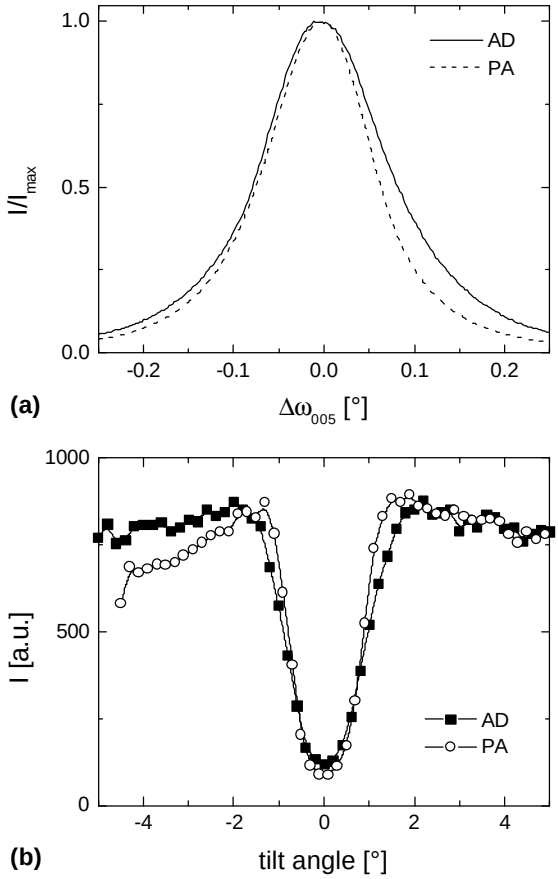

Figure 4.5: E¤ect of post-annealing on the crystallinity of 110 nm thick $YBa_2Cu_3O_{7\,i\,\pm}$ …lms on (100) $SrTiO_3$: (a) XRD (005)-rocking curve for the …lm with an as-grown dislocation density n_{disl} = 50 $^1m^{i\,2}$, and (b) RBS [001] channel dip measurement for the Ba signal of the …lm with an as-grown n_{disl} = 68 $^1m^{i\,2}$ (AD = as-deposited; PA = post-annealed). Since both the XRD peak and the RBS channel dip narrow, we conclude that the crystallinity improves upon annealing.

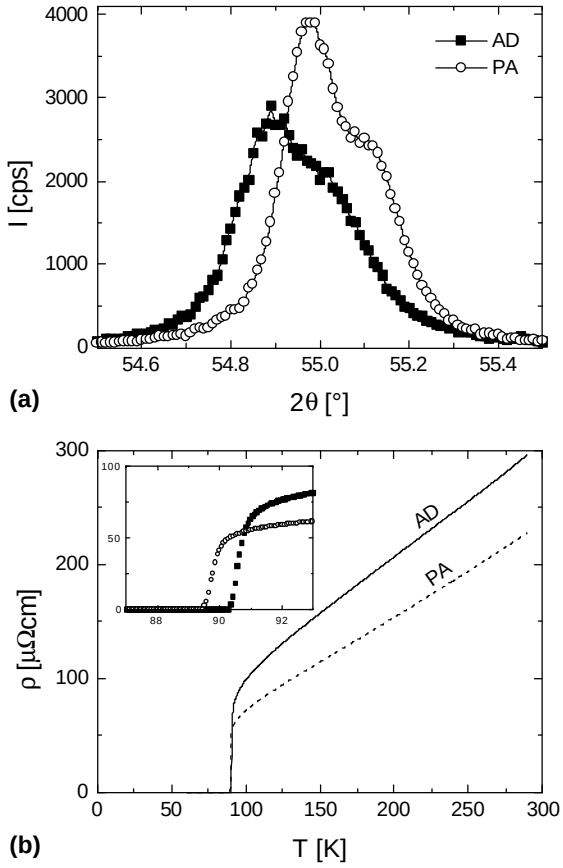

Figure 4.6: E¤ect of post-annealing on the oxygen content and ordering of the 110 nm thick $YBa_2Cu_3O_{7-\delta}$ film on (100) $SrTiO_3$ with as-grown dislocation density $n_{disl} = 68\ \mu m^{-2}$: (a) XRD $\theta - 2\theta$ scans around the (007)-re‡ection, showing a shift to slightly higher angles, an intensity increase and a decrease of the width of the peak and (b) the resistivity ρ as a function of temperature T, revealing that both ρ and T_c go down (AD = as-deposited; PA = post-annealed). These observations are indicative of improved crystallinity and overdoping upon annealing.

Summarizing, there are multiple e¤ects of post-annealing on the microstructure. All e¤ects are more pronounced in …lms with a higher as-grown dislocation density, since these …lms are deposited at a substrate temperature lower than the annealing temperature ($T_{sub} < T_a$). Our observations have some important implications for producing …lms with an extremely low or high dislocation density, while maintaining a critical temperature above 90 K (see chapter 3). First, ultra-low temperature deposition (T_{sub} ¿ 800±C) and post-annealing cannot be combined to produce …lms with both high n_{disl} and good crystallinity, since dislocations are annihilated. Therefore, we are bound to manipulate the deposition conditions to obtain n_{disl} À 68 $^{1}m^{2}$, for instance by using higher deposition rates. An alternative method to increase n_{disl}, making use of an additional processing step, will be presented in chapter 5. Secondly, in low n_{disl} …lms, dislocations are too far apart to annihilate by annealing, implying that higher anneal temperatures T_a (> T_{sub}) and/or longer annealing times t_a are necessary to produce essentially dislocation-free …lms. Preliminary experiments indicate that the surface roughness and island density are reduced far more by annealing 240 minutes (instead of 30 minutes), suggesting that threading dislocations can indeed be eliminated.

4.3 Vortex pinning mechanisms

In our $YBa_2Cu_3O_{7\,i\,\pm}$ thin …lms di¤erent types of correlated disorder are naturally present, among which are linear defects (dislocations), planar defects (twin boundaries), precipitates and thickness ‡uctuations. The microstructural e¤ects of post-annealing described above make it possible to probe the in‡uence of di¤erent natural defects on the superconducting current density $j_s(B;T)$ and therefore on vortex pinning in these …lms. We discuss these pinning e¤ects and the in‡uence of point defects below, using additional (HR)TEM observations to identify some defects.

4.3.1 Linear defects

In literature, many experimental observations point to the importance of pinning by dislocations. Apart from the direct observation of the interaction between vortices and crystal dislocations in $Bi_2Sr_2CaCu_2O_8$ [32] and Nb [33] single crystals[4], there were numerous attempts to relate the density of spiral outcrops (screw dislocations) in $YBa_2Cu_3O_{7\,i\,\pm}$ thin …lms to the superconducting properties [11, 34]. However, as most of these studies consider (i) only spirals (i.e., a fraction of all dislocations) and (ii) only the magnitude of the superconducting current density at zero magnetic …eld and usually at 77 K, a signi…cant correlation could not be established.
We …nd that the characteristic shape of $j_s(B;T)$ is independent of both the dislocation density and the post-anneal procedure. In agreement with the results of chapter 3, the characteristic …eld at low temperatures is determined by the total dislocation density

[4] We note that the density of dislocations in single crystals is usually orders of magnitude smaller than in epitaxial …lms.

as measured by wet-chemical etching, according to:

$$B^{\alpha} \approx 0.7 n_{disl} \copyright_0. \quad (4.1)$$

Both B^{α} and $j_s(B < B^{\alpha})$ are a function of the superconducting parameters [i.e., the coherence length $\xi = \xi(T)$ and the magnetic penetration depth $\lambda = \lambda(T)$]. The temperature dependence of these parameters in combination with thermal fluctuations, which decrease the pinning energy, are responsible for the observed decrease in $B^{\alpha}(T)$ and $j_s(B < B^{\alpha}; T)$ with increasing temperature [25].

Post-annealing of a sample with a high as-grown n_{disl} (see Fig. 4.2), reduces B^{α}. This is a direct consequence of the annihilation of dislocations during annealing ($n_{disl} = 68 \rightarrow 43\ \mu m^{-2}$, see Fig. 4.4). Indeed, B^{α} corresponds well with the measured density of dislocations after post-annealing, following Eq. (4.1). However, the reason for the increase in $j_s(B < B^{\alpha})$ is not a priori clear. In the single vortex regime, where vortex-vortex interactions can be neglected, the current density is determined by the depinning of isolated vortices from linear defects. Therefore, the same value of $j_s(B < B^{\alpha})$ is expected for all films, independently of n_{disl}. Before post-annealing, however, films with a low as-grown dislocation density usually carry somewhat larger currents than films with a high as-grown n_{disl} (see Fig. 4.1 and 4.2 for an example). This is a consequence of the method used to increase n_{disl}. Since high dislocation densities are induced at relatively low substrate temperatures (750°C in this investigation), the corresponding rocking curves are usually broader (typically, $\phi\omega_{005} \approx 0.2°$) and the resistivities are higher ($\rho_{RT} \approx 300\ \mu\Omega$-cm) compared to low n_{disl} films ($\phi\omega_{005} \approx 0.1°$ and $\rho_{RT} \approx 250\ \mu\Omega$-cm). These effects are indicative of a poorer crystallinity and lower doping. Post-annealing (partly) corrects for both issues and the current increases in the high n_{disl} film. Indeed, similar effects of post-annealing on the superconducting current density in $YBa_2Cu_3O_{7-\delta}$ films have been reported [35]. The improvement in overall crystallinity (including oxygen stoichiometry) of the films, ensures that the depression in the superconducting order parameter as well as ξ and λ are the same for all films. Probably, due to the sharpening of the pinning potential upon annealing, $j_s(B < B^{\alpha})$ approaches a universal value of 6 ± 10^{11} A/m^2 at 4.2 K, characteristic for pinning of a single vortex by a dislocation. Surprisingly, the overdoping upon annealing does not affect the current density. Note that when taking relaxation effects into account [25], at low temperatures and small magnetic fields we find a universal critical current density j_c that is close to the depairing current density limit $j_0 \approx 4 \pm 10^{12}$ A/m^2 and consequently $j_c \approx 0.2 j_0$.

As linear defects play a dominant role for pinning in these films, we started a cross-sectional TEM investigation.[5] Generally, dislocations are difficult to observe in cross-section [36], as their density is relatively low and their core size is small [37]. Despite

[5] TEM measurements are performed by B.J. Kooi (Materials Science Centre, University of Groningen) in a JEOL 4000 EX/II microscope operating at 400 kV (point resolution of 0.165 nm). Cross-section specimens are prepared by a standard procedure: face-to-face glued specimens in cross-section geometry are polished down to a final thickness of about 15 μm using a Tripod polisher, followed by a 4 kV ion milling. To prevent damaging of the $YBa_2Cu_3O_{7-\delta}$ film, it turned out essential to use liquid-nitrogen cooling during this ion milling. Care was taken to prevent contamination of the surface during TEM specimen treatment.

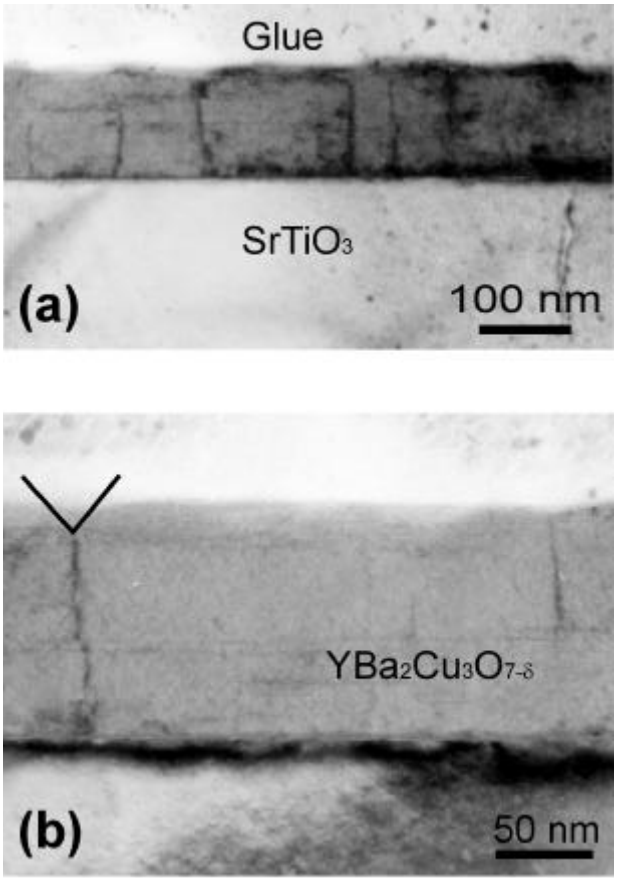

Figure 4.7: Low magni…cation cross-sectional "2-beam" bright …eld TEM images of a 120 nm $YBa_2Cu_3O_{7\,i\,\pm}$ …lm on (100) $SrTiO_3$ with a high dislocation density (this speci…c …lm was shortly etched in Br/ethanol): (a) a high density of threading dislocations originating at the interface and extending all the way up to the surface can be distinguished and (b) the correlation between a threading dislocation and an etch pit is schematically shown; simultaneous observation of etch pits and dislocations turned out to be di¢cult (only by varying the defocus a correlation could be established)

di¢culties in the TEM sample preparation, we were able to identify threading dislocations in a sample with a high dislocation density, see the "2-beam" bright …eld images in Fig. 4.7 (strong di¤racting beam parallel to the c-axis). Dislocations originating at the substrate-…lm interface and extending up to the surface in a direction close to the c-axis can be seen. By varying the di¤raction vector g in dark …eld, the threading dislocations can not be discerned when g is parallel to the c-axis, suggesting that these are screw dislocations. This speci…c …lm was shortly etched in 1% Br/ethanol in order to correlate etch pits and dislocations directly. Since pits or dislocations can only be discerned by varying the defocus, simultaneous observation of both etch pits and threading dislocations is di¢cult. However, it appears that etch pits are present at the positions where dislocation lines emerge at the surface, as schematically indicated in Fig. 4.7(b). We note, that preferential etch pit formation was recently unambiguously related to threading dislocations of screw and mixed character in …lms of GaN on (0001)-sapphire [38], combining AFM and cross-sectional TEM analysis. Thus, wet-chemical etching in a dislocation sensitive etchand reveals all dislocations emerging at the surface of a …lm.

Finally we note that the linear defects we found by TEM resemble the "columnar growth defect" structures as reported by Lowndes et al. [39] in $YBa_2Cu_3O_{7\,i\,\pm}$ …lms grown on 1.6± miscut, mosaic (100) $LaAlO_3$ substrates. Unfortunately, the nature of those defects was not further characterized. The appearance of an extra (asymmetric) peak in the angular dependence of j_s at a …eld direction close to the c-axis was associated with a vortex pinning e¤ect by these columns. Clearly, a peak in the angular dependence of j_s is expected when the magnetic …eld is parallel to the linear defects. However, they also report that the peak e¤ect is absent in …lms on ‡at (100) $SrTiO_3$ substrates. This observation is in contradiction with the results of Roas et al. [40], who show that an additional peak arises at low …elds. So far, we also did not detect the expected peak e¤ect by means of angular dependent torque magnetometry. However, this discrepancy may be related to the method (transport or inductive) and the exact procedure used to measure the peak e¤ect. Apart from this issue, all results point to dislocations being the strong pinning sites in $YBa_2Cu_3O_{7\,i\,\pm}$ …lms. In the remaining part we will show that all other types of correlated disorder are far less important.

4.3.2 Planar defects

A network of planar defects in principle provides for an alternative source of strong pinning [41], with a similar matching behavior. At low …elds, the vortices will be concentrated at the planar defects. At higher …elds, vortex-vortex interactions play a role and not all vortices can be accommodated by planar defects. The cross-over …eld is set by the condition that the vortex spacing becomes of the order of ¸. Assuming that the planar defects are spaced by a distance d, Doornbos et al. [42] calculated a cross-over …eld

$$B^{\alpha} ¼ \frac{2©_0}{¸\,d}. \qquad (4.2)$$

Using experimentally determined characteristic …elds, we …nd defect spacings that should be of the same order as the dislocation spacing ($d \frac{1}{4} d_{disl} \frac{1}{4} 100$ nm). Therefore, our experimental results could also be interpreted in terms of strong pinning by a network of planar defects. Below, we consider three types of planar defects: twin boundaries, anti-phase boundaries and (low-angle) grain boundaries. Also, the relation between threading dislocations, twinning dislocations and low-angle grain boundaries is investigated. We note that vortices can slide along the planar defects. They are thus not very e¤ective in one direction.

Twin boundaries

During the tetragonal-to-orthorhombic phase transition upon cooling down, (110) and ($\bar{1}10$) twins form. In Fig. 4.8, a planar view TEM image[6] is shown of an as-grown sample with a low dislocation density (about $10^{1} m^{i 2}$ as estimated from the island density), showing that twins of each orientation are distributed in domains, containing either (110) or ($\bar{1}10$) twin boundaries. To relieve the mismatch between the domains, twinning dislocations [43] with a dislocation line parallel to the c-axis will be formed at the domain boundaries if the mutual distance between subsequent twin planes in the domains is large enough (i.e., larger than 50 nm). However, this distance for the …lm investigated is generally less than 40 nm [see Fig. 4.8(b)], which avoids the necessity of introducing twinning dislocation at the domain boundaries. Furthermore, assuming that the threading dislocations are twinning dislocations, they are expected to be distributed in a network which is characterized by the twin domain length scale (about 1 ^{1}m, see Fig. 4.8). Clearly, this length scale is much larger than the threading dislocation spacing. In addition, twinning dislocations need to have an edge component in order to accommodate the mismatch, while we observe mainly screw dislocations. Apparently, the deformations are elastically accommodated and we conclude that twinning dislocations are not present in our $YBa_2Cu_3O_{7 i \pm}$ …lms. Since the twin planes are parallel to the c-axis, these planar defects might give rise to matching …eld behavior. In our experiment, the annealing must have changed the twin structure, since the …lms are cooled down in a very di¤erent way: the as-deposited sample is quenched in pure oxygen (> 100 mbar) to room temperature within a few minutes, whereas the post-annealed sample is cooled down much more slowly. It has been shown that post-annealed samples exhibit longer and more ordered twins due the improved kinetics [44]. Yet, no signi…cant di¤erence in $j_s(B;T)$ is found in the low n_{disl} …lm (see Fig. 4.1), indicating that twin boundaries are relatively unimportant compared to linear defect pinning. Indeed, by means of detwinning the same $YBa_2Cu_3O_{7 i \pm}$ single crystal it was shown that twins only contribute to vortex pinning at high temperatures [45]. However, the measured current densities in twinned single crystals are still orders of magnitude smaller [46] than in …lms for all temperatures and magnetic …elds. Therefore, we conclude that twin boundaries are not important pinning sites in …lms.

[6] Plan-view specimens were ground, dimpled and ion milled from one side in order to obtain an electron transparent area just in the …lm surface. Care was taken to prevent contamination of the surface during TEM specimen treatment.

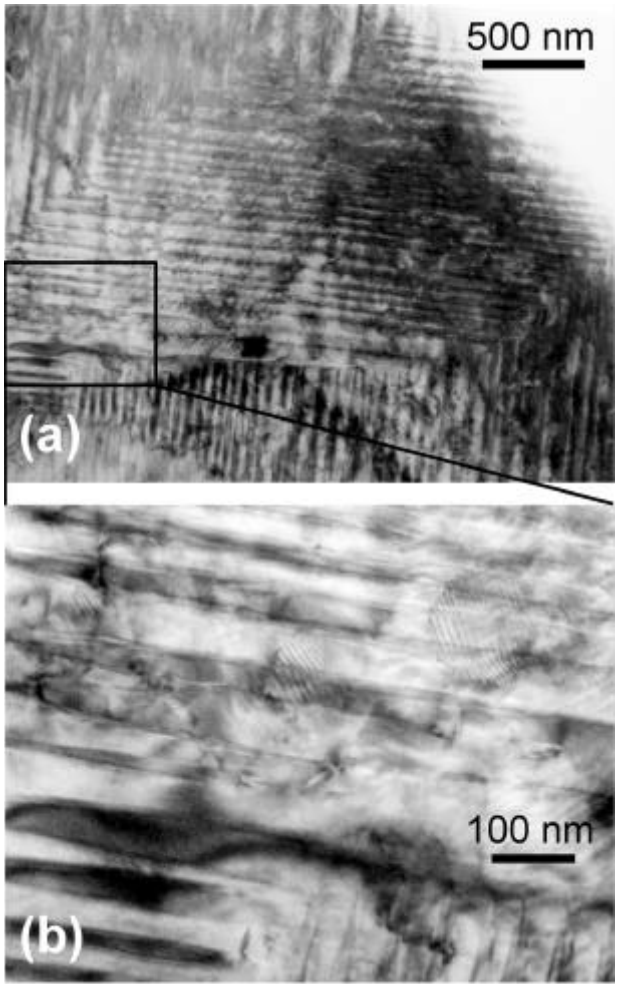

Figure 4.8: Planar view TEM images of a 500 nm thick $YBa_2Cu_3O_{7-\delta}$ film on (100) $SrTiO_3$ with a low dislocation density ($n_{disl} \approx 10^{10}\,m^{-2}$), showing (a) domains containing only one orientation of twin planes and (b) a close-up of such a domain, showing that the mutual distance between subsequent twin planes within the domain is generally less than 40 nm. Note that the length scale of the twin domains is much larger than the average distance between threading dislocations (250 nm).

Anti-phase boundaries

Anti-phase boundaries (APB's) may be induced by vicinal steps in the substrate (0.4 nm in height, corresponding to ¼ c=3) [47]. Generally, APB's are easily annihilated by inserting stacking faults parallel to the ab-plane. Therefore, in order to generate a signi…cant number of APB's that persist over a large part of the …lm thickness, substrates with a large miscut angle are needed. For this purpose, (106) $SrTiO_3$ substrates have been employed [6, 7, 8], which have a miscut angle of 9.5± with respect to the (100) plane. Indeed an anisotropy in j_s was reported in these miscut samples: along the vicinal steps a higher current density is found than perpendicular to them. We used substrates with a vicinal angle of only 0.15± and the number of APB's is expected to be small. Although we previously found indications for the existence of a network of anti-phase boundaries [48], our present TEM investigations did not con…rm such networks. We attribute this di¤erence to (i) the use of better quality substrates (smaller miscut angles, di¤erent supplier, better characterization) and (ii) our new substrate preparation and cleaning procedure.[7] Although APB's are absent in our …lms on ‡at substrates, we …nd current densities that are as high as those obtained on miscut samples [6, 7, 8]. In our opinion, vortex pinning in …lms on miscut substrates may also be dominated by threading dislocations, while the reduction in j_s in the direction normal to the substrate steps arises from a reduction in crystallinity in this direction. As shown here, crystallinity in‡uences the magnitude of the superconducting current and can, therefore, account for an anisotropy in j_s.

(Low-angle) grain boundaries

As discussed above, any network of planar defects might give rise to matching …eld behavior, see Eq. (4.2). In particular, the observed island morphology of the …lms suggest that the islands could be separated by (hidden) grain boundaries [3]. Since large angle (> 5±) grain boundaries strongly a¤ect the magnitude of the superconducting current density [49], the observed large currents imply that only low-angle (< 5±) grain boundaries can be present. In chapter 3 we found a scaling between the island density n_{island} and threading dislocation density n_{disl} and observed that the dislocations are situated around the islands. Therefore, it is tempting to assume that the threading dislocations are distributed in low-angle grain boundaries, separating the growth islands.

We can calculate the angle # between adjacent islands using the Shockley-Read formula [50]:

$$d_{disl} = \frac{b}{2\sin(\#/2)}, \tag{4.3}$$

where b is the magnitude of the Burger's vector and d_{disl} is the average distance between dislocations ($d_{disl} = 1/\sqrt{n_{disl}}$). Although we observe mostly screw dislocations,

[7] We discuss this procedure in chapter 6. It will be shown that we have essentially SrO-terminated (100) $SrTiO_3$ substrates. The termination only a¤ects the microstructure of ultra thin …lms (< 25 nm). There is no signi…cant di¤erence in superconducting and microstructural parameters in thicker …lms.

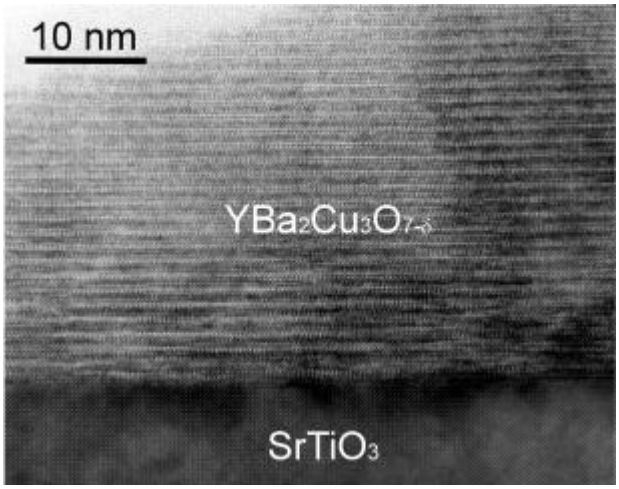

Figure 4.9: Cross-sectional high resolution TEM image of a 135 nm thick $YBa_2Cu_3O_{7-\delta}$ film on (100) $SrTiO_3$ with a low dislocation density, showing the perfect parallelism of the atomic layers. No grain boundaries are observed over a cross-sectional range of several microns.

we assume that $b = 0.39$ nm.[8] Taking the extremes for the dislocation density, we find $0.12 < \# < 0.18^{\pm}$. In our opinion, these misorientations are elastically accommodated and do not influence the coupling between islands.

In addition, upon annealing films with a high as-grown n_{disl}, the one-to-one correspondence between island and dislocation density is lost, see Fig. 4.3 and 4.4. This allows us to discriminate between individual linear defects and dislocations located in low angle grain boundaries. For this particular high n_{disl} film, we find that upon annealing (i) n_{disl} decreases from 68 to 43 μm^{-2}, (ii) n_{island} decreases faster from 66 to 30 μm^{-2}, while (iii) B^* (10 K) drops from 90 mT to 65 mT. Following Eq. (4.1), $B^*(PA)/B^*(AD) = 0.72$ resembles $n_{disl}(PA)/n_{disl}(AD) = 0.63$ and not $n_{island}(PA)/n_{island}(AD) = 0.45$. Here, we used the notation AD = as-deposited and PA = post-annealed. This confirms that B^* is determined by the dislocation density rather than some other defect related to the island density (such as low-angle grain boundaries).[9]

Finally, in our TEM investigation we were unable to reveal any grain boundaries, both in cross-section and in planar view. An example of a high resolution cross-sectional TEM image of a low dislocation density film is shown in Fig. 4.9. The atomic layers

[8] As a low angle grain boundary consists of an array of edge dislocations, we take b equal to the average in-plane lattice constant of $YBa_2Cu_3O_{7-\delta}$ ($\frac{1}{4}$ 0.39 nm).

[9] As discussed in chapter 3, this effect is even more clear in sputtered $YBa_2Cu_3O_{7-\delta}$ films, where the island density is orders of magnitude smaller than the measured threading dislocation density.

are continuous over tens of microns apart from some stacking faults parallel to the ab-plane (also introduced by the ion milling during TEM sample preparation).

4.3.3 Point defects

The e¤ect of point defects on the superconducting properties is di¢cult to capture due to the numerous types of point defects that may be present (vacancies and interstitials in various sublattices, cation disorder, etc.). Moreover, since point defects are usually associated with weak collective pinning e¤ects [51], they have relatively little in‡uence on j_s at low magnetic …elds in …lms containing linear defects. In general, a post-anneal treatment reduces the point defect concentration, since equilibrium is approached much closer than during the …lm growth process. As a result, the pinning capability should decrease [52, 53]. Focussing on the low …eld behavior, we …nd that in the sample with a low as-grown n_{disl}, $j_s(B;T)$ is independent of the post-anneal treatment.
On the other hand, at high …elds a weak e¤ect of point disorder on $j_s(B;T)$ was demonstrated [54] in $YBa_2Cu_3O_{7-\pm}$ …lms after the introduction of point defects by low energetic (25 MeV) irradiation with ^{16}O ions. In our picture of linear defect pinning, above $B^¤$ each linear defect pins one vortex and the additional vortices are pinned by other defects [12]. Therefore, at …elds $B \gg B^¤$ point defects may play a role in combination with linear defects. Surprisingly, the characteristic power-law dependence at high …elds does not change upon post-annealing, see Fig. 4.1 and 4.2. Yet, the relative amount of di¤erent types of point defects must have changed, implying that, in …rst approximation, point defects do not determine the high magnetic …eld behavior.
In fact, the robustness of the high …eld behavior suggests that linear defects still play an important role [25]. The high-…eld power-law exponent $®(T)$ is either close to $-\frac{1}{2}$ (low n_{disl}) or -1 (high n_{disl}), which can be understood from vortex shear between unpinned vortices and vortices pinned by linear defects [24, 55] and collective pinning by linear defects [24], respectively. The cross-over takes place at a dislocation density of the order $1=¸^2 = 45\ ^1m^2$ at low temperatures [25]. Although the details of the pinning mechanism operative at high …elds are not clear to us at this moment, all results point to linear defects still being e¤ective at $B \gg B^¤$.

4.3.4 Precipitates

Also a high density of precipitates facilitates vortex pinning [15, 16, 17], since a vortex can gain condensation energy. Within $YBa_2Cu_3O_{7-\pm}$ …lms mostly Y_2O_3 precipitates have been found [56]. By planar view TEM we also …nd some Y_2O_3 precipitates. Since their density is relatively low ($4/\ ^1m^2$ in the sample shown in Fig. 4.8), we infer that their pinning e¤ect is insigni…cant. On the other hand, precipitates and dislocations are closely connected, since around a precipitate dislocations can be generated [56]. As will be shown in chapter 5, we can employ this e¤ect to increase n_{disl} in our …lms: by depositing Y_2O_3 precipitates on a bare substrate prior to the actual …lm deposition we can substantially increase n_{disl} in the …lm deposited on top. This issue is also encountered in melt-textured $YBa_2Cu_3O_{7-\pm}/Y_2BaCuO_5$ composites. Although these

211 precipitates are generally believed to be the origin of the high current densities found in these materials [57], our results imply that (additional) dislocations generated by Y_2BaCuO_5 precipitates might well be the actual reason for the high currents in these bulk materials [58]. The precipitate density naturally present in our …lms, however, is too low to fully account for the high density of threading dislocations.

4.3.5 Surface roughness e¤ects

In our explanation for the higher current densities in …lms compared to single crystals so far, we left out the contribution from thickness ‡uctuations [18, 19, 20, 21]. In principle, roughness contributes to the pinning of vortices, since a vortex may lower its energy by minimizing its length [19]. Obviously, roughness e¤ects are more important in …lms compared to single crystals due to their relatively small thickness. As the substrate-…lm interface is atomically ‡at [59] (see also Fig. 4.9), we concentrate on the e¤ect of surface roughness. Assuming a sinusoidal thickness modulation $\pm t \sin(2\pi x/L)$, the pinning force per unit length f_p is calculated to be [19]:

$$f_p = \frac{2\pi\varepsilon_l \pm t}{Lt}. \tag{4.4}$$

In this expression, ε_l is the line energy of a vortex [51]. Clearly, smoother surface modulations reduce vortex pinning. Annealing reduces the surface roughness (the rms roughness after annealing is about half of the roughness of the as-grown samples). However, we …nd no corresponding decrease in the superconducting current density upon annealing. Therefore, we conclude that the contribution of the surface to $j_s(B;T)$ is negligible compared to linear defect pinning.

In conclusion, we have shown that linear defect pinning dominates in thin …lms of $YBa_2Cu_3O_{7-\pm}$ for the full temperature and magnetic …eld range investigated, irrespective of the density of threading dislocations and the anneal treatment. In order to tune the superconducting current density $j_s(B;T)$, we …rst need to control the density of these natural linear defects and their distribution. This is only possible if we know the origin of the dislocations. Although we have shown that the threading dislocations are neither related to low-angle grain boundaries nor to twin domain boundaries, the exact mechanism by which they are formed has not been identi…ed. This will be the subject of the three following chapters.

4.4 Conclusions

We correlate the microstructure of $YBa_2Cu_3O_{7-\pm}$ thin …lms, laser ablated on (100) $SrTiO_3$ substrates, to the superconducting current density $j_s(B;T)$. The defect structure of these …lms is characterized by threading dislocations, surface corrugations, twin planes, precipitates, and point defects. As a tool to manipulate the relative amount of these defects, we employ an ex-situ post-anneal treatment at a temperature close to the average deposition temperature.

We …nd that:

(i) Threading dislocations are the dominant pinning sites for vortices, giving rise to the well-known matching …eld behavior in $j_s(B;T)$: it is constant up to a characteristic …eld $B^¤(T)$ and decreases rapidly according to a power-law $B^{®(T)}$ above $B^¤$. On the average, $j_s(B < B^¤;T)$ decreases slightly with increasing as-grown dislocation density n_{disl}. We attribute this e¤ect to the somewhat poorer quality of these …lms, which determines the exact shape of the pinning potential. Annealing the …lms indeed reveals a universal $j_s(B < B^¤; 4{:}2\ K) = 6 £ 10^{11}\ A/m^2$, as expected for linear defect pinning in the single vortex regime. As a result, the superconducting current density characteristics can now be summarized by three phenomenological parameters only: $B^¤$, $j_s(B < B^¤)$ and ®. Here, $B^¤$ is proportional to n_{disl}, while ® is close to $¡\frac{1}{2}$ for $n_{disl} \cdot 45\ ¹m^{¡2}$ and close to $¡1$ for $n_{disl} \gg 45\ ¹m^{¡2}$, indicative of a shear and a collective pinning mechanism, respectively.

(ii) Some dislocations are annihilated during annealing of …lms with a high as-grown n_{disl} (small dislocation spacing) and consequently $B^¤$ decreases. Moreover, the one-to-one correspondence between island density n_{island} and n_{disl} is lost upon annealing. This allows us to discriminate between individual dislocations and dislocations being part of low-angle grain boundaries. As $B^¤$ follows the measured n_{disl} and not n_{island}, the islands are not loosely connected by means of low-angle grain boundaries (or some other defect related to the island size).

(iii) By post-annealing, the surface roughness and the point defect density decrease, while also the twin structure changes. Since in …lms with a low as-grown n_{disl} neither $j_s(B;T)$ nor n_{disl} are a¤ected at all, we argue that these type of defects do not contribute signi…cantly to vortex pinning at low magnetic …elds. In addition, it appears that overdoping does not a¤ect the magnitude of $j_s(B;T)$.

As a …nal step, we perform cross-sectional and planar view transmission electron microscopy investigations to verify these conclusions. Indeed, threading dislocations are observed. These dislocations are neither part of low-angle grain boundaries nor are they related to twin domain boundaries. In addition, the precipitate density is very low, while anti-phase boundaries are absent.

We conclude that threading dislocations fully determine the vortex pinning properties of thin …lms of $YBa_2Cu_3O_{7¡±}$, recon…rming our conclusion of chapter 3. Remarkably, it appears that even the high magnetic …eld behavior seems to be determined by the presence of linear defects. Apparently, the vortex-vortex interactions stabilize the entire vortex lattice up to …elds as high as 7 T. Therefore, the growth-induced, ordered threading dislocations in $YBa_2Cu_3O_{7¡±}$ …lms are extremely interesting both from a technological and a fundamental point of view.

References

[1] R. Ramesh, D.M. Hwang, T. Venkatesan, T.S. Ravi, L. Nazar, A. Inam, X.D. Wu, B. Dutta, G. Thomas, A.F. Marshall, and T.H. Geballe, Science 247, 57 (1990)

[2] K.S. Harshavardhan, M. Rajeswari, D.M. Hwang, C.Y. Chen, T. Sands, T. Venkatesan, J.E. Tkaczyk, K.W. Lay, and A. Safari, Appl. Phys. Lett. 60, 1902 (1992)

[3] E. Mezzetti, R. Gerbaldo, G. Ghigo, L. Gozzelino, B. Minetti, C. Camerlingo, A. Monaco, G. Cuttone, and A. Rovelli, Phys. Rev. B 60, 7623 (1999)

[4] H. Safar, J.Y. Coulter, M.P. Maley, S. Foltyn, P. Arendt, X.D. Wu, and J.Q. Willis, Phys. Rev. B 52, R9875 (1995)

[5] C. Villard, G. Koren, D. Cohen, E. Polturak, B. Thrane, and D. Chateignier, Phys. Rev. Lett. 77, 3913 (1996)

[6] T. Haage, J. Zegenhagen, J.Q. Li, H.-U. Habermeier, M. Cardona, Ch. Jooss, R. Warthmann, A. Forkl, and H. Kronmüller, Phys. Rev. B 56, 8404 (1997)

[7] Ch. Jooss, R. Warthmann, H. Kronmüller, T. Haage, H.-U. Habermeier, and J. Zegenhagen, Phys. Rev. Lett. 82, 632 (1999)

[8] Ch. Jooss, R. Warthmann, and H. Kronmüller, Phys. Rev. B 61, 12433 (2000)

[9] Ch. Gerber, D. Anselmetti, J.G. Bednorz, J. Mannhart, and D.G. Schlom, Nature 350, 279 (1991)

[10] M. Hawley, I.D. Raistrick, J.G. Beery, and R.J. Houlton, Science 251, 1587 (1991)

[11] J. Mannhart, D. Anselmetti, J.G. Bednorz, A. Catana, Ch. Gerber, K.A. Müller, and D.G. Schlom, Z. Phys. B 86, 177 (1992)

[12] H. Douwes, P.H. Kes, Ch. Gerber, and J. Mannhart, Cryogenics 33, 486 (1993)

[13] V.M. Pan, A.L. Kasatkin, V.L. Svetchnikov, and H.W. Zandbergen, Cryogenics 33, 21 (1993)

[14] A. Diáz, L. Mechin, P. Berghuis, and J.E. Evetts, Phys. Rev. Lett. 80, 3855 (1998)

[15] M. Murakami, M. Morita, K. Doi, and K. Miyamoto, Jpn. J. Appl. Phys. 28, 1189 (1989)

[16] K. Watanabe, T. Matsushita, N. Kobayashi, H. Kawabe, E. Aoyagi, K. Hiraga, H. Yamane, H. Kurosawa, T. Hirai, and Y. Muto, Appl. Phys. Lett. 56, 1490 (1990)

[17] Y.J. Tian, L.P. Guo, L. Li, Y.Q. Zhou, Y. Yang, Z.X. Zhao, S.F. Xu, H.B. Lu, Y.L. Zhou, Z.H. Chen, D.F. Cui, and G.Z. Yang, Appl. Phys. Lett. 65, 234 (1994)

[18] M. McElfresh, T.G. Miller, D.M. Schai¤er, R. Reifenberger, R.E. Muenchenhausen, M. Hawley, S.R. Foltyn, and X.D. Wu, J. Appl. Phys. 71, 5099 (1992)

[19] P. Kes, in Materials and crystallographic aspects of HT_c-superconductivity, edited by E. Kaldis (Kluwer Academic, Dordrecht, 1997), p. 407

[20] Ch. Jooss, A. Forkl, R. Warthmann, H.-U. Habermeier, B. Leibold, and H. Kronmüller, Physica C 266, 235 (1996)

[21] Ch. Jooss, A. Forkl and H. Kronmüller, Physica C 268, 87 (1996)ndon) 399, 439 (1999)

[22] F.C. Klaassen, G. Doornbos, J.M. Huijbregtse, B. Dam, and R. Griessen, J. Low Temp. Phys. 117, 1549 (1999)

[23] D.R. Nelson and V.M. Vinokur, Phys. Rev. Lett. 68. 2398 (1992)

[24] D.R. Nelson and V.M. Vinokur, Phys. Rev B 48, 13060 (1993)

[25] F.C. Klaassen, G. Doornbos, J.M. Huijbregtse, R.C.F. van der Geest, B. Dam, and R. Griessen (to be published)

[26] P. Chaudhari, R.H. Koch, R.B. Laibowitz, T.R. McGuire, and R.J. Gambino, Phys. Rev. Lett. 58, 2684 (1987)

[27] See for instance L. Civale, A.D. Marwick, M.W. McElfresh, T.K. Worthington, A.P. Malozemo¤, F.H. Holtzberg, J.R. Thompson, and M.A. Kirk, Phys. Rev. Lett. 65, 1164 (1990) and references therein.

[28] L. Civale, Supercond. Sci. Technol. 10, A11 (1997)

[29] R. Feenstra, D.K. Christen, C.E. Klabunde, and J.D. Budai, Phys. Rev. B 45, 7555 (1992)

[30] M. Qvarford, K. Heeck, J.G. Lensink, R.J. Wijngaarden, and R. Griessen, Rev. Sci. Instrum. 63, 5726 (1992)

[31] D. Hüttner, O. Meyer, J. Reiner, and G. Linker, Nucl. Instr. and Meth. in Phys. Res. B 118. 578 (1996)

[32] K.E. Bagnall, I.V. Grigorieva, J.W. Steeds, G. Balakrishnan, and D. McK Paul, Supercond. Sci. Technol. 8, 605 (1995)

[33] S. Horiuchi, M. Cantoni, M. Uchida, T. Tsuruta, and Y. Matsui, Appl. Phys. Lett. 73, 1293 (1998)

[34] T. Ishida, K. Okuda, K. Hirata, H.P. Lang, and H.-J. Günterodt, Physica C 266, 1 (1996)

[35] H. Huhtinen, E. Lähderanta and P. Paturi, J. Low Temp. Phys. 117, 795 (1999)

[36] D.G. Schlom, D. Anselmetti, J.G. Bednorz, R.F. Broom, A. Catana, T. Frey, Ch. Gerber, H.-J. Günterhodt, H.P. Lang, and J. Mannhart, Z. Phys. B 86, 163 (1992)

[37] Y. Gao, K.L. Merkle, G. Bai, H.L.M. Chang, and D.J. Lam, Physica C 174, 1 (1991)

[38] T. Hino, S. Tomiya, T. Miyajima, K. Yanashima, S. Hashimoto, and M. Ikeda, Appl. Phys. Lett. 76, 3421 (2000)

[39] D.H. Lowndes, D.K. Christen, C.E. Klabunde, Z.L. Wang, D.M. Kroeger, J.D. Budai, Shen Zhu, and D.P. Norton, Phys. Rev. Lett. 74, 2355 (1995)

[40] B. Roas, L. Schultz and G. Saemann-Ishenko, Phys. Rev. Lett. 64, 479 (1990)

[41] A. Gurevich and L.D. Cooley, Phys. Rev. 50, 13563 (1994)

[42] G. Doornbos, B. Dam, J.C. Martinez, R. Surdeanu, U. Poppe, and R. Griessen, Physica C 282-287, 2303 (1997)

[43] Y. Zhu and M. Suenaga, Phil. Mag. A 66, 457 (1992)

[44] B.M. Lairson, S.K. Streiffer, and J.V. Bravman, Phys. Rev. B 42, 10067 (1990)

[45] L.J. Swartzendruber, D.L. Kaiser, F.W. Gayle, L.H. Bennet, and A. Roytburd, Appl. Phys. Lett. 58, 1566 (1991)

[46] J.Z. Liu, Y.X. Jia, R.N. Shelton, and M.J. Fluss, Phys. Rev. Lett. 66, 1354 (1991)

[47] J.G. Wen, C.Træholt and H.W. Zandbergen, Physica C 205, 354 (1993)

[48] B. Dam, C. Træholt, B. Stäuble-Pümpin, J. Rector, and D.G. De Groot, J. Alloys and Compounds 251, 27 (1997)

[49] N.F. Heinig, R.D. Redwing, J.E. Nordman, and D.C. Larbalestier, Phys. Rev. B 60, 1409 (1999)

[50] J.P. Hirth and J. Lothe, in Theory of dislocations (Wiley, New York, 1982)

[51] G. Blatter, M.V. Feigel'man, V.B. Geshkenbein, A.I. Larkin, and V.M. Vinokur, Rev. Mod. Phys. 66, 1125 (1994)

[52] T.L. Hylton and M.R. Beasley, Phys. Rev. B 41, 11669 (1990)

[53] L.R. Tessler, J. Provost and A. Maignan, Appl. Phys. Lett. 58, 528 (1991)

[54] B. Roas, B. Hensel, G. Saemann-Ischenko, and L. Schultz, Appl. Phys. Lett. 54, 1051 (1989)

[55] R. Wördenweber, Phys. Rev. B 46, 3076 (1992)

[56] A. Catana, R.F. Broom, J.G. Bednorz, J. Mannhart, and D.G. Schlom, Appl. Phys. Lett. 60, 1016 (1992)

[57] B. Martínez, X. Obradors, A. Gou, V. Gomis, S. Piñol, J. Fontcuberta, and H. van Tol, Phys. Rev. B 53, 2797 (1996)

[58] B. Martínez, F. Sandiumenge, T. Puig, X. Obradors, L. Richard, and J. Rabier, Appl. Phys. Lett. 74, 73 (1999)

[59] J.G. Wen, T. Morishita, N. Koshizuka, C. Traeholt, and H.W. Zandbergen, Appl. Phys. Lett. 66, 1830 (1995)

Chapter 5

Mechanisms of dislocation formation

Having identi…ed threading dislocations as the dominant ‡ux pinning centers in thin …lms of $YBa_2Cu_3O_{7\,i\,\pm}$ deposited on (100) $SrTiO_3$ substrates, we now proceed to investigate the process of dislocation formation. We group the possible mechanisms into two main categories: (i) substrate-induced dislocations (such as inheritance of dislocations from the substrate and release of substrate-…lm mis…t strain) and (ii) growth-induced dislocations (merging of misaligned growth fronts). After exploring these mechanisms, incorporating some new experimental results, we conclude that the last mechanism is operative. It is illustrated that dislocation formation is closely related to the $YBa_2Cu_3O_{7\,i\,\pm}$ nucleation and growth mechanism and proceeds either via the (initial) coalescence of growth islands or via overgrowing precipitates that are preferentially induced in the nucleation stage. Although we can not yet determine unambiguously which mechanism is operative, experimental evidence is presented in favor of precipitate generated threading dislocations. If con…rmed, this would o¤er great opportunities for tailoring the linear defect distribution.[1]

[1]This chapter is based on the paper by J.M. Huijbregtse, B. Dam, R.C.F. van der Geest, F.C. Klaassen, R. Elberse, J.H. Rector, and R. Griessen, Phys. Rev. B 62, 1338 (2000)

5.1 Introduction

Typically, pulsed laser deposited $YBa_2Cu_3O_{7-\delta}$ films are characterized by a high density of threading dislocations. Here, we investigate how these dislocations are generated. In chapter 4 we excluded the possibility that the threading dislocations are part of low-angle grain boundaries. From the length scale difference we concluded that they are also not related to the twin structure. By means of our dislocation specific etching technique, we found in chapter 3 that the dislocations are introduced in the early stages of growth at or close to the substrate-film interface. This observation implies that the mechanism for dislocation formation in the thin films is either related to the substrate or to the initial stages of growth of $YBa_2Cu_3O_{7-\delta}$ itself. Other important ingredients that need to be explained are the self-organization of defects and the increase in dislocation density when lowering the substrate temperature.

In this chapter, we consider the three most likely mechanisms [1] for dislocation formation in the growth of hetero-epitaxial oxides:

(i) Inheritance of dislocations [2, 3]: Linear defects in the $SrTiO_3$ substrate may be reproduced by the $YBa_2Cu_3O_{7-\delta}$ film deposited on it.

(ii) Release of misfit strain [4]: The lattice mismatch between substrate and film induces strain during the growth of $YBa_2Cu_3O_{7-\delta}$ films. Since the elastic strain energy increases with film thickness, it is expected that this strain is released by introducing misfit dislocations above a certain critical thickness t_c [5].

(iii) Merging of misaligned growth fronts [3, 4]: During deposition, growth fronts of different heights and/or orientation merge, which may result in the formation of a dislocation. Within this mechanism we can distinguish [6] coalescence of two different growth fronts (island coalescence) and recombination of the same growth front. The latter process occurs when growth fronts flow over small irregularities, for instance non-stoichiometric precipitates (precipitate induced dislocations).

These mechanisms are discussed in more detail below. It is argued that only the merging of misaligned growth fronts can account for the observed features and the results of some preliminary experiments are presented. At this point, however, we can not yet discriminate unambiguously between island coalescence and the influence of precipitates.
In chapter 6 of this thesis, a method will be developed to investigate the influence of precipitates properly. Finally, in chapter 7 the details of the growth mechanism are discussed and it is shown that the dislocation formation mechanism is a natural consequence of the hetero-epitaxial growth mechanism of oxide thin films.

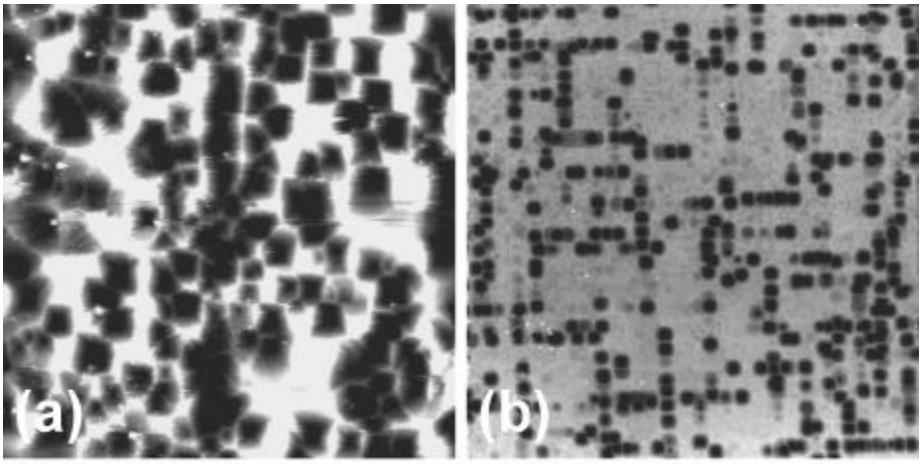

Figure 5.1: AFM height images of two (100) $SrTiO_3$ substrates, etched for 30 s in a 1 HF : 2 HNO_3 : 2 H_2O solution, showing the spread in dislocation density n_{disl} between two di¤erent substrates: (a) a typical substrate with $n_{disl} = 10^{i2}$ $^1m^{i2}$ (image size 100 £ 100 $^1m^2$) and (b) a "bad" substrate with $n_{disl} = 1$ $^1m^{i2}$ (image size 20 £ 20 $^1m^2$).

5.2 Substrate-induced dislocations

In this section, we investigate the two mechanism that are related to the nature of the substrate (i.e., inheritance and release of mis…t strain). Determining the dislocation density in the substrate material and using larger lattice mismatched substrates, respectively, allows us to exclude these mechanisms.

Inheritance of dislocations

As Eissler, Wang and Dietsche [2] suggested that dislocations are inherited from the substrate, we determined the dislocation density in $SrTiO_3$ substrates by means of etching in 1 HF: 2 HNO_3: 2 H_2O. As in the etching of $YBa_2Cu_3O_{7\,i\,\pm}$ …lms, etch pits form at linear defect sites. In …gure 5.1 AFM images of two di¤erent $SrTiO_3$ substrates are shown after etching (note the large scan sizes), giving an idea of the range of dislocation densities that can be found in the substrate material. Usually, we …nd densities that are three orders of magnitude smaller (10^{i2} $^1m^{i2}$) than those in the …lms (10 $^1m^{i2}$), see Fig. 5.1(a). The highest dislocation density observed in substrates so far [about 1 $^1m^{i2}$, see Fig. 5.1(b)], is still smaller than the lowest dislocation density achieved in …lms, indicating that inheritance is not the main origin of dislocations in …lms.

This is again shown, when we arti…cially create linear defects in the $SrTiO_3$ substrate by bombardment with 500 keV Xe^{4+} (with a dose of 200 $^1m^{i2}$). $YBa_2Cu_3O_{7\,i\,\pm}$

…lms grown on these substrates, all show the expected dislocation densities (i.e., of the order of 10^{11} m^{-2}) rather than the implanted dose in the substrate (we checked that the linear defects due to implantation were still present after …lm deposition by etching o¤ the …lm and subsequently etching the substrate). Although inheritance cannot be ruled out completely, we conclude that the linear defects in the …lm are relatively insensitive to the surface properties of the substrate.

Release of mis…t strain

Another possibility for the formation of dislocations at the interface is the relaxation of strain, originating from the mismatch between substrate and …lm.[2] Generally, a …lm may release this strain either by introducing mis…t dislocations [4] or by forming cracks [7]. Clearly, crack formation does not take place in our $YBa_2Cu_3O_{7-\delta}$ …lms and we will concentrate on the formation of mis…t relieving dislocations. Because the substrate-…lm mismatch is in the ab-plane, the mechanism leading to the creation of dislocations along the c-axis is not a priori clear. It has been suggested [4, 5] that dislocation half-loops created at the …lm surface glide towards the substrate-…lm interface to form strain relieving mis…t dislocations. The dislocation segments left at each end of the mis…t dislocation thread the …lm (parallel to the c-axis).

Such dislocation half-loops must have at least an edge component in order to relieve the in-plane substrate-…lm mis…t. However, as was shown in chapter 4, the threading dislocations that we …nd in our …lms are mainly screw dislocations, making this mechanism very unlikely. In addition, the activation energy for the formation of such half-loops is extremely high [1]. It also fails to explain why the number of dislocations created at the interface decreases substantially when growing a …lm with larger islands, i.e. at higher substrate temperatures. Given the large activation energy associated with the formation of half-loops [1], one would rather expect a larger number of loops (and thus a larger number of threading dislocations) at higher deposition temperatures. Moreover, we do not observe the merging of etch pits upon repeated etching or any other sign that they originate from dislocation half-loops.

The most convincing argument, however, against the in‡uence of the substrate mismatch on n_{disl} is found in $YBa_2Cu_3O_{7-\delta}$ …lms deposited on (100) MgO substrates.[3] Since the mismatch between $YBa_2Cu_3O_{7-\delta}$ and MgO is about 9%, which is much larger than the mismatch with $SrTiO_3$ (1.2%), more strain relieving dislocations are needed when using MgO substrates. Indeed, dislocation densities up to 10^{13} m^{-2} have been revealed by transmission electron microscopy (TEM) of $YBa_2Cu_3O_{7-\delta}$ …lms on MgO [8]. In Fig. 5.2, AFM images of the surface morphology of two $YBa_2Cu_3O_{7-\delta}$ …lms laser deposited on MgO with di¤erent dislocation densities are shown. It turns out that also on MgO the dislocation density can be decreased by increasing the substrate temperature T_{sub} and/or the oxygen pressure p_{O_2}, analogous to …lms deposited

[2] A detailed experimental investigation and discussion of the strain relaxation process will be presented in chapter 7.

[3] All …lms presented in this chapter are prepared in the QUESTEK set-up, using $3{:}0 < d_{T-S} < 3{:}5$ cm, $750 < T_{sub} < 850$±C and $15 < p_{O_2} < 50$ Pa at a ‡uence J = 1:3 J/cm^2 (as measured at the target).

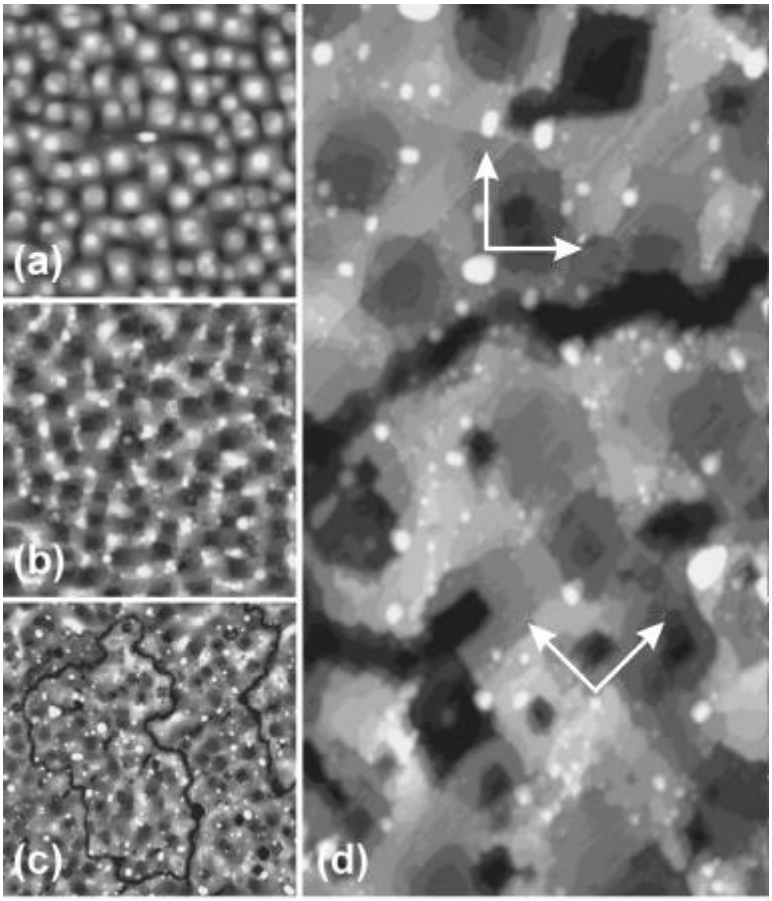

Figure 5.2: AFM height images of two $YBa_2Cu_3O_{7-\pm}$ …lms deposited on (100) MgO substrates with a high (n_{disl} = 24 $^{1}m^{-2}$) and a low (n_{disl} = 8 $^{1}m^{-2}$) dislocation density. The thickness of …lm with a high n_{disl} shown in (a) and (b) is 160 nm, while the …lm with a low n_{disl} in (c) and (d) is 100 nm thick: (a) as-grown surface morphology (n_{island} = 27 $^{1}m^{-2}$, image size 3:0 £ 3:0 $^{1}m^{2}$), (b) same …lm but now etched for 25 s in 1% Br-ethanol and (c) the low dislocation density …lm after etching for 25 s, showing that grain boundaries are also revealed (image size 5:0 £ 5:0 $^{1}m^{2}$). In (d) a close up (1:07 £ 2:04 $^{1}m^{2}$) of a high angle grain boundary in (c) is shown; the 45$^{\pm}$ rotation of etch pits across the boundary is clari…ed by arrows.

on $SrTiO_3$. Also, the surface morphology of …lms grown on $SrTiO_3$ (see chapter 3) and on MgO [Fig. 5.2(a)] is comparable. A clear island structure is again observed and no indication of spiral outcrops is found. Upon etching, etch pits form with a density equal to the island density [Fig. 5.2(b)], indicating that no additional dislocations along the c-axis are created as compared to …lms on $SrTiO_3$. Mis…t may induce in-plane dislocations. However, these dislocations do not in‡uence the characteristic …eld dependence of the critical current density, when the applied …eld is parallel to the c-axis (i.e., perpendicular to the mis…t dislocations).
Etching $YBa_2Cu_3O_{7-\delta}$ …lms deposited at high T_{sub} (small n_{disl}) on MgO reveals the presence of additional grain boundaries [(Fig. 5.2(c) and (d)]. The amount of grain boundaries increases with increasing substrate temperature. Since the edges of the etch pits are always parallel to the [100] and [010] directions of $YBa_2Cu_3O_{7-\delta}$ (see chapter 3), the orientation of etch pits in the di¤erent grains in Fig. 5.2(d) implies that these are 45± grain boundaries.[4] Indeed, 45± in plane rotationally misaligned $YBa_2Cu_3O_{7-\delta}$ domains have been observed on MgO [9] at a density that increases with increasing substrate temperature [10]. We note that these grain boundaries may consist of dislocations, thereby explaining the high densities of dislocations that were observed by TEM [8].
Apart from the introduction of grain boundaries at high substrate temperatures, the use of a larger mismatched substrates does not induce additional growth dislocations. Combined with the arguments given above, we conclude that the release of mis…t strain is not the main mechanism for introducing dislocations along the c-axis of the …lm.

5.3 Growth-induced dislocations

Having excluded the substrate as the origin of threading dislocation, it is clear that the mechanism for dislocation formation is closely related to the …rst stages of hetero-epitaxial growth. It has been suggested that dislocations are induced when misaligned growth fronts meet [3, 4] for instance at the intersection of nuclei that originated a non-integral number of unit cells away from each other [11]. Clearly, coalescence of the …rst layer of growth islands can yield dislocations that persist all the way up to the …lm surface. There are a number of experimental arguments which are in favor of such an island coalescence mechanism. First of all, the tunability of the dislocation density by means of the island density. Lowering the deposition temperature, results in a reduced surface mobility of the impinging atom species. As a result, the number of nuclei increases and, correspondingly, the number of island coalescence events, generating more dislocations.
In fact any growth process that generates misaligned growth fronts could in principle act as a source for dislocations. Therefore, also precipitates can well be the cause of such misalignment. Since the dislocations form at or close to the substrate-…lm

[4] We …nd that the superconducting current density j_s in this …lm on (100) MgO is orders of magnitude smaller than in comparable …lms on (100) $SrTiO_3$, showing that 45± grain boundaries act as weak links.

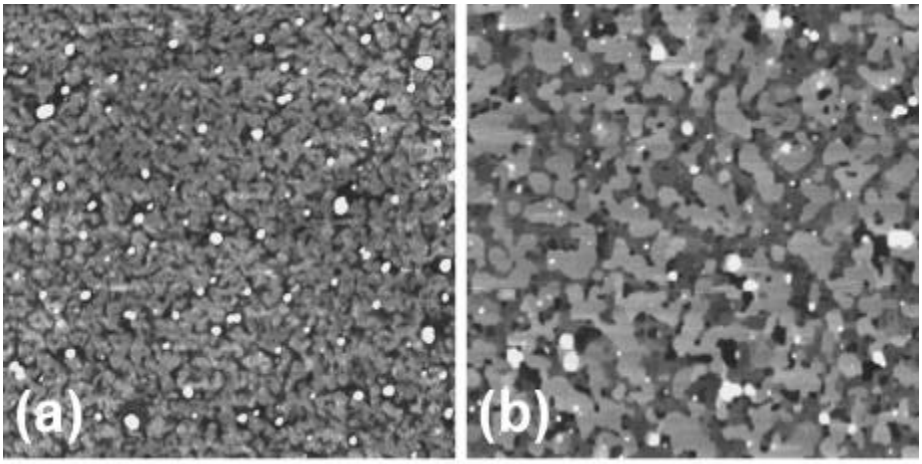

Figure 5.3: AFM height images (2:0 £ 2:0 ¹m^2) of two ultra thin YBaCuO …lms deposited on (100) $SrTiO_3$ of (a) about one monolayer, showing precipitates (22 ¹m^{-2}) embedded in the …rst monolayer and (b) approximately four monolayers, showing only a few precipitates which lie on top of the growth layers and are, therefore, not related to the initial precipitates in (a). These results indicate that the initial precipitates are either overgrown or have dissolved upon continuing the growth process.

interface, this means that such secondary phases have to form preferentially during the growth of the …rst monolayers of $YBa_2Cu_3O_{7-\pm}$. This might well be the case, since in hetero-epitaxial growth the nature of the nucleus is determined by a delicate balance of surface/interface energy and crystallization energy [12]. It has been observed both by in situ scanning tunneling microscopy [13] and TEM [14, 15] that the …rst monolayer consists of a phase di¤erent from $YBa_2Cu_3O_{7-\pm}$ on $SrTiO_3$. In that case, the remaining constituents tend to form precipitates, presumably Y_2O_3 or CuO_x [16]. Indeed, Matijasevic et al. [16] observed a high density of precipitates when depositing less than a monolayer of $SmBa_2Cu_3O_{7-\pm}$ (123) on $SrTiO_3$ by means of molecular beam epitaxy. They could reduce the precipitate density signi…cantly by properly adjusting the 123 composition of the …rst monolayer towards a 1:3:3 cation stoichiometry. Also, TEM observations [17] on one unit cell thick $YBa_2Cu_3O_{7-\pm}$ …lms grown on (001) Y-ZrO_2 substrates grown by pulsed laser deposition show preferential formation of CuO_x precipitates in the initial growth stages. Such precipitates obstruct the propagation of a growth front, leading to the merging of two misaligned branches of the same growth when they are overgrown (see for instance Fig. 7 in Ref. [1] or Fig. 6 in Ref. [6]). Consequently, it is likely that dislocations form at precipitate sites.

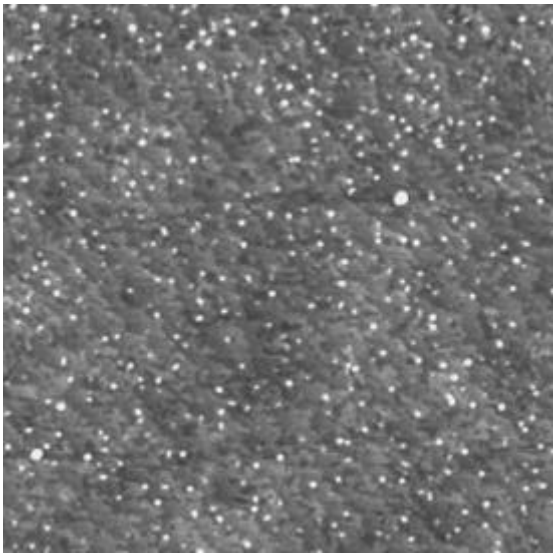

Figure 5.4: AFM height image (3:0 £ 3:0 $^1m^2$) of Y_2O_3 precipitates laser deposited on a (100) $SrTiO_3$ substrate. The density of Y_2O_3 precipitates is 54 $^1m^{i\,2}$. The vicinal steps in the substrate of 0.4 nm in height are along the [110] direction and are separated 177 nm, corresponding to a miscut angle of 0.13$^{\pm}$.

In the scenario of precipitate induced dislocations, the temperature dependence of the dislocation density is explained in terms of the segregation kinetics of the precipitates. At lower temperatures, the spacing between precipitates is smaller due to the smaller surface di¤usion distance, resulting in a higher precipitate density (higher dislocation density). The self-organization of dislocations can be understood by assuming that the kinetics are di¤usion controlled.

We have therefore two mechanisms, i.e. dislocations induced by overgrowing precipitates or by islands coalescence, which are potentially leading to the observed phenomena. In order to decide which mechanism is dominant we started investigating ultra thin …lms. In Fig. 5.3(a) an AFM image, recorded ex-situ, of a $YBa_2Cu_3O_{7\,i\,\pm}$ …lm with a thickness slightly over one unit cell (u.c.) is shown. The substrate is fully covered with one monolayer of $YBa_2Cu_3O_{7\,i\,\pm}$ (or a related phase [13, 14, 15, 16]). Embedded in this matrix, we observe a signi…cant number of precipitates (22 $^1m^{i\,2}$). As shown in Fig. 5.3(b), these precipitates are almost absent in …lms of 4 u.c. in thickness, showing that the initial precipitates are either overgrown or have dissolved again (and are incorporated as defects in the …lm). Apparently, precipitates are characteristic for the …rst layer only.

Nevertheless, these secondary phases may generate dislocations when they are overgrown. The density of precipitates is larger than the dislocation density as expected

for a thicker $YBa_2Cu_3O_{7-\delta}$ film deposited under the same deposition conditions (7.8 μm^{-2}). However, we should stress that not all precipitates necessarily generate dislocation when they are overgrown.
To prove that precipitates can generate dislocations, we deposited small particles from a Y_2O_3 target on a bare $SrTiO_3$ substrate prior to the actual film deposition, see Fig. 5.4. In this figure Y_2O_3 precipitates can be distinguished with a density of 54 μm^{-2}. Now depositing a $YBa_2Cu_3O_{7-\delta}$ film on top of this precipitate structure at a substrate temperature of 850°C, yields a film with a threading dislocation density of 41 μm^{-2}. This is more than 5 times larger than the dislocation density in films deposited under identical condition on clean substrates (7.8 μm^{-2}) and we conclude that precipitates serve as nucleation sites for dislocations.

Having shown that (i) preferential precipitation takes place in the first stages of $YBa_2Cu_3O_{7-\delta}$ growth and (ii) Y_2O_3 precipitates induce additional dislocation, it is tempting to conclude that dislocations are induced by precipitates formed in the first monolayer as a result of the peculiarities of the nucleation mechanism. However, island coalescence can equally well explain the temperature dependence of the dislocation density and their distribution. Therefore, in order to decide which one of the two mechanisms is operative, we first need to control the preferential precipitation process (chapter 6).

5.4 Conclusions

As an introduction to the remaining part of this thesis, we discussed various mechanisms by which threading dislocations can be induced in $YBa_2Cu_3O_{7-\delta}$ films. It is shown that linear defects are not related to the $SrTiO_3$ substrate. First, the dislocation density in the substrate is typically two orders of magnitude lower than in the film. Secondly, increasing the misfit between substrate and film by using (100) MgO (9% misfit) instead of (100) $SrTiO_3$ (1% mismatch) we find comparable dislocation densities in the corresponding films, showing that our threading dislocations are not misfit dislocations.
We conclude that dislocations are induced as a consequence of the growth process itself via merging of misaligned growth fronts. At points where misoriented growth fronts meet, dislocation formation is facilitated. We identify at least one mechanism: we can enhance the density of pinning sites by depositing a layer of Y_2O_3 precipitates before starting the $YBa_2Cu_3O_{7-\delta}$ growth process. This opens up new possibilities in tailoring the in-plane threading dislocation distribution. For instance by depositing a lattice of precipitates prior to the actual film growth, it may be possible to observe the predicted [18] Mott-insulator vortex phase (see chapter 3).
Clearly, precipitation in the first monolayer resulting from the peculiarities of the nucleation mechanism of $YBa_2Cu_3O_{7-\delta}$ on $SrTiO_3$ (preferential precipitation) can account for the introduction of dislocations. In addition, also the temperature dependence of their density and distribution can be explained in a qualitative way. Although we find evidence for preferential precipitation in the first monolayers, there is a sec-

ond mechanism which accounts equally well for all observed characteristics: island coalescence. We will explore these two mechanisms in the remaining two chapters of this thesis.

References

[1] B. Stäuble-Pümpin, V.C. Matijasevic, B. Ilge, J.E. Mooij, W.J.A.M. Peterse, P.M.L.O. Scholte, F. Tuinstra, H.J. Venvik, D.S. Wai, C. Træholt, J.G. Wen, and H.W. Zandbergen, Phys. Rev. B 52, 7604 (1995)

[2] D. Eissler, H.S. Wang, and W. Dietsche, Appl. Phys. Lett. 62, 1292 (1993)

[3] D.G. Schlom, D. Anselmetti, J.G. Bednorz, R.F. Broom, A. Catana, T. Frey, Ch. Gerber, H.-J. Günterhodt, H.P. Lang, and J. Mannhart, Z. Phys. B 86, 163 (1992)

[4] S.J. Pennycook, M.F. Chisholm, D.E. Jesson, R. Feenstra, S. Zhu, X.Y. Zheng, and D.J. Lowndes, Physica C 202, 1 (1992)

[5] M. Yeadon, M. Aindow, F. Wellhöfer, and J.S. Abell, J. Cryst. Growth 172, 145 (1997)

[6] D.G. Schlom, D. Anselmetti, J.G. Bednorz, Ch. Gerber, and J. Mannhart, J. Cryst. Growth 137, 259 (1994)

[7] M. Bauer, F. Baudenbacher, and H. Kinder, Physica C 246, 113 (1995)

[8] V. Svetchnikov, V. Pan, C. Traeholt, and H. Zandbergen, IEEE Trans. Appl. Supercond. 7, 1396 (1997)

[9] T.S. Ravi, D.M. Hwang, R. Ramesh, Siu Wai Chan, L. Nazar, C.Y. Chen, A. Inam, and T. Venkatesan, Phys. Rev. B 42, 10141 (1990)

[10] M. Kusunoki, Y. Takano, M. Makaida, and S. Ohshima, Physica C 321, 81 (1999)

[11] S.K. Strei¤er, B.M. Lairson, C.B. Eom, B.M. Clemens, J.C. Bravman, and T.H. Geballe, Phys. Rev. B 43, 13007 (1991)

[12] B. Dam and B. Stäuble-Pümpin, J. Mater. Sci.: Mater.Electron. 9, 217 (1998)

[13] T. Haage, J. Zegenhagen, H.-U. Habermeier, and M. Cardona, Phys. Rev. Lett. 80, 4225 (1998)

[14] J.G. Wen, T. Morishita, N. Koshizuka, C. Traeholt, and H.W. Zandbergen, Appl. Phys. Lett. 66, 1830 (1995)

[15] H.W. Zandbergen, J.G. Wen, C. Traeholt, and V. Svetchnikov, J. Alloys Compd. 195, 85 (1993)

[16] V.C. Matijasevic, B. Ilge, B. Stäuble-Pümpin, G. Rietveld, F. Tuinstra, and J.E. Mooij, Phys. Rev. Lett. 76, 4765 (1996)

[17] J.A. Alarco, G. Brorsson, H. Olin, and E. Olsson, J. Appl. Phys. 75, 3202 (1994)

[18] D.R. Nelson and V.M. Vinokur, Phys. Rev. Lett. 68, 2398 (1992)

Chapter 6

The …rst stages of hetero-epitaxial growth: phase stability

We investigate the origin of preferential precipitation in $YBa_2Cu_3O_{7\ i\ \pm}$ (123) …lms by varying the (100) $SrTiO_3$ substrate termination. Using a newly developed ex-situ method to prepare SrO-terminated substrates in addition to the well-known TiO_2-termination, it is shown that: (i) preferential precipitation occurs when depositing submonolayer 123 …lms on SrO-terminated $SrTiO_3$ and (ii) such precipitates are absent on the TiO_2-termination. The substrate termination determines both the starting and terminating layer of the 123 phase. Similar e¤ects are observed in submonolayer thick …lms with cation stoichiometries of 122, 124 and 133. However, when growing several 123 monolayers on SrO-terminated substrates, no precipitates are formed. Instead, defects are introduced to accommodate the o¤-stoichiometry. Hence, the density of threading dislocations in thick …lms does not depend on the substrate termination, excluding preferential precipitation as the main origin of threading dislocation.[1]

[1]This chapter is based on the paper by J.M. Huijbregtse, J.H. Rector, and B. Dam, accepted for publication in Physica C (2001)

6.1 Introduction

In the previous chapter, we concluded that the merging of misaligned growth fronts [1] accounts for all the characteristics of the threading dislocation structure in thin …lms of $YBa_2Cu_3O_{7-\pm}$ on $SrTiO_3$. Misalignment is caused either by the coalescence of growth islands, or by growth fronts ‡owing over irregularities, such as precipitates [2]. Depositing Y_2O_3 particles prior to the actual …lm deposition, indeed generates dislocations. On the other hand, since dislocations only form at or close to the interface, such precipitates must form preferentially in the early stages of hetero-epitaxial growth. Why would such a preferential precipitation process occur at all? If the phase that initially forms has a cation composition di¤erent from 123 (such as 122 or 133) [3], supplying the 123 composition automatically results in the formation of precipitates for the …rst monolayer (in addition to the 122 or 133 phase). Indeed, in the case of $SmBa_2Cu_3O_{7-\pm}$ …lms grown by molecular beam epitaxy it was shown [4] that such a precipitation process occurs. It was suppressed by properly adjusting the composition of the …rst monolayer towards a 133 stoichiometry, con…rming non-unit cell nucleation. Since the exact stacking sequence is governed by the substrate-…lm interaction, the substrate terminating layer is expected to have a large in‡uence on the precipitate density and, possibly, on the dislocation density.

In this chapter we report on the …rst stages of hetero-epitaxial growth, comparing SrO and TiO_2-terminated (100) $SrTiO_3$ substrates. Kawasaki et al. [5] have shown that TiO_2-terminated $SrTiO_3$ substrates can be produced by selectively etching o¤ SrO in a pH-controlled bu¤ered NH_4-HF (BHF) solution. This procedure results in nearly 100% TiO_2-terminated $SrTiO_3$ substrates, as was con…rmed by ion beam analysis techniques [5, 6, 7, 8, 9]. Recently, Koster et al. [10] improved this procedure. Prior to the BHF etching, the substrates are dipped in water, leading to the formation of Sr-hydroxyls at the surface. These hydroxyls are easily removed in the BHF solution (a process which depends much less critically on the pH of the solution). After etching, the substrates are annealed at 950±C in ‡owing oxygen to straighten the pattern of vicinal steps, leaving the TiO_2 termination una¤ected. So far, however, there are no analogue ex-situ treatments that reproducibly yield SrO-terminated substrates. Instead, a monolayer of SrO was deposited on TiO_2-terminated substrates [11, 12, 13]. There are also reports [5, 14, 15] on the homo-epitaxial growth of $SrTiO_3$ …lms on TiO_2-terminated substrates having SrO as the stable terminating layer. In both cases, however, additional in-situ processing steps are performed prior to the actual thin …lm deposition.

Here, we show that the SrO-termination can be obtained reproducibly by annealing $SrTiO_3$ substrates in ‡owing oxygen, after mechano-chemical polishing and cleaning in 1-propanol. Thereby we can study the in‡uence of the substrate-…lm interaction on the nucleation of $YBa_2Cu_3O_{7-\pm}$ …lms. It is found that the …rst stages of growth of $YBa_2Cu_3O_{7-\pm}$ (123) are completely di¤erent on both type of substrates: preferential precipitation is observed on SrO, whereas 123 nucleates precipitate-free on the TiO_2 termination. Preferential precipitation can also be prevented by supplying 122 or 133 as the cation composition of the initial growth layer. Remarkably, precipitates disappear when growing thicker 123 …lms on SrO-terminated $SrTiO_3$, indicating that

the o¤-stoichiometries are incorporated during …lm growth in the form of defects. Accordingly, we …nd no e¤ect of the substrate termination on the dislocation density in thick …lms. We conclude that preferential precipitation is not the main origin of these threading dislocations.

This chapter is organized as follows. First, we explore the nature of the (100) $SrTiO_3$ substrate termination. In the main part of the chapter, we investigate the preferential precipitation process in submonolayer thick YBaCuO …lms as a function of substrate termination and initial cation stoichiometry. Finally, the e¤ect of these precipitates on the formation of threading dislocations is discussed.

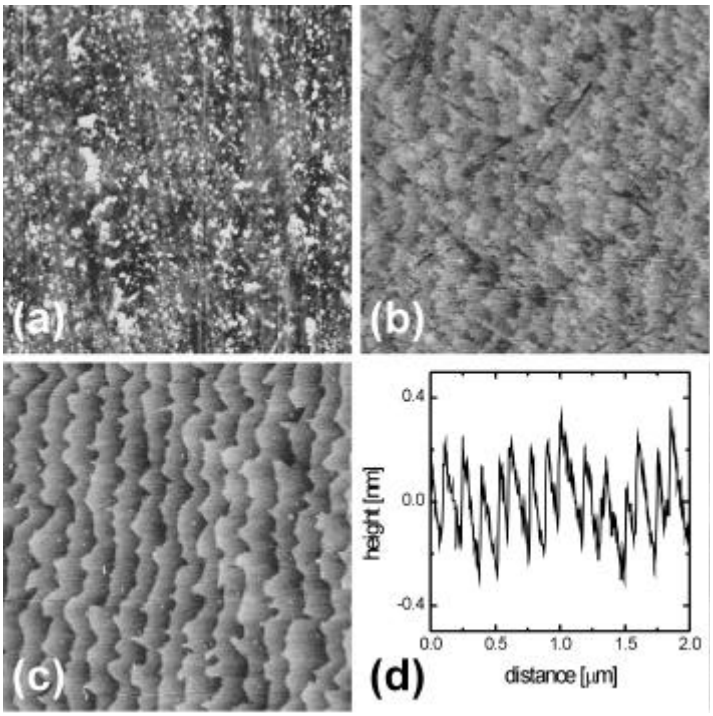

Figure 6.1: E¤ect of cleaning and annealing of (100) $SrTiO_3$ substrates. AFM height images (2.0 x 2.0 $^1m^2$) of the same substrate: (a) as delivered, i.e. after the mechano-chemical polishing procedure, (b) after cleaning in 1-propanol the vicinal steps are revealed and (c) upon annealing at 900±C for 5 hours in a O_2-‡ow of 0.5 l/minute the steps become more pronounced and straighten considerably. The height scales are 5 nm, 2.5 nm and 2.5 nm, respectively. In (d) a cross section taken from (c) is given, showing steps of 0.4 nm in height only. Since the spacing between consecutive steps is irregular, the cross section shows some height modulations due to the ‡attening procedure (i.e., levelling with respect to the average height).

6.2 Single terminated (100) $SrTiO_3$

We have used epi-polished (100) $SrTiO_3$ substrates with an average miscut angle of 0.15± from various suppliers.[2] The as-received substrates are …rst cleaned in 1-propanol under applying mechanical force and subsequently dried in air using a spinner. Next, the substrates are annealed in a quartz tube oven, using an oxygen ‡ow of 0.5 l/minute: the substrates are heated at a rate of 15±C/minute to the annealing temperature T_a of 900±C, annealed at this temperature for a time t_a = 5 hours and then slowly cooled down (rate < 15±C/minute). To analyze the surface morphology of both the $SrTiO_3$ substrates and the …lms deposited on top of them, we use scanning probe microscopy in air. Atomic Force Microscopy (AFM) measurements are performed both in the tapping mode and in the contact mode using Si and Si_3N_4 tips, respectively. The images presented in this chapter are all obtained by tapping mode AFM, unless mentioned otherwise.
The surface morphology of the as-received (100) $SrTiO_3$ substrates, i.e. after mechano-chemical polishing, is very rough, see Fig. 6.1(a). By cleaning the substrates in 1-propanol under applying mechanical force all remains of the etching procedure are wiped o¤ within a few seconds [Fig. 6.1(b)]. This is a quick and e¢cient cleaning procedure to reveal the rough vicinal steps, mainly 0.4 nm, some 0.2 nm in height. In order to straighten the steps, an additional heat treatment is needed at a temperature above 800±C [10, 16, 17]. We anneal the substrates for 5 hours at 900±C in ‡owing O_2 (at 0.5 l/minute), see Fig. 6.1(c). Indeed, the steps straighten, although some roughness is still present. As can be seen in Fig. 6.1(d), the step height is now 0.4 nm for all steps, corresponding to the unit cell of $SrTiO_3$ (3.905 Å), implying that we have a single terminated substrate after the annealing procedure.[3]

6.2.1 Determining the termination

To determine the nature of the substrate termination, we performed AFM height and friction measurements on commercially available TiO_2-terminated $SrTiO_3$ (TiO_2-$SrTiO_3$) substrates[4] and compare these results with similar experiments performed on $SrTiO_3$ surfaces cleaned in 1-propanol and subsequently oxygen annealed. From the di¤erence in stability of both surfaces in air and the di¤erences in wetting of TiO_2 and SrO …lms on both substrate terminations, we conclude that our recipe yields essentially SrO-terminated $SrTiO_3$ (SrO-$SrTiO_3$).

[2] Commercially available single crystalline (100) $SrTiO_3$ substrates measuring 10 £ 10 £ 1 mm^3 are obtained from ESCETE (Enschede, The Netherlands) and Crystal GmbH (Berlin, Germany).

[3] We claim that our substrates are single terminated within the resolution of the AFM. A truly single termination can be veri…ed by ion beam analysis. However, even in these type of measurements additional high temperature cleaning steps are necessary, possibly in‡uencing the termination. Therefore, the only method to unambiguously prove that a substrate is truly single terminated is by in-situ atomic resolution imaging.

[4] These TiO_2-terminated substrates are produced by ESCETE according to the procedure described in [10].

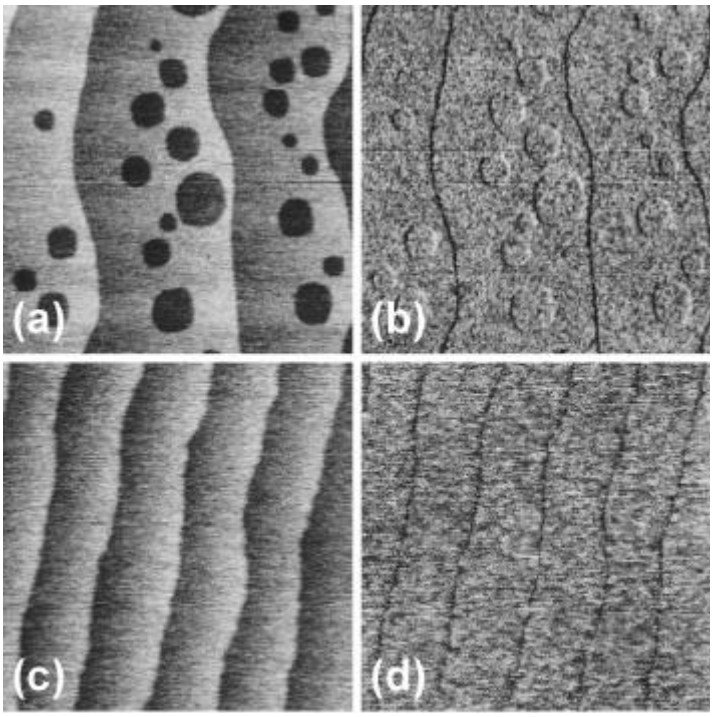

Figure 6.2: Simultaneously recorded AFM contact mode height (left, height scale 2.5 nm) and friction (right, full scale 0.05 V) images of two (100) $SrTiO_3$ substrates: (a,b) TiO_2-terminated and (c,d) 1-propanol cleaned and subsequently annealed at 900±C for 5 hours in an O_2-‡ow. The scan size is 1.0 ¹m; both the scan conditions and the image conditions (color table, contrast, etc.) are the same for all images. All vicinal steps are 0.4 nm in height, including the holes in the TiO_2-terminated substrate.

Friction measurements

AFM friction measurements in principle provide a tool to determine the substrate termination [18]. In Fig. 6.2, the results of contact mode AFM measurements on both type of substrates are shown. The scan conditions, including the tip, are exactly the same. Both substrates were scanned directly after each other. In both height images [Fig. 6.2(a,c)] only vicinal steps of 0.4 nm in height are discerned. This was recon...rmed by tapping mode AFM measurements. Probably, the 1 unit cell deep holes in the TiO_2-terminated substrate [Fig. 6.2(a,b)] are not annihilated during annealing, because the annealing time t_a for this very low miscut substrate (< 0.05±) was too short. Because we do not observe any friction contrast within each image [Fig. 6.2(b,d)], both substrates are characterized by a single terminating layer.

As the vicinal steps can be more clearly discerned in the upper images, the results suggest that there is a di¤erence between the two types of substrates. However, this may also be an e¤ect of the tip wearing out. In fact, this is exactly the problem in determining the substrate termination by friction: absolute friction measurements are extremely di¢cult to obtain. Therefore, we can not conclude which termination is associated with the larger friction force. Moreover, in literature con‡icting results are presented. High friction domains are associated both with the TiO_2 surface [10] and with the SrO surface [9, 13, 18]. Although AFM friction measurements are a useful tool in proving that a substrate is single terminated, we conclude that it is not a good method to determine the surface layer in case of a single substrate termination.

Aging e¤ects

Since SrO and TiO_2 are chemically very di¤erent, we examine the stability of the surface of both types of substrates in air, see Fig. 6.3. We …nd that TiO_2-terminated substrates are not a¤ected by storage in air at least for a period of several months, see Fig. 6.3(a). This is in sharp contrast with the substrates treated with 1-propanol and subsequently annealed. As seen in Fig. 6.3(b,c,d), the surface degrades with time (note the larger height scales). Since TiO_2 is known to be stable in air [19] and SrO is not, we conclude that the termination of these substrates is SrO.

Another example of surface degradation is shown in Fig. 6.4 for a substrate with a dual termination. In the cross section in Fig. 6.4(b) steps of 0.2 nm in height can be discerned. We note that a dual termination is rarely observed after our 1-propanol cleaning and annealing treatment. Apparently, the annealing time is too short for this speci…c substrate to yield a single termination. Based on the previous results, we expect that the termination covering most of the surface is SrO. After storing this substrate in air for 2 months, we indeed …nd that the substrate termination covering most of the surface has roughened, whereas the remaining area did not deteriorate, see Fig. 6.4(c) [note the larger height scale]. This con…rms that SrO is unstable in air.

In literature, it has been suggested that SrO reacts with water [9, 15], possibly transforming into a Sr-hydroxyl complex [10]. The a¢nity of SrO for H_2O can be understood, if one realizes that the surface layer relaxes (rumpling). This rumpling causes the surface to polarize. Both shell model calculations [20, 21, 22] and …rst principles total energy calculations [23, 24] predict such a surface relaxation, although the details di¤er. Experimentally, it was recently found [25] that only the SrO surface exhibits a signi…cant inward relaxation (of the Sr atoms). As a result, the H_2O molecules (dipoles) are electrostatically attracted by the SrO surface, causing a higher reactivity with the SrO surface than with the TiO_2 surface. In order to verify the a¢nity for water, we soaked both type of substrates in H_2O. Since we observed a quick degradation of the SrO-terminated substrates, whereas the TiO_2-terminated substrates remained una¤ected we conclude that the aging e¤ects are caused by water.

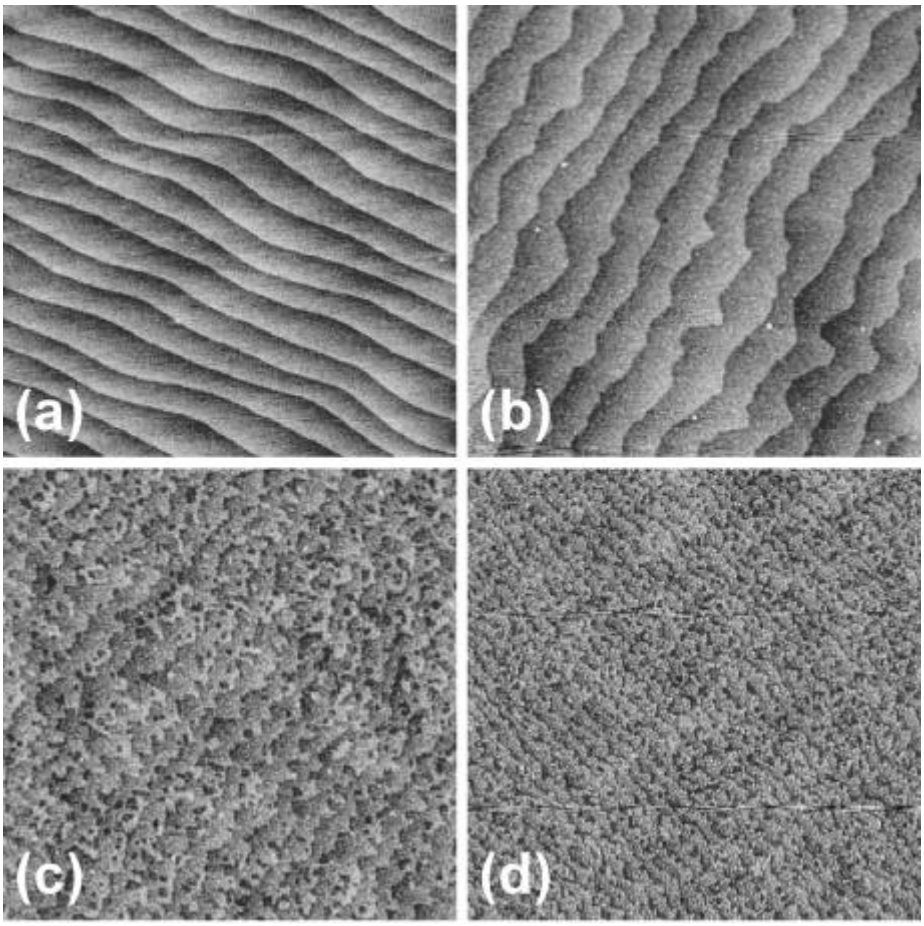

Figure 6.3: Stability of di¤erently treated (100) $SrTiO_3$ substrates in air. Shown are AFM height images of 2.0 x 2.0 $^{1}m^{2}$: (a) a TiO_2-terminated substrate after 1 month storage in air and 1-propanol cleaned, oxygen annealed substrates after storage in air for (b) 2 weeks, (c) 6 weeks and (d) 2 months. The height scales are 2.5 nm, 4 nm, 4 nm and 6 nm, respectively. The surface of the 1-propanol cleaned, oxygen annealed substrates is clearly unstable.

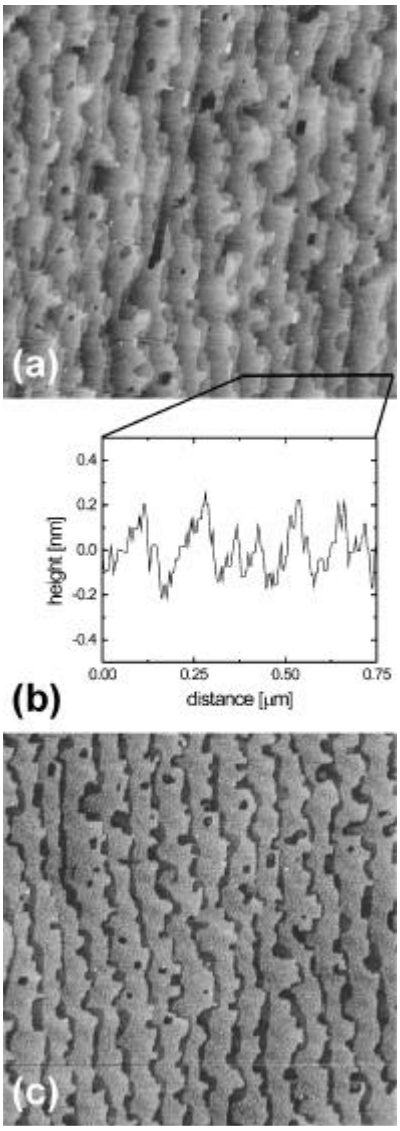

Figure 6.4: AFM height images (2.0 x 2.0 $^{1}m^{2}$) of a (100) $SrTiO_3$ substrate: (a) after 1-propanol cleaning and subsequently annealing at 900±C for 5 hours in an O_2-‡ow of 0.5 l/minute we …nd a dual termination, (b) cross section taken from (a), showing steps of both 0.2 and 0.4 nm in height and (c) the steps which cover most of the surface have roughened after storage in air for a period of two months. The average height di¤erences in (c) between terraces of the same termination is 0.4 nm; the height scales are: (a) 2.5 nm and (c) 5 nm (same image conditions).

Wetting effects

Finally, we study the wetting of thin TiO_2 and SrO films deposited on both type of substrates by means of PLD, see Fig. 6.5. On both substrates [Fig. 6.5(a,b)] we deposit[5] 10 laser shots of TiO_2 and SrO (T_{sub} = 850°C, p_{O_2} = 15 Pa, and d_{T-S} = 3.5 cm), corresponding to a coverage of about 1 monolayer (ML). Since a B-site material does not wet on a B-terminated ABO_3 perovskite [12], we expect clear differences in surface morphology. Indeed, TiO_2 forms very small islands, suggesting a poor wetting, on TiO_2-$SrTiO_3$ [Fig. 6.5(c)], compared to the larger TiO_2 islands on SrO-$SrTiO_3$ [Fig. 6.5(d)]. The deposition of SrO also reveals a difference in surface morphology [Fig. 6.5(e,f)]. However, the wetting effects are very subtle. In order to make the effects more pronounced, we give all thin SrO and TiO_2 films the substrate anneal treatment (5h at 900°C in flowing O_2).

In SrO films, precipitates emerge on the SrO-$SrTiO_3$ [Fig. 6.5(h)], whereas layers are formed that are flat over distances of the order of 1 µm on the TiO_2-$SrTiO_3$ [Fig. 6.5(g)]. The height of the flat layers is either 1.2, 2.0 or 2.7 nm. This corresponds well with the c-axis lattice constant of the Sr-rich Ruddlesden-Popper phases $Sr_{n+1}Ti_nO_{3n+1}$ (c = 11.80, 19.66 and 27.50 Å for n = 1, 2 and 3, respectively [26]). Indeed, the formation of these $SrO(SrTiO_3)_n$ phases can be expected [26] when enriching a TiO_2-terminated $SrTiO_3$ substrate with Sr. The c-axis of the Ruddlesden-Popper phase with n = 1 nicely matches the c-axis of $YBa_2Cu_3O_{7-\pm}$. Therefore, this method (i.e., deposition of one monolayer of SrO followed by annealing) could in principle be used to obtain an ideal substrate with vicinal steps of only 1.2 nm in height and avoid the problem of anti-phase boundaries [27].

Calculations [28] have shown that only a single SrO layer can be grown epitaxially and uniformly on a TiO_2-terminated substrate. With a second monolayer [11], the cubic SrO crystal structure forms with a lattice constant of 5.16 Å. Crystallographically, this SrO crystal is rotated by 45° with respect to the $SrTiO_3$ crystal and we should compare the $SrTiO_3$ lattice constant (3.905 Å) with 5.16 Å/$\sqrt{2}$ = 3.649 Å. Because of this lattice mismatch, annealing SrO films deposited on SrO-$SrTiO_3$ results in the formation of SrO precipitates. The formation of SrO droplets has indeed been observed experimentally after extensively annealing (100) $SrTiO_3$ single crystals [26]. Both TiO_2 films precipitate after annealing, see Fig. 6.5(i,j). This is only expected for the TiO_2-$SrTiO_3$ because of the poor wetting. The amount of material present in the form of precipitates is much larger than deposited. Apparently, material segregates from the bulk towards the surface. Comparing with the original step structures of the $SrTiO_3$ substrates, it is also clear that the steps pattern has changed considerably: step bunching occurs, resulting in steps of multiples of 0.4 nm in height. All these effects make it difficult to understand what exactly is happening upon annealing the TiO_2 films. However, from the remaining images it is clear that there is a difference in behavior of the two type of substrates, reconfirming the difference in substrate terminations.

[5] The films are deposited in the LAMBDA PHYSIK set-up from rotating, polycrystalline, high density stoichiometric TiO_2 target (PRAXAIR, > 99.9% pure raw materials); the SrO films are deposited from a single crystalline SrO target. The laser energy density J is set at 1.4 J/cm^2 (as measured at the target).

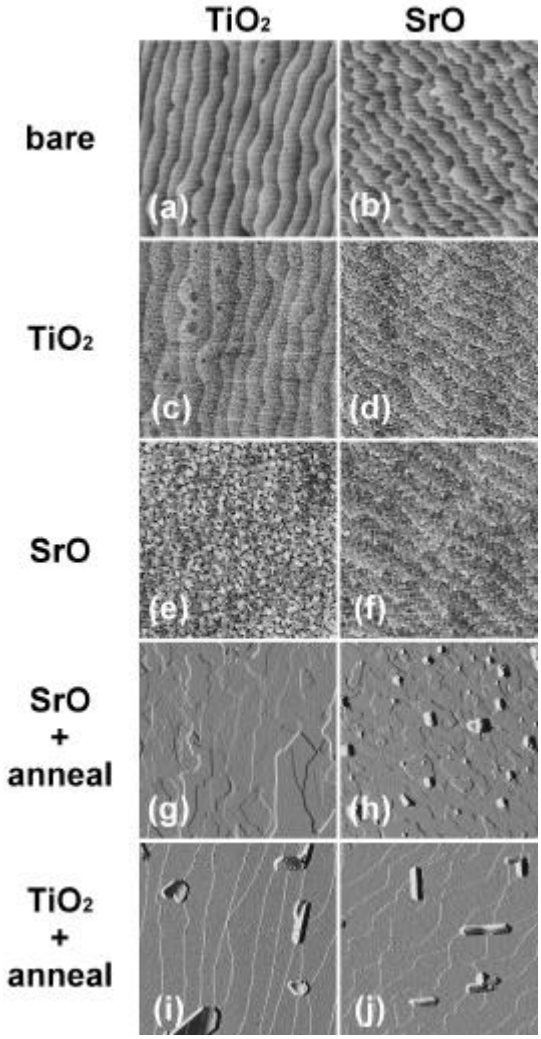

Figure 6.5: Wetting of TiO_2 and SrO …lms on (left) a TiO_2-terminated and (right) a SrO-terminated (100) $SrTiO_3$ substrate. Shown are AFM images of 2.0 x 2.0 $^1m^2$: (a,b) before deposition; (c,d) after laser ablating 10 shots of TiO_2; (e,f) after deposition of 10 shots of SrO; (g,h) same …lms as in (e,f) but now annealed at 900$^{\pm}$C for 5 hours in a 0.5 l/min. O_2-‡ow and (i,j) same …lms as in (c,d) but now annealed. All images are height images (height scale 2.5 nm for the bare substrates and 4 nm for the …lms), except those taken after the anneal treatment; these are amplitude images (full scale 0.75 nm for the TiO_2 and 1.5 nm for the SrO …lms). Both the scan and image conditions (color table, contrast, etc.) are the same for all images. The surface structure in (c) is not due to noise, but results from the very small TiO_2 islands.

6.2.2 SrO-terminated substrates

Alternative routes for preparing SrO-terminated $SrTiO_3$ substrates all make use of TiO_2-terminated substrates. Two in-situ methods can be followed to convert the termination into SrO:

1. Deposition of SrO [11, 12, 13]. Indeed, one monolayer SrO can be grown epitaxially on TiO_2-$SrTiO_3$ [11]. As mentioned above, a second SrO monolayer forms the cubic SrO crystal structure [28] together with the …rst monolayer. Therefore, not only the lattice matching between …lm and substrate will be in‡uenced by using more than one monolayer of SrO as a bu¤er layer, but also precipitates may form [11, 26] which strongly deteriorate the substrate surface morphology.

2. Deposition of $SrTiO_3$. From literature [5, 14, 15] it appears that the terminating layer of $SrTiO_3$ …lms is SrO, suggesting that homo-epitaxial growth of $SrTiO_3$ can be used to produce a SrO-terminated substrate. However, Nakamura et al. [6] report that TiO_2 is the main terminating layer of the $SrTiO_3$ and show that the stable surface layer in fact depends both on the deposition technique and the deposition conditions used [29]. Therefore, one should be careful when using this method, as it does not necessarily yield the desired substrate termination.

In both cases it is crucial to deposit (multiples of) one monolayer. In practice this can only be realized by in-situ monitoring the growth process by means of Re‡ection High-Energy Electron Di¤raction (RHEED). Apart from the fact that one more deposition step is needed, deposition of the bu¤er layer may require deposition conditions which are in con‡ict with the …lm deposition conditions. Clearly, both in-situ methods have disadvantages compared to our ex-situ method to produce SrO-terminated substrates. In fact, we can directly compare method 1 with our ex-situ method [Figs. 6.5(e) vs. (b)]. Although our AFM measurements are performed ex-situ, we believe that the starting situation for thin …lm deposition is much better de…ned using our process.

6.3 Preferential precipitation of YBaCuO

In this section, we investigate preferential precipitation in YBaCuO …lms as a function of the substrate termination and initial cation stoichiometry of the …lm. Before taking a look at the di¤erences in hetero-epitaxial growth on TiO_2 and SrO-terminated (100) $SrTiO_3$ substrates, we …rst review some general aspects of $YBa_2Cu_3O_{7-\delta}$ …lm growth. Next, the experimental results are presented. Finally, a new stacking sequence model for the …rst monolayer of YBaCuO is proposed which accounts for the experimental observations.

6.3.1 Origin

To understand the phase stability of the …rst layer of $YBa_2Cu_3O_{7-\pm}$, we summarize earlier experimental observations that were reported in literature. RHEED measurements have shown that $YBa_2Cu_3O_{7-\pm}$ grows unit cell by unit cell on $SrTiO_3$ if all elements are continuously and stoichiometrically supplied [30]. This indicates that $YBa_2Cu_3O_{7-\pm}$ maintains its termination during growth at all times. Experimentally, two terminating layers of $YBa_2Cu_3O_{7-\pm}$ …lms are observed: BaO [31, 32, 33] and CuO [34, 35, 36].
On the other hand, the starting atomic layer of $YBa_2Cu_3O_{7-\pm}$ is determined by the surface chemistry and the interaction between the $SrTiO_3$ substrate and the $YBa_2Cu_3O_{7-\pm}$ …lm [37]. In order to continue the perovskite type stacking of the substrate across the interface as much as possible, the stacking sequence of the $YBa_2Cu_3O_{7-\pm}$ has to be either BaO or Y on TiO_2 (and CuO_2 or CuO on SrO).
Since Y has a residual charge of 3+, whereas TiO_2 has none, charge neutral BaO is the best layer to start the $YBa_2Cu_3O_{7-\pm}$ structure with. Indeed, High Resolution Transmission Electron Microscopy (HRTEM) observations con…rmed the TiO_2-BaO-CuO_2-Y-CuO_2-BaO-CuO-... stacking sequence on TiO_2-$SrTiO_3$ [37]. However, molecular dynamics simulations [28, 38] show a signi…cant amount of stress built-up at the TiO_2-BaO interface, in contrast to the SrO-BaO interface which is almost stress-free. This stress is accommodated by defects in the …lm some unit cells away from the interface, resulting in a bending of the atomic planes in three dimension [37].
The exact stacking sequence of $YBa_2Cu_3O_{7-\pm}$ on SrO-terminated $SrTiO_3$ has not been determined unambiguously yet. Assuming that stress is less important than the continuation of the substrate structure, either CuO_2 or CuO is expected as the …rst layer. Since CuO_2 has a residual charge, the most likely starting layer is CuO [18]. However, the CuO_2 plane was reported to be the starting layer on the SrO termination [39].
Now, if the starting layer of the 123 unit cell as dictated by the substrate termination is di¤erent from the starting layer of the thermodynamically determined unit cell, the initial phase may be di¤erent from the one intended (i.e., non-unit cell nucleation). For instance, it has been suggested that the …rst layer is 133 instead of 123 [4]. As a result of the 123 composition being supplied, the remaining constituents will form precipitates. In these experiments, however, the substrate termination was not identi…ed.

6.3.2 Experimental observations

In chapter 5, we found that on SrO-$SrTiO_3$ the …rst monolayer of 123 is indeed unstable, leading to preferential precipitation. By tailoring the initial …lm stoichiometry with respect to the substrate termination, it should in principle be possible to prevent this precipitation. Having access to di¤erent substrate terminations allows us to study the substrate-…lm interaction process in more detail. Therefore, we deposited YBaCuO …lms with cation stoichiometries of 122, 123, 124 and 133 on both type

of substrates (5 shots at T_{sub} = 830±C, p_{O_2} = 15 Pa, and $d_{T\,i\,S}$ = 3:5 cm).[6] After deposition all …lms are immediately transferred to the AFM in order to minimize possible degradation e¤ects. In Fig. 6.6 the results are shown for submonolayer thick YBaCuO …lms (¼ 0:7 monolayer) on TiO_2-$SrTiO_3$. Precipitates are only observed in the case of 124, suggesting that one monolayer of 124 is unstable on TiO_2-terminated substrates.

We …nd that 122 and 133 …lms thicker than one monolayer cannot be grown precipitate-free, since these phases are unstable. Apparently, the monolayers of 122 or 133 are stabilized by the interaction with the substrate [33]. Taking the 123 stacking sequence as the only one allowed, we expect [37] the following stacking sequence on TiO_2-$SrTiO_3$:

::: ¡ TiO_2 ¡ BaO ¡ CuO_2 ¡ Y ¡ CuO_2 ¡ BaO ¡ CuO ¡ BaO ¡ ::: .

Following this stacking sequence 122, 123 and 133 can be grown on TiO_2 taking again BaO and CuO as the only possible terminating planes. On the other hand, 124 cannot be formed following this stacking sequence. Instead, the 123 phase is formed in combination with some CuO_x precipitates.

The results for SrO-$SrTiO_3$ are more di¢cult to interpret, since the exact stacking sequence is not clear in this case. In Fig. 6.7 the nucleation of 122, 123, 124 and 133 …lms deposited on SrO-terminated $SrTiO_3$ is shown. Again 122 and 133 can be formed, whereas 124 is unstable. In addition, now also 123 is not stable. This is in agreement with our previous observation in chapter 5 that precipitates are formed when depositing 123 on SrO-$SrTiO_3$. Clearly, the starting layer must be di¤erent compared to TiO_2-$SrTiO_3$. As discussed above, the most likely starting layer is CuO, resulting in a stacking sequence of

::: ¡ SrO ¡ CuO ¡ BaO ¡ CuO_2 ¡ Y ¡ CuO_2 ¡ BaO ¡ CuO ¡ BaO ¡ ::: .

However, this stacking sequence cannot explain any of our observations.

[6] All YBaCuO are deposited in the LAMBDA PHYSIK set-up from rotating, polycrystalline, high density stoichiometric targets (PRAXAIR, > 99.9% pure raw materials). The laser energy density J is set at 1.4 J/cm^2 (as measured at the target).

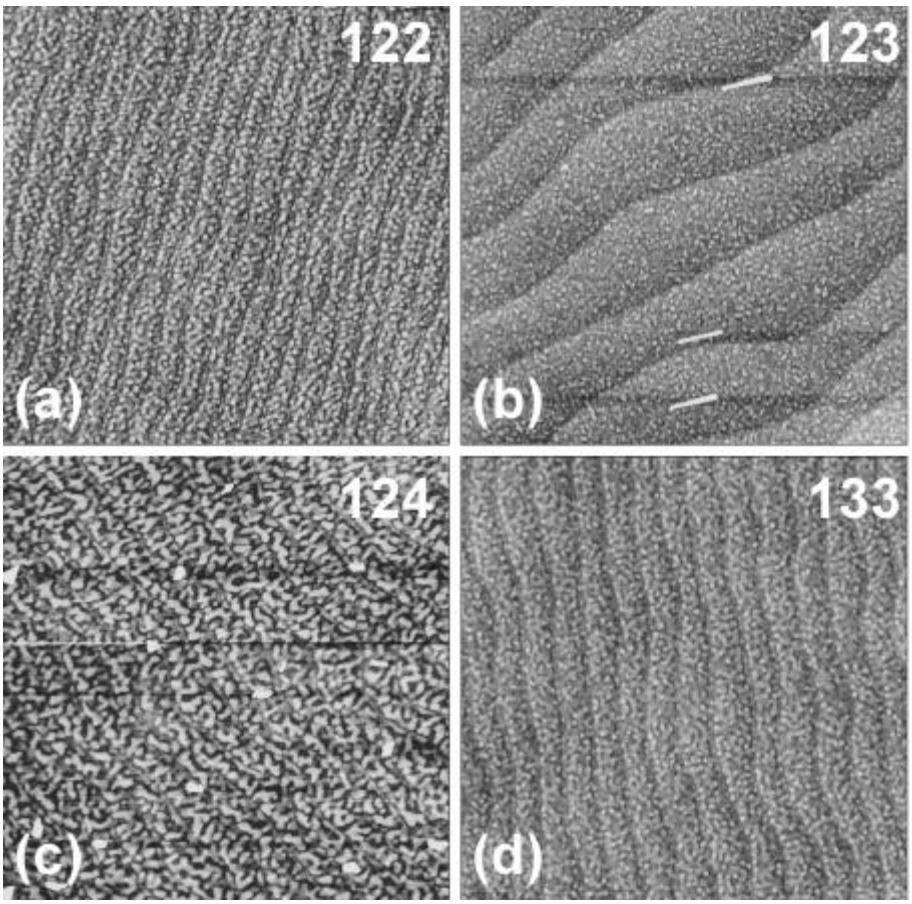

Figure 6.6: AFM height images (2.0 x 2.0 $^{1}m^{2}$) of submonolayer thick YBaCuO …lms deposited on TiO_2-terminated (100) $SrTiO_3$ substrates, supplying di¤erent cation stoichiometries: (a) 122, (b) 123, (c) 124, and (d) 133. Both the scan and image conditions (color table, contrast, etc.) are the same for all images; the height scale is 5 nm. Precipitates are only formed when supplying 124. The three elongated particles on the 123 …lm are an AFM artifact.

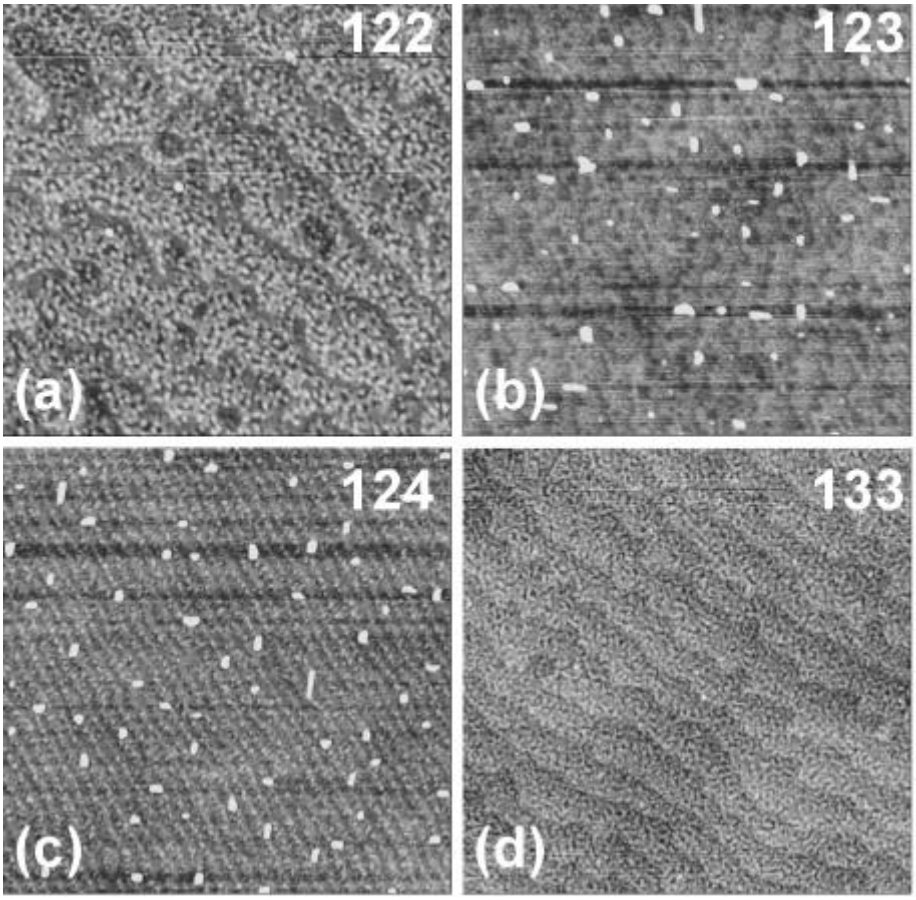

Figure 6.7: AFM height images (2.0 x 2.0 $^{1}m^{2}$) of submonolayer thick YBaCuO …lms deposited on SrO-terminated (100) $SrTiO_3$ substrates supplying di¤erent cation stoichiometries: (a) 122, (b) 123, (c) 124, and (d) 133. Both the scan and image conditions (color table, contrast, etc.) are the same for all images; the height scale is 5 nm. Preferential precipitation takes place in the 123 and 124 …lms.

6.3.3 Stacking sequence

In this section, we propose an alternative stacking sequence model, which is valid for both substrate terminations. It is based on the following assumptions:

1. The 123 stacking sequence (i.e. ... -BaO-CuO_2-Y-CuO_2-BaO-CuO- ...). is always followed.
2. The terminating plane of the 123 phase is either BaO [31, 32, 33] or CuO [34, 35, 36], but only one termination is possible on a given substrate. We assume that the terminating plane of the 123 phase is dictated by the substrate termination: on TiO_2-$SrTiO_3$ the terminating plane of 123 is CuO, whereas it is BaO on SrO-$SrTiO_3$.
3. The starting layer on TiO_2-$SrTiO_3$ is BaO, in agreement with experimental observations [37].
4. BaO can be formed as a separate phase, both directly on the substrate [12, 33, 40] and on top of the 123 phase [34].

The resulting stacking sequences are shown in Fig. 6.8. Let us consider the 133 stacking …rst. Surprisingly, on both substrates the starting layer is charge neutral BaO. In both situations, 133 may be viewed as a single 123 unit cell and an additional BaO layer. The starting BaO layer on the TiO_2 termination is part of the CuO-terminated 123 unit cell and an additional BaO layer forms on top, whereas BaO serves as a template layer for the BaO-terminated 123 unit cell on SrO-$SrTiO_3$.[7] Indeed, BaO has been successfully used as a bu¤er layer for 123 growth on SrO-$SrTiO_3$ [12]. It has also been pointed out [3] that an additional BaO layer is often present on top of the 123 structure due to its charge neutrality and low surface energy [40]. We note that the BaO layer on SrO may be shifted [41] by $(\frac{1}{2},\frac{1}{2},0)$ in order to continue the perovskite stacking of the substrate across the interface as closely as possible.
Now, supplying a monolayer with the 123 stoichiometry is exactly su¢cient to form the CuO-terminated 123 on TiO_2. However, it is not possible to form BaO-terminated 123 and a BaO template layer on SrO-$SrTiO_3$ (at least the 133 stoichiometry is needed). Then, the most likely scenario is that a 122 phase forms on SrO, leaving the remaining Cu to form CuO_x precipitates. In the same way it is also clear that 124 cannot be constructed: the additional CuO or CuO_2 layer does not match with CuO-terminated 123 on TiO_2-$SrTiO_3$, while BaO-terminated 123 cannot be formed since there is not enough Ba present to form the required BaO template layer …rst on SrO-$SrTiO_3$. Again, we expect that the precipitates are mainly CuO_x. This is in agreement with

[7] We note that the starting BaO layer must be followed by a di¤erent layer in 133 on SrO-$SrTiO_3$ and TiO_2-$SrTiO_3$, since otherwise the same stacking sequence applies on both substrates. In that case also 123 can be formed precipitate-free on both terminations, in contradiction with our experimental observations.

	TiO_2 termination	SrO termination
122	BaO CuO_2 Y CuO_2 BaO --------- TiO_2 SrO	BaO CuO_2 Y CuO_2 BaO --------- SrO TiO_2
123	CuO BaO CuO_2 Y CuO_2 BaO --------- TiO_2 SrO	122 + CuO_x
124	123 + CuO_x	122 + 2CuO_x
133	BaO CuO BaO CuO_2 Y CuO_2 BaO --------- TiO_2 SrO	BaO CuO_2 Y CuO_2 BaO CuO BaO --------- SrO TiO_2

Figure 6.8: Proposed stacking sequences of YBaCuO on TiO_2 and SrO-terminated $SrTiO_3$ substrates supplying the cation stoichiometries 122, 123, 124, and 133. The 122 structure is stabilized by the substrate, while 133 consist of a monolayer of BaO and either CuO-terminated 123 (on TiO_2-$SrTiO_3$) or BaO-terminated 123 (SrO-$SrTiO_3$).

what is usually observed [33, 42, 43]. Moreover, more precipitates are expected for 124 on SrO than for both 123 on SrO and 124 on TiO_2. Comparing the appropriate …gures, this indeed seems to be the case.
Finally, we stress that one should be careful in drawing conclusions concerning the stacking sequence from AFM measurements only. In any case, it is clear that the nucleation of YBaCuO depends strongly on both the termination of the substrate and the initial composition that is supplied. Hence, careful preparation as well as characterization of substrates down to the atomic scale are extremely important. In fact, many controversies in literature may be related to di¤erences in substrate terminations (SrO, TiO_2 or dual) or even poor substrate quality.

In summary, we can prevent preferential precipitation in submonolayer thick YBaCuO …lms by manipulating both the substrate termination and the initial …lm composition. On TiO_2-terminated surfaces the starting layer as dictated by the substrate and the starting layer of the 123 phase are the same, resulting in the absence of precipitates. On SrO-terminated substrates, precipitation of 123 may be prevented by depositing 122 or 133, prior to the actual 123 deposition.

6.4 E¤ect on threading dislocations

The original purpose of our investigation of the preferential precipitation in the …rst stages of growth was to …nd a way to prevent or manipulate the formation of threading dislocations in 123. Disappointingly, we …nd no relation between the dislocation density and substrate termination used. Although preferential precipitation is observed on SrO-terminated substrates, these precipitates do not result in an enhanced dislocation density. On the other hand, in chapter 5 we have shown that precipitates (in this case Y_2O_3) can induce dislocations. This paradox may be explained by the di¤erence between the interface region of thick 123 …lms and the very thin …lms discussed here. While in the former case there is a continuous supply of material, here the growth process is stopped, allowing the di¤using species much more time to reach a more stable con…guration. Apparently, in the thicker …lms the excess material is incorporated in the …lm, most likely in the form of point defects and stacking faults. This explanation also accounts for the absence of precipitates at the interface in our cross sectional Transmission Electron Microscope (TEM) studies reported in chapter 4.
To illustrate the dissolution of precipitates during continuous deposition, we deposited 123 …lms (15 shots, about 2 ML thick) on a TiO_2 and a SrO-terminated substrate. The substrate and …lm morphologies are shown in Fig. 6.9. In both …lms no sign of preferential precipitation is observed. Yet, a signi…cant di¤erence in precipitate density was shown for thin layers in the previous section. Therefore, there must be excess Cu in the 123 …lm on SrO-$SrTiO_3$. Indeed, there is a subtle di¤erence in the surface morphology of the two …lms, see Fig. 6.9(b,d). While the YBaCuO nicely reproduces the step structure of the TiO_2-terminated substrate, the vicinal steps on the SrO-terminated substrates can no longer be discerned. As will be shown in

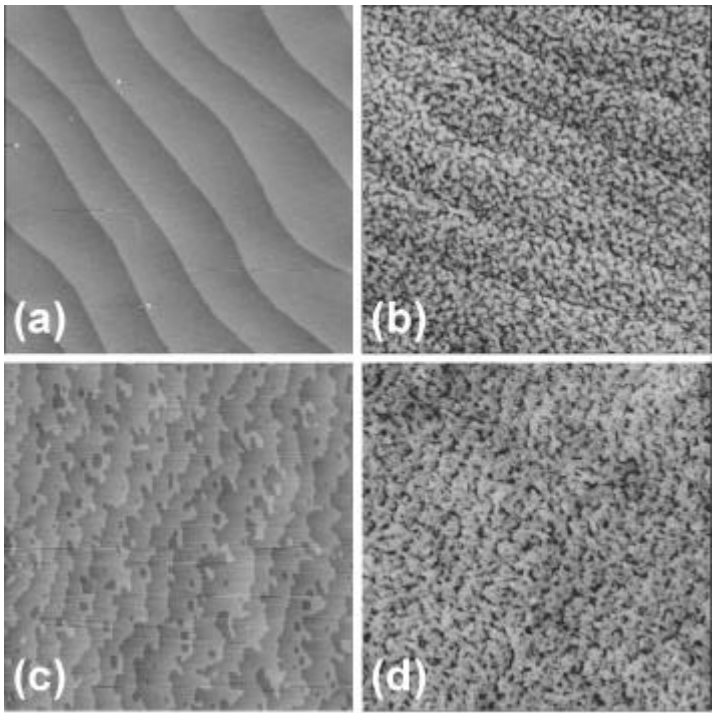

Figure 6.9: AFM height images (2.0 x 2.0 $^1m^2$) of (a) a TiO_2 and (c) a SrO-terminated (100) $SrTiO_3$ substrate used for the deposition of about 2 monolayers (ML) of 123: (b) 2 ML 123 on TiO_2-$SrTiO_3$ and (d) 2 ML 123 on SrO-$SrTiO_3$. The height scale is 5 nm for all images. Preferential precipitation is not observed for both …lms; the substrate structure is reproduced only on the TiO_2 termination.

chapter 7, the substrate structure is reproduced at least up to …lms of 3.5 ML thick on TiO_2-$SrTiO_3$, while the substrate steps could never be traced back on …lms over 1 ML thick on SrO-$SrTiO_3$. Possibly, the excess material forms planar defects that annihilate [34] the anti-phase boundaries which are known to nucleate at substrate steps [27].

At this point we can not decide on the exact mechanism by which dislocations naturally form during growth. Since we have now ruled out the role of preferential precipitation, it leaves us with the merging of slightly misaligned growth islands (island coalescence) as a source of dislocations. To shed more light on this mechanism, we will investigate 1-25 nm thick 123 …lms deposited on both type of substrates in detail by means of AFM and X-ray di¤raction in chapter 7.

6.5 Conclusions

We investigate preferential precipitation and the formation of threading dislocations in $YBa_2Cu_3O_{7\,i\,\pm}$ (123) …lms deposited on (100) $SrTiO_3$. Since the $SrTiO_3$ substrate o¤ers two possible terminations as a starting condition for …lm growth, we compare commercially available TiO_2-terminated substrates with SrO-terminated substrates produced by our newly developed ex-situ method.

We …nd that the …rst stages of hetero-epitaxial growth depend strongly on the substrate termination. In particular, precipitate-free 123 monolayers are only obtained on TiO_2-terminated $SrTiO_3$ substrates. Our results suggest that the terminating plane of the 123 phase on TiO_2-terminated $SrTiO_3$ is CuO, while BaO-terminated 123 forms on the SrO substrate termination. However, on both substrates the starting layer of the 123 phase is BaO. Therefore, when supplying a 123 cation stoichiometry, CuO-terminated 123 nucleates on TiO_2, whereas BaO-terminated 123 can not be formed on SrO-$SrTiO_3$. Instead, a 122 phase forms together with precipitates. However, by supplying a 133 cation composition, …rst a BaO template layer forms on which BaO-terminated 123 nucleates precipitate-free. Clearly, precipitation depends both on the substrate termination and the initial cation stoichiometry that is supplied.

Since arti…cially induced precipitates increase the dislocation density in our …lms, a precipitation process which occurs preferentially in the …rst monolayer would explain the high density of dislocations running from the interface to the $YBa_2Cu_3O_{7\,i\,\pm}$ …lm surface parallel to the c-axis. Yet, we …nd that the dislocation structure of the 123 …lm does not depend on the substrate termination. Apparently, preferential precipitation is not the mechanism of dislocation formation. It appears that precipitation of the 123 …lms on the SrO termination is characteristic for ultra-thin …lms up to approximately 1 monolayer in thickness. When growing thicker …lms, excess species are incorporated in the …lm as point and planar defects and may play an important role in the annihilation of anti-phase boundaries. This will be investigated extensively in the next chapter.

References

[1] B. Stäuble-Pümpin, V.C. Matijasevic, B. Ilge, J.E. Mooij, W.J.A.M. Peterse, P.M.L.O. Scholte, F. Tuinstra, H.J. Venvik, D.S. Wai, C. Træholt, J.G. Wen, and H.W. Zandbergen, Phys. Rev. B 52 (1995) 7064

[2] D.G. Schlom, D. Anselmetti, J.G. Bednorz, Ch. Gerber, and J. Mannhart, J. Cryst. Growth 137 (1994) 259

[3] J.G. Wen, T. Morishita, N. Koshizuka, C. Traeholt, and H.W. Zandbergen, Appl. Phys. Lett. 66 (1995) 1830

[4] V.C. Matijasevic, B. Ilge, B. Stäuble-Pümpin, G. Rietveld, F. Tuinstra, and J.E. Mooij, Phys. Rev. Lett. 76 (1996) 4765

[5] M. Kawasaki, K. Takahashi, T. Maeda, R. Tsuchiya, M. Shinohara, O. Ishiyama, T. Yonezawa, M. Yoshimoto, and H. Koinuma, Science 266 (1994) 1540

[6] T. Nakamura, H. Inada, and M. Ilyama, Jpn. J. Appl. Phys. 36 (1997) 90

[7] A. Ikeda, T. Nishimura, T. Morishita, Y. Kido, Surf. Sci. 433-435 (1999) 520

[8] T. Nishimura, A. Ikeda, H. Namba, T. Morishita, and Y. Kido, Surf. Sci. 421 (1999) 237

[9] K. Iwahori, S. Watanabe, T. Komeda, M. Kawai, A. Saito, Y. Kuwahara, and M. Aono, Jpn. J. Appl. Phys. 38 (1999) 3946

[10] G. Koster, B.L. Kropman, G.J.H.M. Rijnders, D.H.A. Blank, and H. Rogalla, Appl. Phys. Lett. 73 (1998) 2920

[11] H. Nishikawa, M. Kanai, and T. Kawai, J. Cryst. Growth 179 (1997) 467

[12] R. Tsuchiya, M. Kawasaki, H. Kubota, J. Nishino, H. Sato, H. Akoh, and H. Koinuma, Appl. Phys. Lett. 71 (1997) 1570

[13] H. Tanaka, H. Tabata, and T. Kawai, Thin Solid …lms 342 (1999) 4

[14] S. Gonda, H. Nagata, M. Kawasaki, M. Yoshimoto, and H. Koinuma, Physica C 216 (1993) 160

[15] M. Yoshimoto, T. Maeda, K. Shimozono, H. Koinuma, M. Shinohara, Kazuhiro Endo, Appl. Phys. Lett. 65 (1994) 3197

[16] R. Sum, H.P. Lang, and H.J. Günterodt, Physica C 242 (1995) 174

[17] G. Koster, B.L. Kropman, G.J.H.M. Rijnders, D.H.A. Blank, and H. Rogalla, Mat. Sci. Eng. B56 (1998) 209

[18] J. Fompeyrine, R. Berger, H.P. Lang, J. Perret, E. Mächler, Ch. Gerber, and J.-P. Locquet, Appl. Phys. Lett. 72 (1998) 1697

[19] M. Komiyama and M. Gu, Appl. Surf. Sci. 120 (1997) 125

[20] S.P. Chen, J. Mater. Res. 13 (1998) 1848

[21] J. Prade, U. Schröder, W. Kress, F.W. de Wette, and A.D. Kulkarni, J. Phys.: Condens. Matter 5 (1993) 1

[22] S. Dorfman, D. Fuks, and E. Kotomin, Thin Solid Films 318 (1998) 65

[23] Z.-Q. Li, J.-L. Zhu, C.Q. Wu, Z. Tang, and Y. Kawazoe, Phys. Rev. B 58 (1998) 8075

[24] J. Padilla, and D. Vanderbilt, Surf. Sci. 418 (1998) 64

[25] G. Charlton, S. Brennan, C.A. Muryn, R. McGrath, D. Norman, T.S. Turner, and G. Thornton, Surf. Sci. 457 (2000) L376

[26] K. Szot and W. Speier, Phys. Rev. B 60 (1999) 5909

[27] T. Haage, J. Zegenhagen, J.Q. Li, H.-U. Habermeier, M. Cardona, Ch. Jooss, R. Warthmann, A. Forkl, and H. Kronmüller, Phys. Rev. B 56 (1997) 8404

[28] M. Kubo, Y. Oumi, R. Miura, A. Stirling, A. Miyamoto, M. Kawasaki, M. Yoshimoto, and H. Koinuma, Phys. Rev. B 56 (1997) 13535

[29] T. Nakamura, H. Inada, and M. Iiyama, Appl. Surf. Sci. 130-132 (1998) 576

[30] T. Terashima, Y. Bando, K. Iijima, K. Yamamoto, K. Hirata, K. Hayashi, K. Kamigaki and H. Terauchi, Phys. Rev. Lett. 65 (1990) 2684

[31] M. Kawasaki and M. Nantoh, Mater. Res. Bull. XIX (1994) 33

[32] G. Frank, Ch. Ziegler, and W. Gõpel, Phys. Rev. B 43 (1991) 2828

[33] J.-P. Locquet and E. Mächler, Mater. Res. Bull. XIX (1994) 39

[34] K.-i. Shimura, Y. Daitoh, Y. Yano, T. Terashima, Y. Bando, Yuji Matsuda, and S. Komiyama, Physica C 228 (1994) 91

[35] S.J. Pennycook, M.F. Chisholm, D.E. Jesson, R. Feenstra, S. Zhu, X.Y. Zheng, and D.J. Lowndes, Physica C 202 (1992) 1

[36] S. Tanaka, T. Nakamura, M. Iiyama, N. Yoshida, S. Takano, F. Shoji, and K. Oura, Appl. Phys. Lett. 59 (1991) 3637; S. Tanaka, T. Nakamura, H. Tokuda, and M. Iiyama, Appl. Phys. Lett. 62 (1993) 3040

[37] J.C. Wen, C. Traeholt, and H.W. Zandbergen, Physica C 205 (1993) 354

[38] M. Kubo, Y. Oumi, R. Miura, A. Stirling, A. Miyamoto, M. Kawasaki, M. Yoshimoto, and H. Koinuma, J. Chem. Phys. 19 (1998) 8601

[39] R. Ramesh, A. Inam, D.M. Hwang, T.S. Ravi, T. Sands, X.X. Xi, X.D. Wu, Q. Li, T. Venkatesan, and R. Kilaas, J. Mater. Res. 6 (1991) 2264

[40] M. Matsubara, T. Morishita, and I. Hirabayashi, Appl. Phys. Lett. 64 (1994) 1868

[41] G. Koster, G. Rijnders, D.H.A. Blank, and H. Rogalla, Physica C 339, 215 (2000)

[42] K. Hirata, F. Baudenbacher and H. Kinder, Physica C 214 (1993) 272

[43] N. Kanda, M. Kawasaki, T. Kitajima, and H. Koinuma, Phys. Rev. B 56 (1997) 8419

Chapter 7

The …rst stages of hetero-epitaxial growth: coherent islanding

An extensive X-ray di¤raction and atomic force microscope study on the e¤ects of the two (100) $SrTiO_3$ substrate terminations on the nucleation, growth and defect formation in $YBa_2Cu_3O_{7\,i\,\pm}$ …lms is performed. In addition to the di¤erences in nucleation observed in chapter 6, we …nd: (i) pseudomorphic 2D growth up to a critical thickness $t_{c;coh}$ = 7:3 and 19 nm on the SrO and TiO_2-termination, respectively, and (ii) coherent 3D islands (i.e., free of mis…t dislocations) at $t > t_{c;coh}$, which relieve part of the mis…t strain. These results clearly illustrate the importance of interface energy in hetero-epitaxial growth. Furthermore, in-plane XRD measurements reveal a characteristic two components line shape. The broad component originates either from a small coherence length L_k (SrO) or a large tilt angle $\mathbb{R}_!$ (TiO_2), which appears to be correlated to the presence of o¤-stoichiometries and anti-phase boundaries, respectively. The narrow component results from a mosaicity limited in magnitude by the substrate. It is attenuated by the introduction of mis…t dislocations at later growth stages ($t_{c;coh} < 25$ nm $< t_{c;mis}$). Non-mis…t relieving threading dislocations, which are responsible for the high superconducting critical currents, are introduced at the edges of the coherent growth islands. Thicker …lms (t À 25 nm) exhibit identical surface morphologies and dislocation structures, showing that eventually the same microstructure evolves, irrespective of the substrate termination.[1]

[1]The central part of this chapter is based on the paper by J.M. Huijbregtse, B. Dam, B.J. Kooi, A. Mendoza, J.H. Rector, J.Th.M. de Hosson, and R. Griessen, to be submitted to Phys. Rev. B

7.1 Introduction

Fundamental understanding of complex oxide hetero-epitaxy requires detailed experimental and theoretical investigations of the interfacial properties. To simplify the problem from an experimental point of view, atomically ‡at single-terminated ABO_3 perovskite substrates have been developed [1]. Preparing such substrates in either of the two terminations (AO or BO_2), in principle allows for a systematic study of substrate-termination-induced e¤ects on hetero-epitaxial …lm growth. Yet, in literature there are only a few experimental observations clearly pointing to the importance of the nature of the substrate termination. On $SrTiO_3$ substrates for example, it was recently found that the epitaxial relationship with Pt …lms depends critically on the substrate termination [2]. This e¤ect was attributed to a di¤erence in bonding across the interface. Furthermore, it was shown that (100) $SrTiO_3$ …lms can only be grown in a layer-by-layer way on (100) $LaAlO_3$ substrates prepared in the AlO_2-termination due to charge compatibility between the substrate terminating plane (AlO_2^+) and the starting atomic layer of the …lm (TiO_2^j for a trivalent Ti-ion) [3]. These e¤ects con…rm that the interface structure results from a delicate interfacial energy minimization, which was already illustrated in 1994 for the $BaTiO_3$/(100)MgO hetero-epitaxial system [4]. Combining all results, it becomes clear that, in addition to mis…t energy, the substrate-…lm interaction has to be taken into account in any realistic theoretical consideration of hetero-epitaxial growth.

The concept of substrate-…lm interaction is also interesting from a technological point of view. In high-T_c superconducting $La_{2-x}Sr_xCuO_4$ thin …lms for example, it has been shown that the transition temperature T_c can be doubled by making use of the substrate-induced in-plane strain [5]. However, this e¤ect is limited to small …lm thicknesses. At large thicknesses strain relaxation occurs [6] either by introducing mis…t dislocations above a critical thickness $t_{c;mis}$ or by the formation of coherent 3D islands at a thickness $t_{c;coh}$. To take full advantage of hetero-epitaxial strain e¤ects on T_c in …lms, the so-called pseudomorphic growth regime has to be extended. During pseudomorphic growth, the substrate-…lm interaction energy overcompensates the elastic strain energy induced by the lattice mismatch and the …lm adopts the lattice constant of the substrate. Therefore, controlling the substrate-…lm interaction energy in principle allows for a T_c adjustment.

The substrate termination o¤ers an opportunity for manipulating the interaction between the substrate and the …lm at a …xed hetero-epitaxial strain condition. In chapter 6, we have shown that (100) $SrTiO_3$ substrates can indeed be prepared in both terminations. Moreover, by making use of the correct termination, preferential precipitation during the …rst monolayer of $YBa_2Cu_3O_{7-\pm}$ could be fully suppressed. This e¤ect again illustrates that the nature of the substrate termination is an important parameter in the hetero-epitaxial growth of complex oxides.

In the present chapter, we focus our attention to the following stages of growth, including the formation of defects. Combining atomic force microscopy and X-ray di¤raction it becomes clear that the in‡uence of the substrate termination is not restricted to the …rst few atomic layers only. The interaction between the $YBa_2Cu_3O_{7-\pm}$ …lm and the TiO_2-termination is signi…cantly stronger than the interaction with the

SrO-termination. As a result, the overlayer maintains the tetragonal $YBa_2Cu_3O_{6+x}$ crystal structure upon cooling down up to a critical …lm thickness $t_{c;coh}$ of 19 and 7.3 nm for the TiO_2 and SrO-termination, respectively. The pseudomorphic layer exhibits a kind of layer-by-layer growth, while island growth is observed above $t_{c;coh}$, con…rming the well-known Stranski-Krastanow growth mode: 3D islands on top of a thin wetting layer. Surprisingly, the islanding is a coherent process, as mis…t dislocations are introduced at later growth stages ($t_{c;coh} < 25$ nm $< t_{c;mis}$). In addition, we present evidence that the coherent island structure favors the subsequent formation of (non-mis…t relieving) threading dislocations, which are responsible for the high superconducting critical currents in these …lms. At the edges of the coherent islands strain is highly concentrated, which results in a local lowering of the activation energy for dislocation formation. Hence, the threading dislocation structure adopts the self-assembled island structure when these islands merge. Finally, thick …lms (t À 25 nm) exhibit identical properties, independently of the substrate termination.

7.2 AFM and XRD observations

Thin …lms of $YBa_2Cu_3O_{7\,i\,\pm}$ are deposited on SrO and TiO_2-terminated (100) $SrTiO_3$ substrates with a small vicinal angle (typically 0.1±). The untreated substrates are purchased from various suppliers in order to exclude preparation dependent e¤ects. The SrO-termination is obtained following the procedure presented in the chapter 6, whereas TiO_2-terminated substrates are produced according to the modi…ed Kawasaki [7] procedure of Koster et al. [8]. Both the thickness t of the …lms and the substrate temperature T_{sub} are varied in order to investigate the temperature dependence of $YBa_2Cu_3O_{7\,i\,\pm}$ /(100)$SrTiO_3$ hetero-epitaxy. We use substrate heater temperatures T_{sub} = 770, 805 and 850±C, while t is varied from 0.8 nm up to 24.3 nm.[2] For comparison, the results of some additional thick (t À 25 nm) …lms are incorporated.

7.2.1 Surface morphology

In order to minimize possible degradation e¤ects, all …lms are immediately transferred to the atomic force microscope (AFM) after deposition, where we image the surface morphology in the tapping mode. The results of these measurements for …lms deposited at T_{sub} = 805±C with a thickness 0:8 < t < 24:3 nm are shown in Fig. 7.1 and 7.2, comparing both terminations. We note that identical scan and image conditions (contrast, color table, etc.) have been used in these …gures.

We distinguish three main stages in the hetero-epitaxial growth of $YBa_2Cu_3O_{7\,i\,\pm}$ on (100) $SrTiO_3$: a nucleation stage (t . 1:2 nm), a 2D-growth regime (1.2 nm . t < t_c) and, …nally, a 3D-growth regime (t > t_c). The numerical value of the thickness t_c is determined by the substrate termination. In the following, we will shortly discuss these three growth regimes.

[2] All …lms are deposited in the LAMBDA PHYSIK set-up at p_{O_2} = 15 Pa, $d_{T\,i\,S}$ = 3:5 cm and J = 1:4 J/cm^2 (as measured at the target).

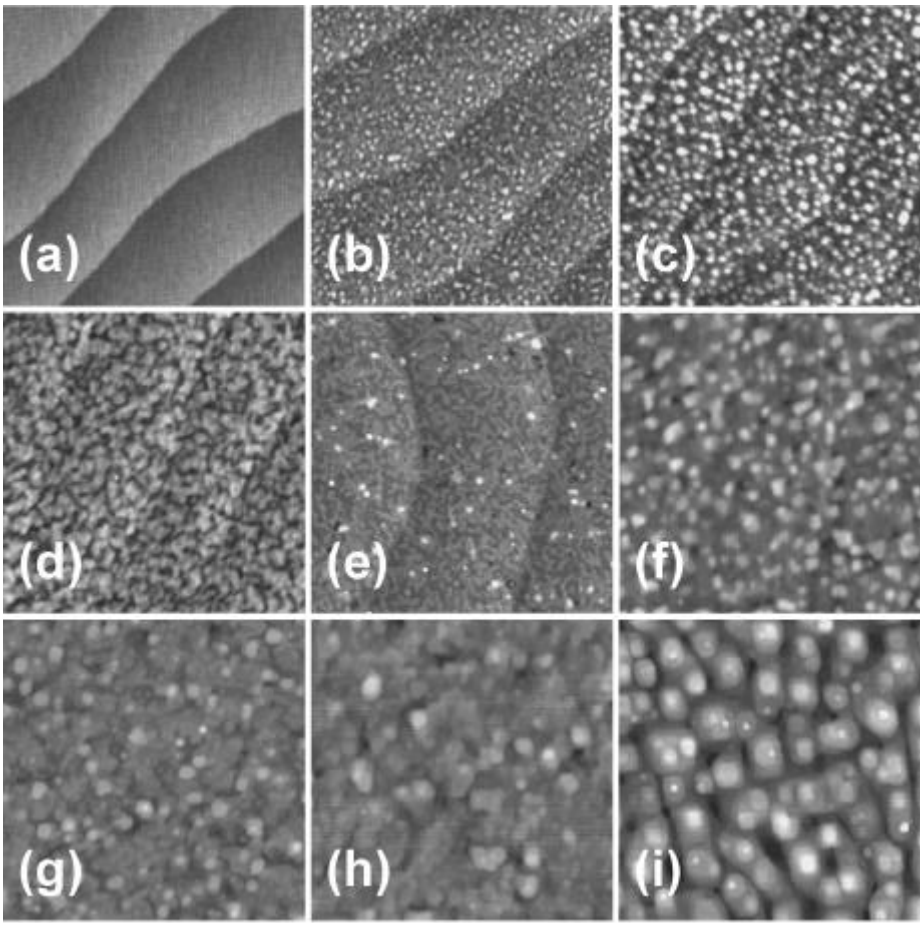

Figure 7.1: 1.0 £ 1.0 $^{1}m^{2}$ AFM height images of $YBa_2Cu_3O_{7\,i\,\pm}$ …lms deposited at 805$^{\pm}$C on TiO_2-terminated (100) $SrTiO_3$ substrates as a function of …lm thickness t: (a) typical bare substrate and (b) t = 0:8 nm, (c) 1.6 nm, (d) 2.4 nm, (e) 3.2 nm, (f) 4.1 nm, (g) 8.1 nm, (h) 16.2 nm, and (i) 24.3 nm. The height scales are: (a ¡ e) 5.0 nm, (f) 7.5 nm, (g) 15.0 nm, (h) 20.0 nm, and (i) 22.5 nm; identical image conditions (contrast, color table, etc.) are used. Note that the substrate structure is initially reproduced by the …lm.

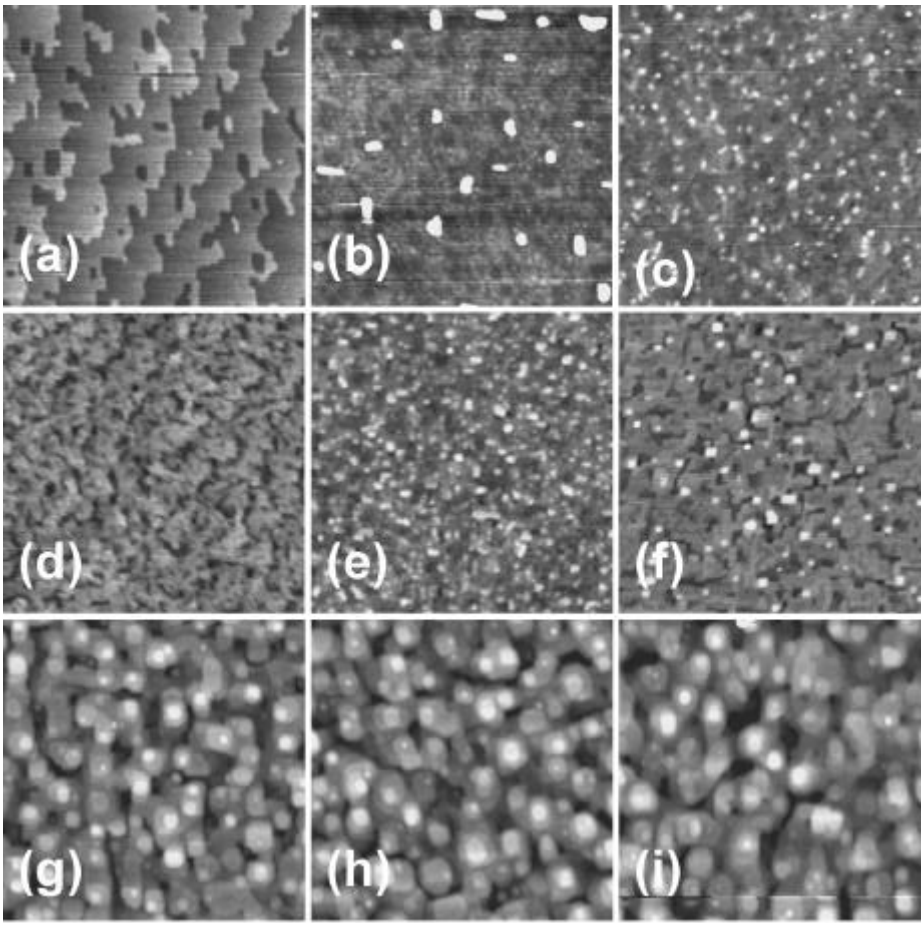

Figure 7.2: 1.0 £ 1.0 $^{1}m^{2}$ AFM height images of $YBa_2Cu_3O_{7\,i\,\pm}$ …lms deposited at 805±C on SrO-terminated (100) $SrTiO_3$ substrates as a function of …lm thickness t: (a) typical bare substrate and (b) t = 0:8 nm, (c) 1.6 nm, (d) 2.4 nm, (e) 3.2 nm, (f) 4.1 nm, (g) 8.1 nm, (h) 11.3 nm, and (i) 16.2 nm. The height scales are: (a ¡ e) 5.0 nm, (f) 7.5 nm, (g,h) 15.0 nm, and (i) 20.0 nm; identical image conditions (contrast, color table, etc.) are used. Preferential precipitation takes place only for submonolayer thin …lms.

Nucleation stage

For t . 1:2 nm the …lms nucleate precipitate-free on the TiO_2-termination, while a high density of precipitates forms on the SrO-termination. As discussed extensively in chapter 6, this preferential precipitation originates from non-unit cell nucleation [9] on SrO-$SrTiO_3$.

2D growth regime

Surprisingly, when growing slightly thicker …lms (t > 1:2 nm) the precipitates are no longer observed. As the o¤-stoichiometry is still present, it must be incorporated in the form of defects. This assumption looks reasonable, since on the TiO_2-termination all vicinal steps are initially reproduced by the $YBa_2Cu_3O_{7\,i\,\pm}$ (i.e., at these steps anti-phase boundaries are created [10]), while on the SrO-termination the steps can no longer be discerned. Apparently, the o¤-stoichiometry is used to accommodate the steps, leading to the immediate annihilation of anti-phase boundaries. On both termination, however, growth proceeds in a 2D layer-by-layer mode, as follows from the relatively small surface roughness.

3D growth regime

Irrespective of the substrate termination, the initially ‡at, almost featureless 2D surface morphology suddenly changes into the islands structure that is well-known from thicker …lms at $t = t_c$. Two interesting phenomena occur: (i) the morphological transition takes place much earlier in the growth process on the SrO-termination (t_c^{SrO} = 7:3 nm) compared to the TiO_2-termination ($t_c^{TiO_2}$ = 19 nm) and (ii) a large part of the initial 2D morphology is rearranged into 3D islands, indicating that it is a metastable con…guration.

In the remaining part of this chapter we will not concentrate on the nucleation stage (i) any longer. Instead, we investigate the following growth stages (ii) and (iii) in more detail. We are especially interested in the formation of defects such as anti-phase boundaries, which may act as strong pinning sites for vortices in these materials [11, 12, 13]. In that sense, also the transition to the 3D island morphology at $t > t_c$ is important. As shown in chapter 3 and 4, …lms exhibiting this speci…c surface morphology contain a high density of threading dislocations and have extremely high critical currents.

7.2.2 Crystal structure

The crystal structure of the …lms is investigated by X-ray di¤raction (XRD) in a 10 kW rotating-anode di¤ractometer, employing $CuK_{®}$ radiation (¸ = 1:541871 Å) in line focus. This two circle-di¤ractometer is equipped with secondary optics, consisting of Soller slits only. First, we determine the …lm thickness t from the Laue …nite size oscillations around the (001)-re‡ection [14, 15, 16]. In ultra thin …lms, the oscillations are usually di¢cult to observe. For those …lms, we estimate t by extrapolating the

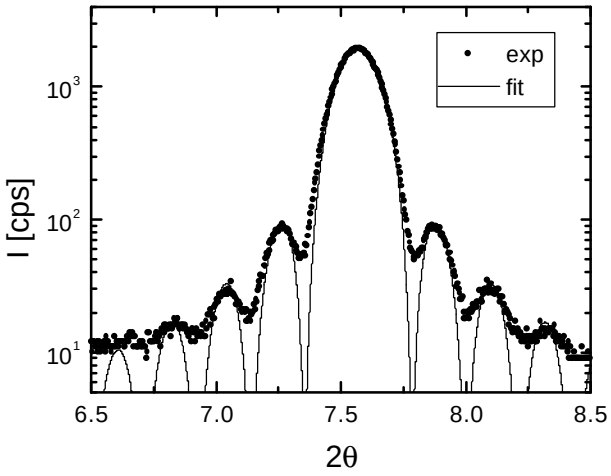

Figure 7.3: XRD measurement around the (001)-re‡ection in the µ ¡ 2µ geometry on a $YBa_2Cu_3O_{7¡±}$ …lm deposited on SrO-terminated (100) $SrTiO_3$. The line corresponds to a …t using the Laue function Eq. (7.1), yielding a …lm thickness t = 41:2 nm.

thickness, measured on thicker …lms deposited under identical deposition conditions, to the amount of material deposited (i.e., the number of laser shots used).
An example of Laue oscillations around the Bragg (001)-re‡ection is shown in Fig. 7.3 for a 41.2 nm thick …lm. The oscillations are …tted with the Laue function [17],

$$I(\mu) = I_0 \frac{\sin^2[N¼(\mu ¡ \mu_1)=\tan\mu_1]}{\sin^2[¼(\mu ¡ \mu_1)=\tan\mu_1]}, \qquad (7.1)$$

only. In this expression I_0 is an intensity scale, N is the number of contributing crystal planes (i.e., t = Nc, where c is the c-axis lattice constant), µ is the scattering angle and $2\mu_1$ is the position of the (001) Bragg peak (typically, μ_1 ¼ 3:75±). In this model no roughness at the interfaces is assumed. As follows from Fig. 7.3, the model explains the frequency and the intensity drop of the maxima well, while the minima are not reproduced. Including the measured AFM surface roughness almost completely accounts for the minima, showing that the interface roughness is extremely small. The average …lm thickness, however, does not change when taking the surface roughness into account. Veri…cation of the …lm thickness by means of glancing incidence X-ray re‡ectivity measurements yields …lm thicknesses that di¤er less than 2%, showing that (001)-Bragg specular scattering can be used to accurately determine …lm thicknesses for this system.

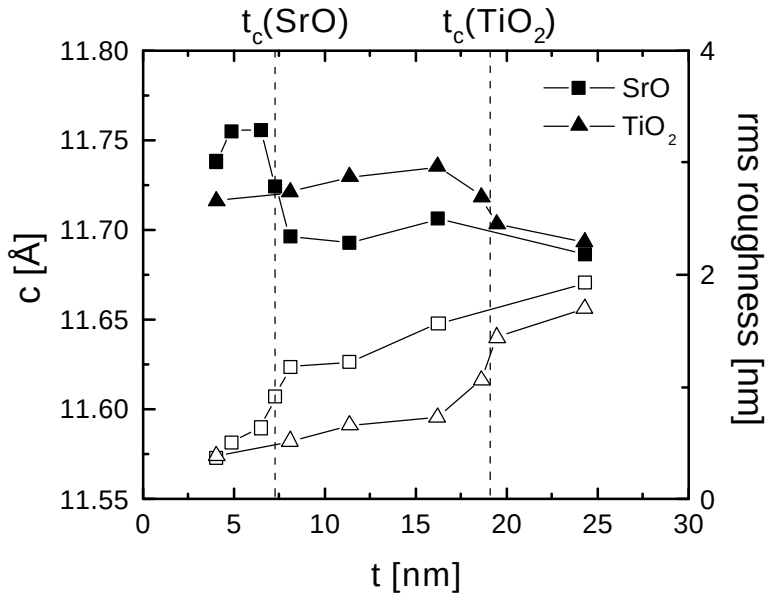

Figure 7.4: C-axis length (solid symbols) of $YBa_2Cu_3O_{7-\delta}$ …lms deposited at T_{sub} = 805±C on SrO and TiO_2-terminated (100) $SrTiO_3$ as a function of …lm thickness t. The drop in c is accompanied by a morphological transition, as indicated by the AFM root-means-square roughness (open symbols). The transition thickness t_c shifts to higher values when depositing …lms at a lower substrate temperature.

Next, we measured the (005)-re‡ection as a function of …lm thickness and substrate temperature on both type of substrates in the µ ¡ 2µ geometry. From the position $2\mu_5$ of the Bragg peak the c-axis value is calculated, using Bragg's law: $c = 5\lambda/(2\sin\mu_5)$. In Fig. 7.4 the measured c-axis is shown as a function of …lm thickness for both terminations at the intermediate substrate temperature of 805±C. Surprisingly, on both terminations we …nd initially an enlarged c-axis (typically, 11.72 to 11.75 Å), which suddenly drops to a more bulk like value (c = 11:6772 Å [18]) at $t > t_c$. Actually, during pseudomorphic growth one would expect a compressed c-axis in ultra thin …lms: initially they grow strained and the larger substrate lattice constant (a = 3:905 Å) should cause Poisson-contraction of the c-axis.

How can we explain the enlarged c-axis? As it is well known that the …lms grow in the tetragonal phase (a = 3:8578 Å; c = 11:8391 Å [18]), Fig. 7.4 implies that the transformation into the orthorhombic form upon cooling down only occurs above t_c: Due to strain, oxygen incorporation is di¢cult and thinner overlayers remain tetragonal $YBa_2Cu_3O_{6+x}$. Indeed, this e¤ect appears to be characteristic for ultrathin

…lms [15, 19, 20]. As a result of the larger lattice constant of the substrate, the c-axis of the tetragonal phase is in fact contracted for $t < t_c$, indicating tensile strain.
These structural features are coupled to the morphological transition of Fig. 7.1 and 7.2 (as indicated by the AFM roughness in Fig. 7.4) and we conclude that pseudomorphic growth occurs below t_c. Apparently, orthorhombic …lms only form upon cooling down …lms with a thickness $t > t_c$, indicating that during growth some kind of strain relaxation process must have taken place at $t = t_c$. Furthermore, we …nd that t_c depends on the substrate temperature used. It shifts to larger values for lower temperatures (from 6.5 nm for $T_{sub} = 850^{\pm}C$ to 8.0 nm for $T_{sub} = 770^{\pm}C$ on the SrO-termination), indicating that the 2D-3D transition is kinetically determined.
These results show the importance of controlling the substrate termination once more. A good control over the substrate termination is essential in achieving a highly reproducible thin …lm deposition process. In fact, many of the controversies in literature may well be related to substrate termination e¤ects. In particular, the lower T_c of ultra thin …lms ($t < t_c$) on the SrO-termination compared to …lms on TiO_2-$SrTiO_3$ [21] may be explained by the size of the tetragonal distortion reported above. As the charge carrier density is related to the oxygen content, tetragonally distorted …lms are underdoped, causing a lowering of T_c. Disappointingly, the fact that the structural phase transition to the orthorhombic structure during cooling down is inhibited for …lms grown in the pseudomorphic regime ($t < t_c$) makes $YBa_2Cu_3O_{7\,i\,\pm}$ / (100) $SrTiO_3$ an unsuitable system to investigate the e¤ect of hetero-epitaxial strain on T_c [5]. The opposite e¤ects of doping and epitaxial strain are di¢cult to separate. Indeed, a T_c-enhancement was not detected in ultra thin sputtered $YBa_2Cu_3O_{7\,i\,\pm}$ …lms [22].

7.2.3 In-plane ordering

To follow the in-plane ordering of the …lms, rocking curves (! scans) were taken around the (005)-re‡ection as a function of …lm thickness. The results are presented in Fig. 7.5 for both terminations. The (005)-rocking curves of $YBa_2Cu_3O_{7\,i\,\pm}$ on both SrO and TiO_2-terminated (100) $SrTiO_3$ substrates initially exhibit two components: a narrow (specular) resolution-limited component and a broader (di¤use) component. The occurrence of two-components in rocking curves are characteristic for high-quality, hetero-epitaxial systems. They are reported in a great diversity of such systems, among which are: ErAs/[001]GaAs [23], Nb/[11$\bar{2}$0]Al_2O_3 [24] and AlN/c-Al_2O_3 [25]. Also in submicron thick $YBa_2Cu_3O_{7\,i\,\pm}$ …lms on (100) $SrTiO_3$ a resolution-limited component was observed [26, 27, 28] although so far only in the (001) and (002)-re‡ection.
Miceli et al. [29] explained the two components by considering a thin hetero-epitaxial …lm as spatially separated mosaic blocks on a substrate. Unlike in a conventional mosaic crystal, the rotational disorder is now bounded in magnitude by the substrate due to the substrate-…lm interaction. For a large number of these crystallites the lattice planes are parallel and in phase (as dictated by the substrate). Hence, the X-rays are scattered coherently, giving rise to the narrow component. On the other hand, the broad component re‡ects the local order within a mosaic block.

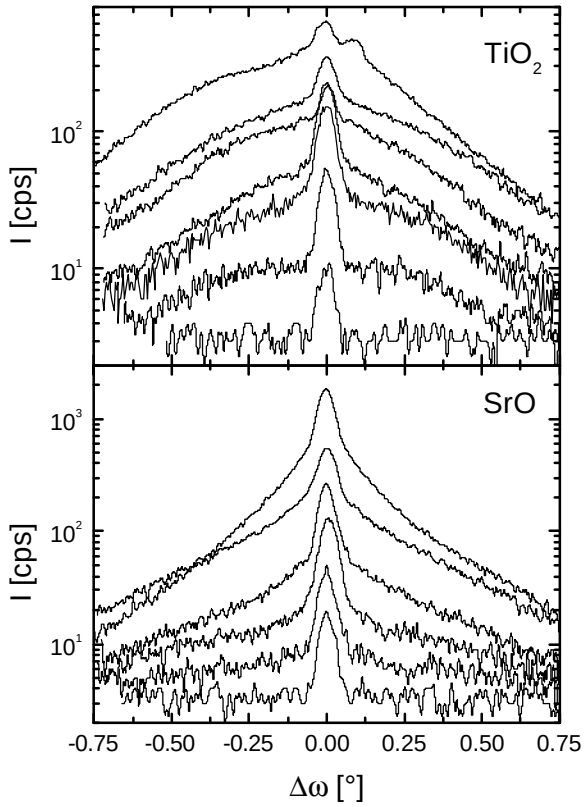

Figure 7.5: (005)-Rocking curves (! scans) of $YBa_2Cu_3O_{7\,i\,\pm}$ …lms deposited at 805±C as a function of …lm thickness t and (100) $SrTiO_3$ termination: (lower panel) t = 3:2, 4.1, 6.5, 8.1, 16.2, and 24.3 nm on SrO and (top panel) t = 3:2, 4.1, 8.1, 11.3, 16.2, 18.6, and 24.3 on TiO_2; t increases from bottom to top.

Focussing on this broad component, we …nd that its shape is in‡uenced by the substrate termination. On the TiO_2-termination a Gaussian pro…le is found, as opposed to a Lorentzian form on the SrO-termination. Generally, the broadening of symmetric (00l)-re‡ections in !-scans is in‡uenced by tilt (rotation around an axis lying along the substrate surface) and small coherence length parallel to the substrate surface [30]. Both an increasing tilt angle $\Theta_!$ or a decreasing in-plane correlation length L_k cause broadening of di¤raction peaks. A Gaussian peak shape is usually associated with large $\Theta_!$, being the main cause of peak broadening, whereas a Lorentzian pro…le is related to a small L_k.
In Fig. 7.6(a) the full width at half maximum (FWHM) of the broad and narrow components are plotted as a function of the …lm thickness. Here, the FWHM was

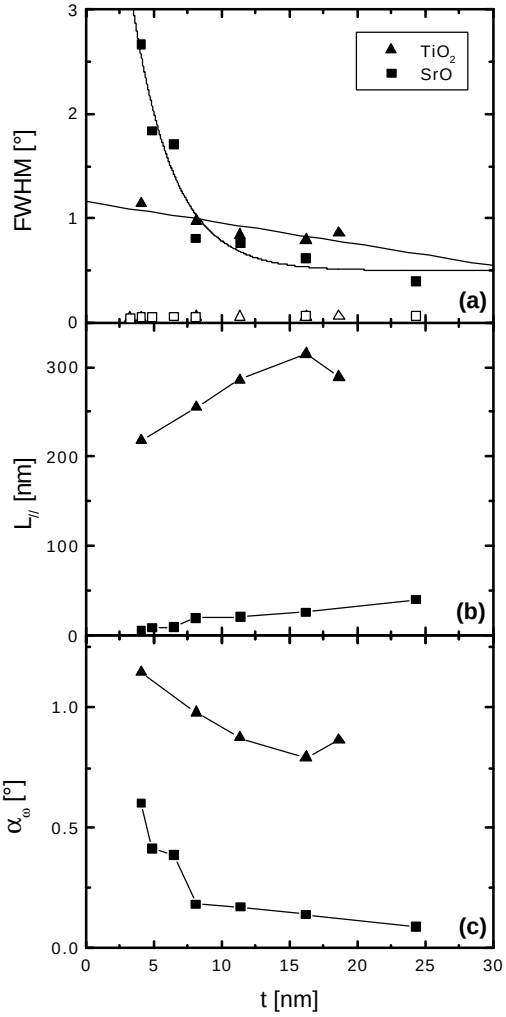

Figure 7.6: Characteristic parameters for the (005)-rocking curves of $YBa_2Cu_3O_{7-\delta}$ films deposited at 805°C on TiO_2 and SrO-terminated (100) $SrTiO_3$ as a function of film thickness t: (a) measured full width at half maximum (FWHM) of the broad (solid symbols) and narrow (open symbols) components; the FWHM of the narrow component is governed by the instrumental resolution (≈ 0.04°), while the FWHM of the broad component decreases exponentially (linear) with t on SrO (TiO_2), as indicated by the solid lines. Using the measured FWHM of the broad component, we calculate: (b) the in-plane correlation length L_k and (c) the tilt angle ω_0 as a function of t, indicating that peak broadening in films on the SrO-termination is due to a small L_k (≈ 25 nm), while on TiO_2-$SrTiO_3$ it is due to a large ω_0 (≈ 1°).

determined by …tting the appropriate two component peak function. It follows that the FWHM of the narrow component is mainly determined by the instrumental resolution.[3] On the other hand, the FWHM of the broad component decreases rapidly with …lm thickness. A linear decrease is found on the TiO_2-termination, while an exponential decrease is observed on SrO-$SrTiO_3$.
Finally, we investigated the temperature dependence of the two component rocking curves on the SrO-termination by depositing additional …lms at T_{sub} = 770 and 850±C. As follows from Fig. 7.7(a), the FWHM of the broad component decays exponentially to 0.5± for all temperatures, whereas the FWHM of the narrow component is close to the instrumental resolution. In the next section, we will discuss these results more thoroughly.

7.3 Nucleation, growth and dislocation formation

In this section, we give a semi-quantitative analysis of the two component rocking curves. To reveal the structural origin of the di¤use and specular component, we combine the AFM and XRD data. Subsequently, the details of the $YBa_2Cu_3O_{7\,¡\,±}$ growth mechanism, including the strain relaxation processes, are discussed. Finally, we identify the mechanism by which threading dislocations, the dominant strong pinning sites for vortices, are formed during this growth mode.

7.3.1 Correlating the two component rocking curves to the defect structure

Here, we concentrate on the origin of the two components in the rocking curves and their dependence on the substrate termination. First, we relate the broad component to the initial stages of growth as imaged by AFM and the formation of anti-phase boundaries in particular. Next, we consider the narrow component and its relation with mis…t dislocations.

Di¤use scattering

To quantity the broadening of the di¤use component in the two component rocking curves of Fig. 7.5, we use the method proposed by De Keijzer et al. [31] to separate the in‡uence of small L_k and large $®_!$. This method has been discussed comprehensively in a paper by Metzger et al [30]. They …t a pseudo-Voigt function, i.e. the convolution of a Cauchy (Lorentzian) $L(!)$ and Gaussian $G(!)$ peak shape,

$$I(!) = I_0 \, f´ L(!) + [1 ¡ ´] G(!)g, \qquad (7.2)$$

to the measured rocking curves $I(!)$. In this expression I_0 is a scaling intensity and $´$ $(0 \;\; ´ \;\; 1)$ is a measure for the "Lorentzianness" of the peak. Determining $´$, the

[3] The instrumental resolution of the rocking $(!)$ scans, as determined by measuring a Si wafer, is approximately 0:04±

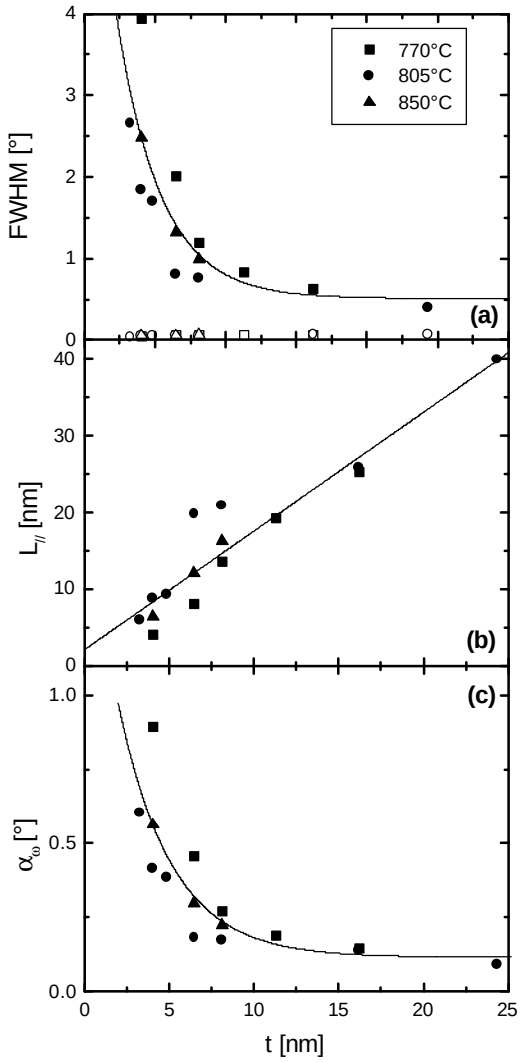

Figure 7.7: Substrate temperature (T_{sub}) dependence of the two component (005)-rocking curves (! scans) obtained on $YBa_2Cu_3O_{7-\delta}$ ...lms on SrO-terminated (100) $SrTiO_3$: (a) FWHM of the broad (solid symbols) and narrow (open symbols) as a function of ...lm thickness t; the FWHM of the broad component decreases exponentially to about 0.5±; while the FWHM of the narrow component is governed by the instrumental resolution (¼ 0:04±). Using the measured FWHM of the broad component, we calculate (b) the in-plane correlation length L_k and (c) the tilt angle ®! as a function of t; L_k increases linearly with t, while ®! saturates at 0.1±. The results do not strongly depend on T_{sub} within the range $770 < T_{sub} < 850$±C.

integral line width $\bar{}_! = \int I(!)d! / I(! = \mu_5)$ and the angular peak position μ_5, both L_k and $®_!$ can be calculated according to [30]:

$$L_k = \frac{0:9¸}{\bar{}_! (0:017475 + 1:500484´ ¡ 0:53156´^2) \sin \mu_5}, \quad (7.3)$$

$$®_! = \bar{}_! \left[0:18446 + 0:812692 \sqrt{1 ¡ 0:998797´ ¡ 0:659603´ + 0:44554´^2} \right]. \quad (7.4)$$

We follow a somewhat di¤erent approach for the broad component in our rocking curves. On the SrO-termination, the shape of the broad component is mainly Lorentzian and we assume that $´ = 0:95$. Similarly for the …lms on the TiO_2-termination (Gaussian), we assume that $´ = 0:05$. We then calculate L_k and $®_!$ as a function of the …lm thickness, see Fig. 7.6(b,c).[4] In agreement with our qualitative argument of the previous section, the narrowing of the broad component has a di¤erent origin on both type of substrates: on SrO-$SrTiO_3$ we …nd a small correlation length of about 25 nm (compared to 250 nm on TiO_2-$SrTiO_3$) and a small tilt angle of about 0.1± (compared to 1± on TiO_2-$SrTiO_3$).

Can we relate these results to the microstructure of the …lms? As shown in chapter 6, the initial stacking sequence on SrO-$SrTiO_3$ is di¤erent from the 123 stacking. Hence, there is some excess material present during nucleation. As discussed in paragraph 7.2.1, this causes the formation of point defects and/or planar defects which annihilate anti-phase boundaries. These defects are localized near the interface and are responsible for the small correlation length. Upon growing thicker …lms the contribution from this interface region becomes smaller and the correlation length increases [see Fig. 7.6(b)]. Calculating the temperature dependence of L_k and $®_!$ for …lms of di¤erent thickness on the SrO-termination, we …nd that both L_k and $®_!$ are approximately temperature independent, see Fig. 7.7(b,c). Within a range of 80±C (which is large in epitaxial …lm growth for a variation in substrate temperature), the same behavior is observed. The correlation length increases linearly with …lm thickness up to 40 nm for a 24.3 nm …lm, which is much smaller than the width of the substrate terraces (about 200 nm). On the other hand, the tilt angle saturates at an angle of about 0.1±. This angle is of the order of the miscut angle of the substrates used ($¼ \arctan(0:4=200) = 0:11^±$). Apparently, the miscut of the substrate is fully accommodated by point defects and/or stacking faults at the interface. In addition, as the o¤-stoichiometry is temperature independent, such a process is indeed expected to be relatively insensitive to the applied growth temperature. Therefore, we conclude that small defects at the interface are the origin of the small in-plane correlation length.

In contrast to …lms on SrO, the 123 stacking sequence is obeyed in …lms on the TiO_2-termination. Therefore, due to the absence of o¤-stoichiometries, the lateral correlation length is much larger ($L_k ¼ 250$ nm). In fact, L_k is of the order of the average terrace spacing of the substrate. In combination with the AFM observation that the substrate steps are reproduced by the …lm on top, it is tempting to corre-

[4] Note that $\bar{}_! = \text{FWHM} £ ¼=2$ for a Lorentzian peak shape; while $\bar{}_! = \text{FWHM} £ \sqrt{¼}=(2\sqrt{\ln 2})$ for a Gaussian.

late the XRD results for the TiO_2-termination with anti-phase boundaries nucleating at substrate steps. In such a picture, anti-phase boundaries cause rotational disorder (large $\Theta_\perp$). In general, anti-phase boundaries are annihilated when growing thicker and thicker by inserting double CuO chains [10]. Indeed, the observations that the substrate structure can no longer be traced back in thicker films (Fig. 7.1) in combination with the decrease in $\Theta_\perp$ [Fig. 7.6(c)] point to such an annihilation process. Moreover, Wen et al. [10] have observed both anti-phase boundaries and bending of the atomic planes in films on TiO_2-$SrTiO_3$ by high resolution transmission electron microscopy (HRTEM). However, the relation between rotational disorder and the occurrence of anti-phase boundaries is not clear to us at the moment. Additional cross sectional TEM measurements are necessary to identify the origin of the rotational disorder.

Specular scattering

An alternative method to determine whether peak broadening is due to small correlation length L_k or large tilt angle $\Theta_\perp$ is measuring the dependence on the scattering vector, i.e. measuring other orders of a reflection. Therefore, (00l)-rocking curves were recorded (with l = 2, 4 and 5). Peak broadening due to a finite in-plane correlation length is characterized by a constant width when measured in units of the parallel scattering vector $q_p = \frac{4\pi}{\lambda}(\cos\mu_5 - \cos\omega)$, while broadening as a result of rotational disorder yields a constant angular width [25]. In Fig. 7.8(a) (00l)-rocking curves are shown for a 16.2 nm $YBa_2Cu_3O_{7-\delta}$ thick film deposited on SrO-$SrTiO_3$. Indeed, plotting the normalized intensity versus the parallel scattering vector shows that the broad component does not depend on the order l of the reflection, suggesting that L_k is the limiting factor. On the other hand, the (00l)-rocking curves for a 165 nm thick film shown in Fig. 7.8(b) exhibit a constant width in angle space ($\phi\omega = \omega - \mu_5$), suggesting that for these films the disorder is purely rotational. In addition, strong specular scattering is not observed.

Miceli et al. [32] attributed a similar cross-over observed for the ErAs/GaAs system to the introduction of misfit-dislocations. In very thin films no misfit dislocations are introduced and in his model the weak disorder limit applies. In this limit, strong specular scattering occurs even for large l and the diffuse scattering is correlation length limited. In thicker films, misfit dislocations are present at the interface to relieve the strain. In this strong disorder limit, both weak specular scattering (quickly decreasing with l) and a diffuse component that is purely rotational in character are expected. This situation applies for the SrO-termination (see Fig. 7.8): only some minor disorder is present in the very thin films (point disorder and/or in-plane stacking faults and no extended defects), giving rise to both correlation length limited diffuse scattering and clear specular scattering. On the other hand, in thick films the disorder has a rotational character and no specular scattering occurs due to the presence of misfit dislocations. In fact, this also explains why the specular component is not observed for higher order reflections in thick $YBa_2Cu_3O_{7-\delta}$ films (l > 2), even when using synchrotron radiation [26].

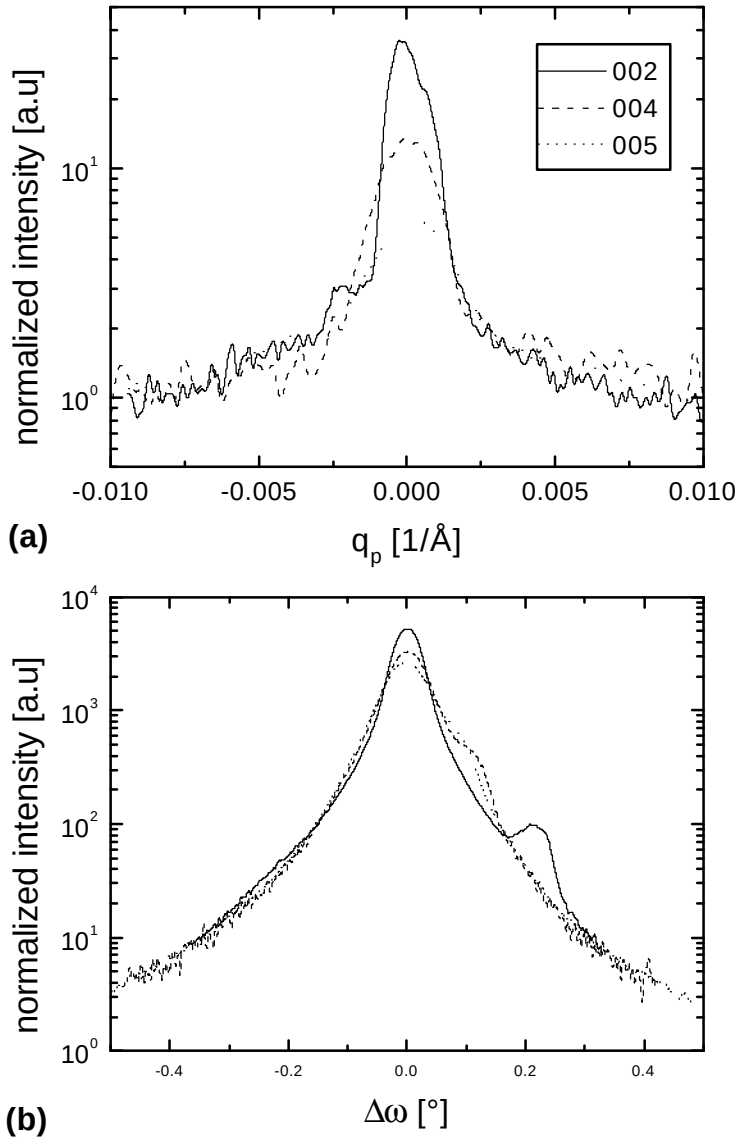

Figure 7.8: Normalized (00l)-rocking curves (! scans; l = 2, 4 and 5) of $YBa_2Cu_3O_{7\,i\,\pm}$ …lms on SrO-terminated (100) $SrTiO_3$: (a) a 16.2 nm thin …lm shows a constant width of the broad component as a function of the parallel scattering vector $q_p = \frac{4\pi}{\lambda}(\cos\mu_5 \,¡\, \cos !)$, characteristic for a small correlation length while (b) a 165 thick …lm exhibits a …xed width as a function of ¢! = ! ¡ μ_5, indicative of rotational disorder (specular scattering is not observed).

On the other hand, we argued that in $YBa_2Cu_3O_{7-\pm}$ …lms on the TiO_2-termination the disorder has already a rotational character (see Fig. 7.6), suggesting that the weak disorder limit does not fully apply here. Although we did not identify the microstructural origin of this rotational disorder unambiguously, additional defects obscure the e¤ect of mis…t dislocations on the shape of the broad component. However, the narrow component depends sensitively on the mis…t dislocation spacing [32]. Thus, the fact that the sharp peak in the (005)-rocking curves in Fig. 7.5 remains clearly visible during the combined structural and morphological transition in …lms on both terminations, indicates that mis…t dislocations are not yet introduced.
This conclusion has an important implication: strain relaxation occurs by forming coherent islands (i.e., islands that are essentially free of mis…t dislocation) at $t = t_c \acute{} t_{c;coh}$. Mis…t dislocation are induced at a later stage of growth ($t > 25$ nm), as evidenced by the disappearance of the sharp component, see Fig. 7.8. In the next section we explore both relaxation mechanisms in full detail.

7.3.2 The coherent Stranski-Krastanow growth mode

Already in the late eighties a structural discontinuity was deduced from re‡ective high energy electron di¤raction data in $YBa_2Cu_3O_{7-\pm}$ …lms on MgO substrates [33]. Later morphological studies using $SrTiO_3$ substrates were interpreted in terms of a classical Stranski-Krastanow (SK) transition [34]: island growth on top of a thin pseudomorphic wetting layer. In general, the SK-growth mode results from a competition between the elastic strain energy due to lattice mismatch and the substrate-…lm interaction energy extending over several monolayers [35]. Ignoring kinetic e¤ects and (…lm) surface energy, the energy E per unit area of a pseudomorphic layer (material A) of thickness t deposited on a substrate (material B) may be written as [35, 36]:

$$E(t) = \left[C\varepsilon^2 - \Phi_{AA} \right] t + c\phi. \qquad (7.5)$$

In this approach C is the Young's modulus of the …lm material, ε is the substrate-…lm mismatch ($\varepsilon = -0{:}012$ for our hetero-epitaxial system growing in the tetragonal phase), and c is the c-axis lattice constant of the …lm. The energy per unit volume of a thick pseudomorphic …lm is given by $C\varepsilon^2 - \Phi_{AA}$ (Φ_{AA} is the energy of bulk chemical AA bonds). At the interface the bonding energy between the substrate and …lm equals $-\Phi_{AB}$. Because of the wetting condition ($\phi = \Phi_{AA} - \Phi_{AB} < 0$), the total energy of the system is lowered and a ‡at layer is favored. As the strain energy of the pseudomorphic wetting layer increases with thickness, strain relaxation takes place at some critical layer thickness t_c and a 2D-3D transition occurs. Classically, relaxation occurs by introducing mis…t dislocations at $t_{c;mis}$ [6], where the release in strain energy balances the dislocation formation energy.
Fig. 7.9(a - d) clearly demonstrate the transition from pseudomorphic growth to 3D island growth, indicative of strain relaxation. Since the specular component in the (005)-rocking curve remains clearly visible during this transition (Fig. 7.5), we concluded that the mismatch strain is not accommodated by mis…t dislocations. Instead, strain relaxation takes place by the formation of coherently strained (i.e., free of mis-

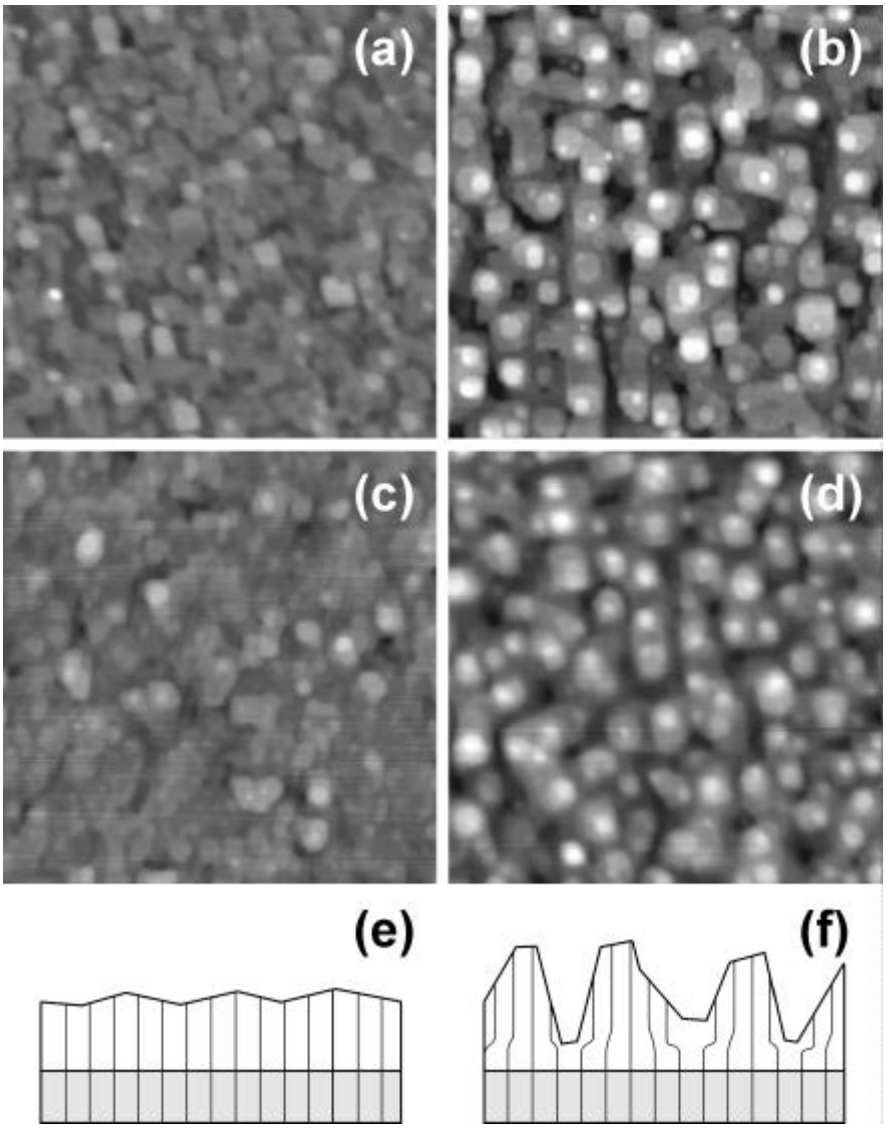

Figure 7.9: 1.0 x 1.0 $^1m^2$ AFM height images of $YBa_2Cu_3O_{7\,i\,\pm}$ …lms deposited at 805±C as a function of …lm thickness and (100) $SrTiO_3$ termination: (a) 4.9 and (b) 8.1 nm on SrO (height scale 15.0 nm); (c) 16.2 and (d) 19.5 nm on TiO_2 (height scale 22.5 nm). In (e,f) the self-organization of the …lm at $t_{c;coh}$ into coherent islands is schematically shown. As strain is concentrated at the edges of the coherent islands (f), the total energy is reduced with respect to the pseudomorphic state (e). However, the surface energy has increased somewhat in this roughening process. At a later growth stage ($t = t_{c;mis}$) the total energy of the coherent state (f) becomes so large that relaxation by mis…t dislocations is more favorable.

…t dislocations) islands above a thickness $t_{c;coh}$ [37, 38], see Fig. 7.9(e,f). Although the total …lm area increases (i.e., the surface energy increases), a signi…cant strain energy release is achieved by forming coherent islands which are more or less strain-free near their top and at the middle of their bases.

The coherent SK-growth mode has been extensively studied in semiconductor heterostructures [36, 39], where it is the cause for the formation of self-assembled quantum dots. Experimentally, it was found that the initial pseudomorphic layer thickness depends sensitively on both the size and the sign of the lattice mismatch [40]. The delay in coherent island formation in tensile systems was explained by strain induced enhancement of the surface step free energy. However, the e¤ect of the interface energy has not yet been addressed experimentally. Here, we introduce a new approach: as both strain energy $C\varepsilon^2 t$ and surface energy during pseudomorphic growth are the same in …lms growing on the SrO or TiO_2-termination, we can isolate the e¤ect of the substrate-…lm interaction energy. We attribute the termination dependence of $t_{c;coh}$ to a di¤erence in interaction between the two substrate terminating planes and the starting atomic layer of the …lm. Following Eq. (7.5) it is clear that a larger substrate-…lm interaction (more negative ¢) stabilizes a thicker wetting layer. Attributing the observed di¤erence in $t_{c;coh}$ to the di¤erence in ¢, the interaction for the two terminations can be compared in …rst approximation by looking at the stacking sequences. Assuming BaO[5] as the starting plane of the $YBa_2Cu_3O_{7-\delta}$ structure [41, 42], we have to consider the way it matches with the perovskite stacking of the substrate. Since BaO closely resembles SrO, it …ts almost perfectly on the TiO_2-termination, maintaining the perovskite con…guration. Continuation of the perovskite stacking on the SrO-termination is impossible and the BaO layer is shifted by $(\frac{1}{2},\frac{1}{2},0)$, forming a rocksalt interface con…guration [43]. Consequently, a smaller interface interaction is expected.

At this point, we must emphasis that the interface interaction may be slightly in‡uenced by the o¤-stoichiometries present in …lms on the SrO-termination. The absolute amount of defects is at most 20%, as estimated from the cation stoichiometry. However, this amount is not entirely concentrated at the interface, but in thicker …lms it is also accommodated in the next layers. In fact, the weaker interaction of the …lm with the SrO-termination as compared to the TiO_2-termination may be responsible for the observation that the vicinal steps in the substrate are so easily overgrown. The o¤-stoichiometry only helps in this accommodation process. In the remaining of this discussion, we concentrate on the e¤ect of the substrate-…lm interaction, rather than on the o¤-stoichiometry.

So far, we discussed our results from the viewpoint of energetics only. However, as follows from the drastic redistribution at $t_{c;coh}$, it is clear that the pseudomorphic layer is metastable. In order to break up this layer, adatoms have to be created and have to di¤use to form the coherent island structure. Such processes are thermally activated [44]. Indeed, we …nd that $t_{c;coh}$ decreases from 8.0 to 6.5 nm for the SrO-termination when increasing the temperature from 770 to 850±C. Moreover, we …nd

[5] As shown in chapter 6, BaO is the …rst atomic layer on both type of substrates, independently of the exact composition of the …rst monolayer (being either 122, 123 or 133).

that the density of 3D islands decreases exponentially with the growth temperature, independently of the termination. The obtained activation energy is 1.7 eV, which is in the range of typical activation energies for surface di¤usion [45]. This suggests that the di¤usion of (detached) adatoms determines the island size and thereby is a critical factor in the surface phase transition. Nevertheless, since we use identical deposition conditions for …lms on both terminations, we assume that the energy of the pseudomorphic layer at the instability thickness is the same for both terminations. From the condition $E(t_{c;coh}^{TiO_2}) = E(t_{c;coh}^{SrO})$, we obtain[6]

$$c\,(\gamma_{YBCO;TiO_2} - \gamma_{YBCO;SrO}) = \left(C\varepsilon^2 - \gamma_{YBCO}\right)\left(t_{c;coh}^{TiO_2} - t_{c;coh}^{SrO}\right). \qquad (7.6)$$

Estimating the Young's modulus C from the elastic sti¤ness constants c_{11} = 211 GPa and c_{12} = 93 GPa [46], according to [47]

$$C = \frac{(c_{11} - c_{12})(c_{11} + 2c_{12})}{(c_{11} + c_{12})}, \qquad (7.7)$$

we …nd an upper limit of $c\,(\gamma_{YBCO;TiO_2} - \gamma_{YBCO;SrO}) = 0{:}40\ J/m^2$ for the di¤erence in substrate-…lm interaction energy for the two terminations. This value is of the correct order of magnitude, since it is within the range of oxide surface energies (typically, 1 J/m^2 [47]).

The enhanced interface interaction for the TiO_2-termination extends the kinetically limited pseudomorphic growth regime. Clearly, at such large thicknesses, coherent islanding only occurs if mis…t dislocation formation is prohibited. Indeed, in complex oxides the activation energy for the formation of mis…t dislocations is huge. Using isotropic dislocation theory, it was calculated [48] that the activation energy to form a dislocation half-loop with a Burger's vector b = [101] is approximately 900 eV. The least conservative estimate, using anisotropic theory and b = [100], still yields an activation energy of 30 eV [49]. Therefore, homogeneous nucleation in these coherent layers is extremely unlikely. Moreover, the substrate-…lm interaction energy is not explicitly taken into account in any existing mis…t dislocation model, which therefore cannot explain the dependence of t_c on the termination.

Finally, the strain energy of the coherent islands rises again with increasing thickness. In general, this always results in the formation of mis…t dislocations at a later stage of growth. The edges of the coherent islands, a location where strain is highly concentrated [50], provide for a lowering of the dislocation formation activation energy. Indeed, from cross-section TEM observations on 120 to 140 nm thick …lms, we …nd that in these thick …lms dislocations accommodate the mis…t. The rocking curves of thick …lms adapt accordingly, see Fig. 7.8(b) and Ref. [26]. These mis…t dislocations must have formed at $t_{c;mis} > t_{c;coh}$. In fact, the observation of symmetric oscillations [51] in the 41.2 nm …lm of Fig. 7.3 suggests that full strain relaxation by mis…t dislocations has taken place, i.e. $t_{c;mis} < 41{:}2$ nm for the SrO-termination. As the coherent island structure formes earlier in …lms on the SrO-termination, mis…t

[6] Note that the …lm surface energy is the same for pseudomorphic (‡at) …lms on both terminations. Therefore, these surface energies cancel when equating the total energies of both …lms.

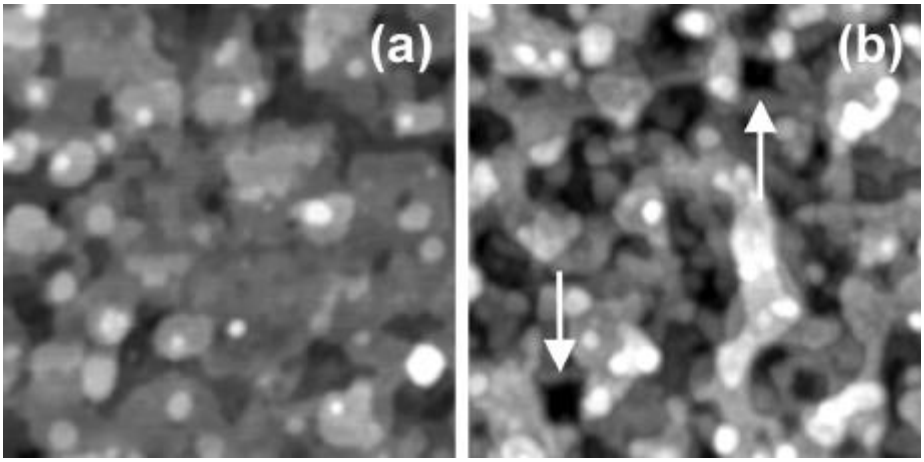

Figure 7.10: 0.5 x 0.5 $^{1}m^{2}$ AFM height images of 11.3 nm thick $YBa_2Cu_3O_{7\,i\,\pm}$ …lms deposited at 805±C on (a) TiO_2 ($t < t_{c;coh}$) and (b) SrO-terminated (100) $SrTiO_3$ ($t > t_{c;coh}$), both etched 5 s in 1% Br-ethanol to reveal dislocations (height scale 15.0 nm). Some sharp-bottomed, square etch pits are indicated by arrows (SrO only). As described in chapter 3, they develop at positions where threading dislocations have formed. Due to the presence of such dislocations, …lms on SrO etch much faster than …lms on TiO_2.

dislocation may be introduced in an earlier growth stage as compared to the TiO_2-termination. However, we did not identify the thickness at which mis…t dislocations are introduced.

In summary, we experimentally veri…ed the importance of the interface interaction for the pseudomorphic layer thickness in the $YBa_2Cu_3O_{7\,i\,\pm}$ / (100) $SrTiO_3$ system. In complex oxides, the large coherent layer thickness is favored due (i) the high interface energy and (ii) the large activation energy for mis…t dislocation formation. Our results show that coherent islanding also occurs in tensile, complex oxide systems. In general, the possibility to prepare a substrate in two surface terminations, allows for a study of the role of interface energy in the SK-growth mode at constant surface and strain energy. In fact, the usual way to study hetero-epitaxial growth (varying the mis…t energy by changing the composition of the overlayer [37]) is a much dirtier experiment, since the composition may also a¤ect the surface and interface energy [40].

7.3.3 Formation of threading dislocations

As strain is highly concentrated at the islands edges, the activation energy for introducing mis…t dislocations is substantially lowered at such locations [50]. Similarly, it has also been suggested [37, 38] that threading dislocations may form at the highly

strained island edges when they merge. In chapter 3 and 4 it was shown that such threading dislocations are the main origin of the high critical current density (10^{12} A/m^2) in high-T_c …lms. Indeed, these threading dislocation where found to originate near the substrate-…lm interface. Moreover, we have observed that the threading dislocations are situated in the trenches around the growth islands, independently of the substrate termination (see chapter 6). Hence, the merging of coherently strained islands is a likely mechanism by which threading dislocations are introduced during growth.
In chapter 4, it was also shown by means of cross-sectional TEM that most of these threading dislocations have a screw character. Therefore, such dislocations do not relieve the mis…t. To verify the relation between formation of threading dislocations and coherent islanding at $t_{c;coh}$, we wet-etched 11.3 nm thick …lms on both terminations in a dislocation speci…c etchand (see Fig. 7.10). The …lm on SrO ($t > t_{c;coh}$) shows some etch pit formation and is etched o¤ much more quickly, whereas the …lm on TiO_2 ($t < t_{c;coh}$) remains seemingly una¤ected. We conclude that threading dislocations are formed due to the merging of coherent islands at $t > t_{c;coh}$, see Fig. 7.11. Initially, the …lms adopt the lattice constant of the substrate and grow pseudomorphic [Fig. 7.11(a)]. At a certain …lm thickness $t_{c;coh}$, which depends on the substrate termination, strain relaxation occurs by forming coherent islands [Fig. 7.11(b)] that are heavily strained at their edges and are more or less strain free near their top and middle of their bases, see Fig. 7.9(e,f). In this 2D-3D roughening process, part of the original pseudomorphic layer breaks up again, showing that it is a kinetically limited metastable con…guration. Upon continuing the growth, the coherent islands merge [Fig. 7.11(c)]. At these points strain is highly concentrated, which lowers the activation energy for dislocation formation. As a result, threading dislocations are introduced at these locations (i.e., in the trenches around the islands).

In fact, this mechanism is closely related to the merging of misaligned growth fronts (island coalescence) as suggested by Schlom et al. [52]. The short-ranged lateral ordering of threading dislocations observed in chapter 3 is due to the lowered activation energy for dislocations at the edges of the self-assembled coherent islands. Since this island structure is kinetically determined, surface di¤usion is the key factor in tuning the dislocation density. By varying the deposition temperature, the island size can be manipulated and, correspondingly, the dislocation density. Hence, the mechanism for the formation of threading dislocations is now qualitatively explained.

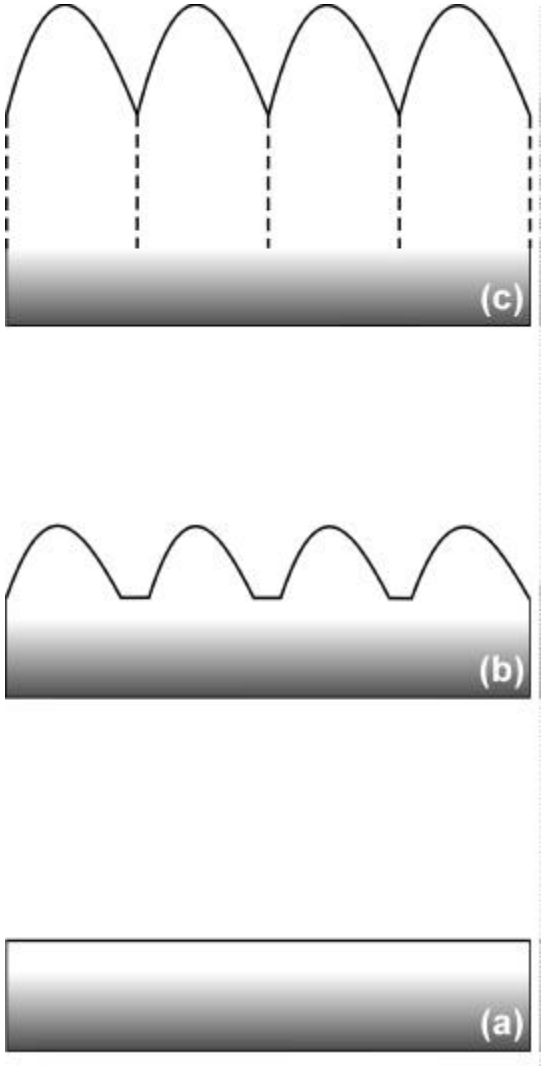

Figure 7.11: Schematic illustration of hetero-epitaxial growth and dislocation formation in $YBa_2Cu_3O_{7-\delta}$ films on (100) $SrTiO_3$: (a) pseudomorphic growth regime ($t < t_{c;coh}$), (b) coherent islanding above $t_{c;coh}$ including part of the original pseudomorphic layer and (c) threading dislocations (dotted lines) are introduced at the island edges when they merge. The substrate termination determines $t_{c;coh}$.

7.4 Conclusions

We introduce a new approach to study hetero-epitaxial growth, using thin …lms of $YBa_2Cu_3O_{7\,i\,\pm}$ on (100) $SrTiO_3$ substrates as a model system. By preparing either SrO or TiO_2-terminated substrates, the in‡uence of the interfacial energy is separated from the mis…t and surface energy. Combining atomic force microscopy and X-ray di¤raction measurements, we …nd that

(i) All …lms initially grow pseudomorphic (i.e., adopting the substrate lattice constant). Up to a critical thickness $t_{c;coh}$ the highly strained, pseudomorphic …lms remain tetragonal upon cooling down. The orthorhombic crystal structure only forms in …lms with a thickness $t > t_{c;coh}$, due to strain relaxation. This relaxation process is accompanied by a morphological transition: the initially ‡at almost featureless structure transforms into a 3D island morphology above $t_{c;coh}$. In other words, the …lms follow the Stranski-Krastanow growth mode. Remarkably, the critical thickness depends strongly on the substrate termination ($t_{c;coh}^{SrO}$ = 7:3 nm and $t_{c;coh}^{TiO_2}$ = 19 nm), showing the importance of interface energy in hetero-epitaxial growth. The substrate-…lm interaction energy is enhanced by 0.40 J/m^2 (upper limit) for the TiO_2-termination, stabilizing the thicker pseudomorphic layer.

(ii) In-plane XRD measurements reveal two components up to a …lm thickness of at least 25 nm. The di¤use component re‡ects the structural order of the individual crystallites and is related to defects at the interface introduced during nucleation. On the SrO-termination point-like disorder and/or in-plane stacking faults limit the in-plane correlation length. On the TiO_2-termination rotational disorder is found, which appears to be related to the occurrence of anti-phase boundaries. The specular component arises from spatially separated individual crystallites that scatter x-rays coherently, since the rotational disorder of these crystallites is bounded in magnitude by the substrate. As described by the model of Miceli et al. [32], the presence of the specular component indicates that mis…t dislocations are not yet present. Therefore, the 2D-3D roughening transition is a coherent strain relaxation process. In fact, $YBa_2Cu_3O_{7\,i\,\pm}$ …lms on (100) $SrTiO_3$ is the …rst hetero-epitaxial complex oxide system in which coherent Stranski-Krastanow growth is found. In addition, it is shown that the coherent islanding is kinetically limited.

(iii) In the case of coherent islanding, the strain energy also increases with increasing …lm thickness. Therefore, eventually mis…t dislocations are introduced. Although we did not exactly identify the thickness $t_{c;mis}$ at which this process occurs, it is clear that $t_{c;coh} < 25\,\text{nm} < t_{c;mis}$. All …lms with a thickness t À 25 nm exhibit identical island morphologies and microstructures, independently of the substrate termination.

In view of the results of Locquet et al. [5], who used epitaxial in-plane strain to raise the T_c, the pseudomorphic growth regime is extremely interesting. Complex oxides

favor a large pseudomorphic layer thickness due to the strong substrate-…lm interaction (and also the large activation energy for mis…t dislocation formation). Clearly, epitaxial strain e¤ects on T_c may bene…t from our observation that the substrate termination can be used as a tool to manipulate the substrate-…lm interaction.
Finally, we identi…ed the mechanism by which threading dislocations are introduced. Since strain is highly concentrated at the coherent island edges, they provide for a lowering of the dislocation formation activation energy. Therefore, the self-assembled coherent island structure favors the subsequent formation of threading dislocations. Indeed, we …nd only (non-mis…t relieving) threading dislocations in …lms exhibiting an islands structure (i.e., for $t > t_{c;coh}$). These threading dislocations act as ordered strong pinning sites for vortices in $YBa_2Cu_3O_{7\,i\,\pm}$ …lms.

References

[1] T. Ohnishi, K. Takahashi, M. Nakamura, M. Kawasaki, M. Yoshimoto, and H. Koinuma, Appl. Phys. Lett. 74, 2531 (1999)

[2] A.D. Polli, T. Wagner, T. Gemming, and M. Rühle, Surf. Sci. 448, 279 (2000)

[3] D.-W. Kim, D.-H. Kim, B.-S. Kang, T.W. Noh, D.R. Lee, and K.-B. Lee, Appl. Phys. Lett. 74, 2176 (1999)

[4] R.A. McKee, F.J. Walker, E.D. Specht, G.E. Jellison, Jr., L.A. Boatner, and J.H. Harding, Phys. Rev. Lett. 72, 2741 (1994)

[5] J.-P. Locquet, J. Perret, J. Fompeyrine, E. Machler, J.W. Seo, and G.V. Tendeloo, Nature (London) 394, 463 (1998)

[6] P. Politi, G. Grenet, A. Marty, A. Ponchet, and J. Villain, Phys. Rep. 324, 271 (2000)

[7] M. Kawasaki, K. Takahashi, T. Maeda, R. Tsuchiya, M. Shinohara, O. Ishiyama, T. Yonezawa, M. Yoshimoto, and H. Koinuma, Science 266, 1540 (1994)

[8] G. Koster, B.L. Kropman, G.J.H.M. Rijnders, D.H.A. Blank, and H. Rogalla, Appl. Phys. Lett. 73, 2920 (1998)

[9] J.G. Wen, T. Morishita, N. Koshizuka, C. Traeholt, and H.W. Zandbergen, Appl. Phys. Lett. 66 (1995) 1830

[10] J.G. Wen, C.Træholt and H.W. Zandbergen, Physica C 205, 354 (1993)

[11] T. Haage, J. Zegenhagen, J.Q. Li, H.-U. Habermeier, M. Cardona, Ch. Jooss, R. Warthmann, A. Forkl, and H. Kronmüller, Phys. Rev. B 56, 8404 (1997)

[12] Ch. Jooss, R. Warthmann, H. Kronmüller, T. Haage, H.-U. Habermeier, and J. Zegenhagen, Phys. Rev. Lett. 82, 632 (1999)

[13] Ch. Jooss, R. Warthmann, and H. Kronmüller, Phys. Rev. B 61, 12433 (2000)

[14] T. Terashima, Y. Bando, K. Iijima, K. Yamamoto, K. Hirata, K. Hayashi, K. Kamigaki and H. Terauchi, Phys. Rev. Lett. 65 (1990) 2684

[15] K. Kamigaki, H. Teauchi, T. Terashima, Y. Bando, K. Iijam, K. Yamamoto, K. Hirata, K. Hayashi, I. Nakagawa, and Y. Tomii, J. Appl. Phys. 68, 3653 (1991)

[16] O. Nakamura, E.E. Fullerton, J. Guimpel, and I.K. Schuller, Appl. Phys. Lett. 60, 120 (1992)

[17] B.E. Warren, X-Ray Di¤raction (Addison-Wesley, London, 1968)

[18] F.S. Galasso, Perovskites and High T_c superconductors (Gordon and Breach science publishers, New York, 1990)

[19] Q.D. Jiang, D.-M. Smilgies, R. Feidenhans'l, M. Cardona, and J. Zegenhagen, Sol. State Comm. 98, 157 (1996)

[20] A. del Vecchio, M.F. de Riccardis, L. Tapfer, C. Camerlingo, and M. Russo, J. Vac. Sci. Technol. A 18, 802 (2000)

[21] T. Nakamura, H. Inada, and M. Iiyama, Appl. Surf. Sci. 130-132 (1998) 576

[22] H.Y. Zhu and W.K. Chu, Appl. Phys. Lett. 76, 3469 (2000)

[23] P.F. Miceli, C.J. Palstrøm, and K.W. Moyers, Appl. Phys. Lett. 58, 160 (1991)

[24] P.M. Reimer, H. Zabel, C.P. Flynn, and J.A. Dura, Phys. Rev. B 45, 11426 (1992)

[25] T. Metzger, R. Höpler, E. Born, S.Christiansen, M. Albrecht, H.P Strunk, O. Ambacher, M. Stutzmann, R. Stömmer, M. Schuster, and H. Göbel, Phys. Stat. Sol. A 162, 529 (1997)

[26] W.-J. Lin, P.D. Hatton, F. Baudenbacher, and J. Santiso, Appl. Phys. Lett. 73. 2995 (1998)

[27] W.J. Lin, P.D. Hatton, F. Baudenbacher, and J. Santiso, Physica B 548, 56 (1998)

[28] W.J. Lin, P.D. Hatton, F. Baudenbacher, and J. Santiso, IEEE Trans. Appl. Supercond. 9, 1852 (1999)

[29] P.F. Miceli and C.J. Palstrøm, Phys. Rev. B 51, 5506 (1995)

[30] T. Metzger, R. Höpler, E. Born, O. Ambacher, M. Stutzmann, R. Stömmer, M. Schuster, H. Göbel, S.Christiansen, M. Albrecht, and H.P Strunk, Phil. Mag. A 77, 1013 (1998)

[31] T.H. de Keijzer, E.J. Mittemeijer, and H.C.F. Rozendal, J. Appl. Crystallogr. 16, 309 (1983)

[32] P.F. Miceli, J. Weatherwax, T. Krentsel, and C.J. Palstrøm, Physica B 221, 230 (1996)

[33] T. Terashima, Y. Bando, K. Iijima, K. Yamamoto, K. Hirata, K. Kamigaki, and H. Terauchi, Physica C 162-164, 615 (1989)

[34] X.-Y. Zheng, D.H. Lowndes, S. Zhu, J.D. Dubai, and R.J. Warmack, Phys. Rev. B 45, 7584 (1992)

[35] I. Daruka and A.-L. Barabási, Phys. Rev. Lett. 79, 3708 (1997)

[36] V.A. Shchukin and D. Bimberg, Rev. Mod. Phys. 71, 1125 (1999)

[37] C.W. Snyder, B.G. Orr, D. Kessler, and L.M. Sander, Phys. Rev. Lett. 66, 302 (1991)

[38] C.W. Snyder, J.F. Mans…eld, and B.G. Orr, Phys. Rev. B 46, 9551 (1992)

[39] See the April issue of MRS Bulletin 21 (1996)

[40] Y.H. Xie , G.H. Gilmer, C. Roland, P.J. Silverman, S.K. Buratto, J.Y. Cheng, E.A. Fitzgerald, A.R. Kortan, S. Schuppler, M.A. Marcus, and P.H. Citrin, Phys. Rev. Lett. 73, 3006 (1994)

[41] V.C. Matijasevic, B. Ilge, B. Stäuble-Pümpin, G. Rietveld, F. Tuinstra, and J.E. Mooij, Phys. Rev. Lett. 76, 4765 (1996)

[42] T. Haage, J. Zegenhagen, H.-U. Habermeier, and M. Cardona, Phys. Rev. Lett. 80, 4225 (1998)

[43] G. Koster, G. Rijnders, D.H.A. Blank, and H. Rogalla, Physica C 339, 215 (2000)

[44] H.T. Dobbs, D.D. Vvedensky, A. Zangwill, J. Johansson, N. Carlsson, and W. Seifert, Phys. Rev. Lett. 79, 897 (1997)

[45] B. Dam and B. Stäuble-Pümpin, J. Mater. Sci.: Mater. Electron. 9, 217 (1998)

[46] M. Bauer, F. Baudenbacher, and H. Kinder, Physica C 246, 113 (1995)

[47] K.-N. Tu, J.W. Mayer, and L.C. Feldman, Electronic Thin Film Science for Electrical Engineers and Materials Scientists (Macmillan, New York, 1992)

[48] B. Stäuble-Pümpin, V.C. Matijasevic, B. Ilge, J.E. Mooij, W.J.A.M. Peterse, P.M.L.O. Scholte, F. Tuinstra, H.J. Venvik, D.S. Wai, C. Træholt, J.G. Wen, and H.W. Zandbergen, Phys. Rev. B 52, 7604 (1995)

[49] B. Stäuble-Pümpin (private communication)

[50] A.G. Cullis, A.J. Pidduck, and M.T. Emeny, Phys. Rev. Lett. 75, 2368 (1995)

[51] W.-J. Lin, P.D. Hatton, F. Baudenbacher, and J. Santiso, Appl. Phys. Lett. 72. 2966 (1998)

[52] D.G. Schlom, D. Anselmetti, J.G. Bednorz, Ch. Gerber, and J. Mannhart, J. Cryst. Growth 137, 259 (1994)

Summary

The three primary characteristics of a type II superconductor are its critical temperature T_c, upper critical …eld H_{c_2} and critical current density j_c. Since the discovery of high temperature superconductors, T_c increased roughly by a factor of …ve and H_{c_2} remained in the hundreds of Tesla. The most spectacular increase was witnessed for j_c which increased by a factor of 10^5 since 1987. This is a direct consequence of the fact that j_c is essentially determined by imperfections. In a perfect superconductor the quantized vortices induced at high …elds are not pinned and start to move as soon as a transport current is fed through the superconductor. Structural defects act as pinning sites for vortices. Hence, up to certain limits, a structurally poor superconductor is more advantageous for high j_c.

This paradox is nicely illustrated in single crystals. Here, vortex pinning is governed by randomly distributed point defects. Such defects act as relatively weak pinning sites and a low j_c is observed. On the other hand, in structurally inferior thin …lms the vortex pinning is so strong that the theoretical limit for j_c comes into sight. The spectacular high currents of $YBa_2Cu_3O_{7\,i\,\pm}$ epitaxial …lms in combination with the relatively poor understanding of pinning in thin …lms are the main motivation for this Ph.D. research.

In this thesis, we answered the following three central questions:

1. What is the structural defect responsible for the extremely high superconducting currents that can be passed without dissipation in $YBa_2Cu_3O_{7\,i\,\pm}$ …lms?

We …nd that threading dislocations are the dominant pinning sites for vortices in $YBa_2Cu_3O_{7\,i\,\pm}$ thin …lms. Such dislocations extend from the substrate-…lm interface all the way up to the …lm surface in a direction parallel to the c-axis of the …lm. To reveal threading dislocations, we applied a suitable wet-chemical etchand. Upon etching …lms in Br-ethanol, sharp-bottomed square etch pits form at sites where dislocations emerge at the …lm surface. In combination with atomic force microscopy, a large part of the …lm can be investigated, which allows for an accurate determination of the dislocation density. Moreover, we …nd that the lateral dislocation distribution exhibits short-range ordering. In a large series of …lms with various dislocation densities, we observe a universal magnetic …eld dependence of the critical current density: the current remains constant up to a characteristic …eld B¤ and decays rapidly at higher …elds. Here, B¤ is directly proportional to the measured density of threading dislocations. In addition, the current density at low …elds is essentially independent of the dislocation density. These are exactly the characteristics of linear defect pinning. Indeed, we …nd threading dislocation by transmission electron microscopy.

The high pinning capability of threading dislocations arises for a number of reasons. First of all, a linear defect pins a vortex over a signi…cant length compared to the …lm thickness. In principle, vortices can even be pinned along their entire length. Secondly, a dislocation has the size of the normal core of the vortex. Hence, the full condensation energy is gained. Indeed, we …nd current densities up to 20% of the theoretical depairing current limit (at small magnetic …elds and low temperatures). At high …elds, there are more vortices than pinning sites. The additional vortices are less strongly pinned and j_c quickly decreases with increasing magnetic …eld. The cross-over between the two regimes occurs at B^{α}. Due to the short-range ordering of defects, the proportionality constant between B^{α} and the dislocation density is essentially equal to the ‡ux quantum at low temperatures. Finally, both j_c and B^{α} decrease with temperature as a result of the temperature dependence of the superconducting parameters and thermal ‡uctuations.
In fact, the ordering of the natural defects makes thin …lms completely di¤erent from single crystals containing randomly distributed arti…cial columnar defects. Apart from the larger j_c at low …elds, also the decrease in current density which magnetic …eld is slower in …lms. Hence, at high …elds the current densities that can be passed through …lms are even higher than in irradiated single crystals. We conclude that the intrinsic, self-organized defect structure of our pulsed laser deposited …lms is far better than the one created by brute force heavy ion bombardment.

2. What is the mechanism by which threading dislocations are induced during …lm growth?

We investigated a large number of mechanisms for introducing threading dislocations. Since the dislocations originate at or near the substrate-…lm interface, they must be induced either by the substrate or during the …rst stages of …lm growth. We …nd that the dislocation structure in the …lm is insensitive to the substrate-…lm lattice mismatch, vicinal steps in the substrate, the termination of the substrate and dislocations already present in the substrate material. Moreover, most threading dislocation are shown to be screw dislocations. Hence, they cannot be related to mis…t dislocations, twinning dislocation or (low-angle) grain boundaries. Such dislocations need to have an edge component.
Instead, the operative mechanism for dislocation formation is a result of the heteroepitaxial growth mechanism of $YBa_2Cu_3O_{7\ i\ \pm}$ …lms on (100) $SrTiO_3$ substrates. We …nd that the …lms follow the well-known Stranski-Krastanow growth mode. Initially, they grow in a 2D mode, adopting the in-plane lattice parameter of the substrate. The corresponding increase in elastic energy is compensated by the large substrate-…lm interaction energy. However, at a certain …lm thickness, the interface energy can no longer compensate the elastic energy and strain relaxation occurs. Surprisingly, strain relaxation does not take place in the classical way by introducing mis…t dislocations. Instead, coherent 3D islands (i.e., free of mis…t dislocations) form that are highly strained at the edges and are more or less stress free near their top and bases. Due to these strain concentrations, the activation energy for introducing dislocations is lowered at the coherent island edges. Threading dislocation are introduced at such

points when islands merge. Indeed, the short-ranged ordered threading dislocation distribution re‡ects the self-assembled island structure. We conclude that threading dislocations result from the peculiarities of the hetero-epitaxial growth mechanism.
In establishing the mechanism of dislocation formation, we developed a new method to obtain single terminated (100) $SrTiO_3$ substrates. By properly cleaning and annealing, it can now be prepared in the (metastable) SrO-termination. This method complements earlier methods to produce TiO_2-terminated substrates. In fact, tuning the substrate termination opens up a new approach to study hetero-epitaxial growth. By growing …lms on both termination, the interface energy is varied, independently of both the …lm surface energy and the substrate-…lm mis…t energy. We showed that the in‡uence of interface energy is severely underestimated in the growth of complex oxides. Depending on the termination, the …lm thickness at which coherent islanding of $YBa_2Cu_3O_{7-\pm}$ occurs can be delayed by a factor of 2.5 for the TiO_2-termination.

3. Can we control the growth process in such a way that we can tune the superconducting properties of the …lms?

We are now in the position to tune the characteristic magnetic …eld dependence of the critical current density $j_c(B)$ in our …lms. We …nd that $j_c(B)$ can be in‡uenced via the threading dislocation density. Inducing dislocations results in: (i) an extension of the plateau $B^¤$ up to which j_c remains constant ($B^¤$ is proportional to the dislocation density), (ii) a decrease of j_c at low magnetic …elds (the pinning energy reduces slightly due to a decrease in the overall structural quality of the …lms) and (iii) a faster decrease of j_c with increasing magnetic …eld at high …elds where $j_c \_ B^{®}$ (the power-law exponent changes from $® ¼ ¡\frac{1}{2}$ to $® ¼ ¡1$).
Tuning the dislocation density is achieved by controlling the coherent island structure. Since the island formation is kinetically determined, surface di¤usion is the relevant parameter. We showed that the substrate temperature is an easy accessible tool to adjust surface di¤usion, which allows for an adjustment of the dislocation density in both directions. By decreasing the substrate temperature, the density can be increased by almost two orders of magnitude, leaving the lateral defect distribution una¤ected. However, at too low substrate temperatures the critical temperature starts to go down. Depositing secondary phases on the bare substrate prior to the actual deposition can be used to add dislocations. When such precipitates are overgrown, dislocations form. On the other hand, so far we were not able to grow truly dislocation-free …lms by increasing the substrate temperature. Alternatively, dislocations can be annihilated by annealing at a temperature around the deposition temperature (typically 800±C) in an oxygen atmosphere. Moreover, the structural quality improves, which results in an increase of the j_c at low magnetic …elds to a truly universal value, independently of the dislocation density.

In conclusion, in this thesis we demonstrated the importance of knowing and controlling the defect structure of a material in order to understand its physical processes. In particular, detailed understanding of the physical properties of the $YBa_2Cu_3O_{7-\pm}$ / (100) $SrTiO_3$ hetero-epitaxial system is only possible if its microstructure is known.

Since the microstructure is formed during preparation (…lm growth), the growth conditions are vital in controlling the physical properties.

Samenvatting

Eén van de belangrijkste eigenschappen van een supergeleider is dat zijn elektrische weerstand verdwijnt beneden een zekere kritische ¡ zij het zeer lage ¡ temperatuur T_c. Dit betekent dat elektrische stromen zonder verliezen (dissipatie) kunnen worden getransporteerd! Naast T_c worden supergeleiders gekarakteriseerd door nog twee parameters: het kritische magneetveld H_{c_2} en de kritische (elektrische) stroomdichtheid j_c. Supergeleiding vindt alleen plaats beneden deze kritische waarden. Het zal duidelijk zijn dat het voor praktische toepassingen belangrijk is om T_c, H_{c_2} en j_c op de een of andere manier zo groot mogelijk te maken.
Met de ontdekking van de hoge-T_c supergeleiders in 1986 is T_c inmiddels een faktor vijf toegenomen tot zo'n 170 K (ongeveer ¡ 100±C), terwijl H_{c_2} onveranderd groot is gebleven (enkele honderden Tesla's). De meest spectaculaire toename is waargenomen voor j_c: maar liefst met een faktor 100.000! Dit is een direkt gevolg van het feit dat j_c wordt bepaald door defekten (kleine foutjes) in de stuktuur van de supergeleider. Dit kan men als volgt inzien. In deze supergeleiders dringt het magneetveld ¡ mits dit veld voldoende sterk is ¡ het materiaal binnen in de vorm van dunne buisjes. Deze buisjes omvatten elk een vaste hoeveelheid magneetveld en worden vortices genoemd. Als er nu tevens een elektrische stroom door de supergeleider wordt gestuurd, ondervinden de vortices een elektro-magnetische kracht. Hoe groter de stroom, des te sterker deze Lorentzkracht op de vortices. Onder invloed van de Lorentzkracht zullen vortices gaan bewegen. Omdat deze beweging dissipatie veroorzaakt, wordt de supergeleidende toestand echter teniet gedaan. In een struktureel perfekte supergeleider (dus zonder defekten) kunnen de vortices ongehinderd bewegen, zodat $j_c = 0$. Met andere woorden: elektrische stromen kunnen niet zonder dissipatie getransporteerd worden. Gelukkig zijn er in echte supergeleiders altijd defekten aanwezig, die de beweging van vortices belemmeren (...guur 1.2). Defekten houden de vortices als het ware vast (we noemen dit pinnen), zodat elektrische stromen toch zonder verliezen kunnen worden gestransporteerd. Dit gaat goed tot de kritische stroomdichtheid is bereikt (nu is $j_c > 0$).
Merkwaardig genoeg kan een struktureel "slechte" supergeleider dus een grotere elektrische stroom zonder verliezen transporteren dan een bijna perfekte supergeleider! Deze paradox komt duidelijk naar voren als we éénkristallen (die weinig en zeer kleine defekten bevatten) met dunne lagen (veel en grote defekten) van hetzelfde supergeleidende materiaal vergelijken. In een éénkristal is de belemmerende werking van de kleine defekten gering, waardoor de elektrische stroomdichtheid j_c die we door zo'n soort supergeleider kunnen sturen voordat de vortices gaan bewegen erg klein is. In dunne lagen daarentegen, pinnen de vele grote defekten de vortices zo sterk dat j_c de theoretische limiet benadert. Hierbij moet men denken aan stroomdichtheden van

de orde van 10.000 miljard Ampère per vierkante meter! Deze spectaculair grote stroomdichtheden zijn inderdaad waargenomen, bijvoorbeeld in dunne lagen van de hoge-T_c supergeleider $YBa_2Cu_3O_{7-\delta}$.
Omdat er nog relatief weinig bekend is over de defekten die verantwoordelijk zijn voor dergelijke grote stroomdichtheden heb ik mij hier in dit promotieonderzoek op geconcentreerd. Hoe zien de defekten eruit? Hoe ontstaan ze? Kunnen we de supergeleidende eigenschappen ¡ door middel van deze defekten ¡ kontroleren? Dit zijn de drie centrale vragen in dit proefschrift.

1. Welk defekt in de microstruktuur van dunne $YBa_2Cu_3O_{7-\delta}$ lagen is nu eigenlijk verantwoordelijk voor de grote elektrische stromen die zonder dissipatie getransporteerd kunnen worden?

In dit promotieonderzoek is naar voren gekomen dat lineaire defekten (zogenaamde dislokaties) verantwoordelijk zijn voor de grote stroomdichtheden. Deze dislokaties ontstaan op het grensvlak tussen het substraat en de dunne laag die daarop gedeponeerd is. Vervolgens lopen ze in een rechte lijn naar het oppervlak van de dunne laag in een richting loodrecht op het substraatoppervlak.
Om dislokaties in dergelijke dunne lagen "zichtbaar" te maken (de laagjes zijn ongeveer 0.0001 mm dik ¡ dat is vele malen dunner dan een haar), hebben we de volgende truc ontwikkeld. We dompelen de dunne laag enkele seconden in een chemisch oplosmiddel (een oplossing van Broom in zeer zuivere alcohol). Het gevolg is dat de dunne laag langzaam oplost (en dus nog dunner wordt). Overal waar dislokaties aan het oppervlak komen, lost de dunne laag net iets sneller op. Hierdoor ontstaan er vierkante putjes met een scherpe bodem in het oppervlak van de laag (zie bijvoorbeeld de voorkant van dit proefschrift). Ieder putje komt precies overeen met één dislokatie. Door nu met een speciale microscoop deze putjes te tellen, kunnen we de dichtheid aan dislokaties nauwkeurig bepalen. Bovendien zien we dat deze putjes min of meer geordend zijn: ze zitten bijna nooit vlak naast elkaar.
Vervolgens hebben we in een hele reeks dunne lagen met verschillende dichtheden aan dislokaties (putjes) de kritische stroomdichtheid j_c gemeten als functie van het magneetveld. Hierbij viel het ons al snel op dat alle dunne lagen zich min of meer hetzelfde gedragen. Voor kleine magneetvelden hangt j_c niet af van het magneetveld dat we aanleggen: we zien dus een plateau. Echter, boven een karakteristiek magneetveld B^* neemt j_c zeer snel af (...guur 3.9). Het blijkt nu dat de (gemeten) waarde van B^* direkt evenredig is met de (gemeten) dichtheid aan etsputjes (dislokaties). Bovendien zien we dat j_c voor alle dunne lagen bij magneetvelden kleiner dan B^* (de plateauwaarde) ongeveer gelijk is qua grootte (...guur 3.10). Dit zijn nu precies de twee karakteristieke eigenschappen die je verwacht wanneer de beweging van vortices belemmerd wordt door lineaire defekten. Immers, bij kleine magneetvelden zijn er weinig vortices en kan iedere vortex door een dislokatie op zijn plek vastgehouden worden. Het resultaat is een zeer grote j_c die niet afhangt van de hoeveelheid dislokaties (zolang het aantal vortices kleiner is dan het aantal dislokaties). Leggen we een sterker magneetveld aan, dan ontstaan er meer vortices. Op een gegeven moment zijn er meer vortices dan defekten en niet iedere vortex kan door een dislokatie vastge-

houden worden (er zijn immers niet genoeg defekten om alle vortices vast te houden). De vortices die niet door een dislokatie vastgehouden worden, kunnen gemakkelijker bewegen. Het gevolg is dat we minder stroom kunnen transporteren zonder verliezen. Met andere woorden: j_c neemt af bij grotere magneetvelden.
Gezien het bovenstaande is niet verbazend dat de waarde van B¤ voorspeld kan worden door de dichtheid aan dislokaties te vermenigvuldigen met de hoeveelheid magneetveld die een vortex draagt. Doordat de dislokaties geordend zijn hoeven bovendien geen extra numerieke faktoren in rekening te worden gebracht. Tot slot vermelden we nog dat we de dislokaties ook daadwerkelijk hebben waargenomen met speciale microscopie (gebruikmakend van elektronenstralen ¡ …guur 4.7).
Waarom kunnen nu juist lineaire defekten vortices zo stevig pinnen? Hiervoor zijn een aantal redenen. Ten eerste, omdat een dislokatie en een vortex parallel aan elkaar staan wordt een vortex over zijn gehele lengte (de dikte van laag) vastgehouden. Het is dus geen lokaal, maar een kollektief e¤ekt. Een tweede reden is dat de breedte van een vortex en een dislokatie van dezelfde orde van grootte zijn, waardoor de vortex ook nog eens over zijn gehele breedte wordt vastgehouden. Het gevolg is dat we stroomdichtheden meten die kunnen oplopen tot zo'n 20% van de theoretische limiet.
Naast dislokaties ¡ die altijd aanwezig zijn in dunne lagen ¡ is er nog een ander type lineaire defekten. Door een materiaal te beschieten met zeer zware, doch kleine deeltjes kun je "buisjes" aanbrengen waarbinnen het materiaal sterk wanordelijk is. Dergelijke buisjes zijn, net als dislokaties, ook over de gehele laag gecorreleerd. Het zijn dus ook lineaire defekten. Deze truc is inderdaad toegepast in éénkristallen (die geen dislokaties bevatten). Zoals te verwachten is, neemt j_c in éénkristallen zeer sterk toe door deze beschieting. Er zijn echter enkele belangrijke verschillen met dislokaties in dunne lagen. Dislokaties worden door de natuur geïntroduceerd. Je krijgt ze als het ware op de koop toe. Het beschieten is een kunstmatig proces dat veel energie (en dus geld) kost. In tegenstelling tot dislokaties, zijn deze kunstmatige defekten niet geordend. Het gevolg is dat j_c in …lms (dislokaties) veel minder snel afneemt dan in beschoten éénkristallen, wanneer we het magneetveld in sterkte laten toenemen. Met andere woorden: dunne lagen kunnen grotere stroomdichtheden transporteren dan dergelijke éénkristallen! Kennelijk is de intrinsieke, door de natuur geordende struktuur van dislokaties in dunne lagen veel e¢ciënter dan de struktuur van lineaire defekten die gecreëerd wordt door middel van "bruut" bombarderen.

2. Hoe worden de dislokaties precies gegenereerd tijdens het maken van de dunne $YBa_2Cu_3O_{7\,i\,\pm}$ lagen?

Omdat de dislokaties ontstaan aan het grensvlak tussen het substraat en de dunne laag komen zij óf voort uit het substraatmateriaal zelf óf vormen zij in de eerste stadia van de groei van de dunne laag. Experimenteel hebben we vastgesteld dat de dislokatiestruktuur ongevoelig is voor het verschil in roosterconstanten tussen het substraatmateriaal en de dunne laag, stappen in het oppervlak van het substraat, de buitenste laag atomen van het substraat en dislokaties die al in het substraat aanwezig zijn. Kennelijk hangen dislokaties in de dunne laag niet samen met het substraat, maar zijn ze het gevolg van een ¡ nog niet geïdenti…ceerd ¡ proces dat

optreedt tijdens het maken van dergelijk dunne lagen. Bovendien nemen we waar dat we te maken hebben met een bepaald type dislokaties: zogenaamde schroef dislokaties. Deze waarneming sluit direkt een groot aantal mogelijke mechanismen uit.
Hoe ontstaan dislokaties dan wel? Hiervoor moeten we in detail kijken naar hoe dergelijk dunne laagjes gemaakt worden (groeien). Uitgaande van een kaal substraat, groeit de laag steeds verder aan (en wordt dus dikker en dikker). We vinden dat de lagen de zogenaamde Stranski-Krastanow groei volgen. Dit houdt in dat de laag in eerste instantie zeer vlak blijft (we noemen dit 2-dimensionale groei). Hierbij neemt een extreem dun laagje de roosterconstante van het substraat over (...guur 7.9). Aangezien de laag hierdoor oprekt, kost dit elastische energie. Deze elastisch energie neemt alleen maar toe naarmate het laagje dikker wordt. Aan de andere kant wordt energie gewonnen doordat nu het substraat en de dunne laag zeer sterk aan elkaar gebonden zijn. Deze interaktie-energie is onafhankelijk van de dikte van de laag. Het gevolg is dat de 2-dimensionale groei slechts goed kan gaan tot een zekere laagdikte, namelijk zolang de interaktie-energie de elastische energie kan compenseren.
Normaal gesproken relaxeert de dunne laag dan door plastische deformatie. Wij vinden echter een ander proces: er treedt zeer sterke verruwing op (zogenaamde 3-dimensionale groei). Het ¡ in eerste instantie vlakke ¡ oppervlak van de dunne laag transformeert tot een struktuur van eilanden (een soort berglandschap). Deze eilanden zijn nog steeds elastisch gedeformeerd. Echter, omdat de deformatie nu zeer sterk geconcentreerd is aan de zijkanten van de eilandjes kost deze toestand veel minder elastische energie. Het belangrijkste gevolg is dat dislokaties zeer gemakkelijk geïntroduceerd kunnen worden op punten waar dergelijke eilanden bij elkaar komen (...guur 7.11). Dit verklaart direkt waarom de dislokatiestruktuur geordend is én samenhangt met de struktuur van de eilandjes (die ook geordend zijn). Kennelijk zijn de dislokaties een direkt gevolg van de merkwaardige groei van een dergelijke dunne laag op een ander, niet goed passend, materiaal (het substraat).
We zijn tot bovenstaande konklusie gekomen door op een slimme manier gebruik te maken van het buitenste laagje atomen van het substraatmateriaal $SrTiO_3$. Dit materiaal bestaat namelijk uit lagen SrO en TiO_2 die elkaar afwisselen. Er was al een methode bekend die TiO_2 als buitenste laag oplevert. Wij hebben een aanvullende methode ontwikkeld die SrO oplevert (...guur 6.1). Daarmee is het nu mogelijk geworden om de groei van twee verschillende materialen op elkaar te besturen volgens een compleet nieuwe methode. Door dunne lagen van hetzelfde materiaal op beide soorten substraten (dus buitenste laag SrO of TiO_2) te prepareren, variëren we slechts de grensvlakenergie tussen het substraat en de laag. De elastische energie en oppervlakte-energie van de dunne laag zijn in beide gevallen hetzelfde. Zodoende hebben we kunnen aantonen dat de grensvlakenergie een veel belangrijker parameter is dan men tot nu toe dacht. Voor dunne $YBa_2Cu_3O_{7\,i\,\pm}$ lagen bijvoorbeeld, kunnen we de overgang van 2 naar 3-dimensionale groei een faktor 2.5 (in laagdikte) vertragen door gebruik te maken van de grotere grensvlak-energie met TiO_2.

3. Kunnen we de preparatie van de dunne $YBa_2Cu_3O_{7-\pm}$ lagen op $SrTiO_3$ substraten zodanig kontroleren dat we de supergeleidende eigenschappen naar wens kunnen sturen?

Met al deze nieuw verworven kennis zijn we in staat om de magneetveldafhankelijkheid van de kritische stroomdichtheid $j_c(B)$ te sturen. We hadden al gevonden dat j_c constant is tot een zeker magneetveld B^{α}. Boven dit veld neemt j_c zeer snel af. We kunnen $j_c(B)$ nu beïnvloeden via de dislokatiedichheid. Als we meer dislokaties introduceren nemen we drie e¤ecten waar. Ten eerste wordt het plateau waarover j_c constant is steeds langer (zoals we in het voorgaande al zagen, neemt B^{α} toe met het aantal dislokaties). Ten tweede neemt de plateauwaarde van j_c bij magneetvelden kleiner dan B^{α} langzaam af. Dit komt omdat de sterkte waarmee dislokaties vortices kunnen vasthouden afneemt doordat de dunne laag als geheel slechter wordt.[1] Tot slot zien we dat de afname van j_c met toenemend magneetveld sneller gaat naarmate we meer dislokaties introduceren.
Hoe kunnen we nu de dislokatiedichtheid sturen? In het voorgaande hebben we gezien dat dislokaties onstaan op punten waar de 3-dimensionale eilanden bij elkaar komen. De grootte van de eilanden bepaalt dus de afstand tussen de dislokaties (en dus hun dichtheid - …guur 3.5). Deze eilandgrootte is kinetisch bepaald. Dit houdt in dat de afstand waarover atomen getransporteerd kunnen worden (ofwel kunnen di¤underen) afhangt van de temperatuur tijdens preparatie. Dit is dus de knop waaraan we moeten draaien om de gewenste dislokatiedichtheid in te stellen! Immers, bij een lage substraattemperatuur tijdens preparatie kunnen de atomen niet ver di¤underen en er ontstaat een struktuur van kleine eilandjes. Het gevolg is dat er veel punten zijn waar eilanden samenkomen en dus zullen er veel dislokaties ontstaan. Door de temperatuur te verlagen kunnen we meer dislokaties generen! Helaas gaat dit proces niet onbeperkt goed. Bij lage temperaturen begint één van de andere kritische parameters (T_c) sterk af te nemen. Een alternatieve methode om de dislokatiedichtheid toch verder te vergroten is om op het kale substrate zeer kleine deeltjes neer te leggen (zogenaamde precipitaten ¡ zie …guur 5.4). Als hieroverheen de dunne laag wordt aangebracht, ontstaan extra dislokaties op deze precipitaten.
In principe moet het nu ook mogelijk zijn om dunne lagen zonder dislokaties te maken (dat wil zeggen: zeer hoge temperaturen gebruiken). Tot op heden zijn we hier echter nog niet in geslaagd. Een methode die hierbij zou kunnen helpen is het langdurig nabehandelen van de dunne lagen in een oven bij zeer hoge temperaturen. We vinden namelijk dat dislokaties dan langzaam verdwijnen.

In dit proefschrift hebben we voor dunne $YBa_2Cu_3O_{7-\pm}$ lagen op $SrTiO_3$ substraten laten zien dat het uiterst belangrijk is om de microstruktuur (defekten) van dergelijke lagen goed in kaart te brengen. Alleen dan is het mogelijk op de fysische processen te

[1] Dit is eigenlijk niet in overeenstemming met hetgeen eerder vermeld werd (namelijk dat de plateauwaarde min of meer constant is). Echter, de geringe afname waarover we hier praten is het gevolg van de methode die we gebruiken om dunne lagen met veel dislokaties te prepareren: wanneer we meer dislocaties introduceren, wordt de …lm automatisch slechter (waardoor de plateauwaarde afneemt). Corrigeren we voor dit e¤ect, dan zien we dat de plateauwaarde inderdaad niet afhangt van de dislocatiedichtheid.

begrijpen. Aangezien de mikrostruktuur wordt gevormd tijdens preparatie, kunnen we ¡ gebruikmakend van de preparatiekondities ¡ nu zelfs de gewenste microstruktuur en dus de gewenste fysische eigenschappen instellen.

List of publications

1. B. Dam, J.H. Rector, J. Huijbregtse, and R. Griessen, Spiral growth in pulsed laser deposited $YBa_2Cu_3O_{7-\delta}$ films, Physica C 282-287 (1997) 559 - 560
2. Jeroen Huijbregtse, Fred Roozeboom, Jilt Sietsma, Johan Donkers, Ton Kuiper, and Erik van de Riet, High-frequency permeability of soft-magnetic Fe-Hf-O films with high resistivity, J. Appl. Phys. 83 (1998) 1569-1574
3. B. Dam, J.H. Rector, J. Johansson, J. Huijbregtse, and D.G. de Groot, Mechanism of incongruent ablation of $SrTiO_3$, J. Appl. Phys. 83 (1998) 3386 - 3389
4. B. Dam, J.H. Rector, J.M. Huijbregtse, and R. Griessen, The transition from 2D-nucleation to spiral growth in pulsed laser deposited $YBa_2Cu_3O_{7-\delta}$ films, Physica C 305 (1998) 1 - 10
5. J.M. Huijbregtse, B. Dam, F.C. Klaassen, G. Doornbos, R. van der Geest, R. Elberse, and R. Griessen, Strong pinning mechanisms in pulsed laser deposited $YBa_2Cu_3O_{7-\delta}$ films, in Advances in science and technology vol. 23: Science and Engineering of HTC superconductivity, edited by P. Vincenzini (Techna Srl., Faenza, 1999) 617 - 624
6. B. Dam, J.M. Huijbregtse, R. van der Geest, R. Elberse, J.H. Rector, S. Freisem, and J. Aarts, Dislocation specific etching of $YBa_2Cu_3O_{7-\delta}$ thin films, in Advances in science and technology vol. 23: Science and Engineering of HTC superconductivity, edited by P. Vincenzini (Techna, Faenza Srl., 1999) 637 - 645
7. F.C. Klaassen, J.M. Huijbregtse, B. Dam, R. van der Geest, G. Doornbos, J.H. Rector, R. Elberse, and R. Griessen, Strong pinning mechanisms in high-T_c superconducting $YBa_2Cu_3O_{7-\delta}$ thin films in Physics and Materials Science of Vortex States, Flux Pinning and Dynamics, edited by R. Kossowsky, B. Bose, V. Pan, and Z. Durusoy (Kluwer Academic, Dordrecht, 1999) 331 - 343
8. B. Dam, J.M. Huijbregtse, F.C. Klaassen, R.C.F. van der Geest, G. Doornbos, J.H. Rector, A.M. Testa, S. Freisem, J.C. Martinez, B. Stäuble-Pümpin, and R. Griessen, Origin of high critical currents in $YBa_2Cu_3O_{7-\delta}$ superconducting thin films, Nature (London) 399 (1999) 439 - 442
9. Oorsprong van de hoge kritische stromen, Nederlands Tijdschrift voor Natuurkunde 65 (1999) 230-231

10. R. Surdeanu, R.J. Wijngaarden, E. Visser, J.M. Huijbregtse, J.H. Rector, B. Dam, and R. Griessen, Kinetic roughening of penetrating ‡ux fronts in high-T_c thin …lm superconductors, Phys. Rev. Lett. 83 (1999) 2054 ¡ 2057

11. J.M. Huijbregtse, B. Dam, J.H. Rector, and R. Griessen, High-quality o¤-stoichiometric $YBa_2Cu_3O_{7\,i\,\pm}$ …lms produced by di¤usion-assisted preferential laser ablation, J. Appl. Phys. 86 (1999) 6528 ¡ 6537

12. J.M. Huijbregtse, F.C. Klaassen, R.C.F. van der Geest, B. Dam, and R. Griessen, Growth-induced strong pinning sites in laser ablated $YBa_2Cu_3O_{7\,i\,\pm}$ …lms with a non-random distribution, J. Low Temp. Phys. 117 (1999) 663 ¡ 667

13. F.C. Klaassen, G. Doornbos, J.M. Huijbregtse, B. Dam, and R. Griessen, Critical current density and dynamical relaxation rate below the matching …eld in thin …lms of $YBa_2Cu_3O_{7\,i\,\pm}$, J. Low Temp. Phys. 117 (1999) 1549 ¡ 1553

14. J.M. Huijbregtse, B. Dam, R.C.F. Van der Geest, F.C. Klaassen, R. Elberse, J.H. Rector, and R. Griessen, Natural strong pinning sites in laser ablated $YBa_2Cu_3O_{7\,i\,\pm}$ thin …lms, Phys. Rev. B 62 (2000) 1338 ¡ 1349

15. John T. Markert, Troy C. Messina, Bernard Dam, Jeroen Huijbregtse, Jan H. Rector, and Ronald Griessen, Laser-ablated thin …lms of in…nite-layer compounds and related materials, in Proceedings of SPIE Vol 4058: Superconducting and Related Oxides: Physics and Nanoengineering, edited by David Pavuna and Ian Bozovic (2000) 141 ¡ 152

16. I.A. Khrebtov, B. Dam, A.D. Tkachenko, F.C. Klaassen, J.M. Huijbregtse, and K.V. Ivanov, YBCO …lms on $SrTiO_3$ substrates with recordly low 1/f noise for bolometer applications, in Proceedings of the 4th European Workshop on Low Temperature Electronics-Wolte 4 (2000) 335 ¡ 339

17. I.A. Krebtov, A.D. Tkachenko, K.V. Ivanov, B. Dam, F.C. Klaassen, and J.M. Huijbregtse, The noise characteristics of YBCO …lms with strong pinning, Techn. Phys. Lett. 26 (2000) 1078 ¡ 1080

18. Rinke J. Wijngaarden, R. Surdeanu, J.M. Huijbregtse, J.H. Rector, B. Dam, J. Einfeld, R. Wördenweber, and R. Griessen, Pattern formation due to nonlinear vortex di¤usion, Physica C 341-348 (2000) 1011 ¡ 1014

19. M. Pannetier, R.J. Wijngaarden, R. Surdeanu, J.M. Huijbregtse, K. Heeck, B. Dam, and R. Griessen, Magneto-optical observation of the in‡uence of an arti…cial periodic magnetic pattern on the pinning of a $YBa_2Cu_3O_{7\,i\,\pm}$ …lm, Physica C 341-348 (2000) 1019 ¡ 1022

20. F.C. Klaassen, G. Doornbos, J.M. Huijbregtse, B. Dam, and R. Griessen, Vortex pinning regimes in thin …lms of $YBa_2Cu_3O_{7\,i\,\pm}$, Physica C 341-348 (2000) 1463 ¡ 1464

21. J.M. Huijbregtse, B. Dam, F.C. Klaassen, J.H. Rector, and R. Griessen, $YBa_2Cu_3O_{7-\delta}$ films with self-organized natural linear defects, Physica C 341-348 (2000) 1985 - 1986

22. J.T. Markert, T.C. Messina, B. Dam, J. Huijbregtse, J. Rector, and R. Griessen, Observation of step-flow growth in laser-ablated thin films of the T'-phase compound Pr_2CuO_4, Physica C 341-348 (2000) 2355 - 2356

23. B. Dam, J.M. Huijbregtse, R.C.F. van der Geest, F.C. Klaassen, J.H. Rector, R. Elberse, and R. Griessen, Controlling the natural strong pinning sites in laser ablated $YBa_2Cu_3O_{7-\delta}$ thin films, Physica C 341-348 (2000) 2327-2330

24. J.M. Huijbregtse, J.H. Rector, and B. Dam, Effect of the two (100) $SrTiO_3$ substrate terminations on the nucleation and growth of $YBa_2Cu_3O_{7-\delta}$ thin films, accepted for publication in Physica C

25. F.C. Klaassen, G. Doornbos, J.M. Huijbregtse, R.C.F. van der Geest, B. Dam, and R. Griessen, General features of vortex pinning by natural linear defects in thin films of $YBa_2Cu_3O_{7-\delta}$, submitted to Phys. Rev. B

26. J.M. Huijbregtse, B. Dam, B.J. Kooi, A. Mendoza, J.H. Rector, J.Th.M. de Hosson, and R. Griessen, Coherent Stranski-Krastanow growth of $YBa_2Cu_3O_{7-\delta}$ on single terminated (100)$SrTiO_3$, to be submitted to Phys. Rev. B

27. J.M. Huijbregtse, F.C. Klaassen, A. Szepielow, J.H. Rector, B. Dam, R. Griessen, B.J. Kooi, and J.Th.M. de Hosson, Vortex pinning in $YBa_2Cu_3O_{7-\delta}$ thin films: identifying the contributions from dislocations, grain boundaries, surface roughness, twin boundaries and point defects, to be submitted to Supercond. Sci. Technol.

Cirruculum Vitae

Jeroen Marcel Huijbregtse werd geboren op 16 juni 1972 te Middelburg. In 1990 voltooide hij het Gymnasium-¯ aan de Stedelijke Scholengemeenschap Middelburg om vervolgens aan zijn studie Materiaalkunde aan de Technische Universiteit in Delft te beginnen. Gedurende deze opleiding werd zijn interesse voor fysica steeds duidelijker. Dit resulteerde in een afstudeerproject binnen de sectie metaalfysica van prof.dr.ir. A. van den Beukel op het gebied van zachtmagnetische dunne …lms voor eventuele toepassing in digitale videokoppen. Het experimentele werk werd uitgevoerd tijdens een negen maanden durende stage bij Philips Research te Eindhoven in de groep Magnetisme van dr. F. Greidanus. In augustus 1996 studeerde hij hierop met lof af. Bovendien werd hem voor dit afstudeeronderzoek ¡ getiteld Soft magnetic FeHfO …lms with a high resistivity: structural investigations and high frequency permeability calculations ¡ de prijs voor "de beste afstudeerder van de studierichting Materiaalkunde in het studiejaar 1995-1996 aan de Technische Universiteit Delft" toegekend. In september 1996 begon hij vervolgens aan zijn promotieonderzoek in de vakgroep Vaste Stof Fysica van prof.dr. R. Griessen aan de Vrije Universiteit te Amsterdam onder direkte beleiding van dr. B. Dam. De resultaten van dit promotieonderzoek zijn vastgelegd in dit proefschrift. Op 1 maart treedt hij als Designer in dienst bij ASM Lithography te Veldhoven in de groep Process Overlay.

The author was born on June 16, 1972 in Middelburg, the Netherlands. After …n-ishing the secondary school in 1990 (Stedelijke Scholengemeenschap Middelburg) he continued his education at the Technical University Delft. Here, he studied Materials Science at the Faculty of Chemical Technology and Materials Science. During his studies, he was more and more attracted towards Physics. As a result, he performed his …nal research project in the group Physics of Metals of prof.dr.ir. A. van den Beukel, entitled Soft magnetic FeHfO …lms with a high resistivity: structural investigations and high frequency permeability calculations. At that time, such …lms were good candidates for application in digital magnetic video recording heads. The experimental work was performed at Philips Research in Eindhoven (the Netherlands) in the group Magnetism of dr. F. Greidanus. He graduated successfully in August 1996 and, in addition, he won the prize for the best graduation of that year at the Materials Science department in Delft. Subsequently, in September 1996 he started his Ph.D. research in the group Condensed Matter Physics of prof.dr. R. Griessen at the Vrije Universiteit in Amsterdam (the Netherlands) under supervision of dr. B. Dam. The results of this research project are described in the present Ph.D. thesis. On March 1, 2001 he starts working as a Designer at ASM Lithography in Veldhoven (the Netherlands) in the group Process Overlay.

Dankwoord

Ongelofelijk, maar het is al weer (ruim) vier en een half jaar geleden dat ik aan mijn promotieonderzoek begon in de vakgroep Vaste Stof Fysica. Ik heb het in die tijd niet alleen uitstekend naar mijn zin gehad, maar ook ontzettend veel geleerd. Op deze plaats wil ik de mensen bedanken die hieraan hebben bijgedragen.
In de eerste plaats Ronald, mijn promotor, voor het gestelde vertrouwen en het mogelijk maken van mijn promotie. Jouw fysisch inzicht en kritische blik hebben een belangrijke bijdrage geleverd aan dit proefschrift. Ik zal de speurtocht naar de exacte oplossing van onze di¤erentiaalvergelijking niet snel vergeten.
Vooral van Bernard, mijn copromotor en directe begeleider, heb ik heel veel opgestoken. Aan de informele kelderbesprekingen samen met jou en Jan (de "basement bikkels") bewaar ik prettige herinneringen. Hier werden de ideeën geboren waarop dit proefschrift gebaseerd is. Jouw enthousiasme en stimulans tot het schrijven van artikelen hebben er toe geleid dat we zo'n produktief team vormden! Je passie voor Italië (en Italiaans koken) heeft aanstekelijk gewerkt: na ons reisje naar Florence ben ik voorgoed verkocht. Ook Jan, de therapeutische junior scientist, ben ik erg dankbaar voor deze samenwerking en zijn eenvoudige oplossingen (waarom moeilijk doen als het ook makkelijk kan?) voor de talloze problemen, niet alleen op het technische vlak.
Zonder mijn "tweeling" promovendus Frodo had dit proefschrift er totaal anders uit gezien. We onderzochten hetzelfde probleem vanuit een verschillende invalshoek. Ik denk dat we hebben bewezen hoe vruchtbaar een dergelijke samenwerking kan zijn. Succes met je promotie!
Hoewel ik redelijk onafhankelijk heb gewerkt van de "Switchable Mirrors" groep (op een enkel irreversibel schakelexperiment van H_2 met YBaCuO na), wil ik hen toch expliciet bedanken voor hun bijdrage aan de goede sfeer binnen en buiten de vakgroep: Sense Jan (de andere Roberto Carlos van Premium Quality), Marcel (heeeh!) en natuurlijk mijn ex-kamergenoot Jacob (keeltje smeren?).
Veel dank ben ik verschuldigd aan de vele studenten die ik de afgelopen jaren heb begeleid bij hun afstuderen of stage. Ronny heeft, met gevaar voor eigen leven, etsen doorontwikkeld tot een reproduceerbaar proces. In het daaropvolgende tijdperk Remko hebben we hier de vruchten van geplukt. Het was een genoegen om jullie te begeleiden! Het werk van Mark is niet expliciet in dit proefschrift naar voren gekomen. Toch wil ik hem bedanken voor zijn tomeloze inzet en enthousiasme. Finally, I should not forget the ¡ in arbitrary order ¡ social and scienti…c contributions from our foreign students Pia and Agnieszka. Thank you all!
Wat is onze vakgroep zonder Gerrie, Nico en de ¡ door Kier geregeerde ¡ ko¢epauze? Juist ja, een chaos. John: I greatly enjoyed your stays in Amsterdam (it did not sink into the sea, you know!). Thanks for the nice time in Austin, Texas. Uiteraard ook

Radu, Chris, Gerben en alle andere (ex-)promovendi, post-docs, sta‡eden, studenten en gasten die ik niet bij name genoemd heb.

Tot slot wil ik mijn ouders en Floor bedanken voor hun onvoorwaardelijke steun in alle fasen van mijn promotietijd.